A Census of Hidden Nuclei in Radio Galaxies

Joanna McAllister

Doctor of Philosophy
The University of Edinburgh
2000

This thesis is my own composition except where indicated in the text.

June 7, 2000

Acknowledgements

I'll try not to make this long list of 'thankyous' resemble an Oscar speech, but I would still like to thank a lot of people both for helping me with my work and for making my first three years in Edinburgh so pleasant. Firstly I'd like to thank my supervisor John Peacock for being so patient with me and putting up with endless interruptions when I had "just a quick question" to ask him. I'd also like to thank various other Observatory folks: Raul Jimenez, Dave Bowen and Ross McLure for lending me programs, spectra and figures, which have helped speed up the completion of this thesis; Omar Almaini, Marek Kukula, Isobel Hook, Susie Ramsay, Paulina and Licia for many useful discussions.

In my first year, Mike and Bill spent many happy hours tormenting me and making me feel at home, thanks. I'd like to give Mike an extra special thankyou, not only for the numerous cups of tea he made to get me out of bed in the mornings, when we shared a flat together, but for his pedantic reading through of my thesis even once he'd left Edinburgh and was living in Germany. I'd also like to thank various non–Observatory people: Viv, for letting me borrow her car, letting me live in her flat and for dragging me up hills; Salyen, for looking after me in various orchestras when I didn't know any else there; Tom, Ross and Roger, for putting up with me never being around the flat for two years; and finally the ladies squash team (and Richard) for actually getting promoted and getting to the BUSA semi–finals under my captaincy.

I'd like to thank my family for supporting me, both emotionally and financially over the past few years and my godfather, John Hilton and his wife Kate for their uncanny knack of providing financial help, which appeared in the post just as I was beginning to think I was going to have to start liking lentils.

Finally I'd like to thank Pete for being, as Mary Poppins would say, Practically Perfect in Every Way.

Abstract

There is now convincing evidence from imaging and polarization studies that the appearance of Active Galactic Nuclei (AGN) depends strongly on orientation. This thesis proposes to address this question by imaging a sample of low–redshift radio–selected galaxies in the infrared, where the obscuration due to dust is reduced, in the hope of providing an unbiased survey of the line–of–sight extinctions towards AGN and the relative numbers of hidden sources. The low redshift of the sample allows the study of similar luminosity Fanaroff–Riley class I and class II sources, with the opportunity to explore the nuclear luminosity function of lower luminosity objects than in previous studies.

Infrared K and L' images were obtained for 28 galaxies. The non–thermal nuclear contribution to the K band flux is then estimated by subtracting a fitted two–dimensional surface brightness galaxy model from each image. The stellar contribution to the L' flux is estimated by fitting simple stellar population models to the optical spectra of a subsample of the objects and calculating the infrared $K - L'$ colour of these fitted populations. Optical spectra were obtained for 13 objects in the sample.

The reddening towards the nucleus is calculated by subtracting the intrinsic $K-L'$ colour of a quasar or starburst from the observed value. Nuclear sources are detected in 10 members of the sample. The intrinsic luminosities of all these sources would put them above the quasar/Seyfert dividing line of $M_V < -23$, making them possible candidates for obscured radio–loud quasars. The correlation between extinction and orientation is then explored. The expected anti–correlation between core–to–lobe ratio R and extinction is not apparent, whilst a possible correlation between extinction and galaxy size is observed, larger galaxies appearing to contain more dust.

Contents

List of Figures

List of Tables

List of Abbreviations

AGN	Active galactic nuclei
BLR	Broad line region
BLRG	Broad line radio galaxy
CCD	Charge–coupled device
CSS	Compact steep spectrum
DWMG	Djorgovski, Weir, Matthews & Graham, 1991
EELR	Extended emission–line region
FR I/II	Fanaroff–Riley radio source, type I/II
FSRQ	Flat spectrum radio quasar
FWHM	Full width half maximum
HST	Hubble Space Telescope
IDS	Image dissector scanner
IMF	Initial mass function
IRAF	Image reduction and analysis facility
IRAS	Infrared Astronomical Satellite
LINER	Low ionisation nuclear emission–line region
MDO	Massive dark object
NLRG	Narrow line radio galaxy
NLXG	Narrow line X–ray galaxy
O1	Owen & Laing, 1989
O2	Owen & White, 1991
OVV	Optically violent variable
PSF	Point spread function
RG	Radio galaxy
RLQ	Radio loud quasar
RQQ	Radio quiet quasar
SSP	Simple stellar population

SSRQ	Steep spectrum radio quasar
Sy 1/2	Seyfert galaxy, type 1/2
UKIRT	United Kingdom Infrared Telescope
ULIRG	Ultra–luminous infrared galaxy
WHT	William Hershel Telescope

Chapter 1

Introduction

There is now convincing evidence that the appearance of active galactic nuclei (AGN) depends strongly on orientation. This thesis proposes to address this question by imaging a sample of low–redshift radio–selected galaxies in the infrared, where the obscuration due to dust is reduced. This is done in the hope of providing an unbiased survey of the line–of–sight extinctions towards AGN, and therefore of measuring the relative numbers of hidden sources.

This introductory chapter will begin by explaining briefly the history of research into AGN over the last century. AGN are highly luminous right across the electromagnetic spectrum from the radio regime to hard X–rays, so as different parts of the spectrum have revealed themselves owing to improvements in technology, so too have the different properties of active galaxies at these wavelengths. This has produced a confusing array of names for objects, depending on their observed properties at various wavelengths, with the nomenclature often being of a more historical than physical origin.

Only very recently, with the advent of sensitive telescopes at all wavelengths are the different pieces of the jigsaw being fitted together successfully into a unified scheme for AGN (Urry & Padovani 1995 and Antonucci 1993). The basic idea is that all AGN are essentially the same object being viewed from different orientations. In the centres of these objects are supermassive ($M > 10^6\,M_\odot$) black holes surrounded by accretion disks of matter spiralling into the hole. As the matter falls into the deep gravitational potential well of the black hole it heats up; potential energy is converted into kinetic energy, resulting in the highly luminous radiation seen in quasars. There also exists a ring of dust, or torus,

around the accretion disk which causes the emitted radiation to be attenuated at wavelengths which are susceptible to absorption, such as the UV and the optical. The torus therefore causes the asymmetry seen between different classes of AGN.

The current observational evidence for supermassive black holes as the central engines of AGN is discussed in section 1.2, the evidence which points towards some kind of axisymmetric obscuration around the central engine is then covered in section 1.3. There are still many questions remaining that require answers, such as understanding the connections between AGN/black hole formation and galaxy formation. A summary of unanswered questions is given in section 1.5.3.

If the unified scheme for radio–loud objects is to stand the test of time then obscured quasar nuclei must be present in the centres of radio galaxies. The difficulties in observing these directly come from uncertain knowledge of the nuclear stellar populations in radio galaxies, which can make galaxy nuclei intrinsically red. The most recent work on finding obscured nuclei is reviewed and also the current understanding of the stellar populations of elliptical galaxies before outlining the work involved in this dissertation.

1.1 The history and taxonomy of AGN

The history of active galaxies began when Fath (1908) took an optical spectrum of NGC 1068 and discovered emission lines in its spectrum, these lines were not found in the spectra of "normal" galaxies. In the following years the progress in understanding these objects was slow, more emission–line galaxies were discovered, but it was not until Seyfert (1943) that these objects became a distinct class which are now known as Seyfert galaxies. The spectra of these objects all had broad emission lines of varying widths > 1000 kms^{-1} and an unresolved stellar–like core. An understanding of the physical processes behind the observations was attempted by Woltjer in 1959. He noted that the stellar–like nuclei were unresolved and therefore must be contained within the central 100 pc of the Seyfert galaxies. From virial arguments $\mathrm{M} \simeq v^2 r/G$ where $v > 1000\,\mathrm{kms}^{-1}$ and $r < 100\,\mathrm{pc}$, the nuclei must also be massive $\mathrm{M} \sim 10^9\,\mathrm{M}_\odot$. He also made initial estimates of the lifetime of the process creating this unusual emission: from the fact that Seyfert nuclei were found in about 1 in 100 spiral galaxies and an age of the Universe of the order of 10^{10} years he estimated that the nuclear emission

must last for at least 10^8 years. This assumes that all spiral galaxies go through a Seyfert phase and is therefore a lower limit on the lifetime.

Many more Seyfert galaxies were discovered in the following years until in 1974 a new slightly more complicated classification scheme was introduced by Khachikian & Weedman (1974). Class 1 Seyferts (Sy1) have broader Balmer (permitted) lines than forbidden lines, whilst class 2 Seyferts (Sy2) have all lines of about the same width. Broad emission lines are caused by emission from fast moving clouds of gas. A single cloud has a radial velocity causing the emission from it to be slightly doppler–shifted from the rest–frame wavelength, the total emission from all the clouds then appears as a broadened emission line. The differences in widths of the lines in Sy1s imply that the permitted lines originate from a different region to forbidden lines, whilst in Sy2s they probably arise from the same region. Here was the first hint that some asymmetric emission may be occurring.

The next major step in the history of AGN involved the discovery of quasars. They were initially found when astronomers were looking for the optical counterparts to some bright radio sources. The first quasar to be discovered was 3C 273 (Hazard, Mackey & Shimmins 1963), the optical component at first appeared to be a star, hence the name quasar or 'quasi–stellar radio source'. A spectrum revealed that the object had broad lines, similar to those seen in Seyfert galaxies but shifted, implying a redshift of ~ 0.16 if the shift could be attributed to the cosmological expansion. It was previously thought that the redshift could possibly be gravitational in origin, but Greenstein & Schmidt (1964) showed that here this was not possible, as differential redshifts over the line–emitting regions would wash out the lines. The luminosity of 3C273 was then calculated to be $L = 4.8 \times 10^{12} L_{\odot}$, fifty times more luminous than the most luminous galaxy known at the time. Inspection of archival photographic plates showed that the quasar was also variable on timescales shorter than a year, so from a light crossing time argument the diameter of the emitting region must be less than one light year. The problem now was to explain how the enormous amount of energy observed could be generated in such a small volume. Type II supernovae could technically produce this much energy, but only over a timescale of a few seconds. Therefore supernovae were unlikely to be at the centres of quasars as quasars were thought to exist for at least 10^8 years. Advocates of the starburst model still claim that hot, dense star clusters at the centres of galaxies could reproduce this phenomenon, providing the rate of supernovae was high enough. It is in-

deed possible that starbursts may be powering less luminous AGN than quasars, but supernovae definitely cannot explain the extremely high luminosities seen in quasars. See section 1.4 for a more complete discussion on this issue. The more accepted explanation nowadays is that the energy arises from accretion onto a supermassive black hole. Whilst the existence of black holes is hotly debated it seems that they must exist at the centres of quasars as no other known physical process can explain the high luminosities and long timescales. Historically it is important to realise that it was Fowler & Hoyle (1963) who first proposed collapsed supermassive stars as a possible source of gravitational energy, whilst Zel'dovich and Novikov were the first to mention supermassive black holes as an energy source in 1964. The main evidence to date towards black holes being situated at the centres of quasars will be covered in section 1.2.

Quasars were not only found as the optical counterparts to bright radio sources, many were also found from their stellar–like appearance on photographic plates. As quasars have very blue spectra compared with stars, a UV excess technique was used to separate the quasars from the stars on photographic plates by comparing the U and the B plates. Ten times more quasars were found than expected from the radio surveys (Sandage 1965) and these objects became known as radio–quiet quasars (RQQ) as opposed to the previously known radio–loud quasars (RLQ); in fact it is something of a misnomer as they are not radio 'quiet', but their radio flux is around 100 times lower than the RLQs. The quantitative criterion for radio loudness is such that $F_5/F_B \geq 10$, where F_5 is the radio flux at 5 GHz and F_B is the B band flux.

Quasars can be represented over limited regions of their spectral energy distribution as a power law

$$f(\nu) \propto \nu^{\alpha} \tag{1.1}$$

although this is most usually plotted as $\log_{10}(\nu f_\nu)$ vs $\log_{10}(\nu)$; which represents the actual energy emitted per unit frequency interval. For example, a source which emits an equal amount of energy at all frequencies would have a value of $\alpha = -1$, so on a $\log_{10}(\nu f_\nu)$ plot, the emission would be a horizontal line, which intuitively implies that the source is equally bright at all wavelengths, whilst on a $\log_{10}(f_\nu)$ plot the emission would have a slope of -1.

Figure 1.1 shows the average spectral energy distributions of RLQs, RQQs and Blazars. It can be seen that although RLQs and RQQs are very similar in the

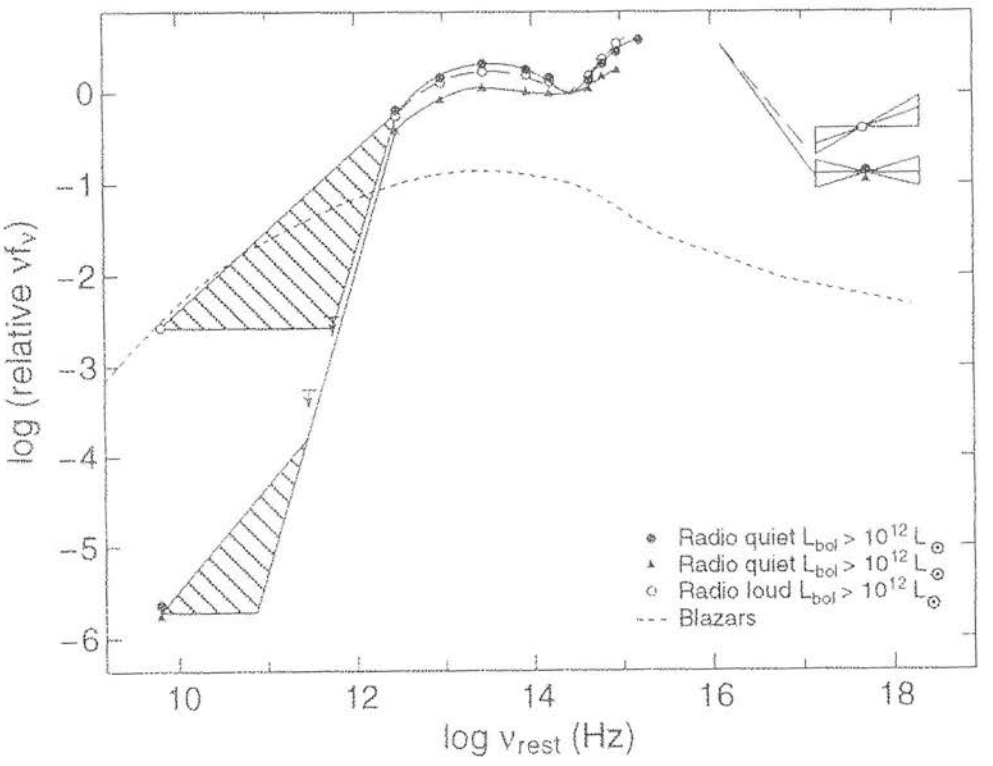

Figure 1.1: The average spectral energy distributions of RLQs, RQQs and Blazars taken from the Palomar–Green survey (Sanders *et al.* 1989).

optical and infrared parts of the spectrum, it is in the radio regime that the main differences occur. There are two 'bumps' in this plot, not thought to be directly caused by the non–thermal radiation from the quasar central source: a 'big blue bump' in the ultraviolet portion of the spectrum and an infrared bump long–wards of $2\,\mu$m. The infrared emission occurs from thermal reradiation from a dusty disk, with the near infrared (1-5 μm) 'bump' being reradiation of heated gas from the outer edges of an accretion disk, or the inner edges of the dusty torus. Black–body emission from an accretion disk peaks in the ultra–violet part of the spectrum, causing the observed 'big blue bump'. The hard X–ray emission is thought to be due to thermal comptonisation in flares above the accretion disk, see section 1.2.3.

The next confusion in the AGN puzzle came from radio surveys. The first quasars to be discovered were associated with radio sources, but it soon became obvious that not all radio sources were associated with quasars, the majority were just ordinary elliptical galaxies, now referred to as radio galaxies. The structure of the radio emission in all these objects was extended, with two thin, highly–collimated

jets ending in large lobes either side of the galaxy. The radio structure of the radio galaxies was found to have larger linear dimensions than in RLQs (Barthel 1989) which implied that RLQs were just a subset of the radio galaxy population but with their jets pointing towards us. This was a major step in the process of unifying RLQs and radio galaxies.

A morphological classification was introduced by Fanaroff & Riley (1974) for radio sources, both radio–loud quasars and radio galaxies. Class I (FR I) sources are weaker and of lower luminosity than class II (FR II) objects and are brightest in the center with weak symmetrical lobes. FR IIs are the classical double radio sources with highly collimated jets extending out towards two edge–brightened lobes. Bridle & Perley (1984) give the break luminosity between the two classes as $L_\nu(1.4\,\mathrm{GHz}) = 10^{32}\,\mathrm{ergs\,s^{-1}\,Hz^{-1}} \equiv 10^{25}\,\mathrm{W\,Hz^{-1}}$ whilst Owen & White (1991) found the break luminosity of the classes to be an increasing function of both optical and radio luminosity. Considering the optical luminosity to be a measure of the size of the galaxy, this implied that the jets needed to be stronger in big galaxies to break through the interstellar medium and emerge as FR II sources. All radio–loud quasars are FR IIs, but even these can be divided into two classes depending on the relative strengths of the central and lobe components. Core–dominated sources have flat radio spectra, whilst lobe–dominated sources have steep spectra. This could be a hint that orientation effects are playing a rôle in the observed properties of quasars. High resolution radio imaging (VLBI) observations of RLQs also showed that they exhibited superluminal motion, meaning that the jets appeared to be moving faster than the speed of light. This can best be explained by the bulk motion of the source close to the line of sight (Blandford, McKee & Rees 1977). Radio galaxies do not exhibit this property as expected by orientation dependent unified schemes.

Compact steep spectrum (CSS) radio sources were found to form another group of objects. These are apparently small sources whose linear size is subgalactic (<15kpc). They were found in both radio galaxies and quasars and made up about 15–30% of radio sources in catalogues (Fanti *et al.* 1990). Statistically it has been shown that most of these objects are not intrinsically large objects seen close to the line of sight. Their small size can either be explained by the jets being trapped by a dense interstellar gas or by the fact that they are young radio sources, seen at an early evolutionary stage. This second scenario is favoured on the basis that the objects are mainly found at high redshift (z>0.2) and are found

in both radio galaxies and quasars.

Another population of radio–loud objects were then discovered which have flat, emission–line free, strongly polarized spectra. These were called BL Lacs after the first object discovered with these properties, BL Lacertae. A subset of quasars with similar, but more luminous, properties to BL Lacs was then found. These were referred to as optically violently variable quasars or OVVs. The two new populations were lumped together and termed 'blazars'. The number of objects found in this category was so small compared to the number of known quasars and radio–galaxies it became apparent that the blazar phenomenon was special. It is now thought that blazar activity is a view of a radio galaxy or quasar directly down the jet axis. The flat radio spectrum is produced by beamed synchrotron emission in the jet. Emission features from the galaxy itself are difficult to distinguish as the highly beamed synchrotron emission completely swamps the galaxy spectrum.

Although radio galaxies at first sight appeared to be normal elliptical galaxies with exceptional radio emission, the optical spectra also provided some clues that the objects contain some type of active nucleus. The spectra split into two types: broad line radio galaxies (BLRG) and narrow line radio galaxies (NLRG). Similar to the Seyfert 1 and 2 classes, the emission is thought to come from two distinct regions, a fast moving broad line region close to the nucleus and a larger, slower moving, more isotropic narrow line region. It was Osterbrock & Parker (1965) who were the first to conclude that the strength of the highly excited emission lines could not be due to photoionisation by an ultraviolet source, but could possibly be explained by collisions between fast moving clouds of gas. It was at this point that the similarities between Seyferts and Quasars became apparent, although Seyferts were lower luminosity objects and appeared to be contained within spiral (Heckman 1978) rather than elliptical galaxies. Weedman (1976) was the first to realise that Seyferts and quasars formed a continuous luminosity sequence. It probably took such a long time to tie the two classes together as the first objects discovered in each class were extremes, which magnified their differences.

The most recent puzzle in the history of AGN has concerned the host galaxies of quasars. It was thought that a difference in host galaxy type may cause the radio–loud and radio–quiet divide. Although quasars were initially identified as stars, Matthews & Sandage (1963) did detect a diffuse halo around a couple of

the early quasars and it has since been generally accepted that all quasars are situated within a host galaxy. The morphology of quasar host galaxies is difficult to ascertain due to the high nuclear:host galaxy ratios. The most successful studies have been in the near infrared where the nuclear:host ratio is lower than at optical wavelengths (Taylor *et al.* 1996) and using the increased sensitivity of the Hubble Space Telescope (HST) (McLure *et al.* 1999). Earlier studies showed that although radio galaxies and RLQs were situated in elliptical hosts, RQQs were more likely to occur in spiral galaxies. The most recent works have turned this accepted scenario around and shown that all *luminous* RQQs also reside in elliptical hosts and there is also no formally significant differences between the properties of these host galaxies at least in the current, albeit small, samples.

The other important wavelength where AGN have been detected but not mentioned in detail so far is the X–ray regime. The first X–ray satellite, UHURU was launched in 1970, since then generations of X–ray telescopes have detected X–ray emission from quasars and Seyferts. The nature of this emission will be discussed in more detail in section 1.2.3. The importance of the X–ray regime is that hard X–rays (energies > 2 keV) can penetrate through almost all obscuring material. They have now been detected coming from galaxies that were otherwise thought to be inactive. This has resulted in growing evidence for a population of galaxies with significant X–ray emission (Boyle *et al.* 1995; Almaini *et al.* 1997 and McHardy *et al.* 1998). The X–ray fluxes are very faint, but due to the large numbers of these objects found in deep X–ray surveys, it means they could contribute significantly to the X–ray background. They have been called narrow line X–ray galaxies (NLXGs) as their optical spectra always contain narrow emission lines with line ratios which would normally classify them as being on the border between starburst and Seyfert 2 objects. The high X–ray luminosities are difficult to attribute to stellar processes, so it is thought that they are low luminosity obscured AGN, with perhaps some starburst activity. The existence of their hard X–ray spectra also adds further weight to the obscured AGN hypothesis as this cannot be explained by stellar processes (Almaini *et al.* 1996).

As mentioned in the previous paragraph NLXGs could contribute significantly to the X–ray background. The X–ray background has been a mystery since its discovery in the 1960s as the spectral shape does not imitate the spectrum of any known X–ray emitting source. A huge population of unknown X–ray emitters must exist in the Universe, as integrating the emission from all known AGN

underestimates the magnitude of the background by at least a factor of four (Fabian *et al.* 1998). It is thought that obscured AGN, such as the newly found population of NLXGs, which do indeed have the necessary hard X–ray spectra, could actually make up the shortfall (Setti & Woltjer 1989 and Comastri *et al.* 1995). If this is true, hard X–ray chosen samples of objects could, in the future, be the only way to find complete samples of AGN in an unbiased way.

The taxonomy of AGN is still extremely confusing, so a summary of the picture presented so far is given in figure 1.2.

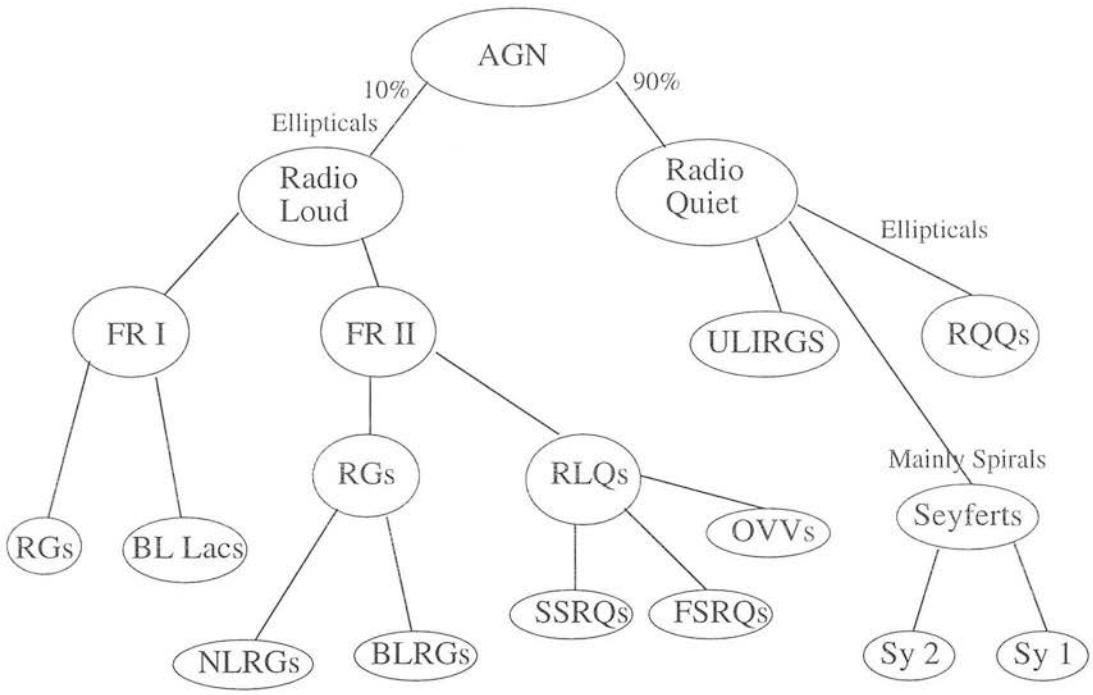

Figure 1.2: A summary of the taxonomy of AGN. The more aligned objects are positioned to the right of each sub–category and the higher luminosity objects are positioned slightly higher than the low luminosity ones. The abbreviations are as given in the text.

1.2 The observational evidence for supermassive black holes in AGN

Nowadays there are two lines of evidence used to demonstrate the existence of supermassive black holes as the central engines of AGN. The first relies on obtaining the physical parameters of the black hole *i.e.* the mass, constraining the

volume within which this mass is contained and then arguing that the central density is so high that the only physically plausible object must be a black hole. This can be done in two ways which are very different and probe very different regions of the galaxy nucleus. X–rays originate from very hot regions close to the central source ($< 20\,R_S$) giving a very important upper limit on the size of the central source. R_S is the Schwarzschild radius of a black hole which is given by

$$R_S = \frac{2GM}{c^2}, \tag{1.2}$$

so the Schwarzschild radius of $10^8\,\mathrm{M}_\odot$ black hole is around 2AU.

Kinematical evidence from very fast moving stars probes the velocity field around the central source but from regions much farther out than the X–rays. Accurate values of the mass contained within this larger central region can be obtained, but the implied densities using these methods can be explained without having to invoke massive black holes. Central stellar clusters could produce the necessary density, but as the central object is seen in most of these cases to be dark *i.e.* the mass–to–light ratio is between ten and few hundred, only a cluster of stellar remnants remains as a possibility. Begelman & Rees (1978) have shown that a cluster of stellar remnants would have a two–body relaxation time of less than 10^8 years so that if any of these exotic objects did once exist they would have collapsed to a black hole by now anyway. This could be an important stage in the formation of black holes. The second method of probing the existence of a black hole relies on studying the shape of X–ray emission lines which are distorted by relativistic effects due to their proximity to the central mass.

1.2.1 X–ray variability

The night–to–night variability of quasars and Seyfert galaxies in optical light (Penston & Cannon 1969; Cannon, Penston & Brett 1971) of the order of a magnitude, showed that the size of the emitting region must be less than a light day, as no source of isotropic radiation can vary faster than the time taken for light to cross it. X–ray variability shows even higher amplitudes and shorter timescales, of the order of minutes (Ulrich, Maraschi & Urry 1997), which indicate that emission is coming from the innermost regions of the galaxy, *e.g.* 10–1000 R_S for some luminous Seyfert 1s.

1.2.2 Direct kinematical observations

The Milky Way: The centre of the Milky Way around the radio source Sagittarius A* is too dusty to see directly using optical imaging. Only in the infrared can the central star cluster be seen. Two separate groups (Ghez *et al.* 1998 and Eckart & Genzel 1997) have monitored the proper motions of the stars in the central 0.3 pc of the Galaxy over the past few years by using speckle imaging on the 10m Keck and the 3.5m NTT telescopes respectively. The results from both groups agree within their errors and they find a massive central object coincident with the radio source, of around $2.5 \times 10^6\,\mathrm{M}_\odot$ within the central $10^{-6}\,\mathrm{pc}^3$. The density of the central dark mass $10^{12}\,\mathrm{M}_\odot\,\mathrm{pc}^{-3}$ is indicative of a central supermassive black hole. This is indeed a revelation as it is the first convincing piece of evidence that a galaxy that would not normally be classified as an AGN contains an object dense enough to be a black hole. However, Donald Lynden–Bell did predict many years ago (Lynden-Bell 1969) that the nuclei of most large galaxies should contain a supermassive black hole, which when inactive should have an anomalously large mass–to–light ratio.

External Galaxies: An extensive review of this area is given by Kormendy & Richstone (1995). Most extragalactic candidates have evidence for a central massive dark object (MDO) either from measures of their stellar or gas dynamics. The stellar dynamics are measured from observed changes in the velocity dispersion towards the centre (Van Der Marel 1999). The most successful gas dynamical measurements have been made using the Faint Object Spectrograph on the Hubble Space Telescope to measure the actual velocity of the gas either side of a nuclear disk in M87 (Harms *et al.* 1994) implying a mass of $\sim 3 \times 10^9\,\mathrm{M}_\odot$ within the central 20 pc. Although this is not quite as convincing as the more recent observations of the Galactic centre, it is claimed that there is no other form of mass concentration that could 'fit' inside this region other than a black hole.

The existence of water masers in NGC 4258 (Miyoshi *et al.* 1995) using VLBI is perhaps one of the most elegant observations indicating a central massive black hole. Masers can only be seen when they and their source of energy are either directly along our line of sight or at 90° to us. This is indeed the observed spatial distribution of the maser spots, indicating a slightly warped Keplerian disk, with a central object well within the central 0.13 pc, the location of the innermost

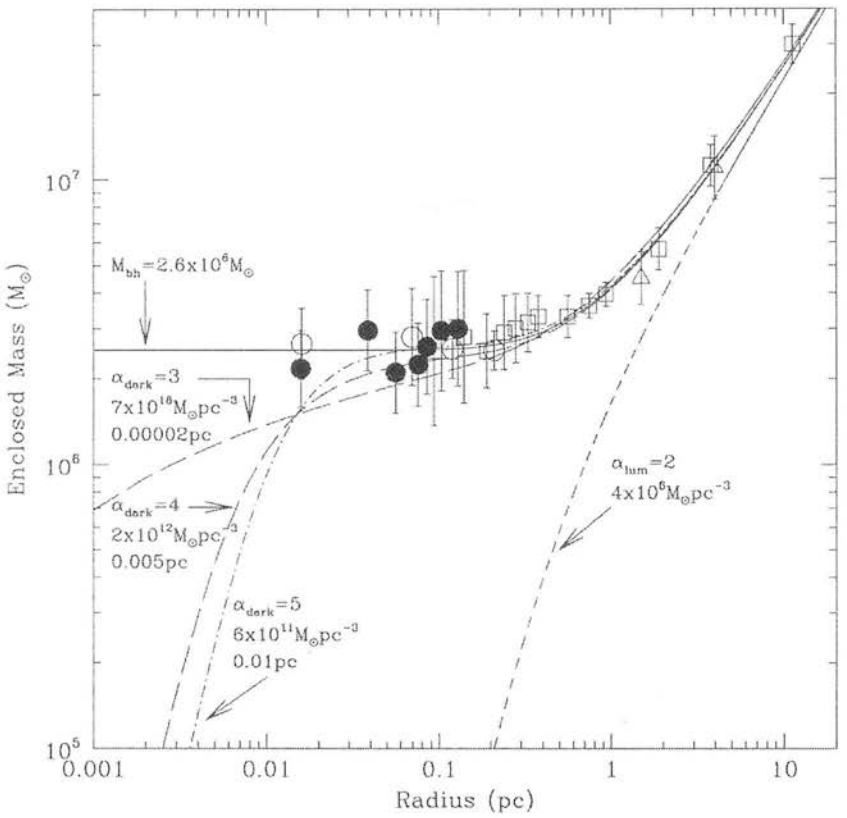

Figure 1.3: Enclosed mass as a function of distance from Sgr A*, taken from Ghez *et al.* 1998. The dotted lines show various power–law fits to the data for dark clusters of stellar remnants. They provide equally good fits to the current data as the flatter black hole model (solid line), but remain physically inviable as the evaporation and collision timescale for such models is less than the age of the Galaxy.

maser spot. The central mass is very accurately measured to be $\sim 3.6 \times 10^7 M_\odot$. The important point here is that the motion of the masers is nearly perfectly Keplerian, if there were many distinct dark objects within the central 0.13pc, then the gravitational potential would have a very different shape.

Reverberation mapping is another technique used to determine the kinematics of the emission–line regions (Peterson 1993). Briefly the idea is that by carefully monitoring the delays between variations in the continuum and the broad–line profiles the size of the broad–line region can be determined. It is assumed that the broad lines respond to changes in the continuum immediately and the time delay is caused by the light travel time between the central source and the broad–line regions (BLR). The distance to the line emitting cloud is then determined whilst

the velocity of the cloud is known from the width of the emission feature, so the size of the central mass can then be measured directly. It has been found that there is also some stratification in the BLR as some emission lines always respond faster than others. The downside to reverberation mapping is that enormous amounts of telescope time are required to monitor even a small number of quasars continuously.

1.2.3 Distortion of Fe spectral lines in the X–ray regime

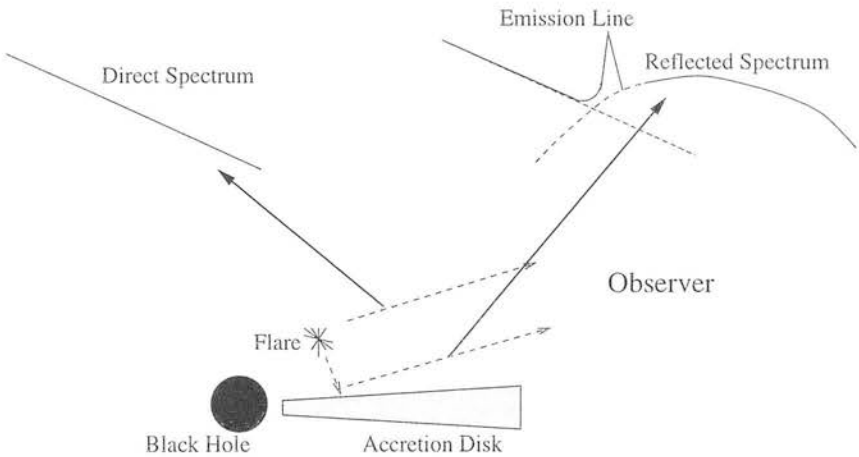

Figure 1.4: Schematic showing the observed hard X–ray emission from an accretion disk. The reflected spectrum has a hump caused by thermal comptonisation, peaking at about 20 keV, superimposed on the direct spectrum of the flare, plus an emission feature caused by fluorescence.

Lines emitted by a disk–like structure have a characteristic double–horned profile due to the shifted emission from the approaching and receding sides of the disk respectively. In X–rays a prominent emission feature is the Fe Kα line, seen mostly in Seyfert galaxies. The hard X–ray emission is thought to originate in flares above the accretion disk in a similar manner to the X–ray emission from the sun. The resulting observed spectrum (see figure 1.4) consists of a sum of the direct emission plus emission back–scattered from the disk. Fluorescence occurs at line energies, causing the observed Fe Kα feature. As this originates from a very hot, fast moving region of the disk close to the central potential, relativistic effects as well as line–broadening need to be taken into consideration when trying to predict the shape of the line profile. Beaming along the direction of motion would cause the blue horn to appear brighter than the red horn whilst

time dilation effects would cause the innermost regions to be redshifted, resulting in a skewed, broad line profile. These broad skewed lines are exactly what is seen in the X–ray spectra of most Seyfert 1 galaxies (Fabian *et al.* 1995; Nandra *et al.* 1997a) and some Seyfert 2 galaxies (Turner *et al.* 1998) indicating that accretion onto a black hole is taking place from a standard 'cold' thin disk. In the case of MCG-6-30-15, a Seyfert 1 galaxy, the line was shifted to such low energies during a minimum state that it implied that the emission must have arisen less than $3R_S$ from the black hole. The most likely explanation is that it must be a spinning Kerr hole (Tanaka *et al.* 1995; Iwasawa *et al.* 1996) as the minimum stable orbit for a Schwarzschild hole is $3R_S$ and only $1.5R_S$ for a Kerr hole. Interestingly this emission line is not seen in the X–ray spectrum of quasars, as it has been found that the strength of the line decreases with increasing luminosity (Nandra *et al.* 1997b). It is thought that the accretion disk becomes increasingly ionised as the accretion rate, and therefore luminosity, increase.

This is probably the best evidence for a black hole given so far. The quality of the data, taken with the ASCA satellite, is still quite noisy so further observations using the new CHANDRA and XMM satellites will allow more accurate comparison with the models.

1.2.4 The black hole vs. galaxy parameter correlations

Once black hole masses have been estimated using one of the above techniques it has been tempting to try to correlate black hole mass with a variety of host galaxy parameters. Magorrian *et al.* (1998) find $M_{BH}/M_{\rm Bulge} \sim$ const ~ 0.006, with a fairly large scatter, whilst earlier work (Kormendy & Richstone 1995) found $M_{BH}/M_{\rm Bulge} \sim 0.003$. This has been thrown into doubt more recently as more reliable black hole mass estimates seem to reduce the black hole masses by around an order of magnitude, increasing the scatter in the correlation even more and questioning whether the correlation exists at all. Franceschini, Vercellone & Fabian (1998) have correlated black hole mass not only with bulge mass but also the infrared, X–ray and radio emission for a small sample of thirteen nearby objects. They confirm the postulated correlation with bulge mass and also find a tight relationship with black hole mass and total radio luminosity at 5 GHz, $L_{\rm 5GHz} \propto M_{BH}^{2.7}$, once the estimated radio emission due to star–formation has been subtracted. There currently appears to be no significant relationship between

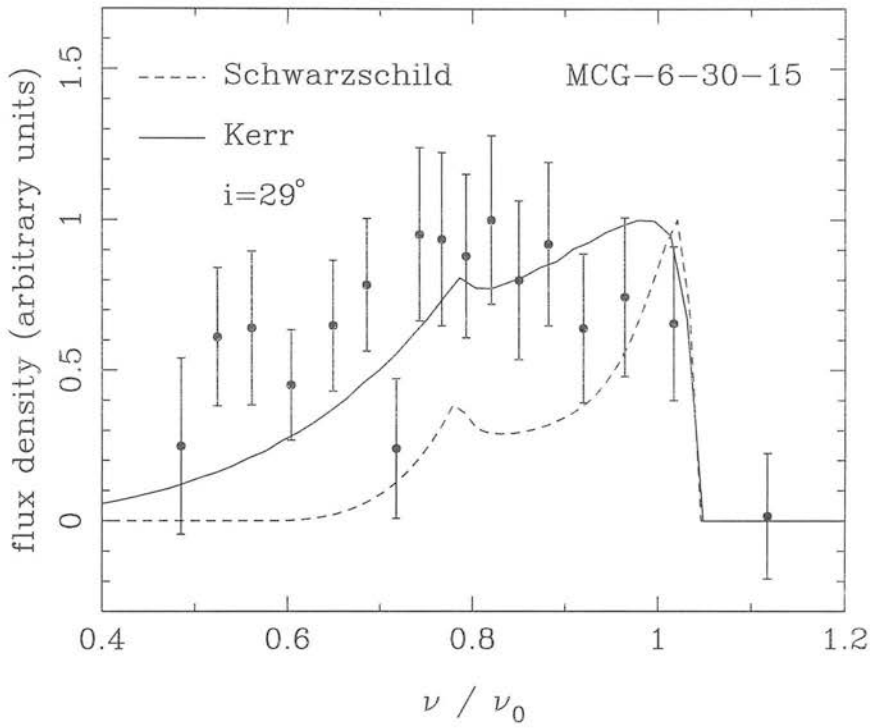

Figure 1.5: Profile of the Fe Kα line in MCG-6-30-15. The lines show the expected profile around a Schwarzschild and Kerr black hole. The Kerr hole fit is extremely good.

infrared or X–ray emission and black hole mass, but as they are predicted to originate in or above the accretion disk this is not surprising. As mentioned above the black hole mass estimates are in doubt and the samples are small, so only time and more accurate measurements will allow a proper analysis of these results, which should be able to shed light on many of the unanswered questions relating to black hole formation. Factors such as accretion efficiency, galaxy merger history and star–formation history could also play a large part in determining the final observed black hole mass. McLeod & Rieke (1995) have suggested that rather than there being actual correlations between black hole mass and various galaxy parameters there is an upper envelope, so that there is a maximum size black hole that a certain size galaxy can accommodate, which could explain the large scatter in the above relationships. In fact they argued this for quasar luminosity rather than black hole mass, but the implications are the same.

1.3 The observational evidence for dusty tori in AGN

Having discussed the evidence for central supermassive black holes in AGN, it is now important to show the various lines of evidence supporting an axisymmetric form of obscuring material, which shall be referred to as a dusty torus (although it may not be exactly torus shaped). Dust affects the central nuclear light in two ways, firstly by dimming, so that any observed flux is greatly attenuated, often allowing faint, scattered light with a polarized spectrum to be seen. Secondly any observed flux is reddened by the obscuring material, as shorter wavelength light is more easily attenuated than longer wavelengths, making the observed spectrum appear redder. The amount of reddening is then related to the amount of obscuring material present along the line of sight.

The most convincing evidence for an obscuring torus is the appearance of Type 1 or broad–line spectra in polarized light of objects that would be classified as Type 2 or narrow–line objects normally. Light is polarized as it is scattered into our line–of–sight by material above and below the obscuring torus. Antonucci & Miller (1985) were the first to use spectropolarimetry to display broad lines in the spectrum of NGC 1068, a nearby well studied Seyfert 2 galaxy. The scattering is mostly caused by electrons as it has been shown to be mainly wavelength independent, whilst some scattering off dust clouds, which is wavelength dependent, has been found for this object (Miller, Goodrich & Mathews 1991). The wavelength dependence of the scattering can be studied by examing the relative amounts of polarized light at different wavelengths. Packham *et al.* (1997) take this further and use infrared imaging of polarized light to detect the regions of enhanced scattering and directly observe the nuclear torus as a silhouette in scattered light. They estimate the diameter of the torus to be 220 pc.

Hidden broad line regions have now been detected in many other Seyfert 2's (Heisler, Lumsden & Bailey 1997) and FRII radio galaxies (Cohen *et al.* 1999). It is important to point out that not all narrow–line objects studied reveal hidden BLRs. This could be due to either a lack of scattering material or an actual lack of fast moving broad–line region clouds. Therefore statistical studies of the relative numbers of hidden BLRs found in polarized light should not be taken too seriously. Cohen *et al.* (1999) have studied three objects in common with the sample used in this study: 3C 33 and Cygnus A which are NLRGs and 3C 445,

the only BLRG in the sample. Both NLRGs do show hidden broad–line regions whilst 3C 445 shows slight reddening which they interpret as a view of the BLR close to the edge of the torus, seen through a very small amount of dust.

Reflection and scattering of light are not the only means of looking inside the torus, infrared wavelengths also provide a more direct method since optical depth decreases with increasing wavelength. Hill, Goodrich & DePoy (1996) successfully used spectrophotometry in the infrared to search for broadened wings on the Paα infrared emission feature. They were also able to demonstrate increased reddening with increasing obscuration. In their sample of eight NLRGs, two BLRGs and one quasar they find the broad–lines more reddened than the narrow lines in all but the quasar and one of the BLRGs. This implies that the obscuring dust is situated between the BLR and the NLR, with one of the BLRGs seen through a smaller amount of dust than the NLRGs, consistent with the obscuration picture given by polarization studies. Economou *et al.* (1995) also used infrared spectroscopy, this time to study the Hα line in the high redshift ($z = 0.937$) object 3C 22. Although the object had previously been classified as a radio galaxy, the broad Hα feature detected allowed it to be reclassified as a reddened quasar, showing that some quasars are seen through modest amounts of dust. Much more will be said on this issue in section 1.6 as the main theme of this work is to use infrared wavelengths to probe the dusty torus.

There have also been many studies attempting to correlate increasing reddening or extinction with viewing angle. The viewing angle is estimated using the parameter R, which is the observed core–to–lobe ratio or core–dominance parameter relating the radio core emission to the emission from the lobes (Orr & Browne 1982). It is thought that the lobe emission is radiated isotropically, whilst the core emission which originates in a jet close to the central engine is highly beamed along the line of sight. This means that R can be taken as an orientation indicator, high R sources having the beamed component along the line of sight. This is a similar but more quantitative method of classifying radio sources into 'flat–spectrum' (high R) and 'steep–spectrum' (low R) as beaming causes the observed flat radio spectrum.

Other orientation dependent indicators have also been shown to correlate with the R parameter. Jackson & Browne (1990) compared the luminosity of the [OIII] λ5007 emission line in what was claimed to be an equally matched sample of quasars and radio galaxies and found the line to be 5–10 times brighter

in quasars. The sample of galaxies has now been shown to be biased towards bright quasars with bright emission lines (Simpson 1998) thereby magnifying the difference between the two classes, but the result still remains that quasars are about twice as luminous in [OIII] than radio galaxies. It is assumed that the line is extinguished in radio galaxies owing to the presence of some obscuring material. Hes, Barthel & Fosbury (1993) then performed a similar analysis, this time looking at the [OII] λ3727 doublet and found no difference between the two classes. This caused a puzzle as the shorter wavelength [OII] line would be expected to suffer more extinction if they were produced in the same region of the galaxy. They suggested that most of the [OIII] emission must be produced close to the nucleus whilst the [OII] emission is produced farther out and is therefore unaffected by any putative torus. Baker (1997) finds an increasing [OII]/[OIII] ratio with decreasing R, which strengthens the case for [OII] being isotropically emitted whilst [OIII] is anisotropic.

As mentioned previously, the infrared $\sim 3\,\mu$m bump in the spectral energy distribution of all radio–loud and radio–quiet quasars is thought to arise from thermal reradiation of dust from the outer edge of an accretion disk or inner edge of a dusty torus. The existence of this bump is thought to be substantial evidence for the existence of a torus. Dust sublimates at about 1500 K so the torus cannot exist in regions where the radiation field is hotter than this. Higher luminosity objects will be hotter farther out, causing the inner edge of the torus to be pushed farther out. This is known as the receding torus model (Lawrence 1991), see figure 1.6 for a schematic representation. The advantage of the model, assuming the height of the torus remains constant, is that as the torus recedes the opening angle increases so that the more luminous objects are more likely to be seen along a line–of–sight directly into the nucleus. This could explain the existence of the large numbers of low–luminosity obscured AGN needed to explain the X–ray background.

Another piece of evidence supporting an axisymmetric form of obscuration comes from the actual imaging of cones of ionised gas either side of the nucleus (Pogge 1988; Tadhunter & Tsvetanov 1989; Wilson & Tsvetanov 1994). The opening angles of the cones seen so far vary between 30°–100°. The images are taken in narrow–band filters centered on the wavelength of an emission feature such as [OIII] λ5007. The continuum radiation is removed to leave a pure emission image by subtracting another image taken in a different filter centered on a continuum

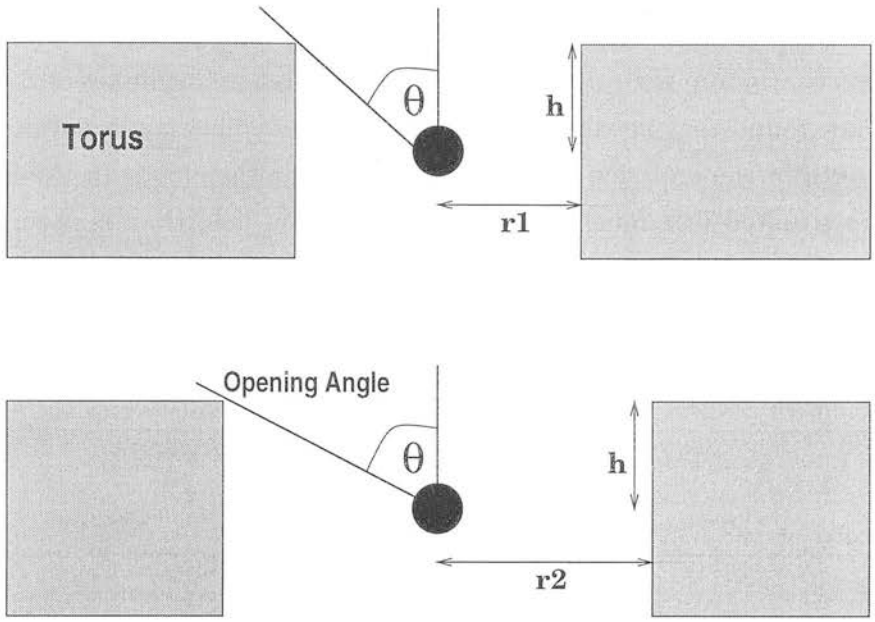

Figure 1.6: Schematic representing the receding torus model. The bottom source is more luminous, pushing the inner edge of the torus out and increasing the opening angle.

region just to one side of the emission feature. This cone of ionised gas is sometimes referred to as the extended narrow–line region (ENLR) or the extended emission line region (EELR). The edges of the cones are sharp and linear which point away from this feature being intrinsic to the gas distribution and instead caused by an anisotropic radiation source exciting the clouds in these regions. What is still uncertain though is whether the radiation illuminating these regions is anisotropic due to the presence of a torus or whether it is collimated closer to the black hole in a similar manner to the optical radiation.

The 'alignment effect' (McCarthy *et al.* 1987; McCarthy 1993; Dunlop & Peacock 1993) is the tendency of EELRs and both the optical and (to a lesser extent) the infrared continuum emission to line up with the axis of the radio jet at high redshift. This is thought to arise from a combination of a couple of processes: the scattering of some of the hidden quasar light into the line of sight *i.e.* the polarized light, and star–formation induced by the radio jet passing through the interstellar medium.

Considering the evidence from the imaging of ionisation cones in Seyfert galaxies and from the alignment effect it is becoming clear that the ionising photons can only travel freely out of the nucleus along the radio jet directions. As a test of this,

Kinney *et al.* (1991) compared the amount of available ionising photons observed in the UV continuum with the observed optical emission line fluxes in a sample of Sy2s. They found that in most cases the observed UV flux could not account for the strength of the emission lines. This means that the clouds in the ionisation cones are situated in a much stronger UV radiation field than is observed from Earth. Mulchaey *et al.* (1994) carried out a similar multiwavelength analysis on a larger sample of Seyfert 1s and 2s and find that whilst the infrared continuum, hard X–ray flux and [OIII] λ5007 ratio are similar, the UV and soft X–ray fluxes are deficient in Seyfert 2s, consistent with an obscuring dusty torus.

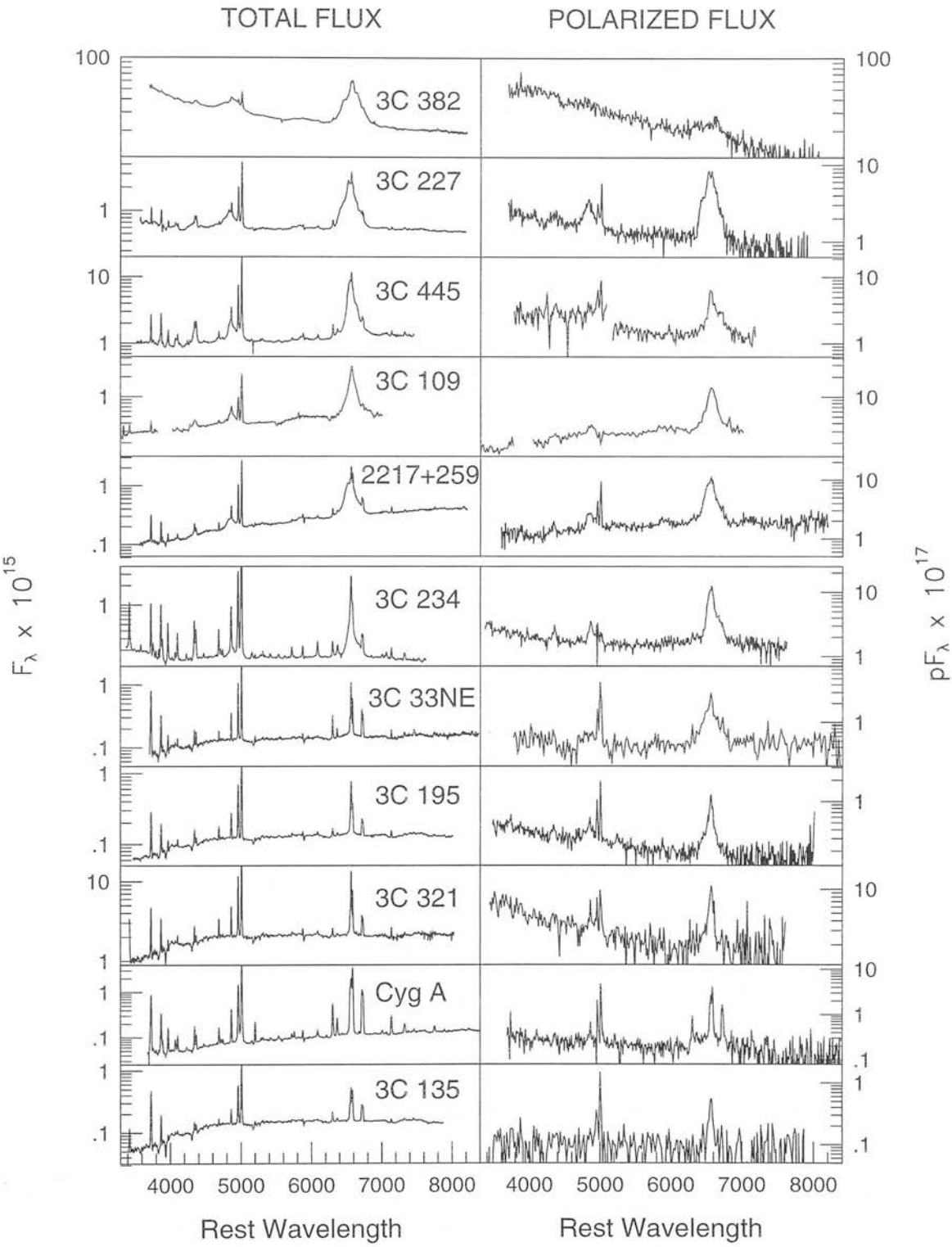

Figure 1.7: Direct and polarized spectra of some NLRGs and BLRGs, taken from Cohen et al., (1999). The broad lines can clearly be seen in the polarized spectra of the NLRGs. 3C445, 3C33 and Cygnus A are objects in the sample used in this study and are all shown to have broad lines.

1.4 The starburst model for quasars

Before moving on to discuss the intricacies of Unified Schemes for AGN it is important to mention other models which could reproduce the observed quasar luminosities. The starburst model advocated by Roberto Terlevich and his collaborators (Terlevich *et al.* 1992; Terlevich *et al.* 1995; Aretxaga, Cid Fernandes & Terlevich 1997) has probably been the most serious alternative for radio–quiet AGN. Briefly the starburst model proposes that gravitational infall produces a high density of stars in the centre of the galaxy which causes massive nuclear star–formation activity. The resulting supernovae are then powerful enough to explain the nuclear luminosities in some AGN without the need for invoking black holes. Although the original models were successful in explaining the high luminosities of quasars, as long as sufficient supernovae were occurring, the main problems with the starburst model were the inability to explain quasar variability, radio emission and morphology, the existence of the broad and narrow–line regions and the lag between the response of the continuum and the emission lines exploited during reverberation mapping. It has since been claimed that rapidly cooling, compact supernova remnants, can form fast–moving shocks which can produce the observed broad–line regions in low–luminosity AGN such as LINERS (Low Ionisation Nuclear Emission–line Regions) and Seyferts. Optical variability is attributed to supernovae explosions and the rapid expansion of their compact remnants. The lag is explained by the time delay between the actual supernova explosion and the time taken to increase the density of the surrounding medium and cause shocks. Unfortunately the starburst model still fails to explain rapid, high amplitude X–ray variability or the shape of the broad iron lines discussed in section 1.2.3.

It is fast becoming accepted in the astronomical community that mergers play an important part in galaxy formation and associated with the mergers are bursts of star–formation (Kolatt *et al.* 1999). An understanding of the starburst phenomenon and the whole process of galaxy evolution is therefore extremely important in understanding the processes occurring in AGN, but from the evidence given in sections 1.2 and 1.3 for the existence of supermassive nuclear black holes and some form of obscuring torus surrounding it, it is clear that the starburst model on its own will not suffice.

1.5 Unified schemes for AGN and remaining questions

The evidence towards supermassive ($10^6 - 10^8\,M_\odot$) black holes at the centres of galaxies, powering the AGN phenomenon, has now been presented. It is now important to consider how this and the evidence towards some type of axisymmetric obscuration blocking the view of the central source at certain angles fit together into a unified scheme for AGN.

The first step in the construction of a unified scheme came when Rowan-Robinson (1977) suggested that the differences between various types of AGN could be simply down to orientation effects. Scheuer & Readhead (1979) then attempted to show that radio–loud quasars were radio–quiet quasars, but seen more end on (more aligned). This was quickly ruled out due to the lack of diffuse radio emission in the radio–quiet objects. Orr & Browne (1982) were more successful when they claimed that flat–spectrum radio quasars (FSRQ) were more aligned versions of steep–spectrum radio quasars (SSRQ), which were again more aligned versions of FRII radio sources (Barthel 1989) with the OVVs being the most highly–aligned objects. Compact steep spectrum objects form the early stage of evolution of these sources. These types of unified schemes are referred to as "weak" schemes as they treat radio–loud and radio–quiet objects as intrinsically different beasts and try to explain the differences within these subgroups simply by orientation effects. Good review articles are given in Antonucci (1993) and Urry & Padovani (1995). The newer "grand" unified schemes attempt to unify all types of AGN using extra parameters such as luminosity and black hole spin as well as orientation. In fact the luminosity can also be considered as dependent solely on black hole parameters *i.e.* accretion rate and mass.

1.5.1 "Weak" unified schemes

Figure 1.8 shows a cartoon of the unified scheme for radio–loud AGN. Radio–quiet objects, such as Seyfert galaxies and RQQs are thought to have a similar geometries but without the radio jets. The radio–quiet analogues of radio galaxies, which should be around ten times more numerous than radio galaxies from the relative numbers of observed RLQs and RQQs, have been difficult to find, so most efforts have concentrated on unifying the smaller radio–loud population

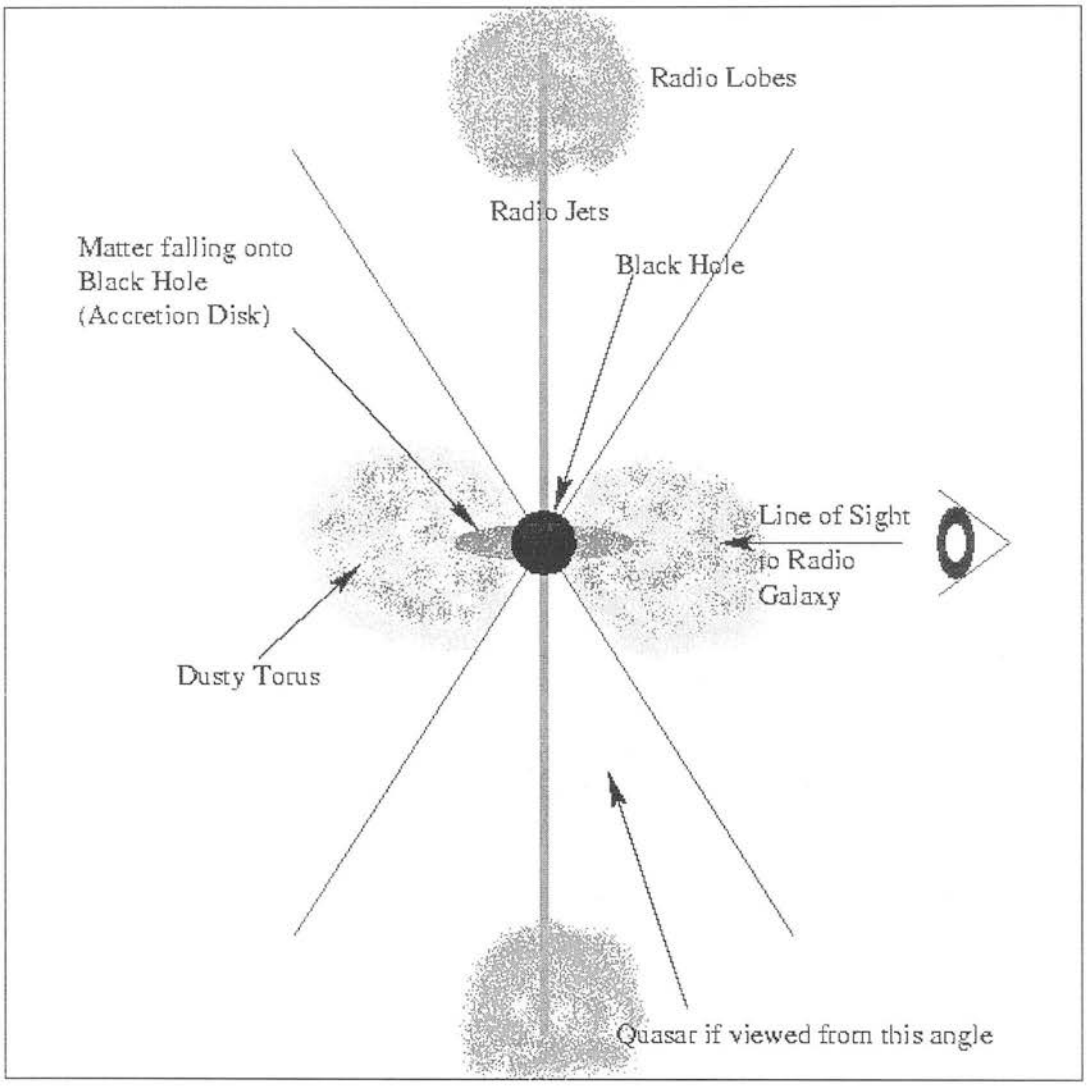

Figure 1.8: Cartoon showing the unified scheme for radio–loud AGN (not to scale).

of objects. However, since the launch of the IRAS satellite a new population of ultra–luminous infrared galaxies (ULIRGS) was discovered. They emit much of their radiation in the infrared which is possibly non–thermal radiation re–radiated from a dusty torus and are the most likely candidates for the radio–quiet analogues of powerful radio galaxies.

Concentrating on unification schemes for radio–loud objects briefly, these are split into two schemes, those for FRI sources and those for the more powerful FRII sources. As mentioned in section 1.1 Barthel (1989) found that the radio structure of FRII radio galaxies in the redshift range $0.5 < z < 1$ has larger linear

dimensions than that of RLQs in the same redshift range, as would be expected if the objects were identical except for their orientation. He also went on to suggest that from the relative numbers of RGs (71%) and RLQs (29%) in the sample, assuming a randomly oriented set of sources, an opening angle of $\sim 45°$ would mark the border between the two types of object. Obviously this does not take into account the possibility of a receding torus, mistaken quasar identity at high redshift (Economou *et al.* 1995) or a fuzzy–edged torus. It has since been shown (Singal 1993) that this statistical analysis does not conform to expectations using a different redshift range, so whilst the unification by orientation idea remains unchallenged, it is probable that other factors do indeed need to be taken into consideration as well. The lower luminosity AGN, BL Lacs and FRIs have also been successfully unified by considering the relative number densities of each type and their luminosity distributions.

1.5.2 "Grand" unified schemes

As mentioned in section 1.1 new results are pointing towards the host galaxies of all luminous radio–loud and radio–quiet objects being virtually indistinguishable from each other and from normal giant elliptical galaxies out to a redshift of $z = 1$. This has allowed "Grand" unification schemes to surface, which consider all AGN phenomenon to be connected via a few intrinsic parameters. New fully relativistic modelling of the black holes, accretion disks and jet dynamics (Koide, Shibata & Kudoh 1999 and Meier 1999) has successfully reproduced the Fanaroff–Riley class dichotomy and the existence of radio–quiet objects mainly by varying the spin of the black hole. A new unified scheme is presented by them and reproduced in figure 1.9, the details of which may not be correct but the ideas may be something to consider in future. The plots are of radio power verses black hole mass and are similar to the Owen & Laing (1989) plot of radio power versus optical luminosity, where FRI and FRII sources inhabit different areas. Their classification of the objects into type A and type B is from Jackson & Wall (1999) where type A are high accretion rate ($\dot{m} = 0.1$) objects such as quasars, "N" radio galaxies (those containing strong, point–like nuclei) and Seyfert galaxies whilst type B are low accretion rate ($\dot{m} = 0.01$) objects such as the majority of radio galaxies, weak radio cores and objects with weak or no narrow line emission. Here $\dot{m}$ is the

accretion rate in units of the maximum Eddington limited accretion rate

$$\dot{M}_{\rm Edd} = 4\pi G M_{BH}/\epsilon\kappa_{\rm es}c \tag{1.3}$$

where M_{BH} is the mass of the central black hole, ϵ the accretion efficiency and $\kappa_{\rm es}$ the electron scattering opacity. The angular momentum j, is in units of the maximum angular momentum of a Kerr black hole

$$J_{max} = GM_{BH}^2/c. \tag{1.4}$$

and $j_{\rm crit}$ is a critical rotation rate distinguishing between FRI and FRII sources.

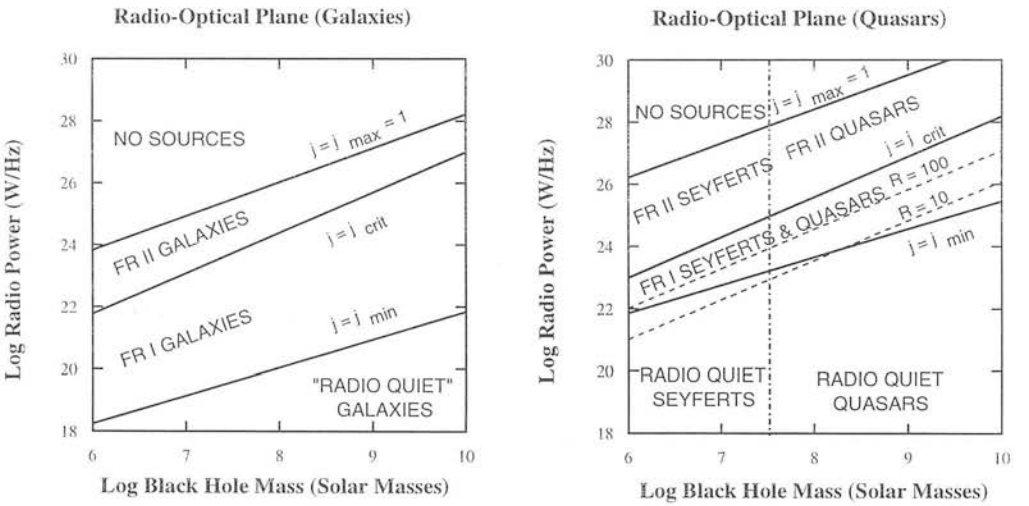

Figure 1.9: A grand unification scheme for AGN, taken from Meier, 1999. The right panel shows the scheme for type A objects (quasars, Seyferts, "N" radio galaxies) high accretion rate objects and the left panel for low accretion rate type B (radio galaxies, weak radio cores).

1.5.3 Remaining questions

There are still many questions which need to be answered before even a provisional understanding of the AGN phenomenon can be reached. Most of the evidence today is pointing towards a coherent picture of galaxy evolution and AGN formation (Kauffmann & Haehnelt 1999) whereby supermassive black holes are formed and fuelled during mergers between galaxies. Nevertheless we still

need to understand:

1 – What triggers black hole formation?

2 – How are supermassive black holes made?

3 – Why are dormant black holes so dark?

4 – What is the feeding/accretion mechanism?

5 – How does the accreting material lose its angular momentum?

6 – How are the jets so highly collimated?

7 – What does the RL/RQ dichotomy actually mean?

8 – Where are the RQ analogues of radio galaxies?

9 – Does host galaxy bulge mass actually correlate with black hole mass?

10 – Do all galaxies contain a black hole?

11 – What is the lifetime of the activity?

12 – How do mergers and environment play a part in the eventual parameters of the AGN?

13 – How does black hole formation connect with star formation?

14 – How do starbursts and the star–formation histories of galaxies affect the AGN parameters?

This thesis does not directly address any of these questions, however any conclusions reached from assessing how and whether the extinction towards the central source correlates with viewing angle will be able to clarify the picture for questions 3, 9 and 10. This in turn will then lead on to provide evidence to answer the remaining questions.

1.6 Evidence for obscured nuclei in radio galaxies

The possibility of finding obscured nuclei in radio galaxies first became realised when Lilly, Longair & Miller (1985) discovered non–stellar radiation in radio galaxies with strong emission lines at $3.5\,\mu$m (L band). They used aperture photometers rather than modern infrared arrays so the spatial extent of the L band flux was unknown. It was therefore impossible to determine whether the excess was connected with an unresolved transmitted quasar continuum or simply a resolved red galaxy nucleus. The invention of infrared arrays allowed Djorgovski *et al.* (1991) (DWMG) to claim the first detection of an unresolved infrared nucleus, in the "archetypical powerful radio galaxy" Cygnus A, although the

claim has since been disregarded as the techniques used have been shown to be flawed (see section 1.6.1). Since then workers have been looking for obscured nuclei in radio galaxies to test the orientation dependent unified schemes for radio–loud AGN. They have concentrated on two galaxies in particular: Cygnus A, the most powerful nearby radio galaxy; and IC 5063, an intermediate radio power galaxy, which has been classified as both a Sy2 and a NLRG by different authors. A summary of the conclusions reached so far for these two galaxies is given in the next two sections along with a brief discussion of the methods used to detect the buried nucleus.

1.6.1 Cygnus A

Cygnus A has been used extensively as a galaxy with which to test unified schemes, it is the most luminous radio source in the nearby universe ($z \ll 1$) and is possibly our nearest laboratory for studying the properties of radio galaxies at high redshift ($z > 1$). Although it is possible that Cygnus A is anomalously radio–loud due to its location in a dense X–ray halo (Barthel & Arnaud 1996) and not at all representative of the general population of radio galaxies, the evidence for the existence of an obscured AGN in Cygnus A is strong. Ionisation cones have been detected in both long–slit spectra (Tadhunter, Metz & Robinson 1994) and narrow–band images (Jackson, Tadhunter & Sparks 1998). Hard nuclear X–rays have been detected by Ueno *et al.* (1994) implying an extinction towards the nucleus of $A_V = 170 \pm 4$ mag assuming a Galactic dust–to–gas ratio, where A_V is the magnitude of extinction in the V band. The most impressive evidence is provided by the existence of broad emission lines seen in scattered light (Ogle *et al.* 1997), see figure 1.7. The detection of the unresolved nucleus itself has been a little more controversial. Thornton, Stockton & Ridgway (1999) have carried out the most recent detailed optical and infrared spectroscopic analysis of the object and find no evidence for broad wings on Paα, implying that the nucleus remains hidden at 2 μm. Ward *et al.* (1991) used the lack of observed broad lines to predict a lower limit on the extinction to the broad line regions to be $A_V > 24$ mag.

Moving onto imaging studies of Cygnus A, DWMG showed that whilst the optical images show a prominent double morphology caused in part by a central dust lane (Stockton, Ridgway & Lilly 1994), the infrared isophotes become generally

rounder until at L' the underlying galaxy is not even detected and only the nucleus is seen (see figure 1.10). To enable an estimate of the extinction towards the nucleus to be made, the contribution of the transmitted quasar flux to the K and L' images needs to be quantified. DWMG used a primitive 'scale and subtract' method to deconvolve the K band image, this involved normalising the images at J and K so they contained equal light in an annulus a few arcseconds from the nucleus, subtracting the shorter wavelength image from the longer one and performing photometry on the residual. As explained in detail in Simpson (1994b) this method is extremely unsatisfactory. The resulting residual will almost always be caused by the fact that the scale lengths of elliptical galaxies tend to decrease with wavelength and is not a representation of the unresolved nuclear component at K. DWMG also assume that the L' flux is entirely non–stellar in origin and do not attempt to estimate the stellar contribution, which turns out to be non–negligible, thereby overestimating the $K - L'$ colour of the nuclear component. More recently Stockton, Ridgway & Lilly (1994) have shown that the infrared K' source remains resolved at $0.3''$ using higher resolution ground–based images, whilst Tadhunter *et al.* (1999) have found a nuclear point source at $2.25\,\mu$m which is ~ 4 times fainter than that estimated by DWMG by using the increased angular resolution of the NICMOS camera on the Hubble Space Telescope. Once the point source has been subtracted from the $\sim K$ band image Tadhunter *et al.* also find a sub–arcsecond scale biconical structure which they attribute to an outflow hollowing out material in a disk either side of the nucleus, similar to structures seen around young stellar objects.

DWMG have estimated the extinction towards the nucleus of Cygnus A in two ways. They assume the nuclear $K-L'$ colour can be attributed to a quasar nucleus "shining through". They then estimate the shape of the intrinsic spectral energy distribution of the quasar at these wavelengths. Extrapolating the high frequency radio data to infrared wavelengths they predict a value of $\alpha = -0.18 \pm 0.03$, whilst extrapolating a parabolic fit to all the radio data points gives a value of $\alpha \simeq -1.0$. It is worth noting that the median value of a quasar SED in the infrared is $\alpha = -1.4$ (Neugebauer *et al.* 1987) which is a far more reliable estimate of the intrinsic quasar spectral shape, extrapolating the radio data recorded over three orders of magnitude in frequency to points two orders of magnitude away is extremely dangerous (Simpson 1994a). Landau *et al.* (1986) obtained some good fits to the observed data using this method of extrapolation, but their baseline

data spanned six orders of magnitude rather just three, and still often failed to accurately fit small portions of the spectrum such as the K–L' region. The intrinsic $K - L'$ colour of the quasar using the different spectral indices is then calculated and subtracted from the observed colour to leave the reddening due to dust extinction, which is then converted to an extinction in visual magnitudes. DWMG then calculated the extinction to be either $A_V = 56 \pm 15$ or $A_V = 38 \pm 15$ depending on the choice of spectral index. Tadhunter *et al.* carry out a similar analysis using their fainter $\sim K$ flux and find $A_V = 86$ or 70 mag using spectral indices of -0.18 and -1.5 respectively. The second method DWMG employed used just the observed value of L' and the extrapolated fits to the radio data to obtain a value of $A_{L'}$ which give higher visual extinctions of $A_V = 83 \pm 13$ and $A_V = 35 \pm 14$. This procedure is equally dangerous owing to the possible stellar nature of the L' flux and continual use of the extrapolations to the radio data.

The most likely value of the extinction towards the infrared nucleus in Cygnus A is that given by Tadhunter *et al.* (1999) of around 70 magnitudes. Unfortunately this is still significantly lower than that estimated from the hard X–ray flux. It is thought that the discrepancy may be because the infrared point source is dominated by hot dust emission from the near–nuclear regions, whilst the X–ray value represents the true extinction to the quasar nucleus. However, X–rays are absorbed by gas and infrared radiation is absorbed by dust. The X–ray extinction is estimated by assuming a standard Galactic gas–to–dust ratio. If the intrinsic gas–to–dust ratio is higher than standard in the centre of Cygnus A, then the inferred extinction would be lowered, resolving the discrepancy between the X–ray and infrared values. Another interpretation is that the X–ray emitting region being more compact than the infrared region is intrinsically more obscured. Packham *et al.* (1998) have also found the nucleus to be highly polarized in K, which could point towards the infrared source being a reflection nebula situated near the nucleus behind a modest amount of foreground dust, therefore being obscured at optical wavelengths.

1.6.2 IC 5063

IC 5063 is a nearby S0 galaxy with a very red $K - L'$ colour of 2.15 in the central 5″ compared with a normal elliptical galaxy value of ~ 0.3 (Axon, Bailey & Hough 1982). The evidence for a hidden AGN nucleus is the presence of broad

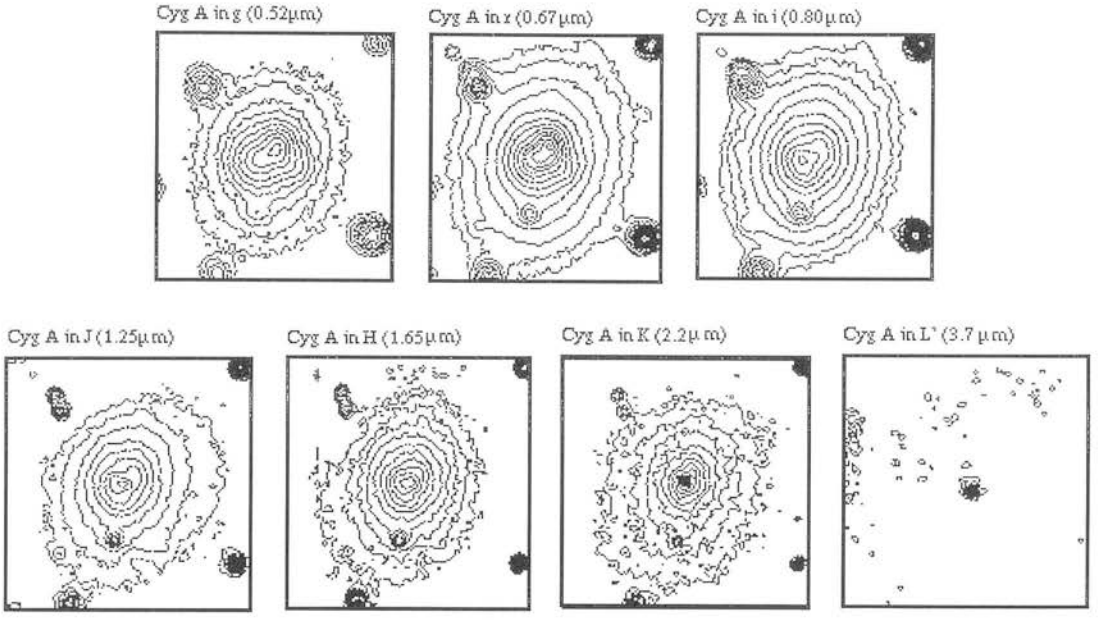

Figure 1.10: Optical and infrared images of Cygnus A taken from Djorgovski *et al.* (1991).

Hα in scattered light (Inglis *et al.* 1993). Although hard X–rays have also been detected (Koyama *et al.* 1992) the extinction value inferred from this observation is uncertain as the X–rays may come from a region of gas surrounding the nucleus as well as from the nucleus itself. A nuclear dust lane has has been inferred from the radial gradient of the $J-K$ colour by Colina, Sparks & Macchetto (1991) who were the first to attempt to detect the hidden infrared nucleus directly. Unfortunately they also use the 'scale and subtract' method to estimate a K band excess of 12.88. Simpson, Ward & Kotilainen (1994) use a more novel approach of deconvolving the galaxy and nucleus at K in the presence of a central dust lane by reconstructing the dust profile from the difference between the observed profile and an $r^{1/4}$ fit to the profile at J (see chapter 4) and then using this to recover the true galaxy surface brightness profile at K. A K band excess of 15.2 mag is then needed to fit the observed K band profile. Using the observed [OIII] λ5007 to infer the intrinsic infrared magnitudes using

$$\begin{aligned} m &= (11.145 \pm 0.775) + 2.5\log_{10} f_0/f_{5007} \\ &\quad +2.5\alpha\log_{10}\frac{\lambda/(1+z)}{5007\mathring{A}} + 2.5\log_{10}(1+z) \end{aligned} \tag{1.5}$$

from Simpson (1994a) where α here is the spectral index between 5007 Å and the infrared, they manage to constrain the possible values of α and A_V to be $\alpha \sim -1$ and $A_V \sim 65$ mag.

A more recent study of this galaxy using HST (Kulkarni *et al.* 1998) finds an unresolved 12.86 magnitude excess in the $\sim K$ filter after scaling this image to match the $\sim H$ band image at 7.5 pixels or 0.57″, similar to the values found by Colina, Sparks & Macchetto (1991) and Axon, Bailey & Hough (1982). They ascribe the excess to hot dust emission in the inner parts of the torus, but it is probably more likely to be an artifact of the scale and subtract procedure due to less nuclear dust emission at K than at H.

1.6.3 This project

One of the main aims of this thesis is a systematic attempt to search nearby radio galaxies for nuclei that are heavily extinguished, but still detectable at L' band if $A_V \lesssim 45$ mag. The sample is selected at low–frequency radio wavelengths to ensure that inclusion is not biased by any *a priori* knowledge of the strength of the nuclear source or depth of obscuring material. The sample contains both FR I and FR II sources of similar luminosities to test whether the incidence of obscured nuclei correlates with radio morphology. The galaxies are not selected on the basis of their emission line spectra as it has already been shown for the powerful 3CR galaxies that emission line strength does correlate with infrared excess (Lilly, Longair & Miller 1985). The important point here is to establish whether this extends down to the less powerful radio galaxies. From the above studies of Cygnus A and IC 5063 it is obviously important to accurately deconvolve the galaxy and nuclear light at both K and L' wavelengths to provide accurate estimates of the extinction towards the nucleus or infrared source. This will give an estimate of the relative numbers of hidden sources, their intrinsic luminosities, and provide some insight into the geometry of the obscuring material.

Simpson, Ward & Wall (1999) are in the process of carrying out the most similar analysis to this work to date. They use an almost identical two–dimensional modelling technique to deconvolve the galaxy and nuclear light at K, but use a less detailed method of predicting the stellar component to the L' flux, using just the spectrum of a star on the red giant branch, β Peg, rather than fitting model stellar populations. Two objects in their sample are in common with the sample here, 3C 33 = 0106+130 and 3C 98 =0356+102. A comparison of the model fits is given in chapter 4 and their results are used to supplement the results obtained here when drawing conclusions from the extinction estimates.

1.7 Radio galaxies, elliptical galaxies and stellar populations

An accurate detection of an obscured nuclear source in a radio galaxy depends crucially on an understanding of the nuclear stellar population. As one of the most clear–cut results in AGN research is that radio–loud AGN always have elliptical host galaxies, we should concentrate on an understanding of the stellar populations in elliptical galaxies.

Galaxies are assembled from two components, a bulge and a disk. The ratio of the bulge to the disk component generally classifies the galaxy on the Hubble sequence. The star–formation histories within the bulge and disk are very different as ongoing star–formation occurs in the gas–rich disks, such as is happening in our own galaxy the Milky Way. In bulges, to first order, the stars are all formed in a single burst of star–formation and then left to age passively. Elliptical galaxies are mostly bulges, with perhaps only a small disk component and therefore their spectra are dominated by the old, red (G and K type) stars left after the hot massive stars have evolved off the main sequence. In fact elliptical galaxies are thought to form from mergers between spiral galaxies (Toomre & Toomre 1972; Toomre 1977) where the massive burst of star–formation is caused by the merger, subsequent bursts of star–formation being due to subsequent mergers. The star–formation history of an elliptical galaxy is therefore intricately linked to the merger history of the galaxy. It is surprising then that the structural properties of elliptical galaxies are so uniform. There are a variety of tight scaling relations which describe the region of parameter space occupied by ellipticals. The Fundamental Plane (Djorgovski & Davis 1987; Dressler *et al.* 1987) is the correlation between velocity dispersion, effective radius and surface brightness, with a scatter of around 20%. The equation of the plane as given by Bender, Burstein & Faber (1997) is

$$\log_{10} r_e = 1.25 \log_{10} \sigma_v + 0.32 < \mu_e > + \text{const} \tag{1.6}$$

where r_e is the effective radius, σ_v the velocity dispersion and $< \mu_e >$ the mean surface brightness at the effective radius. Projections of this plane with larger intrinsic scatter are the Faber–Jackson relation (Faber & Jackson 1976)

$$L \propto \sigma_v^{\alpha}, \tag{1.7}$$

with L the luminosity of the galaxy, $\alpha \sim 3-4$, and the Kormendy relation (Kormendy 1977)

$$r_e \propto \mu_e^{-0.83\pm0.08}. \tag{1.8}$$

Owing to the tightness of the Fundamental Plane it was originally thought that ellipticals were formed in one massive burst of star–formation some time after the Big Bang. Their stellar populations could then be characterised by two properties, age and metallicity. Although it is still true that galaxies can be age–dated, what exactly this age means is confusing. It can be considered to be the age of the majority of the stellar population, *i.e.* a luminosity weighted age. Sometimes there have been no serious episodes of star formation since the formation of the galaxy so the inferred age is the age of the system whilst in other cases the age is just the time since the last major burst of star–formation as most of the stars in the system were reprocessed at that time.

An old stellar population will appear to have a red spectrum but metal–rich populations also appear to be quite red, as the individual stars are cooler than their appropriate metal–poor identical mass counterparts. This leads to the well–known age/metallicity degeneracy problem demonstrated by Worthey (1994), whereby the integrated spectrum of two old stellar populations, separated such that $\Delta \ln \mathrm{age}/\Delta \ln \mathrm{Z} \approx -3/2$, will appear almost identical. Much more will be said on the methods for breaking this degeneracy in chapter 5. Reddening by intervening dust will also cause a stellar population to appear red, so whilst observations point towards the nuclear regions of elliptical galaxies being redder than surrounding regions it is often difficult to pinpoint the cause of this reddening.

1.8 Thesis outline

Chapters 2 and 3 set the scene by describing the reduction and preparation of a sample of infrared images and optical spectra. Chapter 2 introduces the sample of radio galaxies to be studied and then concentrates mainly on the acquisition and reduction of infrared (K and L' band) images of these. Older optical images and some newer ones are also described along with accurate photometric calibrations. The whole catalogue of images obtained is appended at the end of the chapter. Chapter 3 moves on to describe the acquisition and reduction of the spectroscopic

sample. Accurate redshifts and central velocity dispersions are necessary for the subsequent index analysis so these are also estimated here. A catalogue of the spectra is also appended at the end of this chapter.

The bulk of the infrared image analysis is carried out in chapter 4. When looking for obscured nuclei it is vital to deconvolve the elliptical galaxy light and the emission from the non–thermal nuclear source. In L' the galaxy is practically undetected, whilst at K the galaxy is still strong; two dimensional modelling is therefore carried out to estimate the galaxy component, leaving a residual source in many cases. Initial extinction estimates are then made without consideration of the stellar contribution to the L' flux. This is considered in chapter 5, where simple stellar population models are fitted to the optical spectra and nuclear broad–band colours to gain a handle on the central stellar populations in the galaxies. The contribution to the infrared flux is estimated from the models and a reassessment of the nuclear extinction estimates is carried out.

The final chapter studies the correlation which is expected between extinction and viewing angle in most orientation dependent unified schemes. The viability of the obscured sources being unified with radio–loud quasars is considered. Finally the work presented here is summarised.

Throughout a notation for the dimensionless Hubble constant of $h \equiv H_0/100$ is used. The value of the cosmological density parameter is taken to be $\Omega = 1$.

Chapter 2

Optical and infrared imaging of radio loud galaxies

2.1 Introduction

This chapter describes the acquisition and reduction of observations of a sample of radio galaxies at both optical and infrared wavelengths. The observations were taken on the 3.8m United Kingdom Infrared Telescope (UKIRT) on Mauna Kea in Hawaii and the 4.2m William Herschel Telescope (WHT) on La Palma in the Canary Islands. Also described briefly are older optical images taken on a variety of telescopes between 1986 and 1989 which are described in full in David Nicholson's thesis (Nicholson 1990).

The purpose of obtaining calibrated L' images is to see if a nuclear point source is detectable at this wavelength and, if detected, to obtain the magnitude of the nuclear source. K band images are also obtained to provide infrared surface brightness profiles of the galaxies which enable a deconvolution of galaxy and nuclear point source to give a $K - L'$ colour of the nucleus. Optical images are necessary to aid this analysis, providing optical surface brightness profiles and optical–to–infrared radial colour gradients which can give a handle on the radial stellar population gradients within the objects.

The chapter begins with a description of the sample of galaxies used throughout this entire study, then describes the general points to consider when imaging at optical and infrared wavelengths. The reduction procedures employed for all the images are explained with special attention to the reduction of the L' data, where problems were encountered. Photometry within a standard aperture is carried out

on all but the L' images. The use of a standard aperture enables readers to convert the photometry result easily to that for any slightly differently sized aperture. For the L' images, where the underlying galaxy is not detected, photometry is carried out using an aperture which contains essentially the total observed flux from the object. It is also important to determine the radio morphology of each object, *i.e.* which Fanaroff–Riley class they belong to. An internally systematic method of determining this is presented in section 2.8. A catalogue of all the galaxy images is then appended at the end of the chapter.

2.2 The sample

The sample of radio galaxies presented in the thesis is taken from the radio galaxy redshift survey of Peacock & Nicholson (1991). The survey consists of a volume–limited, radio–selected sample of sources with approximate flux density $S > 0.5\,\mathrm{Jy}$ at 1.4 GHz over an area of 9.3 steradians. The all–sky survey was compiled from 4 separate radio surveys, whose properties are presented in table 2.1. The completeness of the survey is about 90%.

Survey	Frequency	Sky Coverage	References
Parkes	2.7 GHz	$\delta \lesssim 24°$	Bolton, Wright & Savage (1979)
Bologna B2	408 MHz	$24° \lesssim \delta \lesssim 40°$	Grueff & Vigotti (1972)
			Grueff & Vigotti (1979)
Jodrell Bank	966 MHz	$40° \lesssim \delta \lesssim 70°$	Cohen *et al.* (1977)
Bonn S5	5 GHz	$\delta \gtrsim 70°$	Kühr *et al.* (1981)
			Kühr *et al.* (1987)

Table 2.1: Radio surveys from which the Peacock & Nicholson radio galaxy redshift survey has been compiled, taken from Nicholson (1990).

The redshift limits of the survey are $0.01 \leq z \leq 0.1$. These limits have been chosen such that the higher limit of $z = 0.1$ corresponds to an apparent magnitude of $B \simeq 17$, so that galaxies at the edge of the survey are still relatively bright and easy to image in the optical. Very nearby radio galaxies are lost from radio surveys owing to over–resolution, so the lower limit of $z = 0.01$ avoids this. The extra limit of $|b| > 15°$ avoids obscuration along the line–of–sight in the galactic plane. The total survey contains 310 galaxies of which $\sim 10\%$ are known to be bright quasars or BL Lac objects, which are already thought to be harbouring

accreting black holes. The other 90% may, or may not, be found to contain hidden quasar nuclei. Redshifts and exact positions for all the galaxies are available and Nicholson (1990) has also already obtained some optical (B & I band) images of the sample. The relatively low redshift limits of the sample means that it is possible to obtain high–resolution, high signal–to–noise images of a large number of the sample in only a few observing nights.

The subsample of galaxies presented in this thesis contain twenty–six galaxies from the Parkes survey, nine from the Bologna survey, four from the Jodrell Bank survey and none from the Bonn survey, owing to the declination limits introduced by the infrared imaging at UKIRT. Therefore all the objects are selected at a frequency of 2.7GHz or less. The Bologna and Jodrell Bank surveys are particularly useful as a basis to obtain an unbiased sample of radio galaxies, as the low selection frequencies employed pick up objects independent of their orientation. Low frequencies are less affected by dust obscuration than higher frequencies, so the sample is not limited to those galaxies associated with strong, compact, and possibly beamed radio sources. This means that any orientation effects implied by unification schemes for radio galaxies and radio–loud quasars (Urry & Padovani 1995) do not affect inclusion in the sample. However, it is important to question whether the Parkes sample could contain a high proportion of core–dominated sources with spectral indices of $\alpha > -0.5$. Core–dominated sources are generally found in quasars which represent a very small fraction of the radio sources at redshifts less than $z = 0.1$, therefore no significant bias should be introduced.

Figure 2.1 shows a histogram of the redshift distribution of the entire survey compared to the sub–sample of galaxies presented in this thesis. It can be seen that the chosen objects are not a representative sample of the survey, concentrating on objects around $z = 0.03$. This is to enable a study of similar luminosity, similar redshift FR I and FR II sources, as inferring any properties from a comparison of nearby FR I sources with higher redshift FR II sources would be meaningless. Fanaroff & Riley (1974) note that there is a sharp division in radio power between the two classes, occurring at $P_{1.4\mathrm{GHZ}} \simeq 10^{25}\,\mathrm{WHz}^{-1}$. At $z = 0.03$ a radio luminosity of 0.5 Jy corresponds to a power of $P \simeq 8 \times 10^{23}\,\mathrm{WHz}^{-1}$ implying that many FR I sources as well as the more powerful FR II sources can be detected.

Table 2.2 introduces the sample of radio galaxies observed for this study. One of the objects, 2221−023, is a broad–line "N" radio galaxy whilst another, 1652+398,

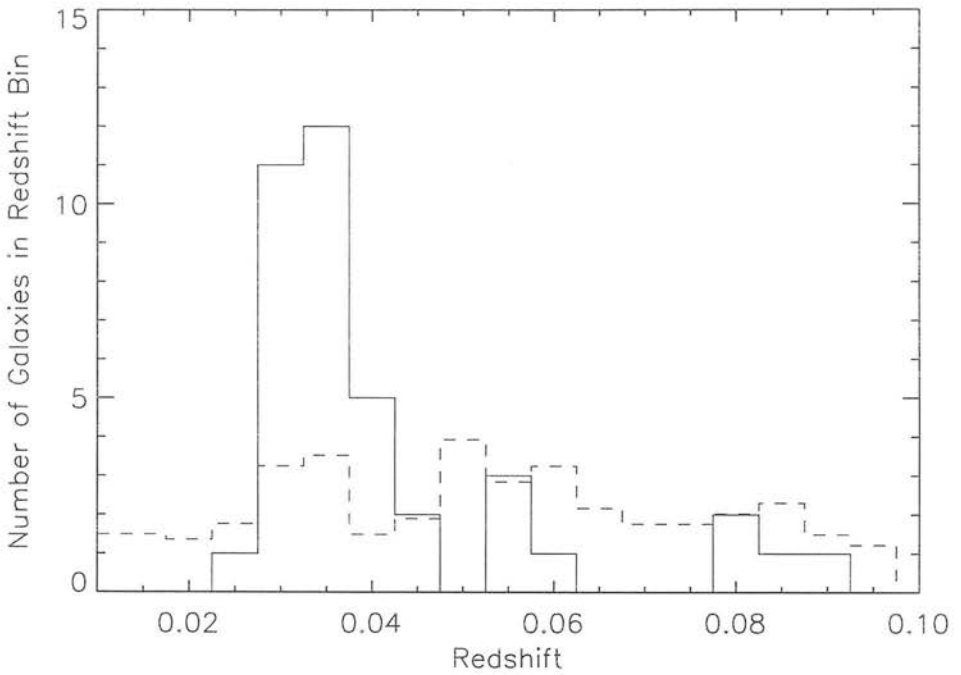

Figure 2.1: Histogram of the redshift distribution of the sample of observed galaxies. The width of each redshift bin is 0.005.The solid line shows the distribution of the observed sample of galaxies, whilst the dashed line is the redshift distribution of the entire survey normalised to the number of observed galaxies.

is a BL Lac. The radio morphology is not presented in this table as it is not available in the literature for all the objects and is worked out systematically in the manner of Owen & Laing (1989) using the total radio power and I band absolute magnitude in section 2.8.

Name	Alternative Names	$\alpha_{opt}(1950)$	$\delta_{opt}(1950)$	$\pm''$	$S_{1.4}$	m	cz	$\pm$	z	Images Obtained
0055−016	3C29, UGC00595, GIN015	00 55 01.57	−01 39 39.4	0.3	6.09	15.6	13311	200	0.0444	IKL'
0106+130	3C33	01 06 13.80	13 03 44.0	2.0	11.33	15.6	17538	60	0.0585	$IHKL'$
0206+355	UGC01651, 4C35.03	02 06 39.30	35 33 41.0	2.0	1.70	14.6	11212	240	0.0374	$IHKL'$
0207+095	4C09.08	02 07 07.73	09 35 52.6	0.5	1.35	17.0	26472	120	0.0883	$BIKL'$
0208−067		02 08 23.83	−06 47 44.1	0.8	0.61	15.0	12591	150	0.0420	$BIKL'$
0217+017	UGC01797	02 17 23.70	01 42 03.5	0.6	0.63	15.2	12262	150	0.0409	$BIKL'$
0300+162	3C76.1, PGC011499	03 00 27.27	16 14 36.6	0.9	3.21	16.0	9773	180	0.0326	$BIHKL'$ †
0325+023	3C88, UGC02748	03 25 18.19	02 23 20.3	0.4	5.11	15.0	9054	90	0.0302	$BIKL'$ †
0356+102	3C98, PGC014213	03 56 10.21	10 17 31.7	0.3	10.32	15.6	9174	30	0.0306	$BIRHKL'$ †
0419+140	4C14.12	04 19 40.89	14 00 44.9	1.0	1.10	18.0	19278	180	0.0643	$BIKL'$ †
0431−134	PGC015544, GIN190	04 31 51.49	−13 28 23.1	0.9	0.73	16.3	10912	270	0.0364	$BIKL'$ †
0502−103	ARP187, PGC016691	05 02 31.07	−10 18 57.7	1.1	1.18	15.4	11812	150	0.0394	$BIKL'$ †
0755+379	3C189, NGC2484, UGC04125	07 55 09.20	37 55 22.0	2.0	1.87	14.6	12381	240	0.0413	$BIKL'$ †
0833−016	NGC2616, UGC04489	08 33 02.06	−01 40 34.2	1.0	0.93	13.9	8994	120	0.0300	BI †
1004+146	CGCG093−046, KPG224	10 04 09.93	14 37 05.5	1.3	0.88	13.5	8814	150	0.0294	BI †
1040+317	CGCG154−041, PGC031956	10 40 31.00	31 46 45.0	2.0	0.60	16.9	10523	120	0.0351	$BIKL'$
1131+493	IC0708, UGC06549	11 31 16.13	49 20 16.8	0.4	1.03	14.2	10133	500	0.0338	$BIKL'$
1132+492	IC0711, PGC035780	11 32 03.83	49 13 56.2	1.1	0.5	15.2	9713	20	0.0324	$BIKL'$
1309+210	UGC08273	13 09 33.20	21 03 57.0	6.0	0.61	15.0	8994	60	0.0300	IKL'
1350+316	3C293, UGC08782	13 50 03.20	31 41 33.8	0.6	3.77	14.9	13491	60	0.0450	IKL'
1359−113	PGC049940	13 59 01.40	−11 21 58.0	1.0	1.79	15.0	10972	120	0.0366	KL'
1422+268	CGCG163−041, PGC051473	14 22 26.50	26 51 26.0	2.0	0.60	15.8	11092	240	0.0370	IKL'
1452+165	3C306, IC4516, UGC09587, GIN362	14 52 03.32	16 33 27.9	0.5	1.35	14.0	13671	210	0.0456	IKL'
1452−054		14 52 30.50	−05 27 24.0	12.0	0.98	17.0	11182	180	0.0373	$BIKL'$
1514+072	3C317, UGC09799, GIN419	15 14 17.00	07 12 16.7	0.4	3.89	14.5	10493	90	0.0350	IKL'
1601+173	NGC6034	16 01 16.39	17 20 06.8	1.0	0.79	13.5	10613	270	0.0354	IKL'

continued on next page

Name	Alternative Names	$\alpha_{opt}(1950)$	$\delta_{opt}(1950)$	$\pm''$	$S_{1.4}$	m	cz	$\pm$	z	Images Obtained
1602+178	NGC6047, GIN498	16 02 53.93	17 51 53.4	0.4	0.85	14.0	9443	60	0.0315	IKL'
1602+240	NGC6051, UGC10178, GIN487	16 02 48.94	24 04 01.5	2.0	0.63	14.9	9533	60	0.0319	IKL'
1652+398	MRK501	16 52 11.72	39 50 21.7	10.0	0.66	15.1	10103	240	0.0337	BKL'
1658+302	4C30.31, PGC059420	16 58 48.97	30 12 33.2	0.4	0.47	15.9	10523	240	0.0351	IKL'
1706+094	CGCG082−012	17 06 46.00	09 27 49.0	10.0	0.79	15.7	11452	210	0.0381	IKL'
1717−009	3C353, PGC060102	17 17 53.29	−00 55 49.9	0.4	61.39	16.3	9114	90	0.0304	IKL'
1842+455	3C388, PGC062332	18 42 35.44	45 30 21.7	0.4	5.95	17.2	27221	90	0.0908	$BIKL'$
Cygnus A	3C405, PGC063932	19 57 44.45	40 35 46.1	0.3			16811	30	0.0561	HKL'
2221−023	3C445, IRASF22212−0221	22 21 14.76	−02 21 26.1	0.4	5.85	17.0	16848	30	0.0562	$BIRHKL'$ †
2229−086	NPM1G−08.0617	22 29 05.60	−08 39 59.0	1.0	0.76	15.5	24763	180	0.0826	$BIKL'$ †
2243+394	3C452, PGC069671	22 43 32.79	39 25 27.3	0.5	10.05	17.0	24163		0.0806	$BIHKL'$ †
2308+073	NGC7503, PGC070628	23 08 10.20	07 17 52.0	0.5	1.62	14.9	13221	60	0.0441	$BIKL'$ †
2320+203	CGCG454−057, NPM1G20.0607	23 20 50.62	20 18 52.8	0.8	1.03	14.5	11512	180	0.0384	$BIKL'$

Table 2.2: Properties of the sample of galaxies described in this study, taken from Nicholson (1990). Column 1 contains the IAU name of the galaxy; column 2 contains well used alternative names for the objects; columns 3, 4 and 5 are the right ascension, declination and positional accuracy in arcseconds of the object; column 6 is the 1.4 GHz radio flux–density in Jansky; column 7 is the estimated B magnitude; columns 8,9 and 10 are the radial velocity and error in kms^{-1} and the redshift; finally the last column indicates which optical and infrared frames have been acquired, a † implies that optical spectroscopy (see chapter 3) has also been obtained.

2.3 Infrared Observing

2.3.1 Introduction to infrared observing

The main advantage to observing in the infrared (IR) over observing at optical wavelengths is the increased optical depth, which means that we can see further into dusty regions. The optical depth is roughly inversely proportional to wavelength. The measured extinction in the infrared is given by $\tau_\lambda \propto \lambda^{-1.85\pm0.05}$ (Landini *et al.* 1984). For example, in the Milky Way, towards the Galactic centre $A_V = 25$ mag whilst $A_K = 2$ mag.

Stars are approximate blackbody radiators. The emission from a blackbody is isotropic, unpolarised and has a smooth continuous spectrum. The Planck function describes the spectrum of emission from a blackbody and is defined by the equation

$$B_\nu(T) = \frac{2h\nu^3}{c^2(e^{h\nu/kT} - 1)}, \tag{2.1}$$

where B_ν is the intensity of radiation emitted per unit frequency interval at frequency ν from a blackbody of temperature T(K). The peak of the Planck function for objects at about 300–1500 K, such as the emission from hot dust and cool stars is in the near infrared (2–10 μm). Old, evolved stars are also more easily detectable in the IR and tend to trace the old stellar populations in galaxies better than in the optical, where small amounts of newly–formed, hot, luminous stars swamp the observations.

One of the main problems with ground–based observing in the infrared is the transmission through the atmosphere. Observations are severely hampered by absorption from water vapour and other molecules such as CO_2, CO and O_3. At wavelengths between 1–2.5 μm it is the dense forest of OH lines which dominate the atmospheric absorption, the strength of which can vary by a factor of two or more in half an hour. The OH absorption comes from a thin layer of atmosphere at an altitude of around 90 km and the variations are thought to be due to large scale wave motions in the mesopause, an isothermal layer between the mesosphere and the thermosphere. As the background intensity varies so significantly, for successful subtraction of the sky photons exposures must be limited to much less than the variation time–scale, *i.e.* $\ll$ 10 mins. At longer wavelengths (*i.e.* L') thermal emission dominates over the OH emission. As the atmosphere is at a finite temperature it emits blackbody radiation with an emissivity ϵ. The

emissivity is a measure of how opaque the atmosphere is at a certain wavelength, $\epsilon = 1.0$ implies it is totally opaque whilst $\epsilon = 0.1$ represents low absorption where observations are possible. These semi–transparent regions in the infrared sky are called "windows" and the filters used have been developed to sample the spectrum within these regions. Table 2.3 shows the wavelengths and half–max width of the main broad–band infrared filters, a plot of the atmospheric transmission and filter profiles is also given in figure 4.47 where it can be seen that the standard infrared profiles generally follow the shape of the transparent windows in the atmosphere.

Band	λ (μm)	$\Delta\lambda$ (μm)
J	1.25	0.3
H	1.65	0.3
K	2.2	0.4
L	3.45	1.0
L'	3.8	0.65
M	4.7	0.7
nb$M$	4.65	0.25

Table 2.3: Positions and sizes of the main infrared broad–band filters. The second column gives the central wavelength and the third column gives the half–max width of the filter.

At wavelengths $> 13\,\mu$m it is the thermal background from the telescope rather than the atmosphere which plays the most destructive part in the observations, as the telescope is generally a few degrees warmer than the atmosphere. In an attempt to reduce this component, all the instruments are cooled to very low temperatures (35 K) with liquid helium. The mirror is covered in a low–emissivity ($\epsilon = 0.07$) coating of silver and the telescope environment is cooled and carefully ventilated to reduce local atmospheric turbulence. To reduce the atmospheric background emission infrared telescopes need to be sited in high, dry and cold sites such as the top of the 4200m extinct volcano Mauna Kea on Hawaii or in Antarctica.

Infrared detectors are fundamentally different from optical charge–coupled devices (CCDs) not only in the material they are made from, but in the way they are read out. They are constructed from a semiconductor material such as InSb (indium antimonide) in the 1–5 μm range or HgCdTe (mercury, cadmium and tellurium) in the 1–2.5 μm range which is connected to a layer of silicon readout

material by small columns of indium. The silicon readout slab contains separate circuits so that each pixel can be read out independently, rather than using the charge–coupling principle of CCDs which works by shifting the charge around so that only one pixel is being read out at at time, a much slower process. The direct readout of IR detectors allows for a process called non–destructive readout (NDR). This means that the array can be read without affecting the signal level. Each pixel reading has an uncertainty associated with it called the read noise, caused by fluctuations in the voltage during readout. By fitting a slope to multiple independent measurements of the signal in a pixel as it builds up, the effective read noise can be reduced: $\sigma_{NDR} = (n/12)^{-1/2}\sigma_{RD}$ for large n (Chapman *et al.* 1990), where n is the number of independent measurements. The quantum efficiency (QE) of the InSb array is around 80%, although it decreases slightly towards shorter wavelengths. It is much higher than for CCDs where the QE peaks at around 50% at the optimised wavelength and drops off either side.

2.3.2 UKIRT observations

The infrared observations were taken during two observing runs in 1996 using the 1–5 μm imaging camera IRCAM3. The first run, on the nights of 30th–31st March, succeeded in obtaining images in K and L' of 20 radio galaxies and was carried out by Paul Hewett[1]. The second run, carried out by myself and John Peacock[2], on the nights of 6th–8th October, imaged a further 19 radio galaxies plus Cygnus A and 2 radio–quiet galaxies, for comparison with the radio–loud objects. Some H band frames were also taken for those galaxies where a tentative detection of a nuclear source was seen in L'. See table 2.2 for a summary of the observations taken.

The observing procedures for the H and K band images were almost the same for both runs. For the first run two separate K band mosaics of each object were taken which were eventually summed together, whilst only one was taken for the second run to make sure observations of as many different galaxies as possible were obtained. An SBRC (Santa Barbara Research Center) InSb 256×256 array chip was used in "non–destructive" ND–STARE mode. This means that when the chip is reset it is read immediately and then read again after integration.

[1]Institute of Astronomy, University of Cambridge, Madingley Road, Cambridge
[2]Institute for Astronomy, University of Edinburgh, Blackford Hill, Edinburgh

The difference between these two readings is recorded, so removing the bias level automatically. This also lowers the readout noise from about 60 e^- to about 47 e^- (Leggett 1998).

The galaxy image was moved around the chip to obtain 9 frames with 20″ offsets. This is common for infrared observations as the galaxy is in a different position on the detector for each of the 9 frames and allows a different flatfield image to be created for each object by median filtering the 9 frames. Dark frames were taken at around two hourly intervals throughout the entire observing run. The exposure times for each frame were 60 seconds for the first run and 100 seconds for the second run in K, whilst an exposure time of 90 seconds was used for the H band frames. The chip still only takes about 20 seconds to saturate at these wavelengths, so to achieve the required exposure time a number of "coadds" were taken of 10–15 seconds each and summed together to obtain the final frame. The pixel scale of the detector is 0.28″/pixel, so each frame has a 72″×72″ field of view.

The observing strategy in L' was different for each run. L' is a technically difficult waveband to observe in, the sky background is high and unstable, meaning that the chip saturates very quickly. A 'deepwell' bias setting was used, meaning that the bias level is lower than the standard setting, doubling the capacity of the chip which is necessary to avoid entering the non–linear regime of the chip. Even so, the full–well capacity of the chip is 144,000e^-, which combined with the high thermal background means that the maximum exposure time per coadd is about 0.01 seconds. The readout time for infrared detectors is roughly proportional to the number of pixels so reading out the whole 256×256 chip takes 0.12 seconds. It is therefore necessary to use a smaller 64×64 pixel sub–array to reduce the readout time to less than the exposure time.

The smaller chip size gives an 18″×18″ field of view, which is smaller than the size of most ellipticals at the redshift range of the sample. Fortunately the detector area is large enough for these purposes as only the unresolved nuclear source is being imaged, the underlying galaxy is not visible at L'. It was necessary to use the STARE observing mode, where the bias is not subtracted automatically, as the exposure time was much less than 1 second and the extra readout time needed if using the ND–STARE mode makes this type of observation unfeasible.

For the first run 1000 coadds each of 0.01 seconds were summed together to make

a 10 second frame. The galaxy image was moved horizontally across the chip to obtain 3 frames with 5″ offsets. This was carried out 42 times for each object to improve the signal–to–noise ratio (S/N). A dark frame was taken before each set of 42 images. For the second run a slightly different procedure was adopted with 1500 coadds of 0.01 seconds each summed together for each 15 second frame. The image was moved around the chip both vertically and horizontally with 5″ offsets, so the final image was constructed of 9 frames rather than just 3. This was done a minimum of 4 times for each object. Dark frames were again taken at regular intervals throughout the observing run.

Standard stars were taken from the UKIRT standard star lists[3]. "Faint" standards were used for the K and H band whilst "bright" standards were used for L' calibration. Typically five standard star exposures were obtained for each waveband during each night. The K and H band standards were generally observed for a total of 5 seconds whilst the L' standards were observed for 10 seconds.

2.4 Reduction of infrared images

For both optical and infrared images, the raw frames do not just contain signal from the astronomical object of interest, but also from various other components related to the electronics of the detector and the emission from the sky. These all need to be quantified and carefully removed to leave just the signal from the object (or most usually the signal from the object plus the sky). The raw signal components are:

- bias. The initial voltage across the readout device before integration.
- dark current. This is electronic noise which accumulates over time even when the detector is shielded from outside radiation.
- sky and telescope background.
- astronomical signal.

Any signal measured is also subject to a wavelength dependent pixel–to–pixel variation. This means that different pixels would measure different signal even if they were illuminated by a uniform source. The quantification of this variation is very important, which is why flatfield frames are constructed. Flatfield is a bit of a misnomer as the frames themselves are not flat. The point is that when the

[3]Available online at www.jach.hawaii.edu/UKIRT.new/astronomy/standards.html

image frame is divided by a flatfield frame, the output frame should be flat apart from any sky artifacts or astronomical objects.

2.4.1 H and K band images

As the emission from the sky varies with time, the colour of the sky also varies with time, meaning that the sky emission at a particular wavelength is time–dependent. The pixel–to–pixel response is also wavelength dependent, meaning that individual flatfields need to be constructed for each observation. The most common way of doing this at infrared wavelengths is to create the flatfields from the images themselves. The nine images with different offsets are median–filtered. The value of pixel $p(i, j)$ is compared with itself in all nine frames and the median is taken to be the flatfield value at pixel $p(i, j)$. This flatfield image is then normalised to have a mean of unity. The position of the galaxy is different in each of the nine frames, so its presence should not affect the median value. Problems only arise using this method when the size of the galaxy is large: *i.e.* it covers most of the chip. In these cases the median value is biased on the high side, division by the flatfield image causes the galaxy counts to be lowered, therefore underestimating both the size and the luminosity of the galaxy. A few of the radio–galaxies were quite large (0325+023, 2229−086, 0206+355) and the final images did appear to be cosmetically inferior to the images of more compact galaxies. To test the extent of this problem another flatfield was created from frames with the galaxy completely masked out. Final mosaics using both flatfields were then created and compared. From the comparison it appeared that the median–filtering flatfield creation method does produce small dents of about 1% in the flatfield. This accuracy is still acceptable for the analysis in chapter 4 as any dents only affect the wings of the galaxy surface brightness profile and most of the important information is obtained from fits within the central regions.

After experimentation with various reduction techniques it appeared that the UKIRT standard reduction software (IRCAMDR) was the simplest and most appropriate package to use. An ICL (Interactive Command Language) script, which was really an augmentation of the "stred" command in IRCAMDR was written and all the raw frames were input into this. A sketch of the reduction procedure is as follows:

- subtraction of a dark frame, scaled to the exposure time of the image;

- median–filtering flatfield creation;
- division by a normalised flatfield;
- airmass correction to unit airmass, this is described in detail in section 2.5:
- improved offset calculation, initial offsets being taken from the header files;
- sky level corrections between each of the 9 mosaic tiles are calculated and applied;
- bad–pixel masking by replacement with good pixels from overlapping frames;
- final image construction by mosaicing using the improved offsets and averaging all overlapping pixel values;
- K band duplicate images of objects from the first run were averaged, to improve the signal–to–noise.
- scaling to 1 second exposure time.

The telescope was supposed to slew by exactly $20''$ between individual frames and these frames are then mosaiced together to form the final image. Unfortunately it was necessary to recalculate precise offsets from the images by comparing the location of the centres of objects present in multiple frames as the nominal offsets ($20''$) were found to be unreliable by up to $5''$ and were generally around $0.5''$ in error even with the autoguider switched on. The newer offsets were then capable of producing final mosaiced images with the point spread function of any stars in a mosaiced image equal to the seeing width as measured from a single frame.

The differences in the sky level between mosaic frames were found by first calculating the median of the pixels in each overlap region, then finding the optimum correction for each frame to obtain a "flat" sky across the final mosaic. The bad pixels are actually hot, or non–functioning pixels, whose location is known for each detector. They are easily flagged by using a standard mask available with the reduction software. The standard stars were reduced in the same manner.

2.4.2 L' images

Initially the L' images were reduced identically to the H and K band images, but this was found not to be ideal as structure was present in the rows and columns of the raw frames. This appears to have been caused by the electronics of the readout, owing to the very short exposure times and high number of summed coadds. It is also possible that the structure is caused by saturation (Simpson, private communication) as the detector is susceptible to saturating every fourth

row. The problem with reducing L' images is illustrated in figure 2.2(a) which shows one of the worst cases of the problem. At worst, the actual level of the structure in the frames was very small at only 0.08% of the sky level. Although it was not known whether the effect was additive or multiplicative, the extremely low level of the effect allowed it to be treated in an additive fashion, thereby ensuring that the resulting photometry values remained unaffected.

(a) Standard Reduction (b) Modified Reduction

Figure 2.2: Example of a reduced L' image highlighting the reduction problems

A successful technique was found that initially removed the chessboard structure and prepared the frames for further reduction. It was as follows:

- Removal of frame–to–frame variation: the mean value of each frame was found and each frame was then divided by this average.
- Scaling: the average value over a set of nine frames was found, a global average, each frame was then multiplied by this.
- Flatfielding: a normalised median–filtered flatfield was created and the frames were divided by this.
- Residual structure removal: a σ–clipped column–mean was calculated for each column in a frame and the column was divided by this value. The same was then done for the rows of the frame. A clipping value of 2.5σ was used for both the columns and rows.

The next step in the reduction procedure, creating the final mosaics, was similar to that described in section 2.4.1 for the H and K band data, with some slight differences to try to correct for telescope offset inaccuracies. It is important to

try and register the frames properly as the final objective is to assess whether any of the nuclear sources detected are unresolved and could harbour a quasar–like central engine. Unfortunately the signal in all the individual frames was too faint to be able to estimate accurate offsets, so all the frames from a particular offset were summed together before being processed. If the telescope offset variations were systematic and the nuclear signal strong enough, then new improved offsets could be obtained before final mosaicing although this was only possible in a very few objects (see figure 2.3(b)). For the rest of the objects the residual structure corrected frames were simply dark–subracted, median–filtered and flatfielded, bias–level corrected, airmass corrected, bad–pixel masked and then mosaiced (see figure 2.3(a)). The similarity of the two images in figure 2.3 is encouraging as it implies that the default telescope offsets for the smaller 5″ slews of the telescope in the L' data are not as faulty as those found using the larger 20″ slews. All the images of the same object were then summed together. The standard star frames were also reduced in this way.

One of the aims of this project is to examine the unresolved nature of the L' source, however the uncertainty in offsets meant that this was not a realistic possibility. Comparing the photometry of the total source with that expected of the nuclear stellar component still allows an estimate of the relative amounts of stellar and non–stellar flux, so very little information is lost.

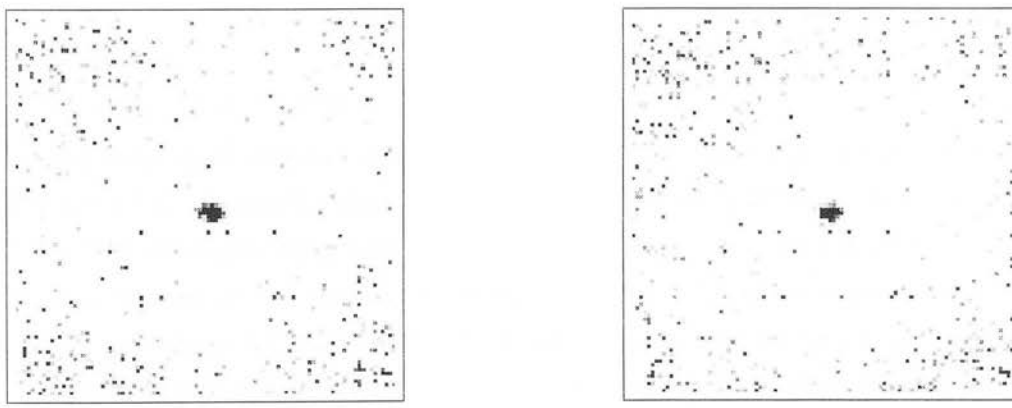

(a) Telescope Offsets (b) Improved Offsets

Figure 2.3: PKS 0356+102 in L' reduced using two different reduction procedures.

2.5 Photometry of infrared images

Photometry is the measurement of the brightness (or magnitude) of an object on a standard system. The basics of digital aperture photometry involve summing up the observed counts within a given radius of the centre of the object, subtracting the contribution from sky background within that region, leaving just the counts from the object. The sky background level is measured in an annulus far enough away from the object to be uncontaminated by object flux, whilst being close enough to give a representative measure of the sky flux beneath the object. The counts are then converted to magnitudes on a standard system via observations of standard calibrating stars. The apparent magnitude of an object in a particular waveband is defined as:

$$m = -2.5 \log_{10} \left[\frac{\text{counts}}{\text{exp}} \right] + \text{z}_{\text{pt}} \tag{2.2}$$

where z_{pt} is the zero point and 'exp' is the exposure time. The system used here defines the zero point so that the star Vega (α-Lyrae) has a magnitude of zero in all wavebands.

Photometric calibration equations need to be determined first from the standard star observations, in order to quantify the change in zeropoint with airmass and time. The calibrations take the form of

$$\text{z}_{\text{pt}} = \alpha + \beta(\sec\chi - 1) + \gamma(t - t_0) \tag{2.3}$$

where α is a constant offset term, β is a term proportional to the airmass ($\sec\chi$) and γ is a term which can be added in cases where the conditions are not stable (photometric) and the zeropoint changes with time. However the frames have already been corrected to unit airmass by the standard software. The airmass correction was done by multiplying the observed counts per second by $10^{\text{am}\times\text{ev}/2.5}$ where 'am' is the airmass of the observation and 'ev' is the extinction coefficient (in magnitudes per unit airmass) for the filter used. The extinction coefficients used here were: $H = 0.060$, $K = 0.080$ and $L' = 0.090$, which were the default values provided by the IRCAMDR software. They appear to be reasonable values to use since the measured values are variable. The median Mauna Kea extinction values from 1980–1996 were[4] $H = 0.059$, $K = 0.088$, $L' = 0.093$, whilst the

[4] http://www.jach.hawaii.edu/UKIRT.new/astronomy/exts.html

median values for the 1980–1986 period (Krisciunas *et al.* 1987) were $H = 0.051$, $K = 0.070$, $L' = 0.088$.

Ideally the airmass correction would be incorporated into the calibration equation to obtain a more accurate zeropoint and standard stars would be taken to cover the whole range of airmasses the objects cover. In this case though, the objects and standard stars chosen for observation were those in the galaxy survey or standard star list which were close to the zenith at the time of the observation, the maximum airmass from both observing runs was 1.68 and the median was between 1.05 and 1.1, therefore making the maximum correction for airmass around 0.05 magnitudes. If the extinction coefficient used for this correction was in error by 0.01 then the error in the photometry would be less than 0.01 mags: which is much less than the measured dispersion in zeropoints or the Poisson noise errors on each standard star measurement. So whilst the airmass corrections employed would be inappropriate for observations at high airmass, they are suitable for the range of airmasses used here.

Photometry was carried out firstly on the standard stars. An aperture was chosen which contained effectively all the flux from the star whilst avoiding including a large amount of sky–only pixels, which increase the uncertainty in the measurement. This was generally around 10 pixels in radius, or a 5.5″ aperture. The sky was calculated as a σ–clipped mean in a 10 pixel annulus around the star, at a radius of 15 pixels. The uncertainty associated with the zeropoints on each night was estimated by summing in quadrature the various sources of error: Poisson noise errors; error in the actual published magnitude of the standard star; and finally the rms variation of the zeropoint over the night of observations.

Table 2.4 gives the zeropoint and associated error for each night of observations. Although no time–dependent term is included, figure 2.4 shows the zeropoint estimated from each standard star and the time at which it was taken, which gives an idea of the fluctuations of each zeropoint over time. The conditions were photometric on all but the final night of observations. The zeropoints given here for the final night are only for a single standard taken during the middle of the observing period, where the conditions were believed to be stable. The photometry from this night can only be considered as an upper limit of the magnitude of the object. The lower limit of the magnitudes can be estimated from figure 2.4. The H band magnitudes estimated from images taken towards the beginning of the night are probably no more than 0.5 magnitudes too high,

Night	Zeropoint [mag]	±
K run 1	22.364	0.029
L' run 1	20.811	0.060
K run 2 night 1	22.398	0.099
L' run 2, night 1	20.717	0.109
K run 2, night 2	22.357	0.103
H run 2, night 2	22.889	0.027
L' run 2, night 2	20.670	0.186
H run 2, night 3	< 22.889	
L' run 2, night 3	< 20.893	

Table 2.4: Table of nightly zeropoint measurements from standard stars

whilst those taken at the end of the night, where the conditions have deteriorated drastically, could be up to 1.5 magnitudes in error. The lower limits on the L' magnitudes from the final night have similar sized errors associated with them. The infrared photometry has been compared where possible with published values in the literature (mainly for objects which are also in the 3CR catelogue) and the values all agree within the quoted errors.

2.6 Optical observing

Optical images are obtained to supplement the infrared images and to gain information on the optical to infrared colours of the stellar populations. In addition surface photometry of the I band images is used in conjunction with the radio luminosity measurements to predict the radio morphology.

Imaging at optical wavelengths ($\sim$ 3000–8000 Å) is generally more straightforward than infrared imaging. The main problem encountered is the noise introduced by cosmic rays passing through the detector, producing very high counts in the affected pixels. Luckily these events are random and can usually be removed by averaging multiple observations of one object and ignoring pixels that are many times higher than the expected noise value, see section 2.6.1 for more discussion on this issue.

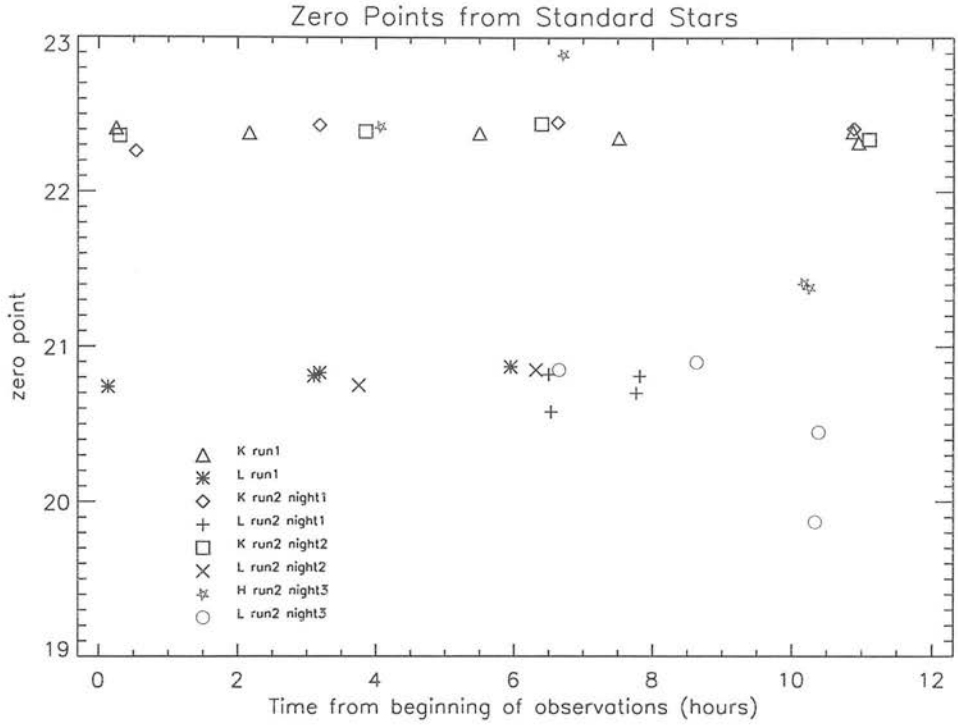

Figure 2.4: Plot of the nightly zeropoint changes with time from the beginning of observations

2.6.1 WHT observations and reduction

The new optical images were taken on 26th–29th November 1997 by myself, John Peacock and Raul Jimenez[5] during a run mainly devoted to spectroscopy. They were taken using the auxiliary port of the 4.2m William Herschel Telescope (WHT). The objects chosen were those for which we already had infrared images obtained at UKIRT the previous October. The detector was a TEK5 CCD with 1024×1024 pixels, each 24 μm square. The pixel scale was 0.11″/pixel. Two exposures were taken of each object for cosmic–ray removal purposes. The exposure times were around 180 seconds in B and 120 seconds in I, but this varied slightly depending on the magnitude of the object. No standards were taken as the conditions were not photometric. Twilight flatfields and a dark image for each waveband were also taken.

The raw optical images were all reduced using standard procedures in the IRAF[6] software environment. Prior to exposure, a voltage is applied across the readout

[5]Institute for Astronomy, University of Edinburgh, Blackford Hill, Edinburgh
[6]Image Reduction and Analysis Facility.

device which results in an initial number of counts, called the bias or zero level. The astronomical signal is then the number of counts above this level. The bias level can be easily determined from the overscan regions and then subtracted from the frames. The overscan regions are regions at the edges of the chip where the CCD has continued to clock across and read out beyond the edge of the actual detector. The bias level is subtracted line–by–line from each individual frame by linear interpolation between the overscan regions at the edges of the frame. This is preferable to subtracting just a single number for the whole frame as the readout device, and therefore the bias level, is sensitive to temperature. The temperature of the detector can vary over the time taken taken to read the chip, causing a gradient across the chip. Unfortunately there may also be pixel–to–pixel variations in the bias level which cannot be removed by a subtracting a simple linear polynomial. These variations can be determined by taking bias frames. A bias frame is a frame that is read out before the detector is exposed, sometimes called a zero–second exposure. Bias frames were taken at the beginning and end of each night of observations. These frames were summed together to create a master bias frame for the whole run. The bias level was then subtracted from the master frame as explained above to leave a frame containing just structure in the bias. This bias master frame was then subtracted from both the object and flatfield frames.

A flatfield image is a measure of each pixel's response to a uniform source. The best way to create a representation of this is to use the twilight sky as a uniform source. The raw twilight–flats were processed by first bias–level correcting them and then subtraction of the bias master frame. A dark frame was not subtracted as it was found that the dark current was practically zero: the mean of a 600 second dark frame was 1 count. The flatfield images from each waveband were then combined together using a cosmic–ray rejection algorithm. Pixels with values higher than 3σ away from the expected pixel value $\langle I \rangle$ were rejected from the combined frame. σ was calculated from the known noise parameters of the frames as

$$\sigma = \left[\left(\frac{\sigma_{read}}{g} \right)^2 + \frac{\langle I \rangle}{g} \right]^{\frac{1}{2}} \tag{2.4}$$

where σ_{read} is the read noise in electrons (4.34 e^-), g the gain in electrons per data number (1.13 e^-/ADU) and $\langle I \rangle$ the median value of the pixels being compared. As cosmic ray events often affect the pixels around them at a lower level, all pixels

next to a rejected 'high' pixel were also rejected.

After preparation of the bias and flatfield frames the object frames were then reduced as follows:

- bias–level subtraction;
- trimming of the overscan regions;
- subtraction of bias frame;
- division by the appropriate waveband flatfield frame;
- combining of individual frames to remove cosmic rays;
- normalisation to 1 second exposure time.

Accurate photometry combined with galactic extinction corrections (see section 4.4.2) were not made owing to the lack of calibration images as the images were taken in non–photometric observing conditions.

2.6.2 Pre–existing optical images

I band and some B band images were taken during the late 1980s on the University of Hawaii's 88 inch telescope (UH88) on Mauna Kea, the 3.9m Anglo–Australian Telescope (AAT) in Australia and the 2.5m Isaac Newton Telescope (INT) on the Canary Island of La Palma. The best observations were from the UH88 run where the seeing was sub–arcsecond. Typical exposure times were 180 seconds in I and 300s in B. The reduction of these images is described in Nicholson (1990).

Telescope, Size	Detector	Pixel Size (μm)	Pixel Scale ($''$/pixel)	Weather Conditions
UH 88inch	IfA CCD 500×500	15	0.67 Pointing Problems	Good, cloudless
AAT 3.9m	Thompson CCD 1024×1024	19	0.16	Acceptable
INT 2.5m	RCA CCD 350×512	30	0.74	Run 1 – Dusty Run 2 – Okay

Table 2.5: A summary of the observing runs. The UH88 pixel scale was re–measured by myself by comparison with frames in common with other telescopes and was found to be $\sim 0.67''$/pixel, not 0.41 as quoted in Nicholson (1990).

The value of the gain and readout noise were not given in Nicholson (1990), so they have had to be estimated. Most of the frames were well exposed, so it

has been assumed that the readout noise is neglible and the noise in the sky background is Poisson noise. If this were the case the standard deviation of the sky would be expected to be $\sigma = \sqrt{n}$ where n is the number of photons/pixel. I have measured $\sqrt{g\sigma}$ from the frames and hence estimated g, the gain, which is $\sim 1e^-/\mathrm{ADU}$ for all the CCDs used here.

2.7 Standard aperture photometry results

Table 2.6 presents photometric measurements within a standard diameter for the entire sample of optical and infrared images except those taken in the L' waveband. The L' photometry is presented in table 2.7. A standard diameter aperture of 20 h^{-1} kpc was chosen as it should contain nearly total light for all but the very biggest ellipticals, and is a typical diameter to use for local measurements. For example, Mobasher, Sharples & Ellis (1993) used a standard isophotal aperture of $\mu_B = 23.6$ mag arcsec^{-2}, which contained nearly all the galaxy light and turned out to be between 20 and 30 h^{-1}kpc.

Also given in table 2.6 is a value α (Gunn & Oke 1975), which parameterizes the growth in metric luminosity of the galaxy as a power–law:

$$L(< r) \propto r^{\alpha}, \tag{2.5}$$

This has been calculated by constructing a growth curve (figure 2.5). A line has been fitted between the points on the growth curve in log–log space, the gradient of this line is α. A plot of the change in α as a function of distance from the centre of the galaxy is then constructed (see figure 2.6). This curve has then been interpolated to find the value of the power–law exponent, α, at the radius of the standard aperture.

Some of the galaxies in the sample have bright objects nearby. For those cases where it was not possible to obtain 20 h^{-1}kpc apertures we obtained 10 h^{-1}kpc apertures which can be simply corrected to the standard diameter via an aperture correction

$$A = 2.5\alpha \log_{10}(0.5) \tag{2.6}$$

so now

$$m_{20h^{-1}\mathrm{kpc}} = m_{10h^{-1}\mathrm{kpc}} + A. \tag{2.7}$$

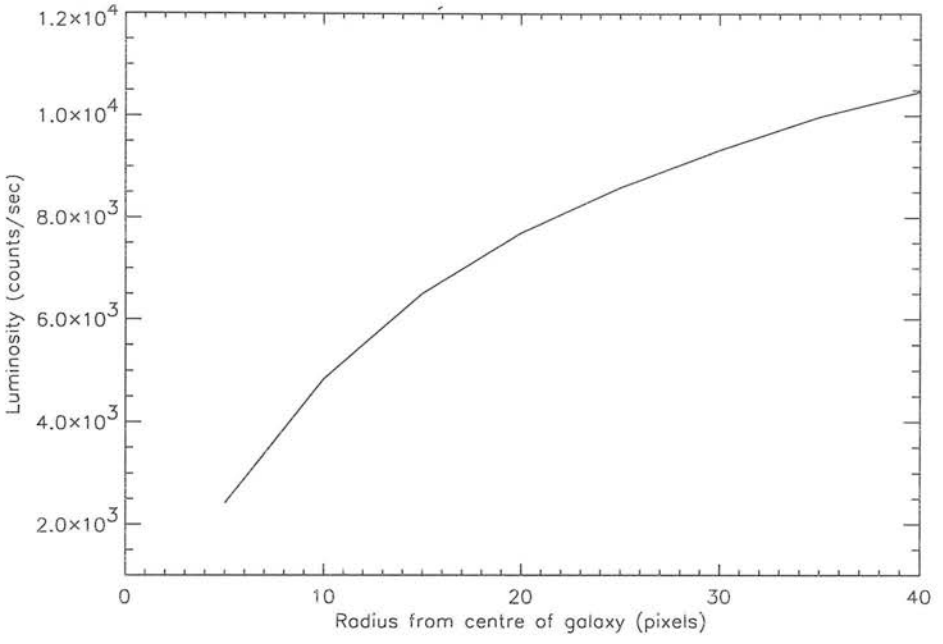

Figure 2.5: I band luminosity growth curve for the galaxy 0055−016

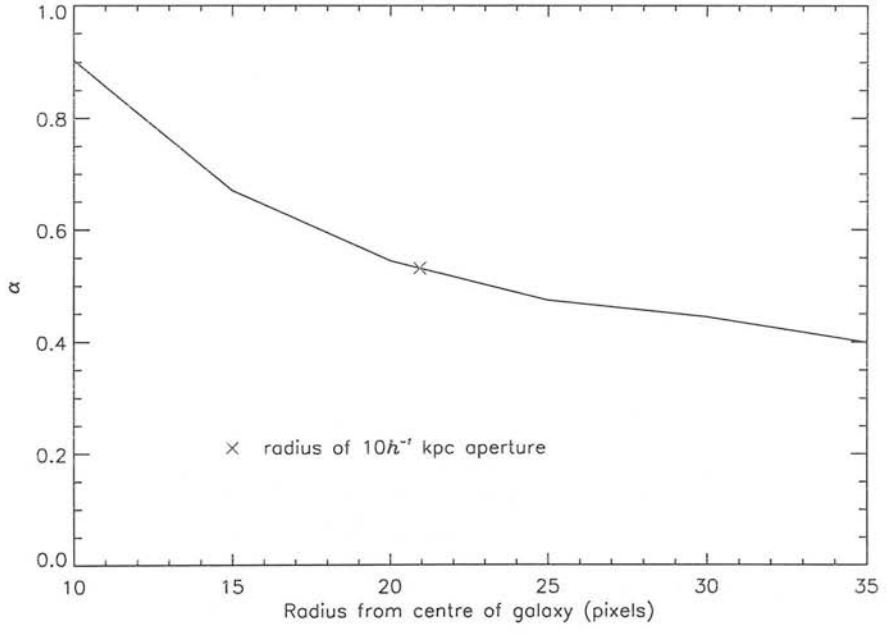

Figure 2.6: Change in α as a function of galaxy radius for 0055−016

Object	Waveband	m(20 h^{-1} kpc)	α	Notes
0055−016	I	13.427 ± 0.023	0.531	
	K'	10.922 ± 0.100	0.433	
0106+130	I	4.332 ± 0.026	0.503	
	H	< 12.418	0.308	1
	K'	11.997 ± 0.100	0.315	
0206+355	I	12.860 ± 0.031	0.623	
	H	< 10.550	0.429	1
	K'	10.286 ± 0.100	0.413	
0207+095	B	17.549 ± 0.046	0.734	
	I	14.803 ± 0.028	0.711	
	K'	12.287 ± 0.103	0.641	
0208−067	B	15.703 ± 0.027	0.423	
	K'	11.163 ± 0.103	0.265	
0217+017	B	15.544 ± 0.026	0.554	
	I	13.169 ± 0.022	0.474	
	K'	10.697 ± 0.103	0.284	
0300+162*	B	16.592 ± 0.034	0.527	2
	I	14.166 ± 0.024	0.461	
	H	< 12.383	0.362	1
	K'	11.781 ± 0.103	0.367	
0325+023	B	15.357 ± 0.025	0.696	
	I	12.958 ± 0.022	0.671	
	K'	10.749 ± 0.103	0.357	
0356+102*	B	16.306 ± 0.030	0.481	2
	I	13.879 ± 0.034	0.505	1
	H	< 11.565	0.357	
	K'	11.604 ± 0.100	0.329	
0419+140	B	19.075 ± 0.088	0.625	
	I(uh)	15.332 ± 0.034	0.578	
	K'	12.063 ± 0.103	0.418	
0431−134*	B	16.305 ± 0.030	0.564	2
	I(uh)	13.819 ± 0.023	0.523	
	K'	11.403 ± 0.103	0.423	
0502−103	B	15.585 ± 0.026	0.488	
	I	13.569 ± 0.022	0.408	
	K'	11.123 ± 0.103	0.225	
0755−379	B	15.092 ± 0.024	0.639	
	I	12.678 ± 0.021	0.604	
	K'	10.488 ± 0.029	0.348	
0833−016	B	14.226 ± 0.022	0.483	double object
	I	12.091 ± 0.021	0.522	

continued on next page

Object	Waveband	m(20 h^{-1} kpc)	α	Notes
1004+146	B	14.386 ± 0.022	0.527	
	I	12.067 ± 0.021	0.493	
1040+317	B	15.630 ± 0.029	0.419	triple object
	I	13.313 ± 0.022	0.404	
	K	11.366 ± 0.030	−0.006	
1131+493	B	12.942 ± 0.021	0.458	
	I	12.379 ± 0.021	0.458	
	K	10.492 ± 0.029	0.179	
1132+492	B	15.149 ± 0.029	0.332	
	I	12.018 ± 0.022	0.314	
	K	11.034 ± 0.029	0.107	
1309+210	I	13.414 ± 0.023	0.361	
	K	10.746 ± 0.030	0.083	
1350+316	I	13.477 ± 0.023	0.578	
	K	11.219 ± 0.030	0.208	
1359−113	K	10.422 ± 0.029	0.308	
1422+268	I	13.948 ± 0.026	0.513	
	K	11.334 ± 0.029	0.309	
1452+165	I	13.317 ± 0.023	0.597	
	K	10.635 ± 0.029	0.353	
1452−054	B	15.721 ± 0.034	0.320	
	I	13.616 ± 0.024	0.264	
	K	11.596 ± 0.030	−0.037	
1514+072	I	12.554 ± 0.022	0.868	
	K	10.652 ± 0.029	0.452	
1601+173	I	12.786 ± 0.022	0.437	
	K	10.626 ± 0.029	0.223	
1602+178*	K	11.166 ± 0.029	0.458	2
1602+240	I	12.212 ± 0.021	0.764	
	K	10.165 ± 0.030	0.409	
1652+398	K	10.023 ± 0.029	0.206	
1658+302*	I	13.337 ± 0.023	0.841	2
	K	11.116 ± 0.029	0.688	
1706+094	I	13.125 ± 0.022	0.417	
	K	10.897 ± 0.029	0.179	
1717−009	I	13.918 ± 0.025	0.542	
	K	11.141 ± 0.030	0.022	
1842+455	B		1.021	
	I	14.572 ± 0.028	0.963	
	K	11.933 ± 0.103	0.895	
Cygnus A	H	11.501 ± 0.027	0.921	

continued on next page

Object	Waveband	m(20 h^{-1} kpc)	α	Notes
	K	11.086 ± 0.100	0.860	
2221−023	B	16.827 ± 0.036	0.193	
	I	< 15.168		saturated image
	H	< 12.197	0.075	1
	K	< 11.085	0.069	saturated image?
2229−086	B	16.620 ± 0.034	0.768	
	I	13.935 ± 0.023	0.747	
	K	11.509 ± 0.103	0.626	
2243+394*	I	15.744 ± 0.049	0.714	2
	H	< 13.387	0.553	
	K	12.851 ± 0.100	0.510	
2308+073	K	10.506 ± 0.100	0.466	
2320−067	B	15.340 ± 0.025	0.542	
	I	12.909 ± 0.022	0.524	
	K	10.606 ± 0.100	0.360	

Table 2.6: Photometry results within a $20h^{-1}$ kpc metric aperture. Note 1 indicates that the results are only an upper limit on the magnitude. The H band results from the final night of infrared observations are uncertain as the conditions were non–photometric. A * indicates that it was not possible to measure a large enough aperture owing to the presence of a nearby object, so these objects have been measured through a smaller 10 h^{-1} kpc aperture (note 2). Also given is the value of the exponent α, such that $L(< r) \propto r^{\alpha}$, where r is either 10 or 20 h^{-1} kpc.

2.7.1 L' Photometry Results

The photometry values for the L' frames are presented in table 2.7. The values are for the total L' flux in a similar manner to the total flux from the standard stars. The apertures were generally between 3–5″, but depended on the accuracy of centering, the photometric aperture, and the observed spatial extent of the source. The 3σ background detection limit of the sources was generally between 13.5 and 14 magnitudes.

Object	L' [mag]	$\pm$ [mag]	Detection [σ]
0055−016	12.91	0.17	6.0
0106+130	11.73	0.20	13.2
0206+355	11.75	0.12	15.0
0207+095	12.96	0.19	5.7
0217+017	12.28	0.23	7.0
0300+162	13.05	0.28	3.8
0325+023	12.45	0.23	5.8
0356+102	11.95	0.12	14.6
0419+140	13.43	0.27	4.3
0431−134	12.33	0.23	6.2
0502−103	11.92	0.14	9.9
0755+379	12.37	0.10	10.9
1040+317	13.33	0.14	6.6
1131+493	12.49	0.09	12.0
1132+492	12.65	0.09	11.6
1309+210	11.72	0.07	19.2
1350+316	12.48	0.08	14.3
1422+268	13.15	0.11	8.3
1452+165	12.76	0.10	10.7
1514+072	13.84	0.24	3.5
1652+398	10.15	0.06	43.4
1842+455	12.72	0.23	6.3
Cygnus A	12.07	0.13	11.0
2221−023	9.02	0.11	109.0
2229−086	12.99	0.28	3.8
2243+394	12.69	0.23	7.7
2308+073	12.02	0.13	11.9
2320+203	12.11	0.13	10.7

Table 2.7: Total L' magnitude of all the objects with L' frames. The statistical value of the detection in σ is also shown.

2.8 Radio morphology

The radio morphology of each object in the sample is an important parameter to possess when attempting to compare any infrared excesses and extinction estimates with unified schemes. FR II sources are expected to be either more luminous or less extinguished than FR I sources, so an initial guess would be that excesses are more likely to be found in FR II sources. The radio morphologies for the powerful and well–studied 3CR sources in the sample are easily found from the literature, whilst the rest are from fainter flux–limited surveys such as

the 4C catalogue, so are expected to be on the whole FR I sources. An extensive search of the literature was carried out to find the morphology of as many objects as possible, the results of this search are presented in table 2.8. Radio contour maps of each object were obtained from the NRAO VLA Sky Survey (NVSS) archive. Some objects were also available on the higher resolution VLA FIRST (Faint Images of the Radio Sky at Twenty centimetres) survey. It was possible to obtain morphologies from the FIRST survey, however the resolution of the NVSS survey was not high enough to determine the morphology of all the objects accurately, so a more systematic approach needed to be found. Owen & Laing (1989) (O1) and Owen & White (1991) (O2) plotted the absolute radio flux against the absolute R band magnitude for a sample of low redshift radio galaxies whose morphology was already known. They found that the FRI/FRII break was a function of both radio and optical luminosity. The FRI and FRII objects inhabited almost distinct regions of the plot. A similar plot for the objects in this sample is shown in figure 2.7. The radio data is taken from table 2.2 whilst the optical luminosity is estimated from the I band images since R band images are not available. Surface brightness profiles were constructed to determine the position of the $\mu_I = 24.5$ mag arcsec^{-2} isophote. The flux was then summed within this isophote and converted to an apparent magnitude. For this analysis values of $H_0 = 75\,\mathrm{kms}^{-1}\,\mathrm{Mpc}^{-1}$ and $\Omega = 1$ were used for ease of comparison with O1 and O2, the apparent magnitudes were then converted to absolute magnitudes. No corrections have been made for K–dimming, galactic absoption or objects along the line of sight as the galaxies are concentrated around the same redshift and the aim is only to determine an internally systematic measure of the radio morphology in the absence of high resolution radio maps. 0419+140 has significantly more Galactic dust extinction than the other objects (see table 3.3, E(B-V)=0.831) the result of any correction would be to move the point in figure 2.7 to the right perhaps shifting it into the FR I region of the plot. The dotted line on the plot is hand–drawn to guide the eye to distinguish between the two regions of the plot. Apart from the two objects which sit on the boundary it is clear that the morphology of the other unknown objects is undoubtedly FR I. The NVSS radio maps of the two borderline objects are presented in figure 2.8, the lack of two distinct edge–brightened lobes, hint at the objects being FR I galaxies.

Object	FR class	Reference
0055−016	I	HST, PP88, FIRST
0106+130	II	O1, PP88
0206+355	I	L97, PP88
0208−067	I	FIRST
0300+162	I	PW81, PP88
0325+023	II	HST, PP88
0356+102	II	HST, O1, PP88
0431−134	I	O2
0755+379	I	O1, FIRST
1004+146	I	O1
1040+317	I	FIRST
1131+493	I	O2, FIRST
1132+492	I	O2, FIRST
1309+210	I	FIRST
1350+316	I	O1, PP88, FIRST
1359−113	I	O2
1422+268	I	FIRST
1514+072	I	HST
1602+240	I	FIRST
1652+398	C	PP88, FIRST
1658+302	I	FIRST
1717−009	II	HST
1842+455	II	HST, O1, PP88
Cygnus A	II	
2221−023	II	HST, FIRST
2229−086	I	O2, FIRST
2243+394	II	HST

Table 2.8: FR classes obtained from the literature and archive data. HST is Martel *et al.* (1999), L97 is Lara *et al.* (1997), PP88 is Prestage & Peacock (1988), PW81 is Peacock & Wall (1981), O1 and O2 are as in the text. FIRST denotes an image has been obtained from the FIRST survey. 1652+398 is marked C, as it is one of the core-dominated BL Lac objects, which are thought to be aligned versions of FR I radio sources.

2.9 Images

The images presented here are all $30h^{-1} \times 30h^{-1}$kpc, to allow for easy comparison of actual galaxy sizes. This also allows an eyeball estimation of the region of the galaxy used in the metric aperture photometry, which was a 20 h^{-1}kpc diameter circle, centered on the centre of the galaxy. North is at the top, east to the left. The greyscaling is between $S - 3\sigma$ and $S + 3\sigma$, where S is the sky level and σ is

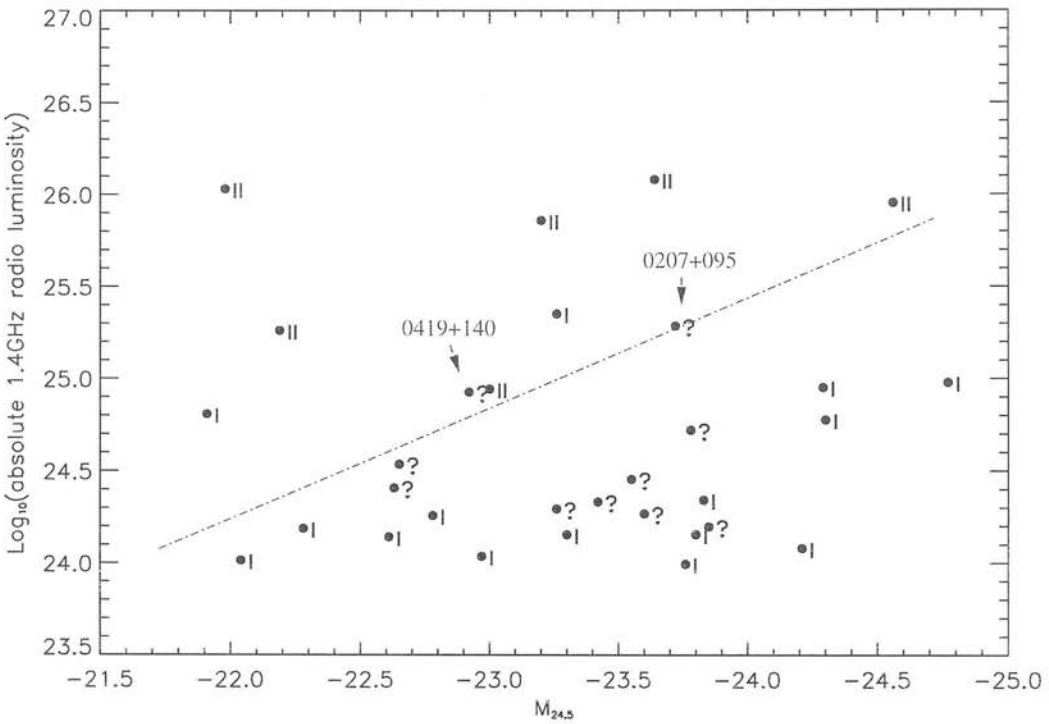

Figure 2.7: The log of the absolute radio power at 1.4 GHz (W Hz^{-1}) versus the absolute $M_{24.5}$ *I* band magnitude. Objects with known Fanaroff–Riley classes from the literature are plotted as 'I' and 'II' and unknown objects as '?'. The line is drawn on by eye to guide the reader to the different regions of the plot occupied by the FR I and FR II sources.

the standard deviation in the sky level. The contour spacing is equidistant in log intensity.

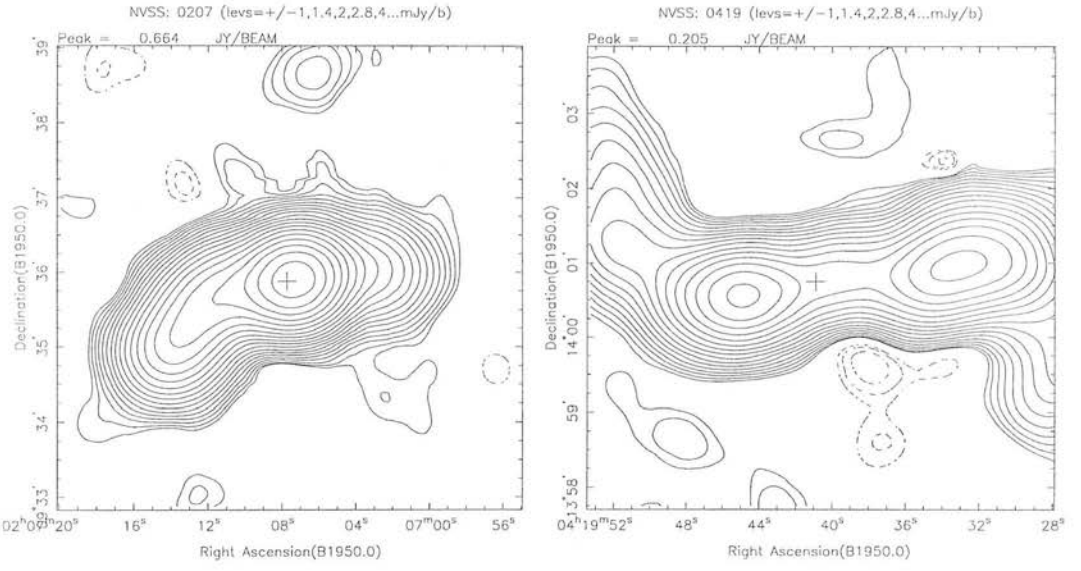

(a) 0207+095 (b) 0419+140

Figure 2.8: Radio maps from the NVSS archive of the two borderline FRI/FRII objects.

Figure 2.9: Images of 0055−016

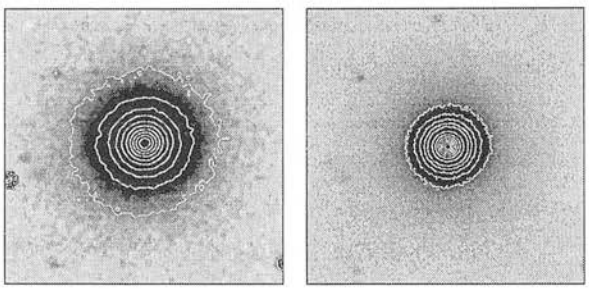

(a) INT I Band

(b) UKIRT K Band (Oct run)

Figure 2.10: Images of 0106+130

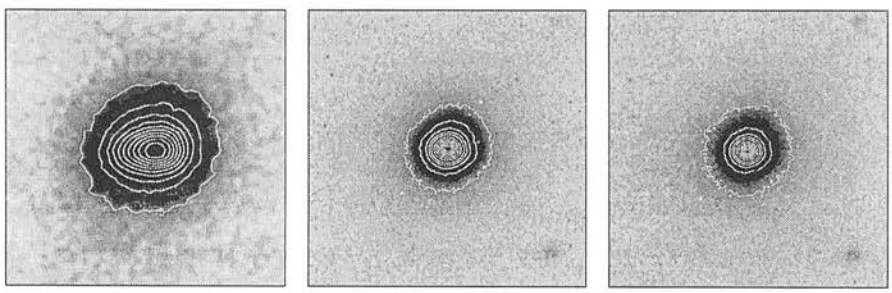

(a) INT I Band

(b) UKIRT H Band (Oct run)

(c) UKIRT K Band (Oct run)

Figure 2.11: Images of 0206+355

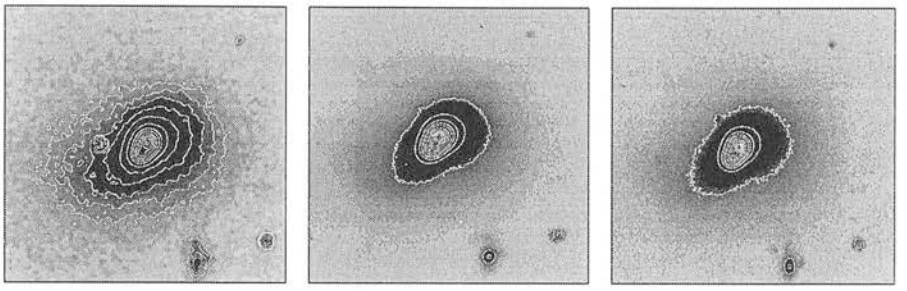

(a) INT I Band

(b) UKIRT H Band (Oct run)

(c) UKIRT K Band (Oct run)

Figure 2.12: Images of 0207+095

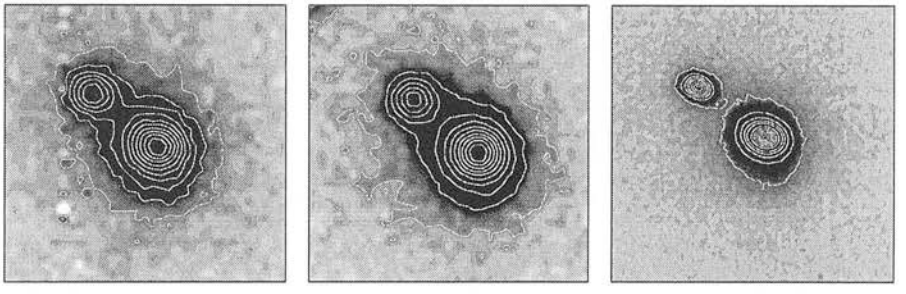

(a) UH B Band

(b) UH I Band

(c) UKIRT K Band (Oct run)

Figure 2.13: Images of 0208−067

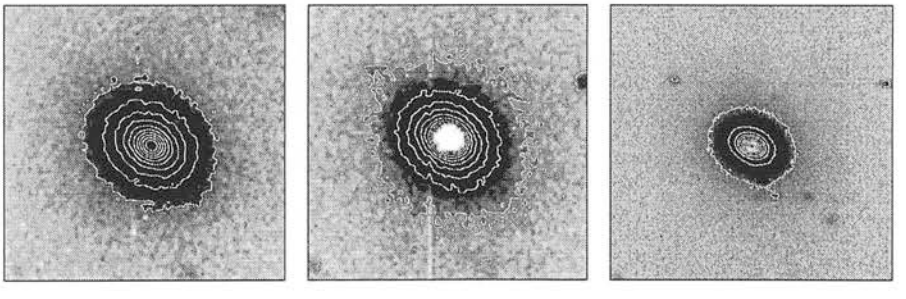

(a) UH B Band

(b) UH I Band (saturated centre)

(c) UKIRT K Band (Oct run)

Figure 2.14: Images of 0217+017

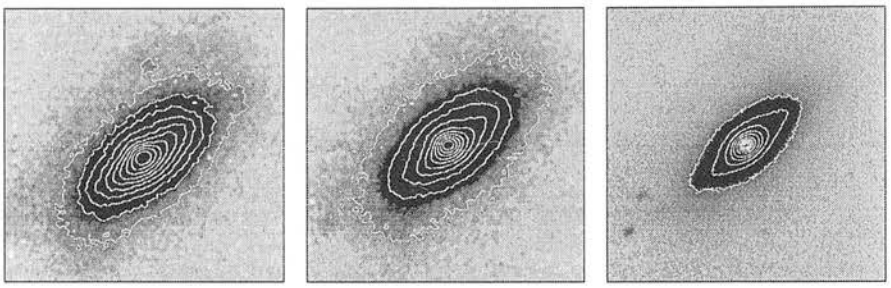

(a) UH B Band (b) UH I Band (c) UKIRT K Band (Oct run)

Figure 2.15: Images of 0300+162

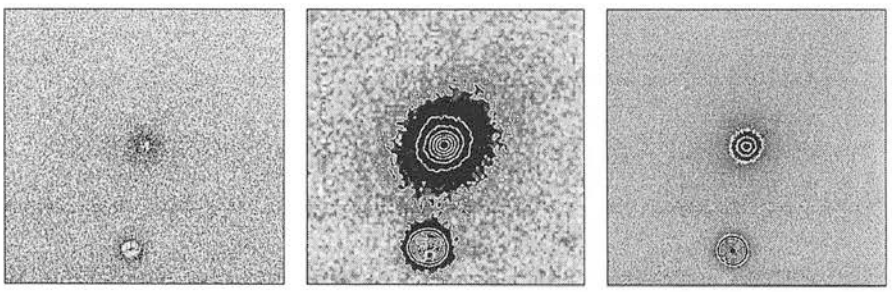

(a) WHT B Band (b) UH B Band (c) WHT I Band

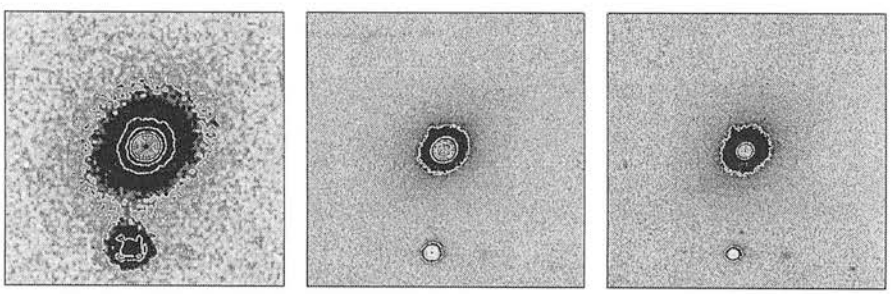

(d) UH I Band (e) UKIRT H Band (Oct run) (f) UKIRT K Band (Oct run)

Figure 2.16: Images of 0325+023

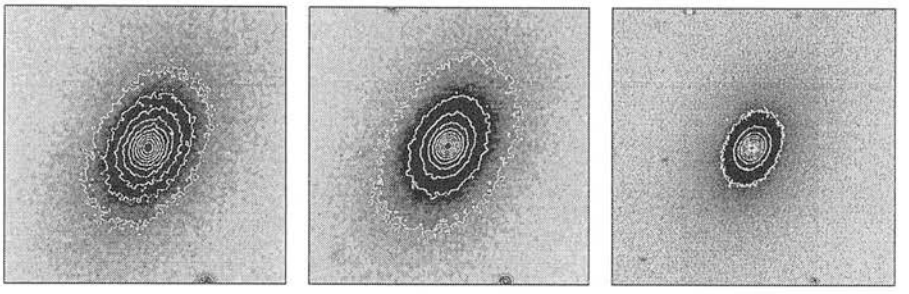

(a) UH B Band (b) UH I Band (c) UKIRT K Band (Oct run)

Figure 2.17: Optical images of 0356+102

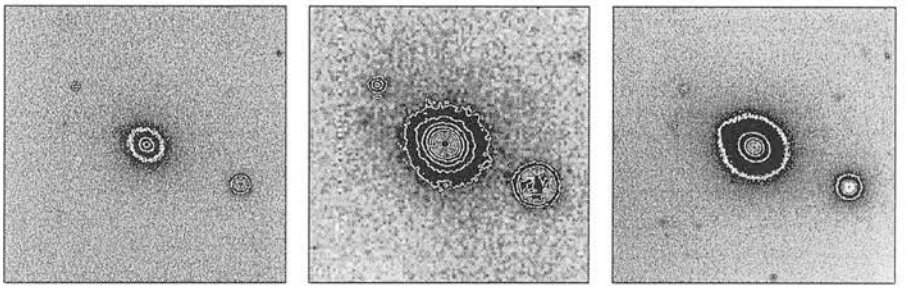

(a) WHT B Band (b) UH B Band (c) WHT I Band

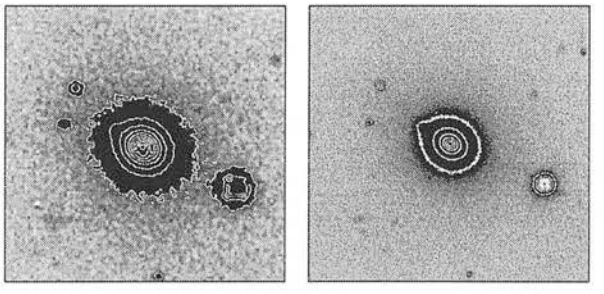

(d) UH I Band (e) WHT R Band

Figure 2.18: Infrared images of 0356+102

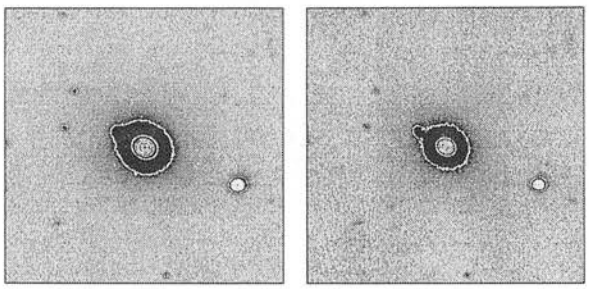

(a) UKIRT H Band (Oct run)

(b) UKIRT K Band (Oct run)

Figure 2.19: Images of 0419+140

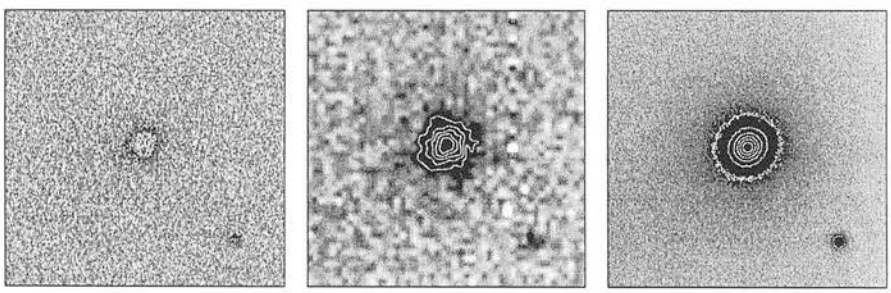

(a) WHT B Band

(b) UH B Band

(c) WHT I Band

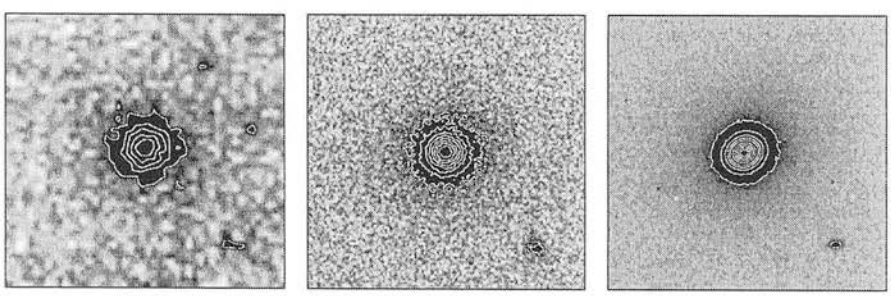

(d) UH I Band

(e) AAT I Band

(f) UKIRT K Band (Oct run)

Figure 2.20: Images of 0431−134

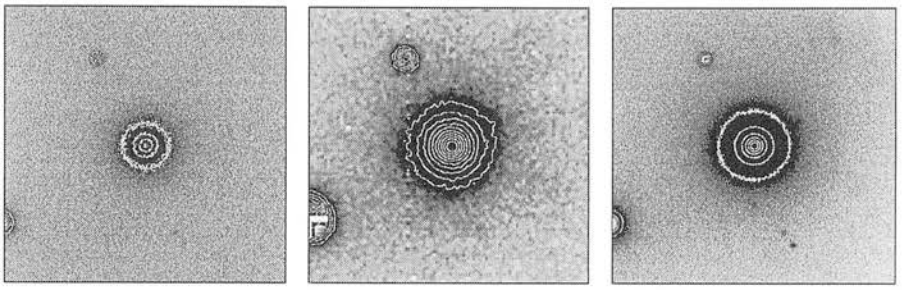

(a) WHT B Band (b) UH B Band (c) WHT I Band

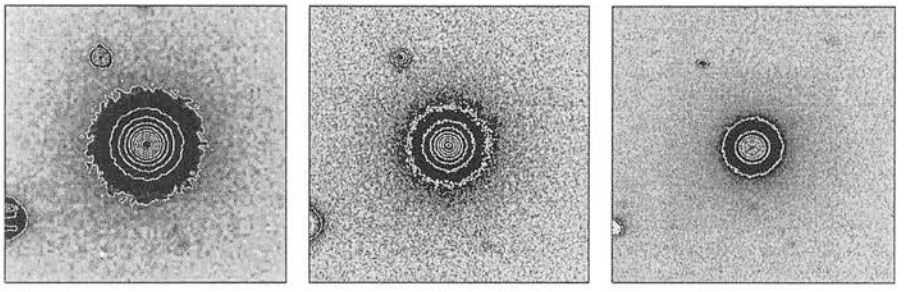

(d) UH I Band (e) AAT I Band (f) UKIRT K Band (Oct run)

Figure 2.21: Images of 0502−103

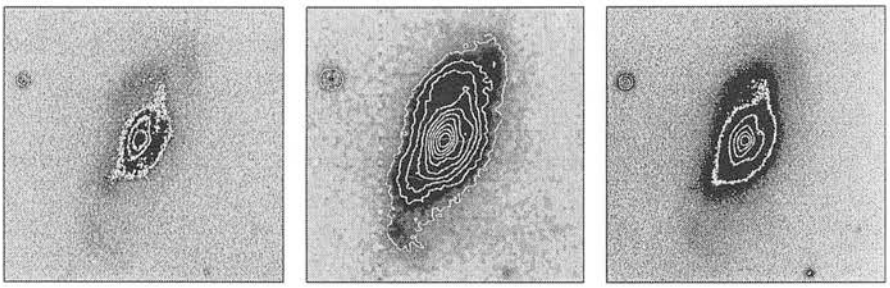

(a) WHT B Band (b) UH B Band (c) WHT I Band

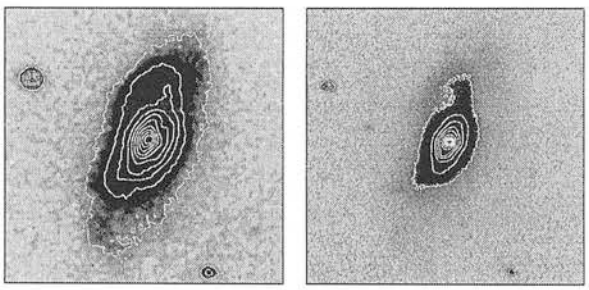

(d) UH I Band (e) UKIRT K Band (Oct run)

Figure 2.22: Images of 0755−379

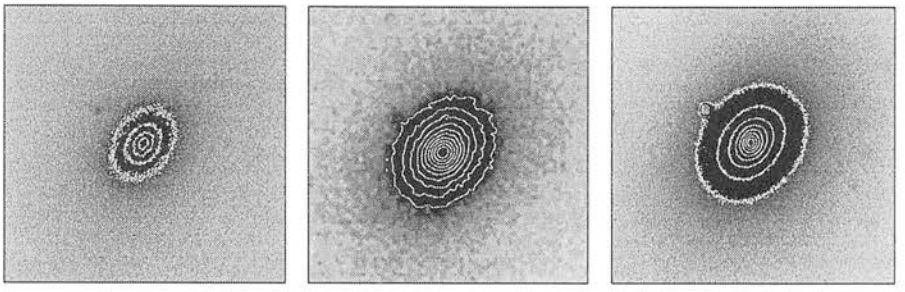

(a) WHT B Band (b) UH B Band (c) WHT I Band

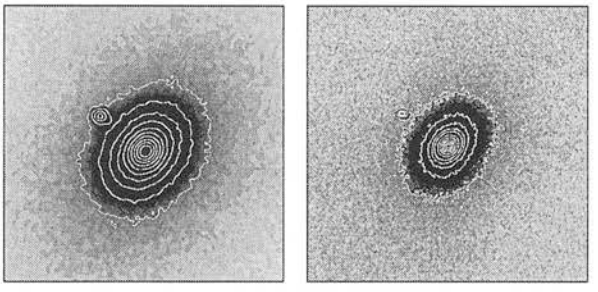

(d) UH I Band (e) UKIRT K Band (Mar run)

Figure 2.23: Images of 0833−016

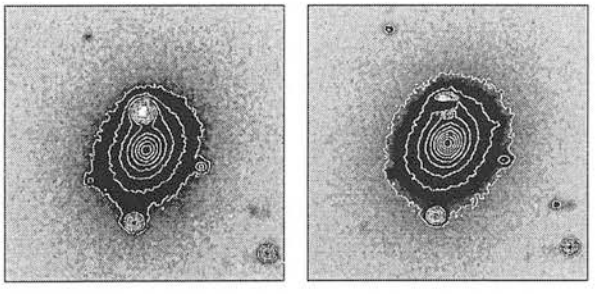

(a) UH B Band (b) UH I Band

Figure 2.24: Images of 1004+146

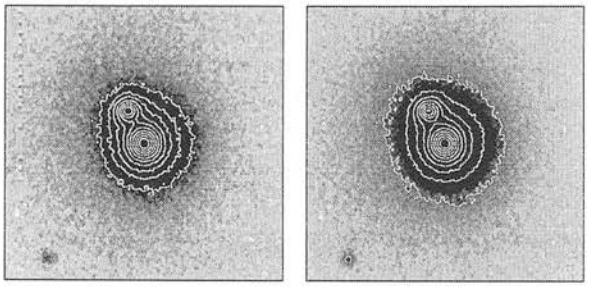

(a) UH B Band (b) UH I Band

Figure 2.25: Images of 1040+317

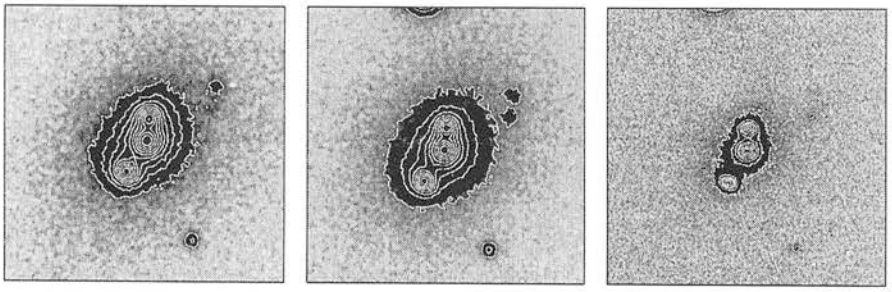

(a) UH B Band (b) UH I Band (c) UKIRT K Band (Mar run)

Figure 2.26: Images of 1131+493

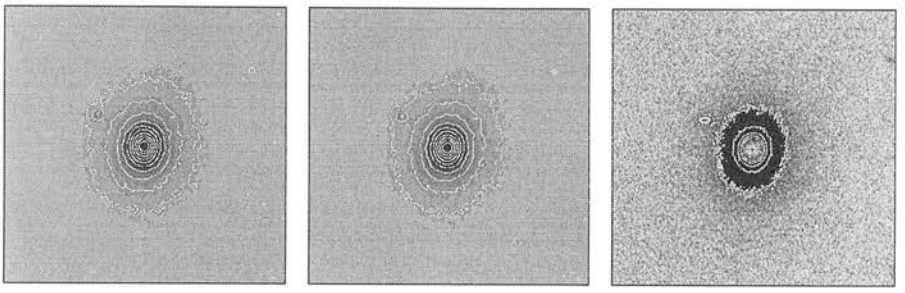

(a) INT B Band (b) INT I Band (c) UKIRT K Band (Mar run)

Figure 2.27: Images of 1132+492

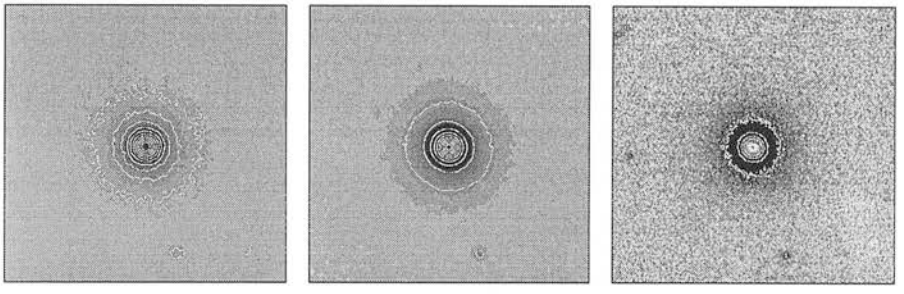

(a) INT B Band (b) INT I Band (c) UKIRT K Band (Mar run)

Figure 2.28: Images of 1309+210

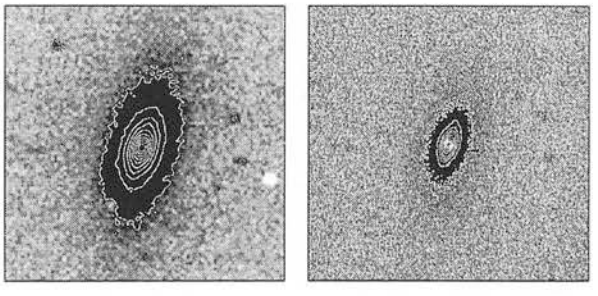

(a) INT I Band (b) UKIRT K Band (Mar run)

Figure 2.29: Images of 1350+316

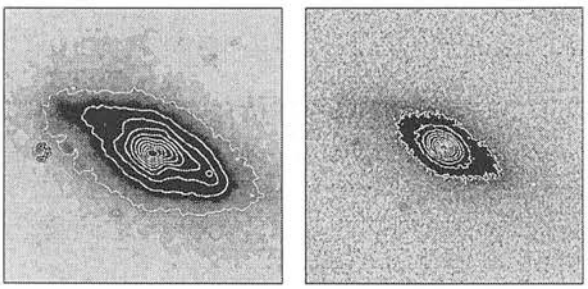

(a) INT I Band

(b) UKIRT K Band (Mar run)

Figure 2.30: Images of 1359−113

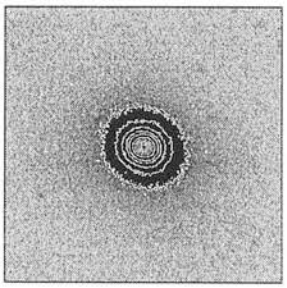

(a) UKIRT K Band (Mar run)

Figure 2.31: Images of 1422+268

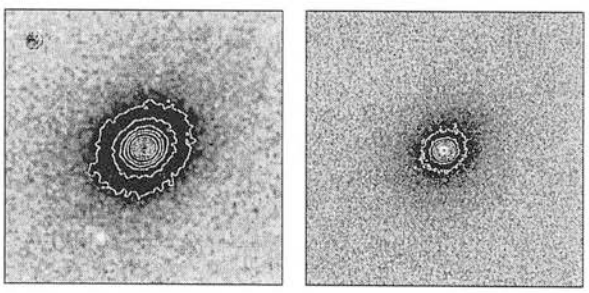

(a) INT I Band

(b) UKIRT K Band (Mar run)

Figure 2.32: Images of 1452+162

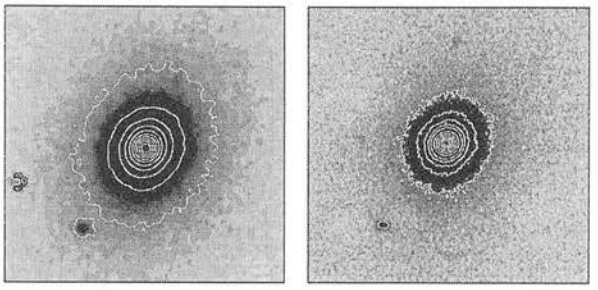

(a) INT I Band (b) UKIRT K Band (Mar run)

Figure 2.33: Images of 1452−054

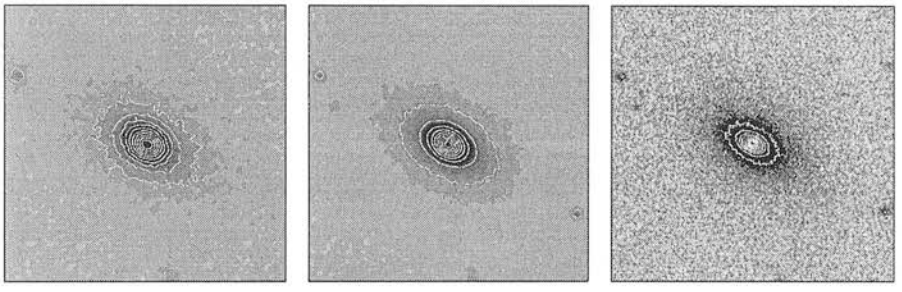

(a) INT B Band (b) INT I Band (c) UKIRT K Band (Mar run)

Figure 2.34: Images of 1514+072

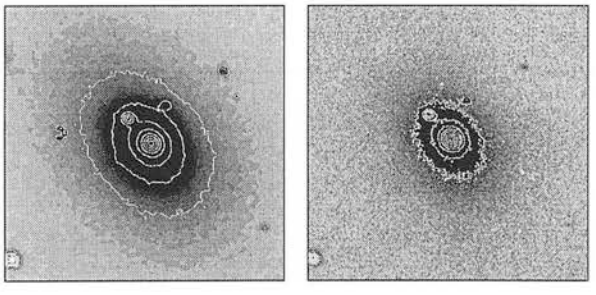

(a) INT I Band (b) UKIRT K Band (Mar run)

Figure 2.35: Images of 1601+173

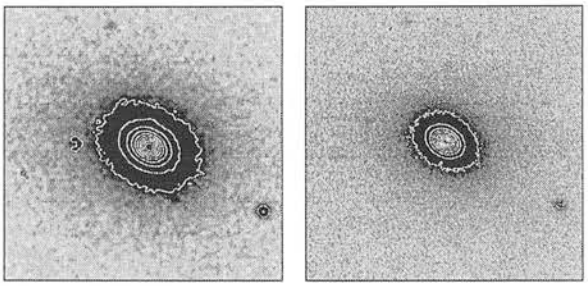

(a) INT I Band (b) UKIRT K Band (Mar run)

Figure 2.36: Images of 1602+178

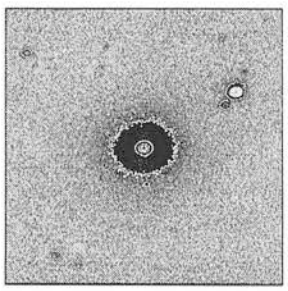

(a) UKIRT K Band (Mar run)

Figure 2.37: Images of 1602+240

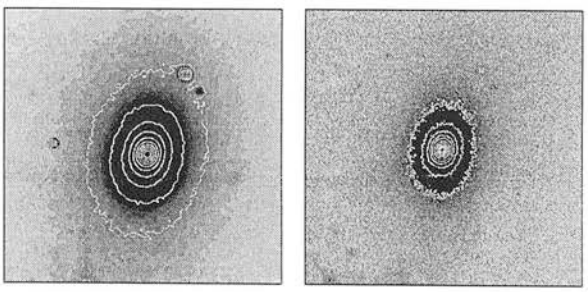

(a) INT I Band (b) UKIRT K Band (Mar run)

Figure 2.38: Images of 1652+398

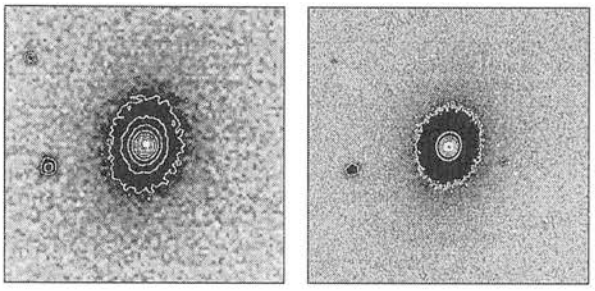

(a) INT B Band

(b) UKIRT K Band (Mar run)

Figure 2.39: Images of 1658+302

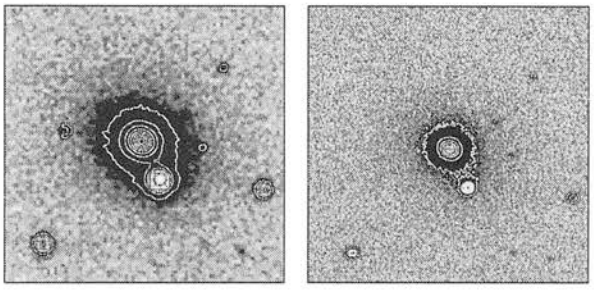

(a) INT I Band

(b) UKIRT K Band (Mar run)

Figure 2.40: Images of 1706+094

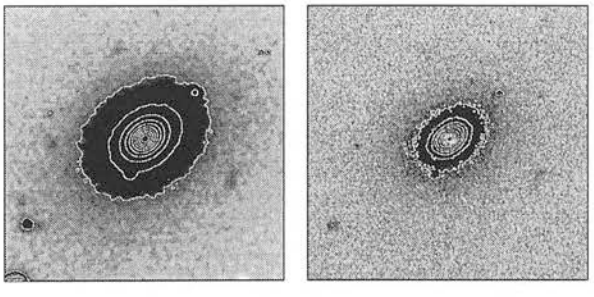

(a) INT I Band

(b) UKIRT K Band (Mar run)

Figure 2.41: Images of 1717−009

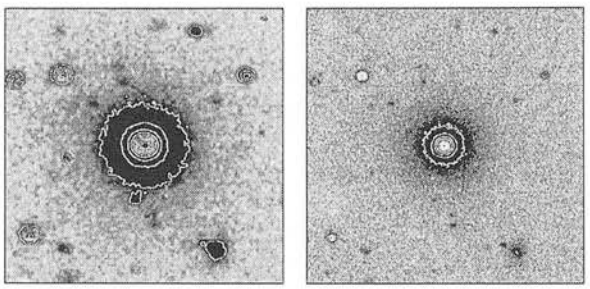

(a) INT I Band

(b) UKIRT K Band (Mar run)

Figure 2.42: Images of 1842+455

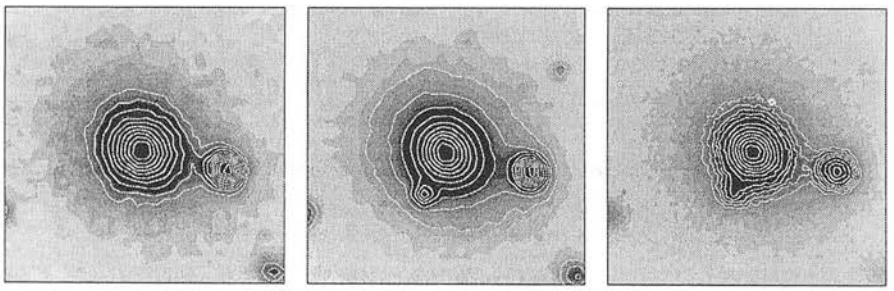

(a) INT B Band

(b) INT I Band

(c) UKIRT K Band (Oct run)

Figure 2.43: Images of Cygnus A

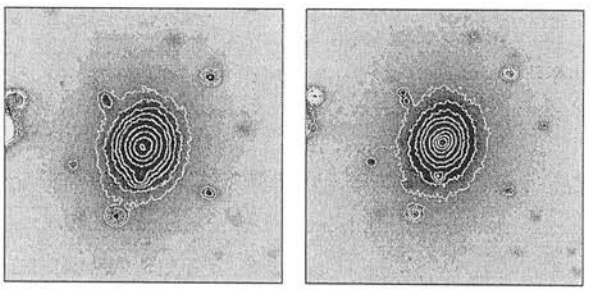

(a) UKIRT H Band (Oct run)

(b) UKIRT K Band (Oct run)

Figure 2.44: Images of 2221−023

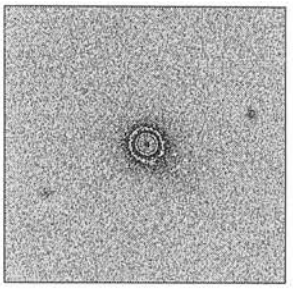

(a) WHT B Band

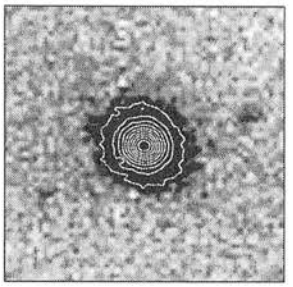

(b) UH B Band

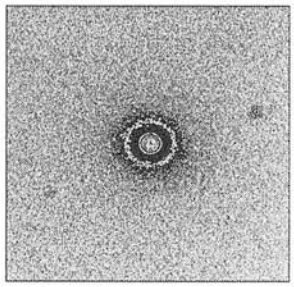

(c) WHT I Band

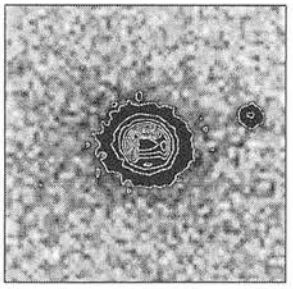

(d) UH I Band

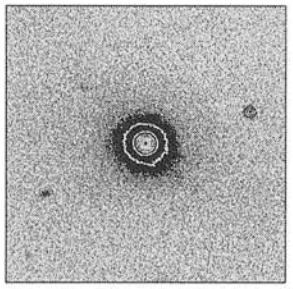

(e) WHT R Band

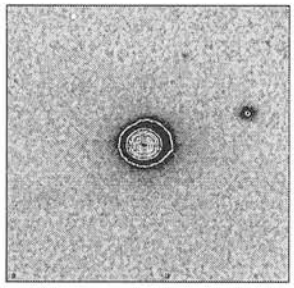

(f) UKIRT H Band (Oct run)

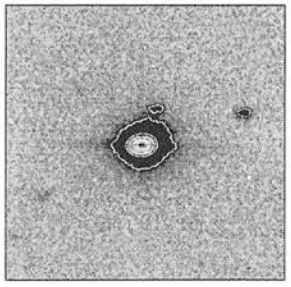

(g) UKIRT K Band (Oct run)

Figure 2.45: Images of 2229−086

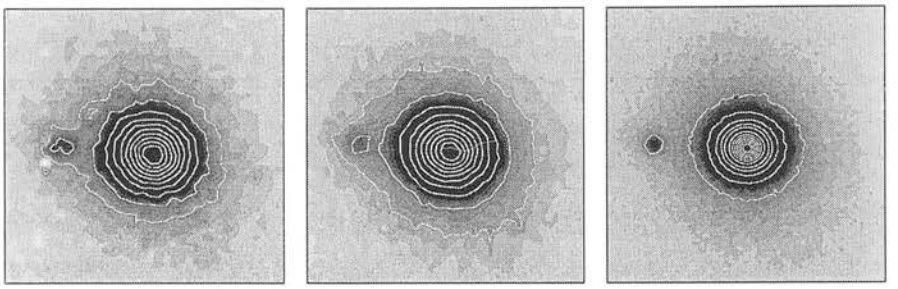

(a) UH B Band (b) UH I Band (c) UKIRT K Band (Oct run)

Figure 2.46: Images of 2243+394

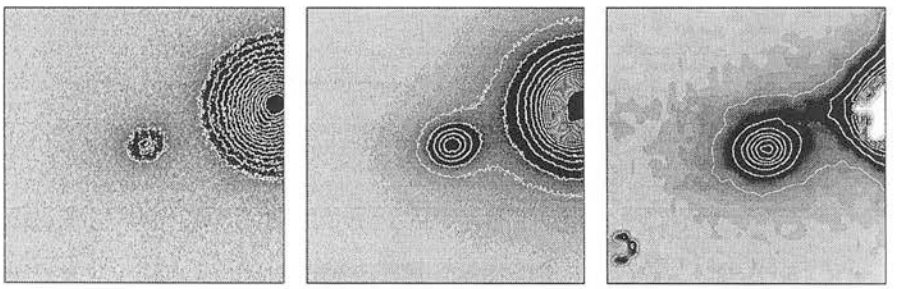

(a) WHT B Band (b) WHT I Band (c) INT I Band

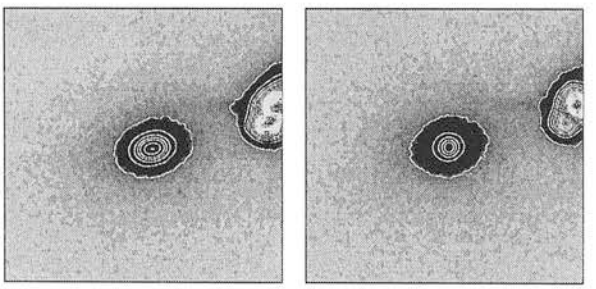

(d) UKIRT H Band (Oct run) (e) UKIRT K Band (Oct run)

Figure 2.47: Images of 2308+073

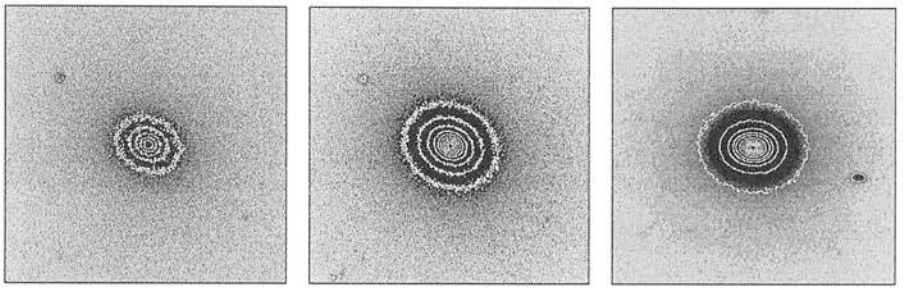

(a) WHT B Band (b) WHT I Band (c) UKIRT K Band (Oct run)

Figure 2.48: Images of 2320−067

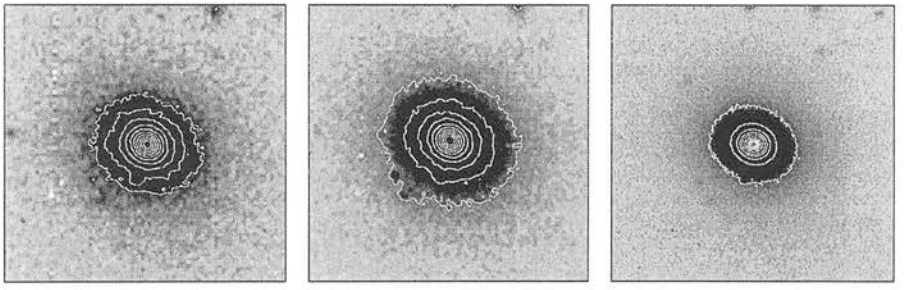

(a) UH B Band (b) UH I Band (c) UKIRT K Band (Oct run)

Chapter 3

Long–slit optical spectroscopy of a sample of radio loud galaxies

3.1 Introduction

This chapter describes the acquisition and reduction of long–slit optical spectra of two samples of elliptical galaxies obtained at the 4.2m William Herschel Telescope (WHT) during 4 nights in November 1997.

The main aim behind obtaining both sets of galaxy spectra is to study various absorption–line features which can allow the age and metallicity of the stellar populations to be predicted and ultimately enable a estimate of the nuclear stellar population. For this to be possible, careful treatment of each spectrum is necessary to ensure that the wavelength calibration, spectrophotometric fluxing and redshift determination are as accurate as possible.

The sample observed is described in section 3.2. Section 3.3 describes the telescope, instruments and observing procedure used to obtain the spectra. Section 3.4 describes the preliminary reduction applied to the two–dimensional frames to remove structure owing to the CCD itself. This is similar to the initial reduction of optical images described in chapter 2, so these aspects are only touched upon again. After spectral extraction, wavelength calibration, flux calibration and extinction correction the spectra are in their final form and ready for the index analysis in chapter 5. Although redshifts for all the galaxies in the sample have been published, they are re–determined in section 3.6 by comparison with velocity standards so that any small errors in the wavelength calibration will not affect the rest–frame wavelengths of the absorption features to be measured and

fitted. Velocity dispersion measurements are also necessary for a careful index analysis, so these are calculated via a cross–correlation technique in section 3.7. A catalogue of the nuclear spectra obtained is presented in section 3.8.

3.2 Spectroscopy sample

The sample consists of a subset of the radio galaxies presented in chapter 2. The choice of objects was largely dependent on whether they were available in the sky at the time of the spectroscopic observing run, although preference was given to those objects with a confident L' detection from the previous imaging observing runs. These galaxies are named below, for further details see table 2.2.

0300+162	0325+023
0356+102	0419+140
0431−134	0502−103
0755+379	0833−016
1004+146	2221−023
2229−086	2243+394
2308+073	

3.3 Observing procedure and setup

Spectroscopy was carried out using ISIS, a double–armed, medium–resolution spectrograph attached to the Cassegrain focus of the WHT. Light travels through the slit and hits a dichroic mirror which splits the incoming light into a red and a blue beam. The beams are directed into separate spectrographs each with optics optimised for their respective wavelength ranges. Inside each spectrograph there is a diffraction grating which disperses the light onto a CCD. Spatial information is recorded along one axis of the CCD whilst the spectral information is dispersed along the other axis. The main instrumental parameters and the setup used are listed in table 3.1.

The EEV10 detector is a very large (2148 × 4200) blue–sensitive CCD which takes 300 seconds to read out. To reduce the readout time the chip was windowed to use just 500 columns and the object was positioned in the centre of this

Observers	J. McAllister & J. Peacock & R. Jimenez	
Dates	26 – 29 November 1997	
Dichroic	6100 Å	(500 Å wide)
Slit Width	1″	
Dekker Position	7	
Channel	Blue Arm	Red Arm
Grating	R300B	R316R
λ_c (central wavelength)	4802 Å	6548 Å
Detector	EEV10	TEK2
Spectral Range	3050–6585 Å	5860–7350 Å
Dispersion	64 Å/mm	62 Å/mm
	1.44 Å/pixel	1.49 Å/pixel
Pixel Size	$13.5\times13.5\,\mu m^2$	$24\times24\,\mu m^2$
Spectral Resolution (FWHM)	$\sim$ 3 Å	$\sim$ 2.9 Å
Spatial Scale	0.19″/pixel	0.33″/pixel
Detector Area Used	500×4200	1250×300
Row Binning	1	1
Column Binning	2	1
Readout Speed	Standard	Quick
Gain	0.75 e^-/ADU	1.62 e^-/ADU
Read noise	7.5 e^-	5.77 e^-

Table 3.1: Spectroscopy parameters and setup.

window, avoiding any non–functioning columns. The readout time could have been reduced even further by using a "quick" readout speed, but this would have increased the read noise quite considerably and was not considered a sensible option. All 4200 rows were kept to allow as large a spectral range as possible. Initially observations in the blue arm were read noise dominated when using the device without any binning. Binning the chip by 2 pixels in the spectral direction appeared to reduce this problem. Soon after the observations were taken, the EEV10 was taken off line as it was found that binning caused high read noise. It is therefore possible that the quoted read noise in table 3.1 is actually a little low ($\sim$ 10%). The red arm chip was a little less volatile and the only changes made were to window the chip, using 300 rows out of a possible 1025 and to use a quick readout speed, as the increase in readnoise of 4.99 to 5.77 from the standard setting was more than compensated for by a decrease in the readout time from 112 to 73 seconds.

The aim of the spectroscopy is to measure absorption features which can help dis-

tinguish between the age and metallicity of the stellar populations. The strongest metallicity indicators are Mg_b at 5177 Å, the Fe features at 5270 and 5335 Å and also the C_2/Fe feature at 4668 Å, so the gratings and dichroic were chosen with this in mind.

Generally a minimum of two exposures were taken of each object to allow for cosmic ray removal. Exposure times were between 600 and 1200 seconds. The slit was positioned across the nucleus of the galaxy. The orientation of the slit on the galaxy depended on the ellipticity of the galaxy. For high ellipticity galaxies the slit was oriented along the major axis of the galaxy to get as much spatial information as possible, whilst for the low ellipticity galaxies and standard stars we chose to orientate the slit at the parallactic angle.

Bias frames and Tungsten flatfield frames were taken at the beginning and end of each night of observations. CuAr+CuNe arc–lamp frames were taken at regular intervals throughout each night to aid wavelength calibration. Observations of some spectrophotometric standard stars were taken for flux calibration purposes. Observations of some late–type K and M stars were also taken. These stars have spectra similar to the observed galaxy spectra and are used as templates for velocity dispersion measurement and correction.

Night	1	2	3	4
Weather	Good	Good	Poor	Fair
Seeing	0.9″	1.1″	2.5″	1.2″
Hours lost to bad weather	1:20	0:00	2:10	1:00

Table 3.2: Summary of observing conditions

3.4 Two–dimensional data reduction

3.4.1 Initial reduction

Initially the reduction procedures for images and spectra were the same. Separate blue and red master bias frames were constructed in the same way as in section 2.6.1. Profiles of the bias frames collapsed along dispersion and spatial axes are presented in figure 3.1. It can be seen that there is structure present in

the frames, so careful removal of this is indeed necessary.

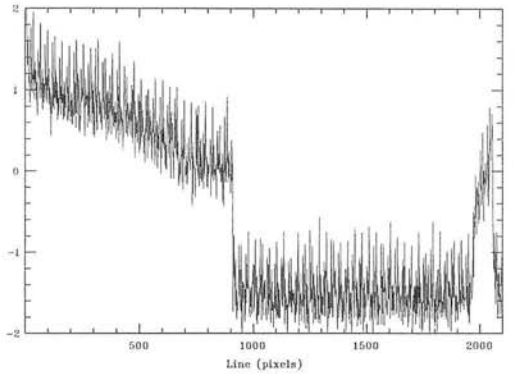

(d) Blue, spectral axis

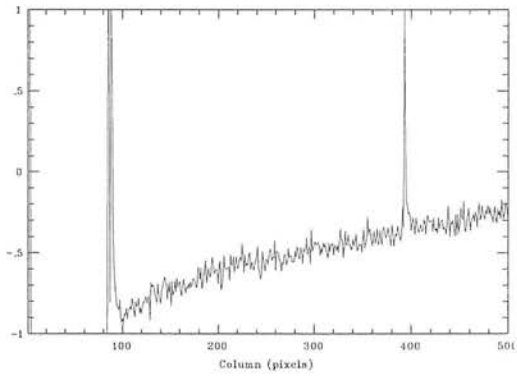

(e) Blue, spatial axis

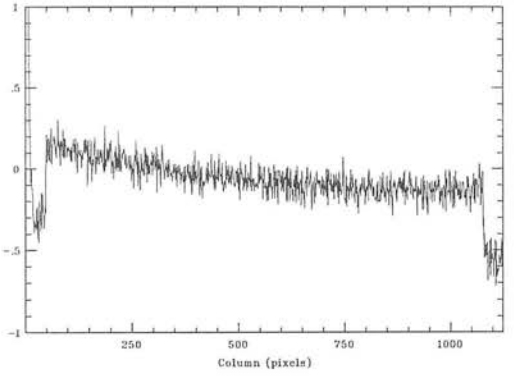

(f) Red, spectral axis

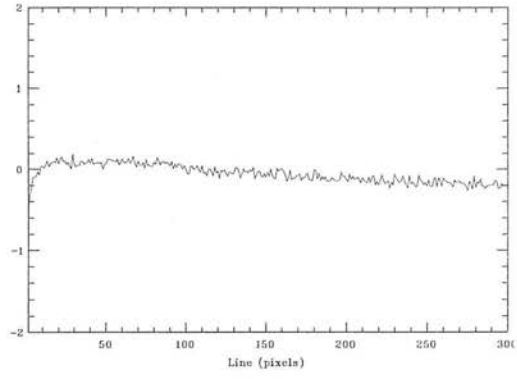

(g) Red, spatial axis

Figure 3.1: Collapsed profiles of bias frames. The left panels show the profile along the longer spectral axis, whilst the right panels show the profile along the spatial direction. In the first panel it can clearly be seen that there is a small step in the structure. In the second panel the spikes are non–functioning columns of the detector.

The flatfields were combined together to produce a master flatfield for each arm. The spectrum of the Tungsten comparison lamp has a smooth continuum shape to it, which is sometimes fitted and removed from the flatfield frame prior to use, leaving only the pixel–to–pixel variations in the chip. This is unnecessary as the correct shape of the spectrum is restored by careful flux calibration, as long as the standards have been reduced in the same manner. The shape of the Tungsten spectrum was therefore left in the flatfield frames for this set of reductions. The bias frames were then subtracted from the flatfields. The two–dimensional im-

age frames were then bias–subtracted, trimmed, divided by appropriate flatfield, multiple exposures were combined to remove most cosmic rays and the combined image was normalised to 1 second exposure time.

3.4.2 Cosmic ray removal

Most cosmic rays were successfully removed by combining multiple raw frames using the `imcombine` task in IRAF, using the `crreject` pixel rejection algorithm, with pixels adjacent to cosmic ray affected pixels also being rejected. Section 2.6.1 describes this.

If multiple exposures of an object were not obtained, say if the weather conditions prevented a second exposure from being taken, cosmic ray removal was more difficult. A very low order polynomial was fitted along each of the spatial axes of the frame using the `lineclean` routine in IRAF. Any pixel that was more than 6σ from the fit was rejected and replaced with the fitted pixel value. Again pixels next to a rejected pixel were also rejected. This appeared to be a successful method of cleaning the frames as illustrated in figure 3.2.

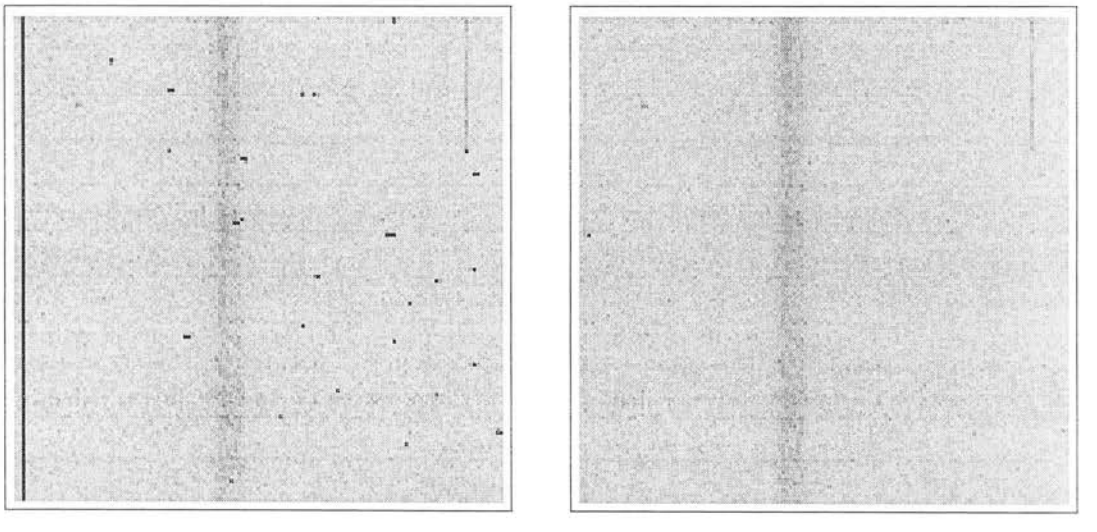

Figure 3.2: Greyscale images of a raw blue–arm frame, before and after cosmic ray removal. The dark column on the left of the first frame and the fainter one near the right–hand side are non–functioning columns. The dark spots are the cosmic ray affected pixels. The galaxy spectrum can be clearly seen down the centre of the images.

3.4.3 Sky subtraction

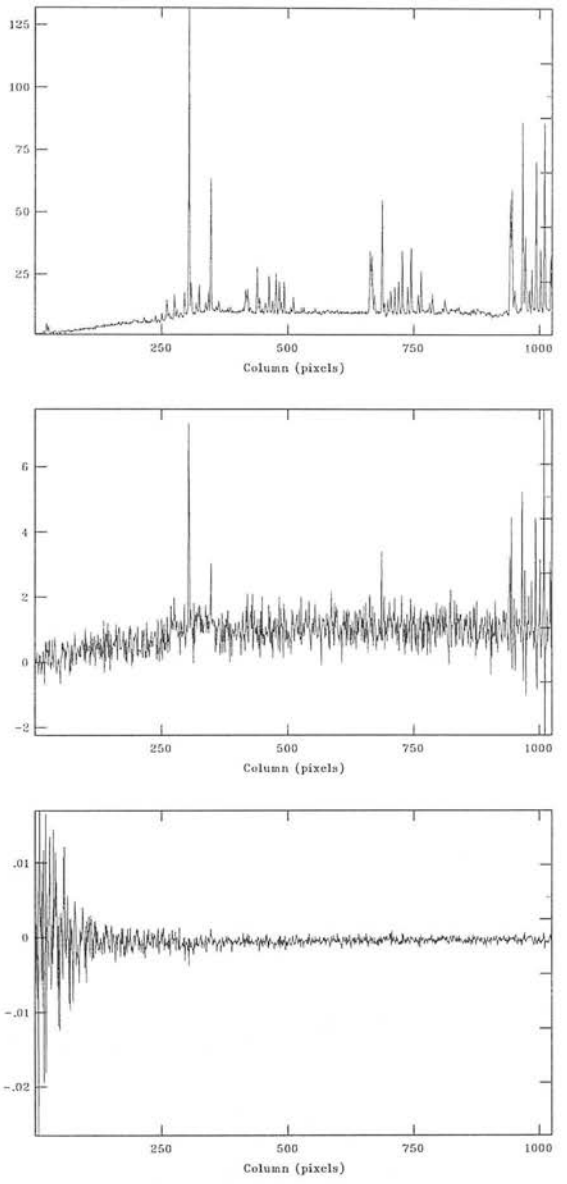

(a) No sky subtraction

(b) Linear sky subtraction

(c) Complete sky subtraction

Figure 3.3: Subtraction of sky emission features. Each frame shows the average of the same sixty rows of the sky region of in a red arm frame. In (a) the sky has not been subtracted at all. In (b) a linear fit has been used to subtract the sky, notice that some of the stronger sky lines are still present. The final frame demonstrates the results of using the optimum sky subtraction technique described in section 3.4.3. Note the different scales used on each panel.

The next step was to subtract the sky from the two–dimensional images. Sky

regions, were defined either side of the central galaxy spectrum and a polynomial fitted along each of the spatial axes. The sky regions were set to be as large as possible whilst still excluding the galaxy. The resulting fit was then subtracted leaving only the galaxy spectrum along the centre of frame.

The main problem encountered here was the accurate subtraction of the sky lines. These occur at wavelengths where the sky has strong emission features. The strength of the features varies with the thickness of the atmosphere, *i.e.* it varies spatially along the slit. Normally a linear fit is good enough to subtract the normal background sky level, but it was found that along sky lines, a higher order fit was necessary to remove them. Figure 3.3 demonstrates this by showing a red arm frame averaged along 60 columns within the background regions, after being fitted with different order polynomials. Eventually an optimum method was found, whereby the median of a nine pixel moving box within the sky regions was fitted with a third order polynomial. For the red–arm frames the median of a seven pixel moving box was used. From figure 3.4 the success of this technique can be viewed.

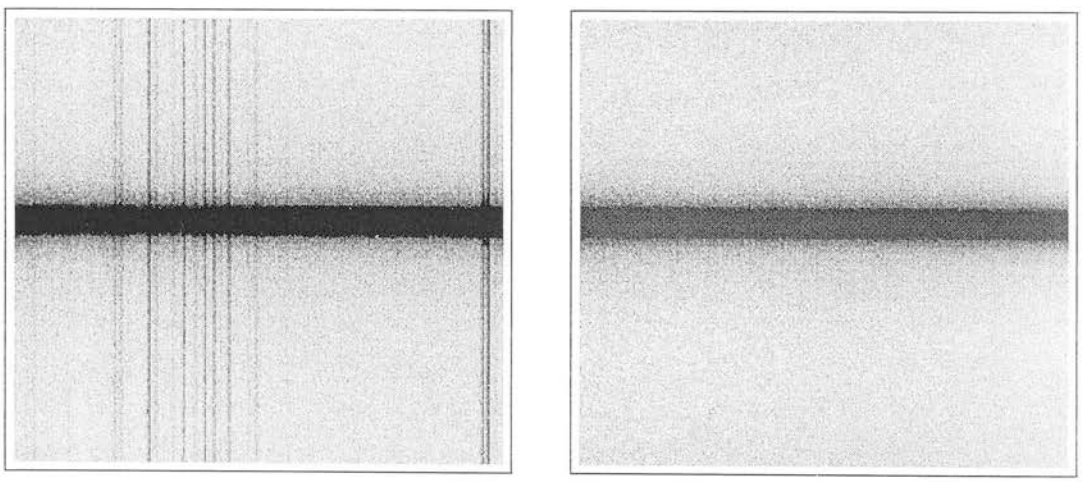

Figure 3.4: Section of a red–arm frame before and after sky subtraction. The galaxy spectrum can be clearly seen dispersed along the rows, with the sky emission lines along the columns.

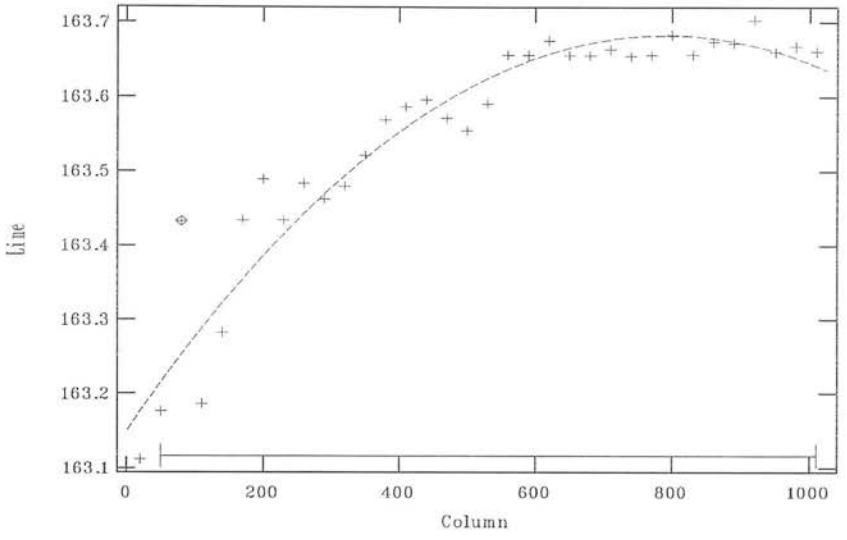

Figure 3.5: Example of the trace being fit to a red–arm frame

3.4.4 Spectral extraction

Having previously mentioned that spatial information is recorded along one axis of the detector and spectral information along the other, it is now important to point out that this is not quite the case. Owing to the optics of the spectrograph and differential atmospheric refraction between the blue and red ends of the spectrum, the final spectrum is curved slightly along the spectral direction. The curve can be followed by tracing out the brightest pixel along each line (or column in the case of the red arm frames) and fitting a low order polynomial to the fit as illustrated in figure 3.5. For the faint objects, locating the brightest pixel was a tricky business, so the centre of the galaxy profile was found by summing around twenty lines of the frame to improve the signal. At the ends of the spectrum the data becomes very noisy as the flux tails off, so these regions have been excluded from the fit. For the red–arm spectra the maximum shift between each end of the frame was about half a pixel, whilst for the very large CCD on the blue arm the shift was up to three pixels.

The one–dimensional spectra were then obtained by defining an aperture for extraction and summing all the pixels within this aperture whilst following the trace along the two–dimensional frame. The same trace was used for all radial extractions of a galaxy, just the central pixel and width of the aperture were changed each time.

3.5 One–dimensional data reduction

3.5.1 Wavelength calibration

Dual arc–lamp frames of CuAr+CuNe were taken for wavelength calibration. CuAr was necessary to cover the whole wavelength range of the blue arm, whilst CuNe was needed to cover the red arm. Initial dispersion solutions were obtained using the IRAF `identify` task for both the red and the blue arm by careful comparison with line–lists. The RMS residuals of both fits were less than 0.06 pixels or about 0.1 Å, so the error in velocity estimation should be less than $6\,\mathrm{kms}^{-1}$. The approximate dispersions were 1.5 Å/pixel for the red arm and 1.73 Å/pixel for the blue arm. The solutions for the rest of the comparison spectra were obtained using the IRAF `reidentify` task which takes the initial wavelengths and line centres and uses them as a starting point for the fit. Each object spectrum was then assigned the closest dispersion solution in time to when the observation was taken. The solution was then applied and the output spectra were sampled on a linear wavelength scale.

3.5.2 Flux calibration

Four spectrophotometric standards were taken over the course of the observing run. These were reduced identically to the galaxy frames, except that the aperture chosen for extraction was wide enough to contain all the flux from the star.

The first step in the process of flux calibrating the spectra is to compare the observed standards with tabulated values of the fluxes of these stars. This was done with the IRAF `standard` task. The spectral resolution of the observed standards was much higher than that in the tabulated calibration file, so the standards were smoothed slightly before use, using a 3–pixel median filter. The counts within bandpasses of width 10 Å were summed and tabulated alongside the actual flux, f_ν, within the bandpass. At this stage regions of the spectrum with prominent atmospheric absorption features were deleted, to avoid them being included in the fit. The next step is to calculate a sensitivity function, S_λ, which is obtained by fitting a function to the calibration points C_λ.

$$C_\lambda = 2.5\log_{10}\left(\frac{O_\lambda}{TB_\lambda F_\lambda}\right) + AE_\lambda, \tag{3.1}$$

where O_λ is the observed counts in the bandpass, T is the exposure time (but

here all images are already normalised to 1 second exposure), B_λ is the width of the bandpass, F_λ is the tabulated flux of the standard star, A is the airmass and finally E_λ is the atmospheric extinction in magnitudes per airmass. The extinction curve used here was the latest one available on the ING website[1].

An average sensitivity function for each arm was obtained by interactively fitting a cubic spline to the average of the calibration points from all but one of the standard stars. This star was excluded from the fit as it was taken during a period of poor weather conditions. Some points near the ends of the spectra were also excluded from the fit. It was necessary to use a fairly high order (5–7) cubic spline to fit the rapidly changing function closely enough. Finally, this function, S_λ, was applied to all the galaxy spectra by use of equation 3.2.

$$F_\lambda = \left(\frac{O_\lambda}{TB_\lambda}\right) 10^{0.4(AE_\lambda - S_\lambda)} \tag{3.2}$$

As the conditions for the run were not photometric it was not possible to obtain absolute flux values from the fluxing procedure but it was still possible to obtain relative values, ensuring that the shape of the spectrum is accurate even if the values are only correct up to a multiplicative constant. For this reason it was possible to average the calibration points and only determine one sensitivity function for each arm.

3.5.3 Extinction correction and dereddening

The next step is to correct the spectra for the effects of interstellar dust along the line of sight within the Milky Way towards the observed galaxy. The dust affects the light in two ways: extinction and reddening. Extinction is the loss of light due to absorption and scattering as it travels through the interstellar medium. Blue light is scattered more than red light, so the galaxy appears redder than it actually is, this is called reddening.

The amount of extinction towards an object is normally given in magnitudes in a filter–band. Observations of an object in the V band with no intervening dust would have apparent magnitude m_0, whilst in the presence of dust the magnitude would be m_D, therefore the extinction A_V is given by

$$A_V = m_D - m_0. \tag{3.3}$$

[1] www.ast.cam.ac.uk/ING/lpinfo/wlext.html

The reddening or colour excess E, is the difference in extinction at different wavebands and is a measure of the amount of dust along the line of sight to the object.

$$\begin{aligned} E(B-V) &= A_B - A_V \\ &= (m_B - m_V)_D - (m_B - m_V)_0, \end{aligned} \tag{3.4}$$

where A_B is the extinction in the B band. The extinction law is then the dependence of extinction A_λ on wavelength λ. For ease of use, the various extinction laws, seen through different amounts of dust are normalised. Normally

$$X = \frac{E(\lambda - V)}{E(B-V)}$$

is plotted against λ^{-1}. A further parameter R is defined such that

$$-X(\lambda \to \infty) = \frac{A_V}{E(B-V)} = R, \tag{3.5}$$

since when $\lambda \to \infty$, $A_\lambda \to 0$. So R is the point where the extinction curve crosses the ordinate axis and is defined as the ratio of total–to–selective extinction; it compares the total extinction along the line of sight A_V to an object with the wavelength dependent extinction $E(B-V)$. The value of R varies from 2.6 to 5.5 depending on the density of the obscuring material, with a mean of 3.1 in the diffuse regions of the Milky Way. This is valid all the way from the ultra–violet portion of the spectrum to $10\,\mu$m (Cardelli, Clayton & Mathis 1988; Rieke & Lebofsky 1985; Mathis & Cardelli 1992).

The Galactic interstellar extinction law has been determined observationally by comparisons of reddened and unreddened stars. The most recent estimates are by Cardelli, Clayton & Mathis (1989) (CCM) and Fitzpatrick (1999) and it is the CCM parameterisation that has been used to deredden the spectra presented here. In this parameterisation the extinction in the optical region ($3000 - 8000$ Å) of the spectrum is fitted by an equation of the form

$$\left\langle \frac{A_\lambda}{A_V} \right\rangle = a(x) + b(x)/R \tag{3.6}$$

where

$$\begin{aligned} x &= 1/\lambda \\ a(x) &= 0.574x^{1.61} \\ b(x) &= -0.527x^{1.61} \\ R &= 3.1 \end{aligned} \tag{3.7}$$

A_V is calculated from equation 3.5 using the relevant estimate of $E(B-V)$ for the object (see table 3.3) and used in equation 3.6 to calculate A_λ for each wavelength. The spectra are dereddened by applying

$$f_{\lambda 0} = f_{\lambda D} \times 10^{0.4 A_\lambda}. \tag{3.8}$$

The value of $E(B-V)$ used, the selective extinction along the line of sight to the object, was estimated from the new full–sky dust maps of Schlegel, Finkbeiner & Davis (1998). The dust maps are constructed from the *COBE*/DIRBE and *IRAS*/ISSA surveys with point sources and zodiacal light removed and are twice as accurate as the older Burstein–Heiles reddening estimates (Burstein & Heiles 1978). The extinction value for each object is given in table 3.3.

Objects	Galactic Coordinates		$E(B-V)$
0055−016	126.46	−64.22	0.035
0106+130	129.44	−49.32	0.027
0206+355	140.28	−24.43	0.094
0207+095	152.80	−48.44	0.080
0208−067	169.07	−62.09	0.024
0217+017	162.72	−53.96	0.048
0300+162	163.06	−35.96	0.136
0325+023	180.97	−42.02	0.124
0356+102	179.84	−31.05	0.224
0419+140	180.81	−24.26	0.831
0431−134	209.78	−36.41	0.146
0502−103	210.14	−28.28	0.107
0755+379	182.68	28.83	0.046
0833−016	227.22	22.07	0.027
1004+146	222.87	49.68	0.048
1040+317	196.23	61.83	0.025
1131+493	152.03	63.46	0.020
1132+492	151.96	63.63	0.016
1309+210	340.58	82.12	0.033
1350+316	54.59	76.06	0.017
1359−113	328.98	47.68	0.064
1422+268	36.91	69.23	0.019
1452−054	349.93	45.62	0.070
1452+165	18.58	59.59	0.023
1514+072	9.42	50.12	0.037
1601+173	44.50	47.59	0.051
1602+178	31.55	44.54	0.046
1602+240	39.96	46.49	0.073
1652+398	63.60	38.86	0.019
1658+302	51.93	35.90	0.030
1706+094	29.79	26.97	0.108
1717−009	22.93	20.56	0.340
1842+455	74.70	20.22	0.078
Cygnus A	76.19	5.76	0.374
2221−023	61.87	−46.71	0.085
2229−086	55.87	−52.05	0.055
2235+408	97.53	−15.07	0.255
2243+394	98.13	−17.06	0.140
2308+073	84.23	−47.57	0.067
2320+203	96.37	−37.66	0.099

Table 3.3: Extinction estimates calculated using the dust maps from Schlegel, Finkbeiner & Davis (1998).

3.6 Redshift determination

For the index analysis in chapter 5 it is necessary to shift the spectra to their rest–frame wavelengths. The precise shift from observed to rest–frame wavelengths for each observation needs to be determined to ensure that all the absorption features to be measured are at exactly the correct wavelengths. Although the redshifts for the entire sample are known, these values are heliocentric rather than observed values, which could introduce systematic errors into the shift. The wavelength calibration could also have small errors, owing to the fact that each spectrum has been assigned the closest dispersion solution in time to the observation. Exact results would have required arcs to be taken before and after each object exposure ensuring the telescope is not moved in the interim. The redshifts have been redetermined for all the blue arm spectra and those red arm spectra where it was possible. As the index analysis is carried out on the blue arm spectra it is more important to have values for these.

Most radial velocity measurements have been obtained by using a Fourier cross–correlation technique, but when it was difficult to get sensible answers *i.e.* for those galaxies with large emission rather than absorption features, the shift was calculated from the positions of the most prominent emission features.

3.6.1 Using absorption features

The cross–correlation technique (Tonry & Davis 1979; Statler 1995) can be used to measure both redshifts and velocity dispersions. Though it is reasonably simple to measure redshifts using the IRAF `fxcor` task, velocity dispersion measurements are more complicated so a separate routine was written to estimate these (see section 3.7 for details).

Let $G(n)$ be the spectrum of a galaxy whose redshift is to be determined and $T(n)$ the spectrum of a template star at zero redshift. Both spectra are continuum subtracted so that the comparison is only between the features in the spectrum rather than the shape as well. This was done by fitting and subtracting polynomials from both spectra in an interactive way. The spectra are then sampled into N equally spaced bins in $\log\lambda$, which is also equal spacing in velocity as

$$\frac{\Delta v}{c} = \frac{\Delta\lambda}{\lambda} = \Delta\log\lambda \tag{3.9}$$

where c is the speed of light.

A normalised cross–correlation function $C(n)$ is then computed:

$$\begin{aligned} C(n) &= G(m) \otimes T(n) \\ &= \frac{1}{N\sigma_G\sigma_T} \sum_{m=0}^{N} G(m)T(m-n) \end{aligned} \tag{3.10}$$

where σ_G and σ_T are the RMS deviations of the spectra:

$$\sigma_G^2 = \frac{1}{N} \sum_{n=0}^{N} G(n)^2 \tag{3.11}$$

similarly for σ_T^2.

Fourier cross–correlation is just an extension of this in Fourier space:

$$\tilde{C}(k) = \frac{1}{N\sigma_G\sigma_T} \tilde{G}(k)\tilde{T}^*(k) \tag{3.12}$$

where $\tilde{C}(k), \tilde{G}(k)$ and $\tilde{T}(k)$ are the Fourier transforms of $C(n), G(n)$ and $T(n)$ respectively, with * denoting the complex conjugate. The advantage of performing the cross correlation in Fourier space is that the unwanted high and low frequency noise can be filtered out.

The radial velocity of the galaxy is then obtained by finding the position of the highest peak, which denotes the best match between galaxy and template. The value of the shift in bins s gives the radial velocity cz where $cz = \Delta v \times s$. It is obvious that the best results are found by using a template with a similar spectrum to the galaxy being observed, but of precisely known radial velocity. The two radial velocity standards used as templates were kindly lent by Dave Bowen[2] and were HD182572 ($v_r = -100.5 \pm 0.4\,\mathrm{kms}^{-1}$) and HD171391 ($v_r = +6.9 \pm 0.2\,\mathrm{kms}^{-1}$), both are G8–type stars with strong absorption features. The templates had a resolution of 6.2 Å, or $350\,\mathrm{kms}^{-1}$ at 5300 Å (Bowen, Pettini & Boyle 1998) which is coarser than the galaxy spectra, so they were interpolated to the resolution of the galaxy spectra prior to cross–correlation. Each object has been cross–correlated with both templates, the results have been averaged and the errors averaged in quadrature. As a cross check, the objects were also cross–correlated with two galaxies, NGC 315 and NGC 772. The results are presented in table 3.4.

[2]Department of Physical Sciences, Princeton University, Princeton, NJ

3.6.2 Using emission features

The IRAF `rvidlines` task was used to recalculate redshifts for those galaxies with prominent emission features. The main features used were the Balmer series, the 4000Å break and the oxygen and calcium lines.

For one galaxy (0502−103) significant rotation was observed, so the radial velocity was determined for each 0.6″ radial extraction separately. The rotation curve derived from emission lines is shown in figure 3.6.

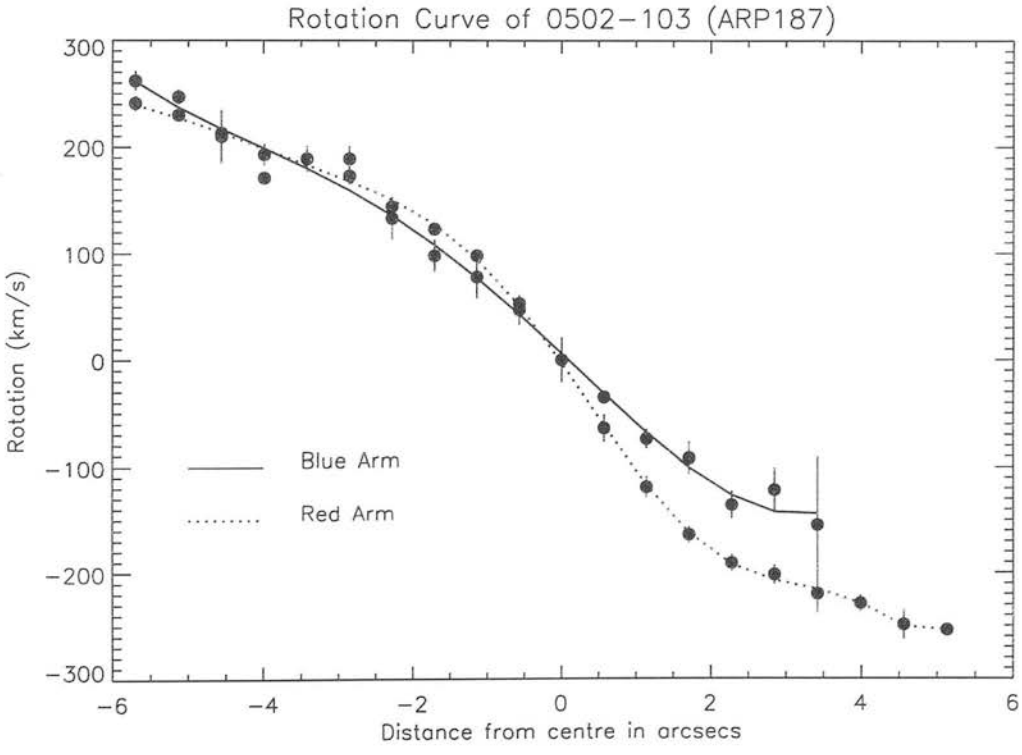

Figure 3.6: The rotation curve of 0502−103.

3.7 Central velocity dispersion determination

3.7.1 Introduction to velocity dispersions

Velocity dispersions in galaxies arise from the fact that stars are moving on randomly oriented orbits, resulting in the final average spectrum having broader and shallower absorption features than the spectra from the individual stars. The

Object	Blue Arm		Red Arm		Published
	cz	$\pm$	cz	$\pm$	Value
0300+162	10020	73	9566		9773
0325+023			8972*	31	9054
0356+102	8985*	32	9077*	9	9174
0419+140	19440	156	19567		19278
0431−134	10233	99	10467	6	10912
0502−103	11840	183	12059*		11812
0755+379	12309*	51	12295*	3	12381
0833−016	9485	89	9058		8994
1004+146	9203	97	8631		8814
2221−023	16858*	45	16960*	42	16848
2229−086	25007	85	24768		24763
	25008*	50			
2243+394	24215*	22	24131	88	24163
2308+073	13172	72	13218		13221

Table 3.4: Radial velocity redeterminations. A * indicates an emission–line estimation. Errors have not been quoted for some of the red arm spectra where a template mismatch made it difficult to provide a sensible estimate, but could be as high as 200 kms^{-1}. Columns 2 and 3 are raw radial velocity shifts between the template and galaxy spectra and are not heliocentric as the it is this raw shift which is applied to the spectra in the analysis. However the final column containing published values are heliocentric.

observed spectrum is a convolution of the intrinsic galaxy spectrum and the velocity distribution function. This distribution function is normally assumed to be Gaussian of width σ, where σ is referred to as the velocity dispersion. Figure 3.7 shows a schematic of this process.

Three techniques have been used to measure velocity dispersions in the past: the cross–correlation method (CC) (Tonry & Davis 1981, Dalle Ore *et al.* 1991), the Fourier quotient method (FQ) (Simkin 1974, Illingworth & Freeman 1974, Sargent *et al.* 1977) and the Fourier correlation quotient method (FCQ) (Bender, Saglia & Gerhard 1994). Di Nella *et al.* (1995) have obtained velocity dispersion results for a sample of galaxies using the three methods independently. From their results it appears that all the methods give answers consistent to within 50 kms^{-1}. Owing to the similar accuracy of the methods the cross–correlation method was chosen to be used here as it is the simplest to use and can work successfully with lower signal–to–noise spectra than the other two methods.

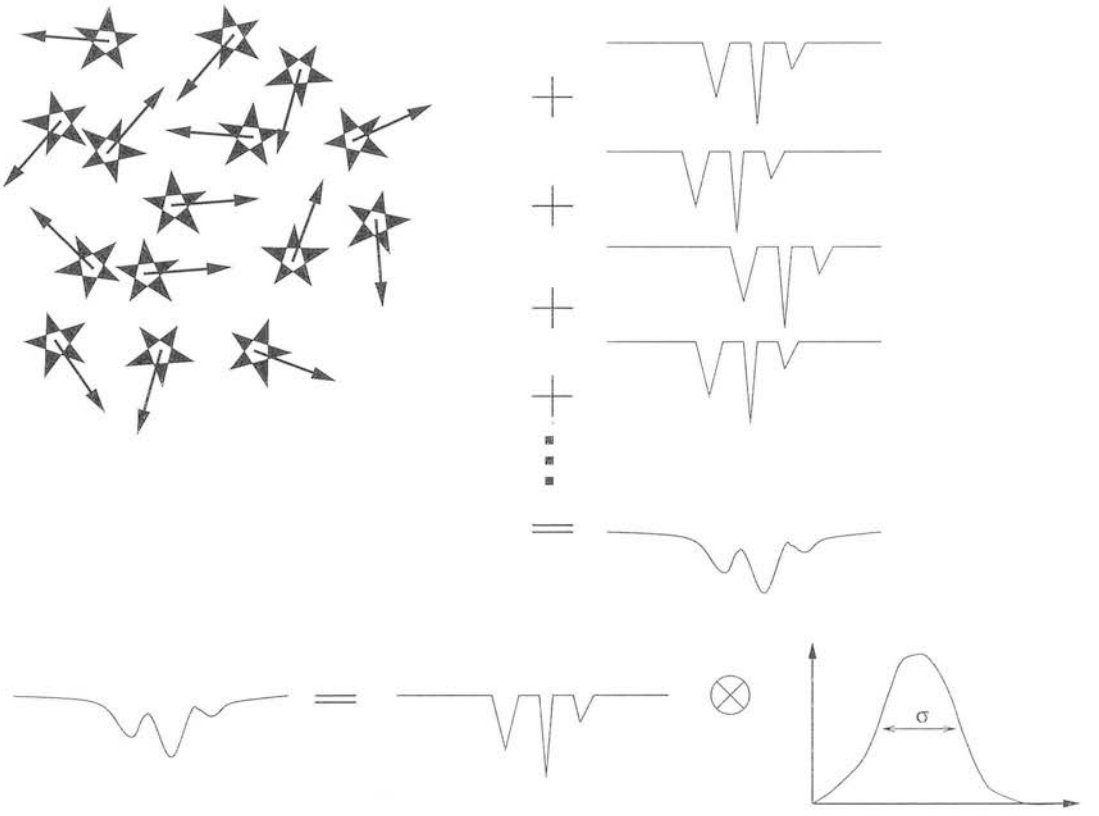

Figure 3.7: Schematic showing how velocity dispersions arise

The method used here is very similar to the one described by Dalle Ore *et al.* (1991). Essentially the galaxy spectrum is convolved with a template spectrum in a similar manner to the radial velocity measurements, although this time it is the width of the cross–correlation peak rather than its position, which is important, as the width of the peak is also a measure of the width of the galaxy features. The spectra are sampled on a log wavelength scale as before so that $x = \ln \lambda$; $g(x)$, $t(x)$ are the galaxy and template spectra respectively, with the galaxy spectrum shifted to its rest–frame wavelength using the results from section 3.6; $v(x)$ is a Gaussian.

$$\begin{aligned} g(x) &= t(x) \otimes v(x) \\ &= t(x) \otimes C\exp\left[\frac{-x^2c^2}{2\sigma^2}\right]. \end{aligned} \tag{3.13}$$

In integral form

$$\begin{aligned} t \otimes g &= \int_{-\infty}^{\infty} t(p)\,\mathrm{d}p \int_{-\infty}^{\infty} v(q)t(p-q)\,\mathrm{d}q \\ &= \int_{-\infty}^{\infty} v(q)\,\mathrm{d}q \int_{-\infty}^{\infty} t(p)t(p-q)\,\mathrm{d}p \end{aligned}$$

$$= \int_{-\infty}^{\infty} v(q)\,(t \otimes t)\,\mathrm{d}q$$
$$= (t \otimes t) \otimes v \qquad (3.14)$$

so velocity broadening acts like a convolution of the template autocorrelation function with v.

The template spectra used were the late–type stars taken at the same time as the galaxy observations. The stars were G102–22 and G10–50, both type M4 and G97–42 an M3.5 star. In fact only G10–50 was used as a template and the others were used to construct a calibration curve. Only the blue arm spectra were used, as experimentation with the red arm spectra showed that the templates did not match up well enough with the galaxy spectra to obtain sensible Gaussian–shaped correlation curves.

3.7.2 Preparation of spectra

The template and galaxy spectra were prepared identically, although the whole spectrum was extracted for the stars and only the central 1.9″ was extracted for the galaxies. Firstly emission lines were interpolated over. Dalle Ore *et al.* (1991) found interpolation unsatisfactory and they spliced in sections of a standard galaxy of a similar line–strength and velocity dispersion to the object being measured. This was not possible here, owing to the small number and range of the spectra in our sample. Splicing also biases the result *a priori* towards the expected value. Interpolation was adequate for all but one galaxy, PKS 2221−023 (3C 445), a broad–line radio galaxy whose emission features completely dominate the spectrum. The galaxy spectra were then shifted to their rest frame wavelengths using the values from table 3.4.

Next the spectra were resampled into logarithmic wavelength bins of width $60\,\mathrm{kms}^{-1}$. ($\Delta \ln \lambda = 2 \times 10^{-4}$). Tests with smaller size bins showed that no extra information could be gained, owing to the spectral resolution. If $\Delta\lambda = 1$ Å at 5000 Å then $v = 60\,\mathrm{kms}^{-1}$. The spectra then needed to be detrended as the information about the width of the absorption lines is only contained in the spectral features and not the continuum. After extensive experimentation attempting to fit the continuum with various polynomials and splines the simplest and most effective method was to use a moving median filter of width $5400\,\mathrm{kms}^{-1}$ or 90 Å at 5000 Å. The width of the filter box was wide enough that the features were not

fitted, whilst still being narrow enough to follow the shape of the spectrum accurately. The original spectrum was then divided by the smoothed spectrum and 1.0 subtracted off to gain a features–only spectrum with a mean of zero. The top line in figure 3.8 shows a raw spectrum, whilst the middle line shows the same spectrum after having the continuum subtracted using our median smoothing method.

It appears that the shape of the cross–correlation function is highly affected by the method used to detrend the spectra. Dalle Ore *et al.* (1991) use a fifth–order polynomial fit and find that they end up with cross–correlation functions with a narrow central peak superimposed on a broad hump. The important information is contained in the width of the central peak, so they try to fit and subtract the baseline from the function itself in an intricate and involved manner. From Figures 3.10 and 3.9 it can be seen that this broad hump is not present in our raw cross–correlation functions, which start almost from zero, suggesting that the continuum treatment was sensible.

3.7.3 Baseline removal and Gaussian fitting

The template and galaxy spectra were then cross–correlated using equation 3.10 in the region 3800–5800 Å. The choice of region included the strong calcium H and K lines just shortward of the 4000 Å break. The main difficulty is in finding a reproducible method of measuring the FWHM of the central peak. A linear baseline was fit between the lowest points of the raw cross–correlation in the channels (-25,0) and (0,25). This baseline was then subtracted off, the peak was normalised to have a maximum of 1.0 and recentered in channel (0). A Gaussian was then fitted to the peak with the only degree of freedom being the width. It was necessary to fit a Gaussian to the peak as experimentation with just taking the FWHM of the peak provided unreproducible results. Some peaks had wings (see figure 3.9) owing to spectral blends, which made the shape slightly non–Gaussian. This then made the measured velocity dispersions over 100 kms^{-1} higher than any literature values. Therefore fitting a Gaussian ensured that the wings did not bias the results. The Gaussian was also weighted so that channels (-10,10) were given more weight than those further out, this is similar to Tonry & Davis (1981) who just fitted a parabola to the upper 11 points of the correlation peak. The positive channels were also weighted slightly higher than the negative

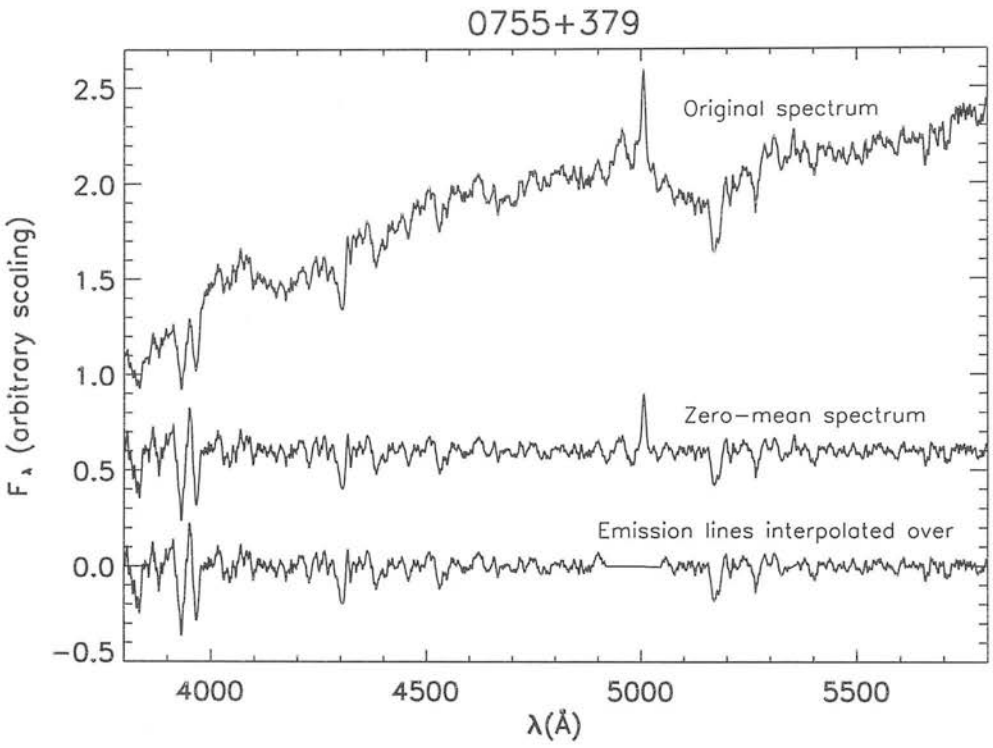

Figure 3.8: Spectra of 0755+379 illustrating the median filtering continuum subtraction method. The top spectrum is the raw spectrum, the second is a zero mean, continuum subtracted spectrum and the final one has had the emission lines removed with linear interpolation

ones as the wings appeared mainly on the negative side.

The calibration of the peak width against velocity dispersion is established empirically by correlating the template with the late–type stars broadened by Gaussians of known width. The Gaussian fitting procedure was identical to that used for the galaxies. A calibration curve is constructed by averaging the results for a given broadening width for all the stars except the template against itself. The noise present in the autocorrelation of the template with itself biases the peak a little too high. The calibration curve used is given in figure 3.11.

3.7.4 Results

As explained above the accuracy in estimating σ, the velocity dispersion, is obviously dependent firstly on getting well matched galaxies and template and secondly on measuring the width of the peak correctly. Dalle Ore *et al.* (1991) state

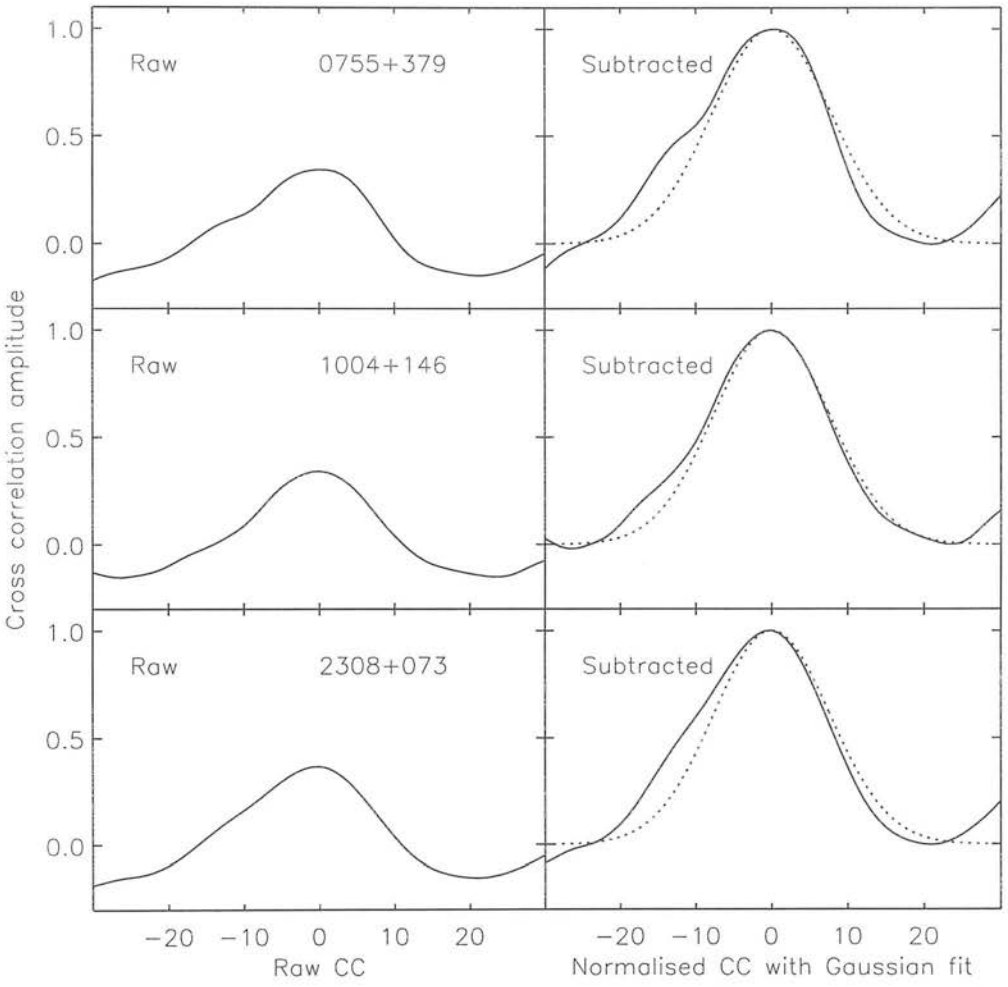

Figure 3.9: Raw and subtracted cross–correlations of the template with various central galaxy spectra. This is similar to figure 3.10 with the left panels showing the raw correlations of the template with the galaxy and the right panels showing the cross–correlation after baseline subtraction and normalisation with the best–fit Gaussian.

that the error in the measured width W scales roughly as

$$\frac{\Delta W}{W} \sim \frac{1}{\sqrt{N_c}} \frac{\Delta y}{y}, \tag{3.15}$$

where $\Delta y/y$ is the typical uncertainty of the cross–correlation function near the peak and N_c is the number of independent data channels in the peak. A conservative estimate of the error is 10% and it is this value that is used in the results below.

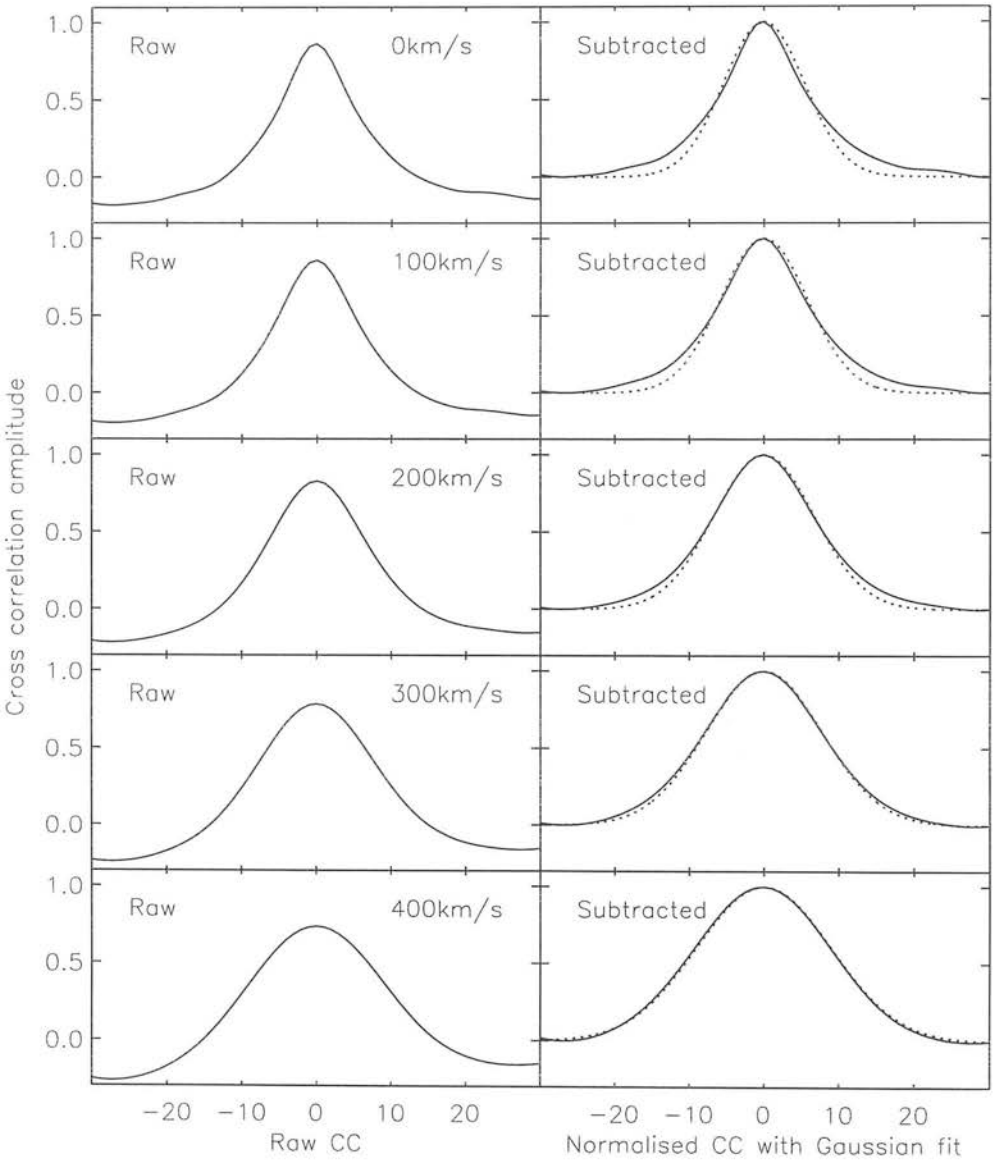

Figure 3.10: Raw and subtracted cross–correlations of the template with a broadened late–type star. The left panels show the raw correlations of the template with the star G102–22. The right panels shows the cross–correlation after baseline subtraction and normalisation. Also shown is the best–fit Gaussian.

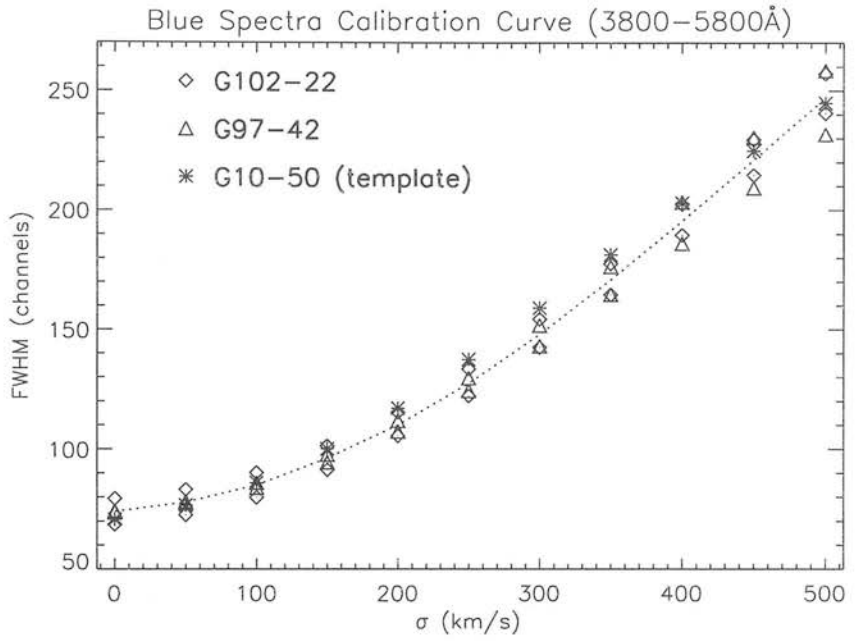

Figure 3.11: The velocity dispersion calibration curve. The ordinate is the FWHM of the Gaussian fitted to the peak of the cross–correlation function after baseline subtraction and scaling. The points represent standard stars broadened with different size Gaussians and the dotted line is the average of all the red stars not including the template.

Object	Velocity Dispersion	Published Value	Reference
0300+162	198	242 ± 26	SHI90
0325+023		189 ± 5	SHI90
0356+102		163 ± 6	SHI90
0419+140	170		
0431−134	207		
0502−103	304		
0755+379	291		
0833−016	271		
1004+146	273	272 ± 19	TD81
2229−086	266		
2243+394	119		
2308+073	278	237 ± 33	WHLD83

Table 3.5: Central velocity dispersion estimates. SHI90 is from Smith, Heckman & Illingworth (1990), TD81 is from Tonry & Davis (1981) and WHLD83 is from White *et al.* (1983).

3.8 Nuclear spectra

The spectra presented here are central 15″ extractions, dereddened for extinction within the Milky Way, normalised to have a value of 1.0 at 5500 Å. The blue and red ends portions of the spectra have been spliced together using an inverse variance weighting summation in the overlap region. The errors have been calculated for this procedure by calculating the RMS of a 10 pixel box around each pixel. The entire spectrum has then been smoothed once for display purposes using a 3 pixel boxcar average.

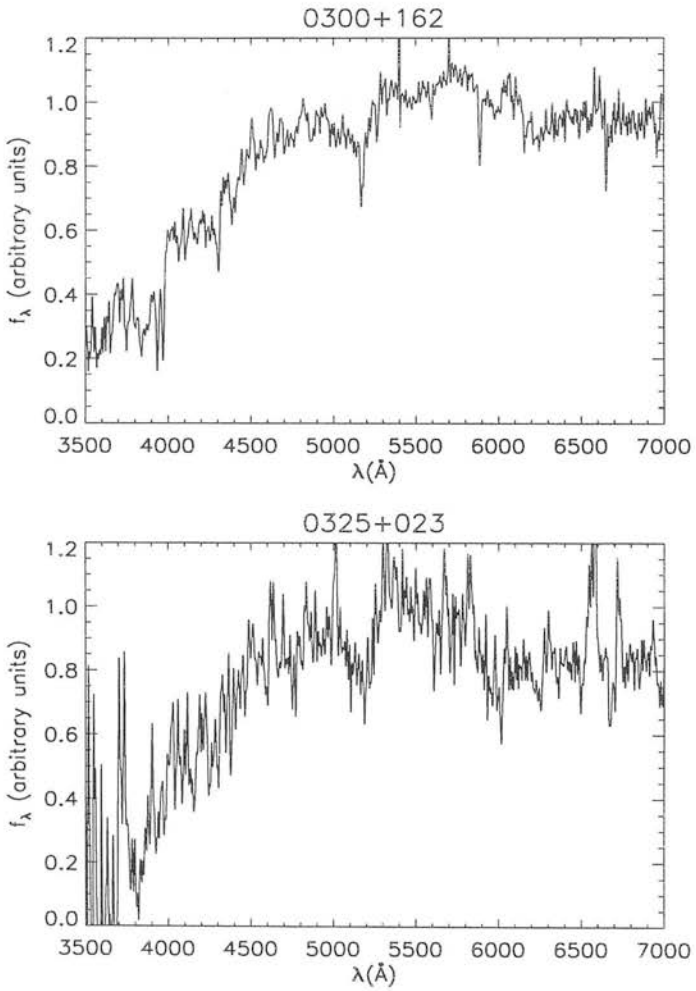

Figure 3.12: Radio galaxy spectra

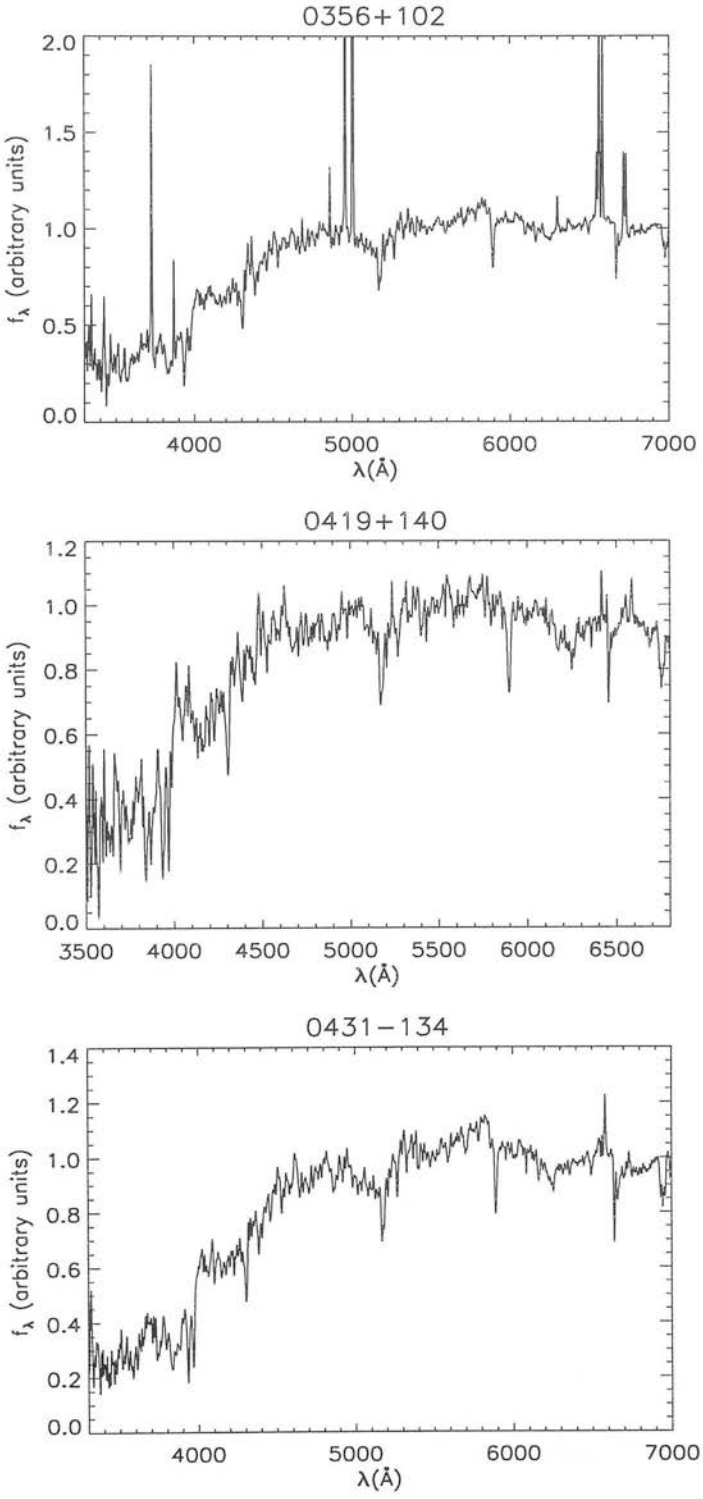

Figure 3.12: Radio galaxy spectra (*cont.*)

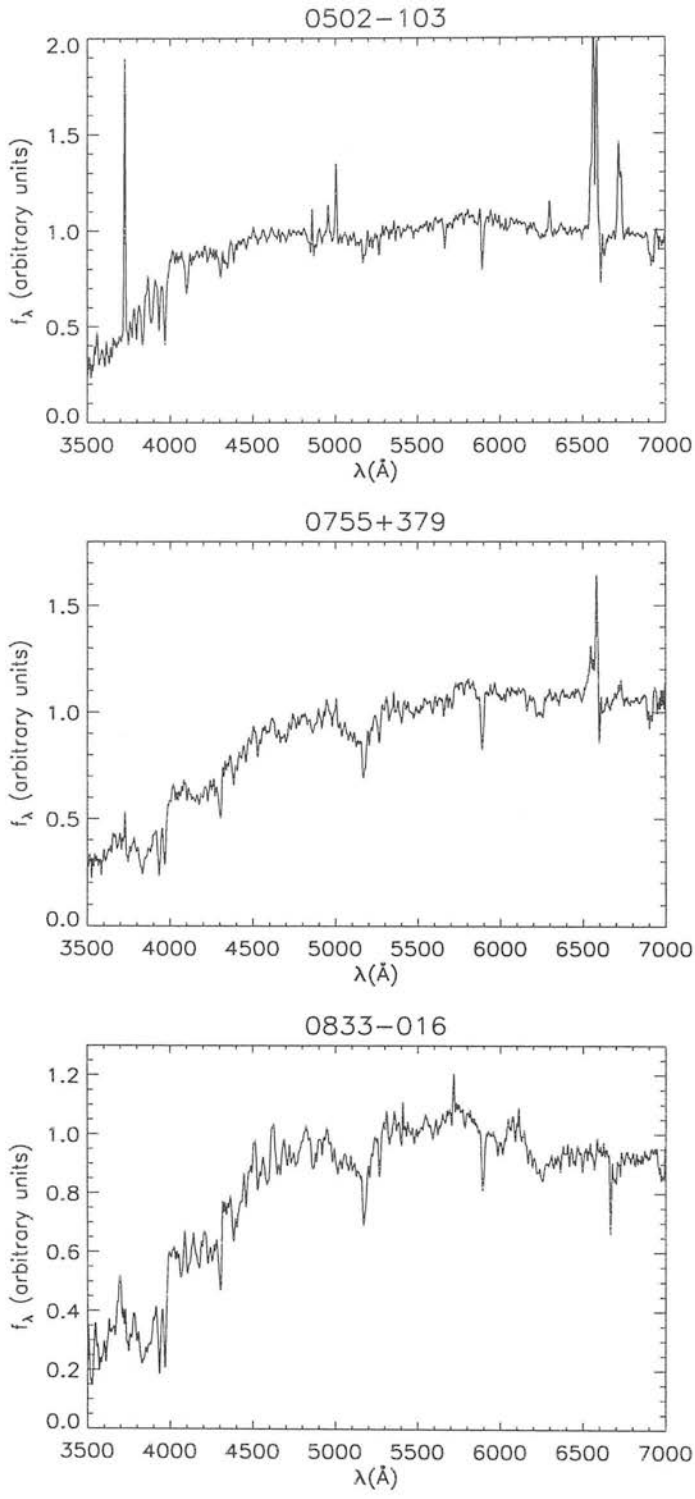

Figure 3.12: Radio galaxy spectra (*cont.*)

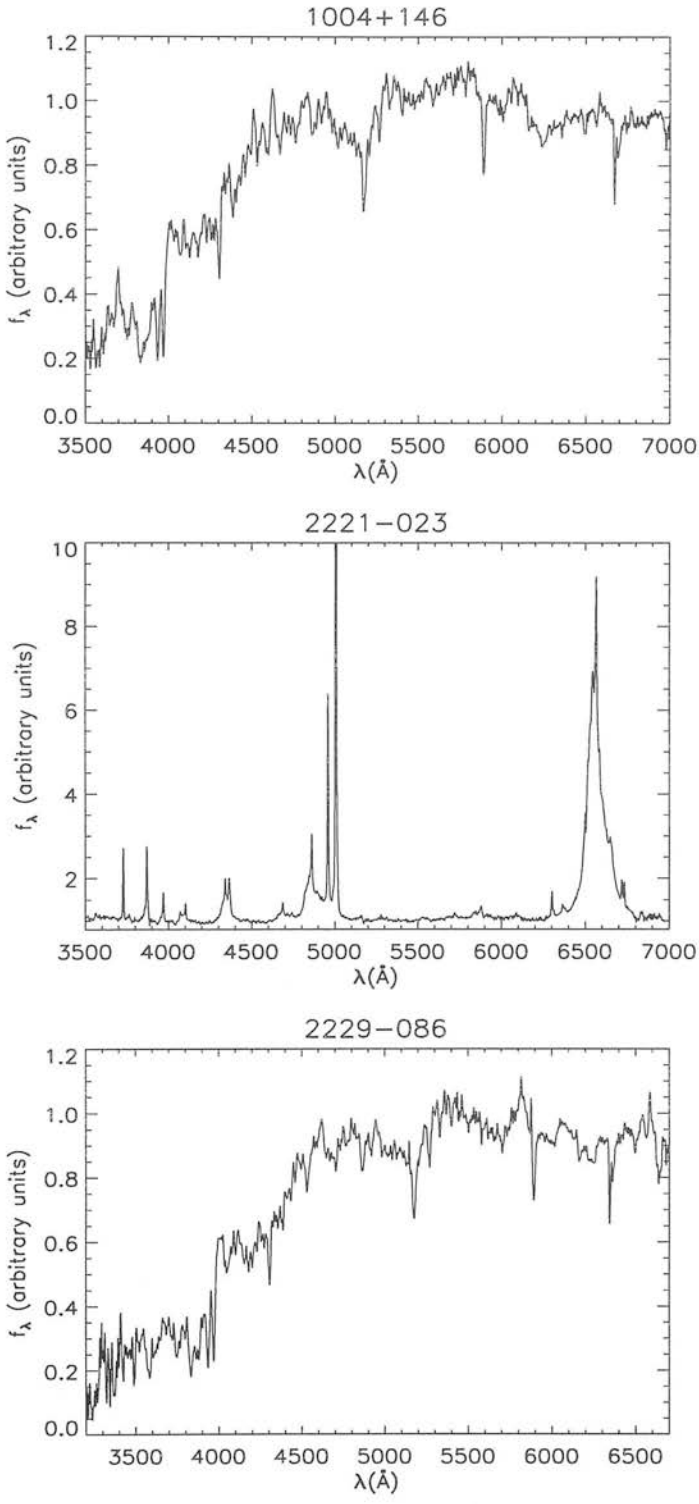

Figure 3.12: Radio galaxy spectra (*cont.*)

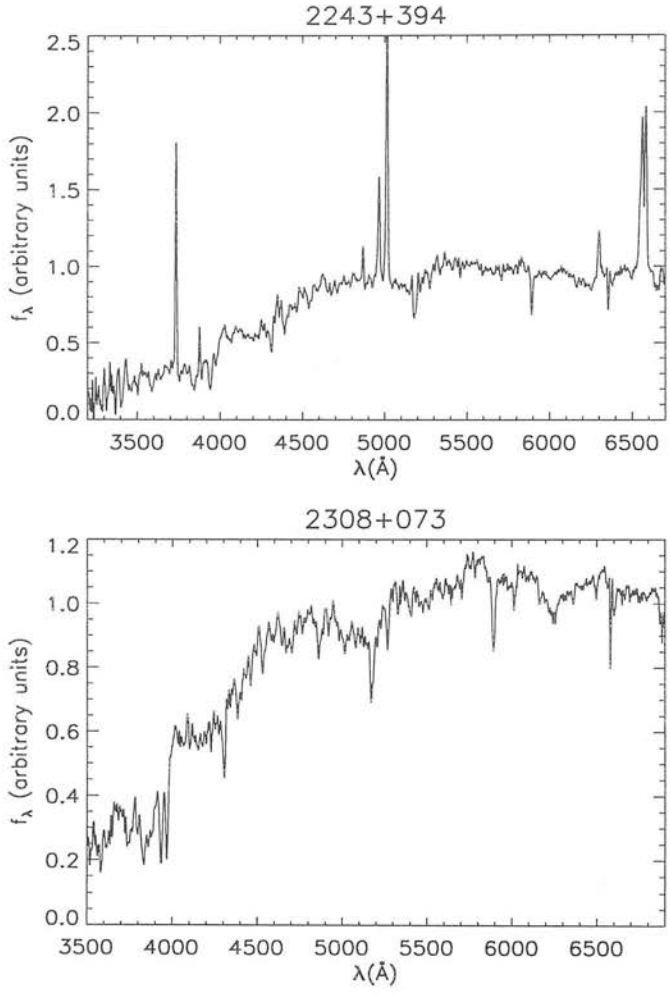

Figure 3.12: Radio galaxy spectra (*cont.*)

Chapter 4

Detecting buried quasars

4.1 Introduction

This chapter aims to provide an estimate of the extinction towards a putative hidden quasar nucleus using the infrared images introduced in chapter 2. Quasar nuclei can be detected as unresolved point sources superimposed on top of the galaxy light at K and simply as unresolved point sources at L'. A typical $K - L'$ value for a quasar nucleus is subtracted from the $K - L'$ colour of the point source giving an estimate of the reddening towards the nucleus. Unfortunately a transmitted quasar continuum is not the only cause of a galaxy nucleus appearing red; the stellar populations of elliptical galaxies are intrinsically redder in the centre, whilst a central dust lane or foreground dust could also produce reddened nuclei. For the initial extinction estimate in this chapter, stellar population and dust effects will not be taken into consideration as they are analysed in detail in chapter 5, where their effect on the whole picture shall be considered.

As mentioned in chapter 1 the stellar and non–stellar components of the K band light need to be deconvolved in order to detect a reddened nuclear point source. Section 4.2.1 uses the 'scale and subtract' method of Djorgovski *et al.* (1991) for the few galaxies for which observations in both H and K bands are available. This is done in order to compare this method with the more robust method of surface brightness modelling, which carried out in section 4.2.2. The inferred extinction towards the nucleus is then estimated in section 4.4.

4.2 Estimating the unresolved nuclear component

4.2.1 Scale and subtract method

The H band frames have been normalised to the K band frames in an annulus $2''$ from the nucleus and $2''$ in width. The H band image has then been subtracted from the K band image leaving a residual 'nucleus', the magnitude of this 'nucleus' is presented in table 4.1. The inferred nuclear values are will be in error as they will underpredict the nucleus in cases where the extinction is low enough to allow a nuclear source to also be seen at H, and overpredict the nucleus in the other cases (Simpson 1994b). It will though be interesting to compare the results of this analysis with the results from the surface brightness profile modelling to see how much in error any authors who have attempted to carry out this kind of analysis before could have been. The value estimated here for the point source in Cygnus A is almost a magnitude brighter than that estimated by DWMG using a similar method, however they use the J and K images rather than the H and K images.

Object	$K_{\rm nuc}$ [mag]	$\pm$	$K - L'_{\rm nuc}$ [mag]	$\pm$
0106+130	15.36	0.11	3.14	0.22
0206+355	14.80	0.10	3.05	0.16
0300+162	14.50	0.10	1.45	0.30
0356+102	15.52	0.10	3.57	0.16
Cygnus A	15.36	0.11	3.29	0.17
2243+394	15.67	0.11	2.98	0.25

Table 4.1: Results from primitive scale–and–subtract method of estimating the nuclear residual

4.2.2 Radial profile fitting of H and K band images

Elliptical galaxies can be well described by a simple exponential profile, known as the $r^{1/4}$ or de Vaucouleurs' law (de Vaucouleurs 1948):

$$I(r) \propto \exp(-r^{1/4}) \tag{4.1}$$

where I is the surface brightness at the radius r. It is usually written such that

$$I(r) = I_e \exp\left\{-7.67\left[\left(\frac{r}{r_e}\right)^{1/4} - 1\right]\right\} \tag{4.2}$$

where r_e, the effective radius, is the radius that encloses half the light of the galaxy. I_e is the surface brightness at that point. The total light from the system under this prescription, calculated by integrating equation 4.2 in the limit as $r \to \infty$, is given by

$$\begin{aligned} L_{tot} &= \frac{8!\exp(7.67)}{(7.67)^8}\pi r_e^2 I_e \\ &\simeq 7.22\pi r_e^2 I_e \end{aligned} \tag{4.3}$$

All the radio galaxies have been fitted with a sophisticated two–dimensional modelling code kindly provided by Ross McLure[12]. The details of this modelling code are given in a series of papers: Taylor *et al.* (1996), McLure *et al.* (1999) and McLure, Dunlop & Kukula (1999). The code was originally designed to model the properties of quasar host galaxies and does this by fitting two components to the observed image: a de Vaucouleurs elliptical galaxy model plus a central unresolved nuclear spike to represent the quasar contribution. The original code has been modified by myself for use in this work, primarily to allow for a dimensionless value of the Hubble constant to be used which outputs the scale–lengths in the appropriate units and various other minor changes.

The advantages in using a full two–dimensional code over the more commonly employed one–dimensional elliptical isophote fitting are enormous (Taylor *et al.* 1996). In the one–dimensional analysis, luminosity profiles are constructed from azimuthally averaging fitted isophotes. The shapes of these isophotes are distorted by both the shape of the point spread function (PSF) and by companion objects. For example, the UKIRT PSF is both elliptical and has two–dimensional structure, see figure 4.1. Using the two–dimensional analysis, companion objects are masked out easily and the shape of the PSF and the galaxy are easily decoupled. Another advantage is that each pixel can be assigned an individual error rather than statistically averaging the errors in an annulus, thereby allowing much better assessment of how the model compares with the original observed data.

[1]Institute for Astronomy, University of Edinburgh, Blackford Hill, Edinburgh
[2]Department of Physics and Astronomy, University of Oxford

The code initially produces a synthetic elliptical galaxy according to equation 4.2. Added to this is a central δ–function, which represents the unresolved nuclear AGN component. The 'galaxy + δ–function' image is then convolved with an image representing the point spread function of the telescope, normalised to 1 second exposure time, to recreate an observed image. This is then compared pixel–by–pixel with the actual observed galaxy image via a χ^2 statistic

$$\chi^2 = \sum_{i=1}^{n} \left[\frac{o_i - m_i}{\sigma_i} \right]^2 . \tag{4.4}$$

The number of pixels being fitted is n, o_i is the value of the ith pixel in the observed frame and m_i is the corresponding pixel in the model frame. σ_i is the value of the error on o_i. Incorrect error estimation will cause the model fitting program to give more weight to certain regions of the frame than others, resulting in incorrect model fits. For the majority of the frame Poisson errors dominate, they are calculated from the gain, readout noise and exposure time as

$$\sigma_i = \frac{\sqrt{I_i g t_{\rm exp} + \sigma_{rd}^2}}{g t_{\rm exp}}, \tag{4.5}$$

where I_i is the counts in pixel i, $t_{\rm exp}$ the exposure time, g the gain and σ_{rd} the readnoise. For the central regions, the galaxy profile is peaky and it was found by Taylor *et al.* (1996) that sampling errors dominate. Sampling errors are calculated by azimuthally averaging the flux in circular annuli around the PSF subtracted image. The final error image is then constructed from sampling errors in the central 1.5″ radius and Poisson errors elsewhere.

The parameters controlling the form of the model galaxy are then varied using a Downhill Simplex method (Press *et al.* 1996), until a minimum value of χ^2 is found. The five free parameters in the model are:

- the luminosity of the nuclear AGN component;
- central brightness of the galaxy;
- scale–length (r_e) of the galaxy;
- the position angle of the galaxy;
- the axial ratio of the galaxy.

Extensive testing on the code (McLure, Dunlop & Kukula 1999) has shown that the best fit galaxy has percentage errors of the order of $\leq 2\%$ for the central brightness and $r_e \leq 5\%$. The errors in the position angle and axial ratio are also $\leq 2\%$. The errors in the estimated nuclear flux are $\leq 3\%$ for the redshift

range of the sample, although this is for an accurate PSF estimation and bright nuclear source. For a very faint nuclear source such as those we are attempting to detect here, the error depends very highly on the PSF chosen (Simpson, Ward & Wall 1999), see below for details. As expected, higher errors in position angle are found for rounder galaxies *i.e.* $a/b < 1.1$ where a is the semi–major axis and b the semi–minor axis. The position angle is measured anti–clockwise from North. Central surface brightness and effective radius are found to be anti–correlated, as expected from the Kormendy relation.

The images and PSFs need to be accurately centered, to within 0.05 pixels, in order to obtain reproducible results for the model fitting. The centres were estimated in each frame using the `center` task in IRAF. This works by extracting a box around the estimated centre and computing the intensity weighted means of the profiles in the box along both the rows and the columns, for example in the x direction

$$x_c = \frac{\Sigma I_i x_i}{\Sigma I_i}. \tag{4.6}$$

An estimation of the sky background level, accurate to greater than 0.01% is necessary to allow proper subtraction of the sky level and proper error estimation. The sky level and standard deviation of the sky level have been estimated in each image in two ways: firstly by repeated σ–clipping of a histogram of the pixel values and secondly by fitting the sky in an annulus around the object, using the IRAF `fitsky` task. The value used in most cases was the σ–clipped one, but this was sometimes a little high in the cases of crowded fields or extremely large galaxies. In such cases the alternative estimate was used. The standard deviation value produced by the σ–clipping method was always higher than using `fitsky` and seemed to be a better estimator of the noise right across the frame.

The existence of nearby objects can severely hamper the fitting procedure. It is therefore possible to define a mask such that pixels in the mask are excluded from the fit. Masks were constructed by inspecting the galaxy image prior to the fitting procedure, identifying all the nearby objects, defining a radius around the object to be excluded from the fit and writing out the positions of all pixels within this radius to a mask file. Cygnus A was slightly more difficult, as it is at low galactic latitude and contains significantly more stellar objects in the frame (50–60), than the other radio galaxies (0–5). There was even a bright stellar object on top of Cygnus A itself, whose position was only discovered after an

initial rough model fit was subtracted from the galaxy frame. It was necessary to run the model fits for Cygnus A with a variety of different masks: too much of the frame masked out and the fit was poorly constrained; insufficient masking and the fit was weighted by some bright objects at large radii. 0206+355 was also difficult as it has another galaxy nearby, either along the line–of–sight or perhaps even interacting. Modelling was attempted firstly by masking out only the nucleus of the second object but without success. Attempts were made then to mask out a whole side of 0206+355, but again with little success. Therefore the only estimate of the magnitude of this nuclear source comes from the scale–and–subtract results.

It is important to have an accurate measure of the PSF of the telescope as it allows us to quantify the blurring of the observations due to seeing affects and telescope optics. Inaccurate measurement of the PSF can introduce serious errors in the model fitting: scattered light, if incorrectly modelled, can lead to overestimates of the galaxy luminosity at large radii; incorrect PSF shape can lead to spurious galaxy morphology results. For this analysis bright, but unsaturated, standard star observations were used. It was important to use bright well–exposed standards, especially for objects with bright nuclear sources, as faint standard stars do not adequately sample the full dynamic range of the PSF. Figure 4.1 shows an image of one of the standard stars used. It can be seen by inspection that the PSF on UKIRT is elliptical rather than the expected circular shape and contains a ghost–type artefact towards the north–west. Ideally a PSF taken either just before or just after each galaxy observation should be used as this provides an accurate measure of the seeing at that time. The next best solution was to use a library of well–exposed stars taken on the same telescope and instrument but at a different time, with a selection of seeing widths so that each galaxy observation can be matched with the most appropriate PSF. A set of 12 stars taken exactly for this purpose on UKIRT with widths between 0.78″ and 1.42″ were again kindly lent by Ross McLure. These PSFs were extremely good for accurately modelling the scattered light and produced stable galaxy fits, such that the position angle, axial ratio, scale length and bulge height changed only within the expected errors using different PSFs. Matching the seeing was crucial as the size of the central nuclear spike fitted changed significantly for different assumed PSFs, see table 4.2 for two examples of this.

Another solution was to use faint stars extracted from the actual galaxy frame

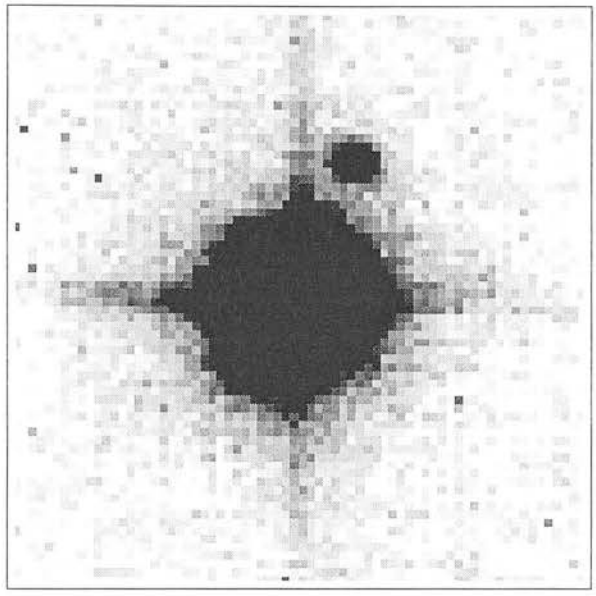

Figure 4.1: Greyscale image of a K band PSF from UKIRT used in the 2–dimensional modelling code

Galaxy	PSF	FWHM ["]	$\chi^2_{\rm red}$	$m_{\rm nuc}$
0106+130	True	0.96		
	2	0.88	1.10	16.50
	3	0.94	1.15	16.22
	4	1.15	1.04	14.83
0356+102	True	0.92		
	2	0.88	1.96	16.07
	3	0.94	1.30	15.28
	4	1.15	1.79	14.79

Table 4.2: Comparison of fits obtained using different PSFs

itself as PSFs. Although a good dynamic range in PSF is necessary for the bright nuclei and quasar fitting, the most important point to consider when modelling radio galaxies is correct knowledge of the seeing width. This is because the shape of the de Vaucouleurs' profile is very peaky in the centre and the nuclear excess is very faint, so an incorrect width will not fit the galaxy central regions properly. Once the fitted model was subtracted from the original frame there was usually still a nuclear excess, not centered exactly on the galaxy centre, but a few pixels to either side.

Eventually an optimum solution was found which used the set of well–exposed stars as PSFs and used the PSF which best matched the FWHM of the stars in the frame. If the required width of the PSF was between two PSFs in the library then

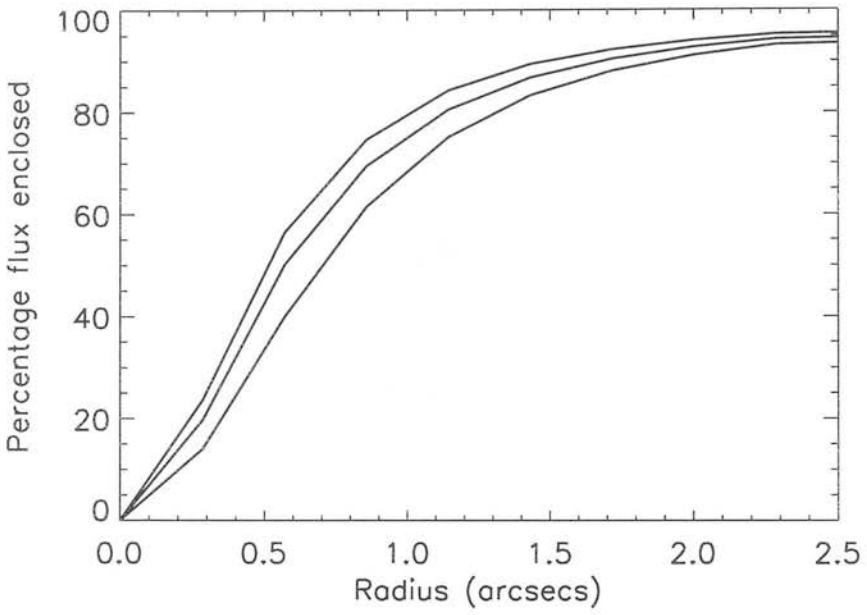

Figure 4.2: Percentage flux enclosed against radius for three PSFs spanning the seeing range of the galaxy sample. The top line is the narrowest PSF, whilst the bottom line is the broadest.

the narrower one was chosen as it would slightly overestimate the central galaxy flux, thereby underestimating any residual. An underestimate of the residual is preferable in this analysis to an overestimation as this will eventually result in a minimum value of the extinction towards any nuclear source, which is a much more informative than the maximum value of the extinction. The spike size was set to zero in the starting simplex, thereby only allowing the four parameters describing the galaxy to be fitted. Photometry on the residual could then be used to estimate the nuclear excess. To ensure that seeing effects did not influence the galaxy fit, the fit was only from 2″ out to a radius where the sky noise dominates – between 15″ – 25″, depending on the size of the galaxy. Figure 4.2 shows the percentage of the total stellar flux contained within a certain radius for the PSFs used. It can be seen that over 85% of the flux is contained within the central 2″ radius or 4″ diameter. As a final check to ensure that the choice of PSF and fitting region did not adversely affect the galaxy fit, the two test galaxies used previously were fitted between 2″–20″ and 1″–20″ using 4 different PSFs. The results are presented in table 4.3. It can be seen that the starting the fit at 2″ does not affect the galaxy fit chosen.

Object	Fitting Region	PSF	m_{gal} [mag]	r_e [h^{-1}kpc]	μ_e [mag/arcsec^2]	Position Angle [°]	Axial Ratio a/b
0106+130	1″–20″	1	11.81	2.94	18.11	122	1.07
		2	11.82	2.85	18.06	122	1.08
		3	11.83	2.90	18.10	122	1.07
		4	11.84	2.88	18.10	121	1.08
	2″–20″	1	11.81	2.96	18.13	122	1.07
		2	11.82	2.88	18.07	122	1.08
		3	11.83	2.93	18.12	122	1.07
		4	11.84	2.91	18.12	122	1.08
0356+102	1″–20″	1	11.35	1.91	18.02	57	1.23
		2	11.36	1.85	17.96	58	1.23
		3	11.36	1.89	18.01	57	1.24
		4	11.38	1.87	18.00	58	1.25
	2″–20″	1	11.35	1.91	18.02	57	1.23
		2	11.36	1.86	17.97	58	1.23
		3	11.36	1.89	18.01	57	1.24
		4	11.38	1.87	18.00	58	1.25

Table 4.3: Results of modelling test to ensure that galaxy fit is not dependent on fitting region or PSF used. The results are presented in the same way as in table 4.5. m_{gal} is the magnitude of the total integrated light as given by equation 4.3. r_e is the effective radius (semi–major axis) and μ_e is the surface brightness at that point.

4.2.3 Nuclear flux estimation

The magnitude of the unresolved nuclear excess was then estimated by photometry on a difference frame, this being the difference between the observed frame and the model. The central portions ($28'' \times 28''$) of these difference frames are presented in section 4.2.4, where the success in accurately fitting and subtracting the galaxy can be seen. Figures 4.3–4.44, show positive excesses (observed > model) as white and negative excesses (observed < model) as black over the background, which has a mean of zero. To give an idea of the range of these excesses in each frame the maximum and minimum pixel values are also given beside each plot. The images are centered on the photometric centres of the galaxies marked as crosses. It can be seen that the excess is not centered on the cross in all cases, especially for the fainter excesses. This should not be surprising as the dynamical centre of the galaxy, where we expect the quasar/black hole to be situated, will not necessarily completely coincide with the photometric centre of the galaxy, say

in the case of multiple nuclei or dynamically distinct nuclei. The position of the radio core should mark the position of the quasar nucleus and ideally photometry centred on this position would give an accurate measure of the possible excess due to the quasar. However, radio positions accurate to around $1/10''$ would be needed and from table 2.2 it can be seen that the positional errors on the radio source were much greater than this.

It is also noticeable from the difference frames that the nuclear regions of most of the galaxies are not smooth and so do not fit a de Vaucouleurs law exactly. Some galaxies have central dust lanes (*e.g.* Cygnus A) so that the model overpredicts the nuclear flux significantly. It has not been possible to estimate the excess nuclear flux for these objects using this method. It is however possible to quantify the size of the point source required to make these galaxies resemble a de Vaucouleurs galaxy. The magnitude of the point source is given in table 4.4. For the other galaxies photometry was carried out using a 10 pixel $\sim 2.8''$ diameter aperture centered on the excess, or the brightest excess in the case of double nuclei. The small aperture was used to avoid including in the photometry any galaxy light that just appeared in the residual image owing to small morphological irregularities. Again using the assumption that the residual is attributable to an unresolved quasar (or nuclear starburst), the flux is scaled by the expected PSF flux within that aperture, which typically contains around 80–90% of the total (see figure 4.2).

Object	m_{nuc} required [mag]
0055−016	14.09
0431−134	15.01
0755+379	14.41
1040+317	16.94
1131+493	14.82
1309+210	13.87
1359−113	13.30
1601+173	14.58
1842+455	16.00
Cygnus A (H)	15.27
Cygnus A (K)	15.11

Table 4.4: Magnitude of nuclear point source required to fit a de Vaucouleurs law

It is important to quantify a detection limit so that any undetected sources can

be taken to be fainter than this limit. This was estimated by taking the error on the nuclear flux to be $\sigma^2 = \bar{e}^2 n$, where $\bar{e}$ is the average value of the error in a 3″ aperture in the error image, consisting of both sampling and Poisson errors, and n is the number of pixels in this aperture. An acceptable signal–to–noise (SN), considering the errors involved in the modelling procedure, was chosen to be 5σ.

The signal–to–noise is estimated from the ratio of counts in the object to the noise. The total counts 'T' are considered to consist of two components: the object 'O' and the sky 'S'.

$$\begin{aligned} SN &= \frac{T-S}{(\sigma_T^2+\sigma_S^2)^{1/2}} \\ &= \frac{O}{(\sigma_O^2+2\sigma_S^2)^{1/2}} \\ &= \frac{O}{(O+2\sigma_S^2)^{1/2}}. \end{aligned} \tag{4.7}$$

From Gaussian statistics on the object counts, $\sigma_O^2 = O$. This quadratic can then be solved for a detection limit in counts within a chosen aperture for a chosen SN such that

$$O_{lim} = \frac{(SN)^2 + (SN)\sqrt{(SN)^2+8\sigma^2}}{2} \tag{4.8}$$

where σ is the error on the nuclear flux calculated above. The detection limit in counts is then converted to a limiting magnitude using the standard conversion.

4.2.4 Results

Table 4.5 gives the results of the profile fitting for all the K and H band images in the sample. These are presented in a similar manner to table 4.3. The errors on the nuclear magnitudes arise from photometric zeropoint errors (see table 2.4) and Poisson noise errors added in quadrature.

Luminosity profiles of the model fits and observed data in azimuthally averaged bins are presented in figures 4.3 – 4.44. The solid line is the model whilst the points with error bars represent the observed data. Most galaxies do seem to be well fit by an $r^{1/4}$ law, especially within the central 10″ or so. Some galaxies deviate from the model beyond this point as they become more disk–like than bulge–like, which is quite common for the biggest elliptical galaxies. Model fitting was also carried out for these disky galaxies using a Freeman disk law (Freeman

1970)

$$I(r) = I_0 \exp\left(-\frac{r}{r_0}\right) \tag{4.9}$$

but it was found that a de Vaucouleurs law was more appropriate to the central regions of all these galaxies, and consistently gave a much lower χ^2 value.

4.2.5 Comparison of Results

The limit on the magnitude of the nuclear point source in Cygnus A of > 17.18 is consistent with the flux of the nuclear point source at $2.25\,\mu$m measured by Tadhunter *et al.* (1999) on the HST of $f_{2.25\,\mu\mathrm{m}} = (4.9\pm1.0)\times10^{-31}\,\mathrm{W\,m^{-2}\,Hz^{-1}} \simeq 17.8$ mag and is completely inconsistent with that measured by DWMG of 16.2 ± 0.5. Stockton, Ridgway & Lilly (1994) also carried out elliptical isophote and one–dimensional surface brightness profile fitting of Cygnus A over the radial range $3.5''$–$12''$. They find an ellipticity of 0.228 $(1 - b/a)$ and position angle of PA $= -13.8^\circ = 166.2^\circ$, which are both comparable to the values found here of 0.194 and 165°, which were estimated over a larger range in radii. However, the value of r_e is given as $65''\pm10''$ which is $\simeq 53\ h^{-1}\mathrm{kpc}^{-1}$, significantly larger than the fitted value of 22.48.

As another test of the reliability of the modelling code, observations of 0106+130 and 0356+102 have been kindly lent by Chris Simpson[3] who has used his modelling code to carry out a nearly identical modelling of these images. Model fitting using our code has produced identical galaxy parameters to his. There are differences though between the results for the nuclear flux. The estimate of the nuclear flux seems to be highly dependent on the choice of PSF and starting simplex. The method used here of estimating the nucleus allows for an excess not centered exactly on the centre of the galaxy isophotes, as is definitely the case in 0356+102, whilst Simpson has forced his code to fit the excess at the centre of the galaxy isophotes, thereby predicting no excess for 0356+102 and underpredicting the nuclear flux in 0106+130.

It is also important to consider whether any emission lines in the K band could be contaminating the images. The only emission line in this region of the spectrum is Paschen α with a rest–frame wavelength of $1.875\,\mu$m (Hill, Goodrich & DePoy 1996), which would correspond to a wavelength of $2.045\,\mu$m for the high-

[3]Subaru Telescope, National Astronomical Observatory of Japan, Hilo, Hawaii

est redshift object in the sample. As can be seen from figure 4.47 the effective filter response of the K band filter at this wavelength is extremely low, so even a strong emission feature would remain virtually undetected by the K band filter. A typical unobscured quasar has a Paα/Hα ratio of 0.05 (see Osterbrock 1989), any obscuration of the Hα line by dust would increase this ratio. The relative strengths of the Hα features seen in figure 3.12 compared to the strength of their continuum are small in all but 2221−023 and therefore contamination by emission features is not an important issue for these objects.

Object	Band	m_{nuc}	±	m_{gal}	r_e	μ_e	Position Angle	Axial Ratio
		[mag]		[mag]	[h^{-1}kpc]	[mag/arcsec^2]	[°]	a/b
0055−016	K	> 17.47		10.24	7.29	19.06	103	1.04
0106+130	H	16.41	0.20	12.17	3.03	18.53	114	1.12
	K	14.80	0.10	11.83	2.93	18.12	122	1.07
0207+095	K	16.11	0.11	12.24	2.75	17.61	45	1.17
0208−067	K	14.80	0.10	10.92	3.35	18.16	60	1.42
0217+017	K	15.23	0.11	10.16	5.48	18.50	131	2.20
0300+162	H	16.29	0.20	11.63	1.68	17.89	130	1.20
	K	14.29	0.10	11.58	1.89	18.08	132	1.20
0325+023	K	15.31	0.11	10.07	8.07	19.90	152	1.46
0356+102	H	15.07	0.20	11.24	2.17	18.19	60	1.21
	K	14.85	0.10	11.36	1.86	17.97	58	1.23
0419+140	K	15.42	0.11	11.84	3.41	18.28	120	1.18
0431−134	K	> 16.94		10.91	2.63	17.92	85	1.06
0502−103	K	> 15.14		10.79	3.11	18.00	158	2.03
0755+379	K	> 17.31		10.08	4.46	17.99	145	1.40
1040+317	K	15.87	0.04	11.19	3.62	18.96	146	1.25
1131+493	K	> 15.40		10.30	2.66	17.49	175	1.24
1132+492	K	15.03	0.04	10.91	1.98	17.55	40	1.06
1309+210	K	> 14.56		10.63	1.00	15.94	163	2.57
1350+316	K	16.31	0.05	10.76	4.29	18.40	61	1.99
1359−113	K	> 15.79		10.01	3.88	17.85	58	1.16
1422+268	K	14.31	0.03	10.99	7.17	19.42	125	1.22
1452+165	K	> 15.64		10.18	4.62	17.95	149	1.17
1452−054	K	15.88	0.04	11.56	1.25	16.90	59	1.88
1514+072	K	15.86	0.04	9.68	13.6	20.33	35	1.33
1601+173	K	> 14.89		10.49	2.07	17.04	59	1.45
1602+178	K	> 15.45		10.62	3.21	18.36	93	1.19
1602+240	K	16.08	0.05	9.72	5.88	18.75	168	1.39
1652+398	K	11.74	0.03	10.13	1.96	16.66	166	1.25
1658+302	K	14.83	0.03	11.19	1.39	16.89	59	1.15
1706+094	K	> 15.26		10.64	2.79	17.67	129	1.51
1717−009	K	14.32	0.03	10.81	3.42	18.76	76	1.04
1842+455	K	> 17.45		10.85	14.37	19.76	46	1.14
Cygnus A	H	> 18.49		10.26	24.32	21.34	165	1.25
	K	> 17.18		9.71	22.48	20.51	165	1.24
2221−023	H	< 12.88		12.48	1.10	16.73	89	1.15
	K	< 11.49		12.34	1.14	16.66	108	1.16
2229−086	K	14.79	0.10	10.78	8.87	18.81	72	1.11
2243+394	H	15.70	0.20	12.79	4.11	19.20	105	1.43
	K	14.81	0.10	12.35	3.75	18.56	110	1.27
2308+073	K	14.82	0.10	10.02	5.60	18.28	86	1.32
2320+203	K	14.36	0.10	10.13	5.44	18.61	64	1.16

Table 4.5: Results of model galaxy fitting. The first column gives the object name and the second gives the waveband of the image being fitted. The third and fourth columns give the estimated nuclear magnitude calculated from the difference image. The rest of the columns give the parameters of the galaxy fit.

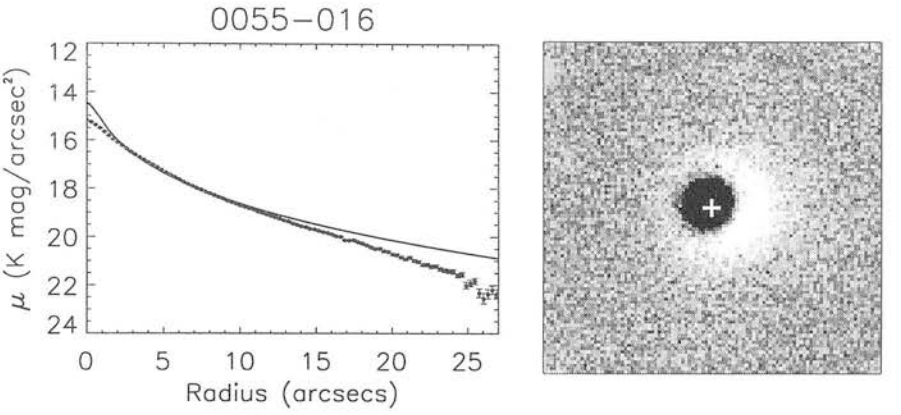

Figure 4.3: Profile of 0055−016 in K band

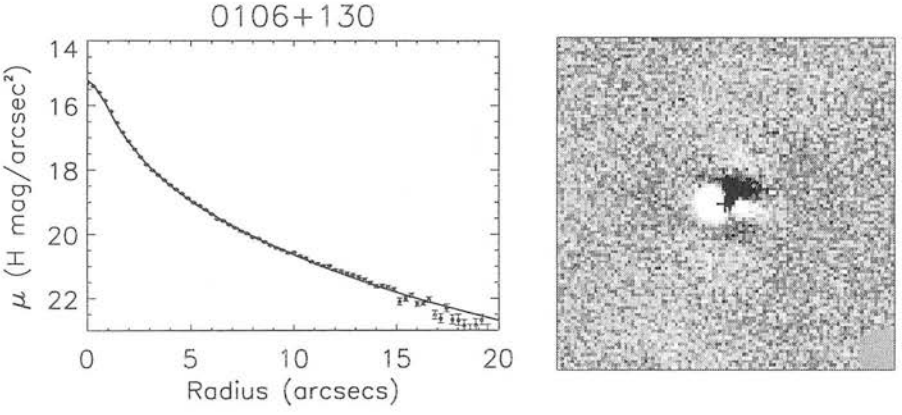

Figure 4.4: Profile of 0106+130 in H band

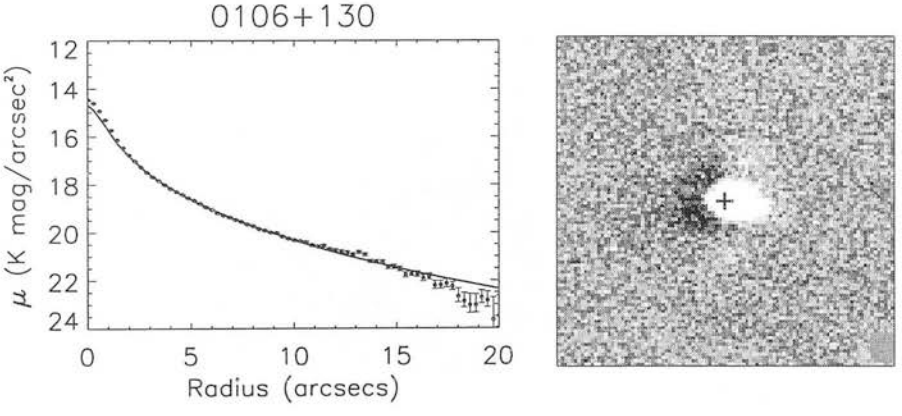

Figure 4.5: Profile of 0106+130 in K band

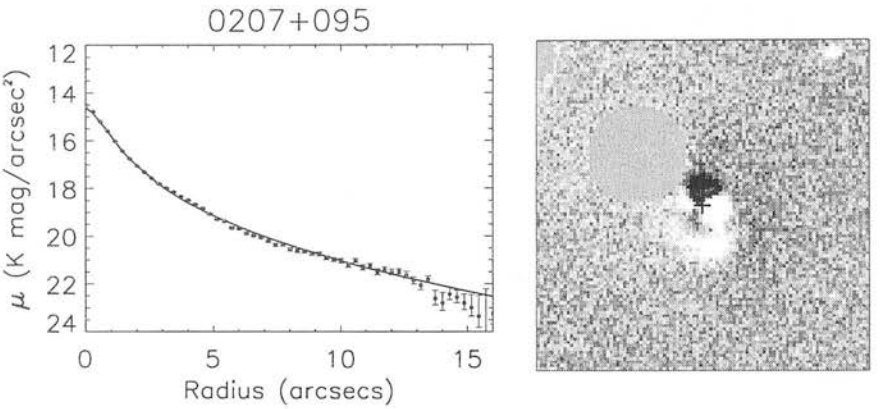

Figure 4.6: Profile of 0207+095 in K band

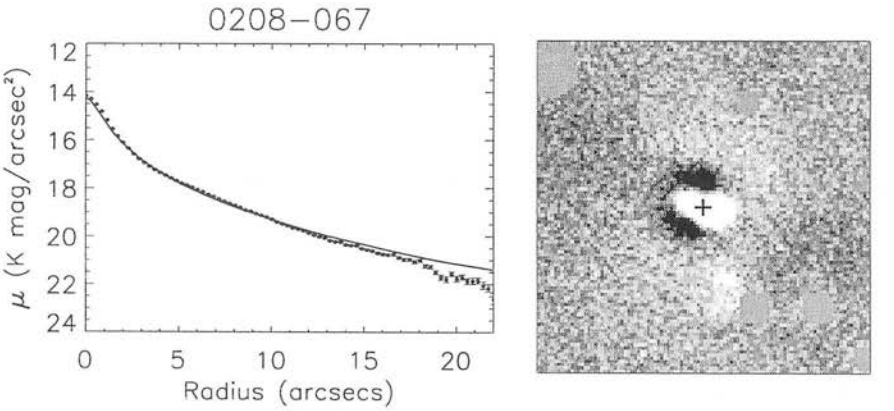

Figure 4.7: Profile of 0208−067 in K band

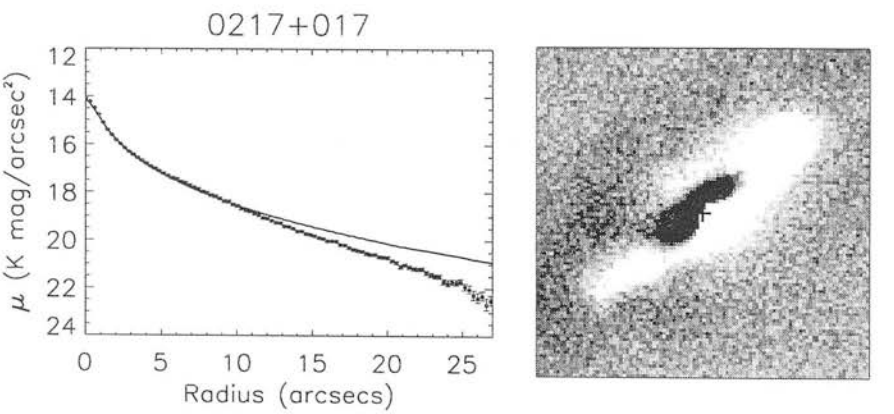

Figure 4.8: Profile of 0217+017 in K band

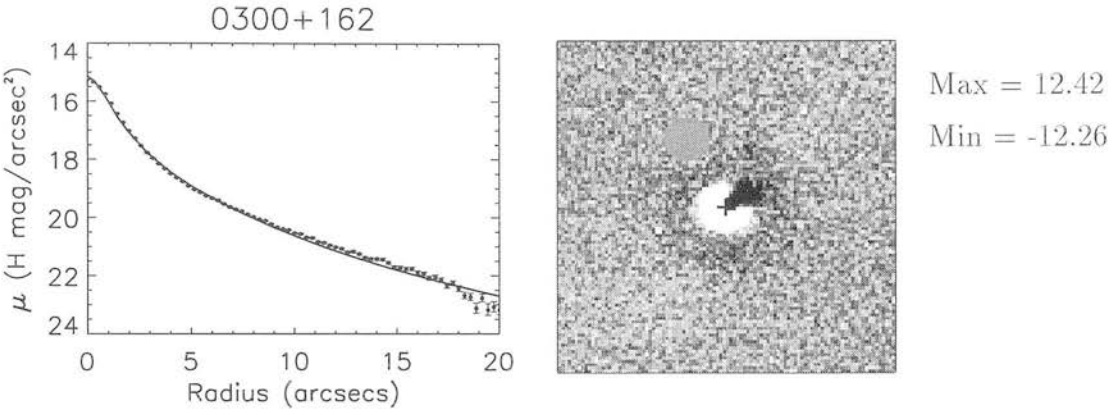

Figure 4.9: Profile of 0300+162 in H band

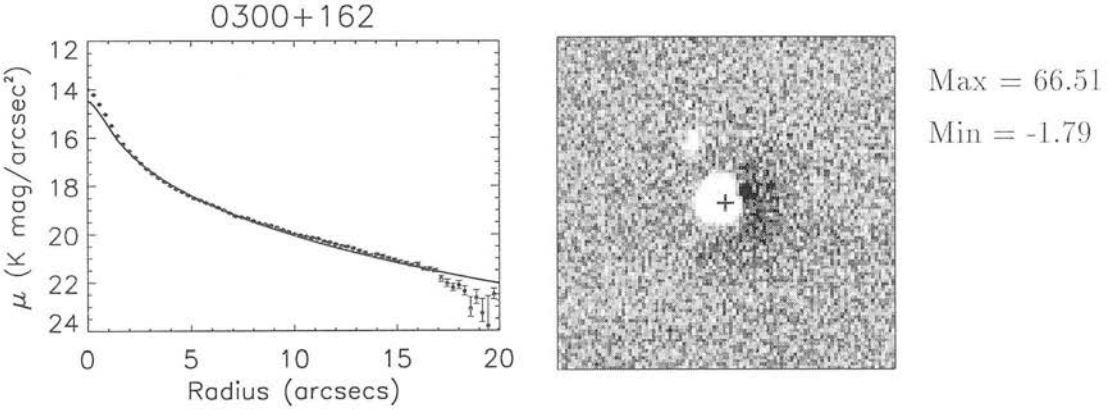

Figure 4.10: Profile of 0300+162 in K band

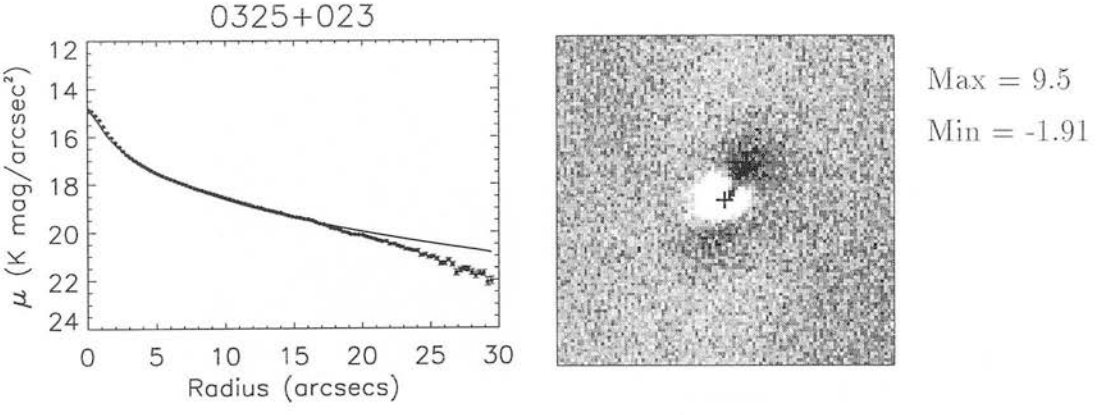

Figure 4.11: Profile of 0325+023 in K band

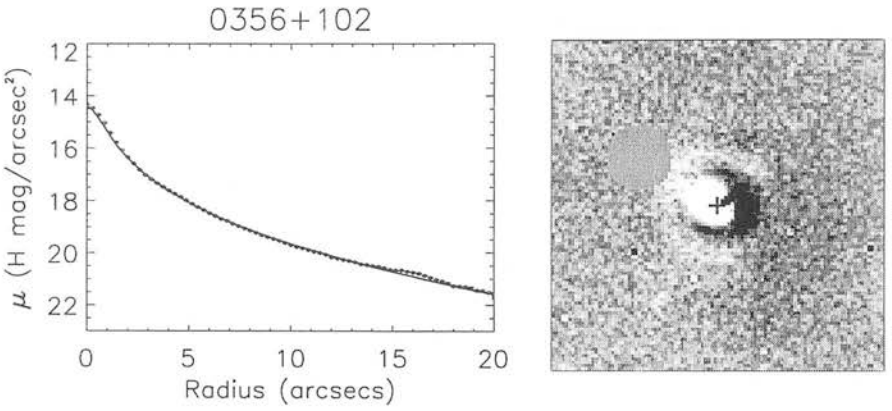

Figure 4.12: Profile of 0356+102 in H band

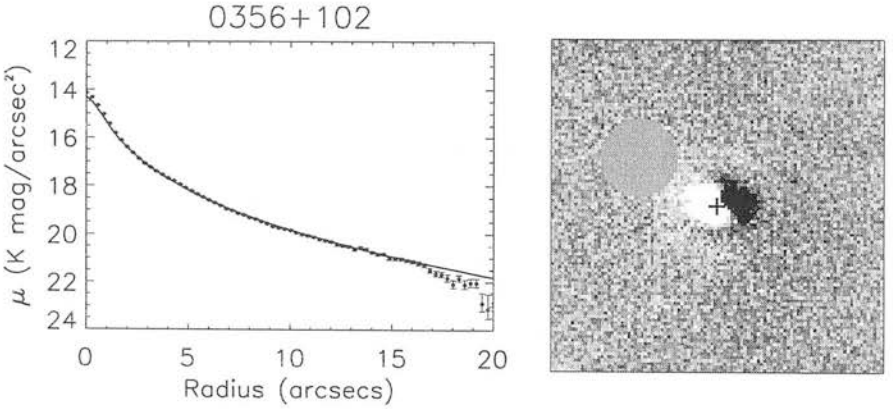

Figure 4.13: Profile of 0356+102 in K band

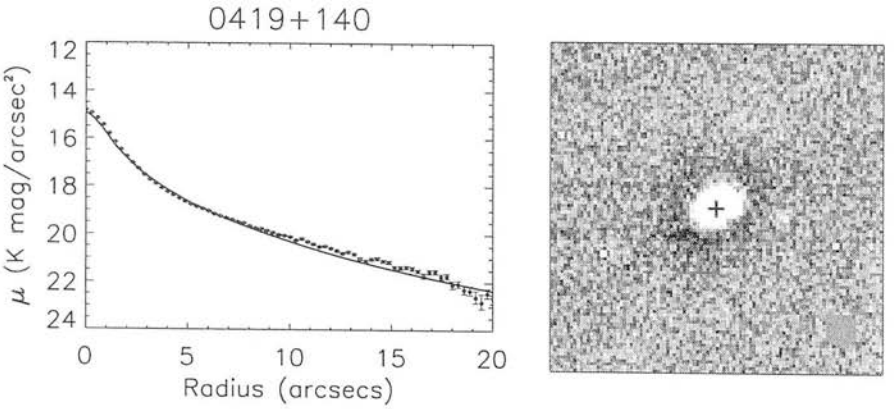

Figure 4.14: Profile of 0419+140 in K band

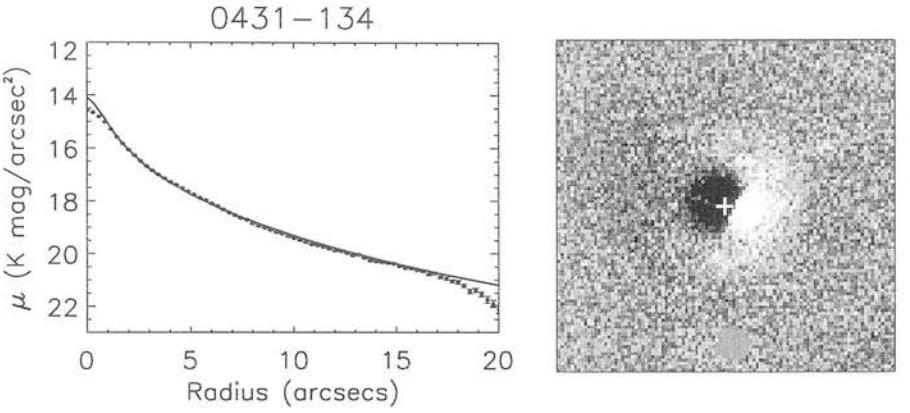

Figure 4.15: Profile of 0431−134 in K band

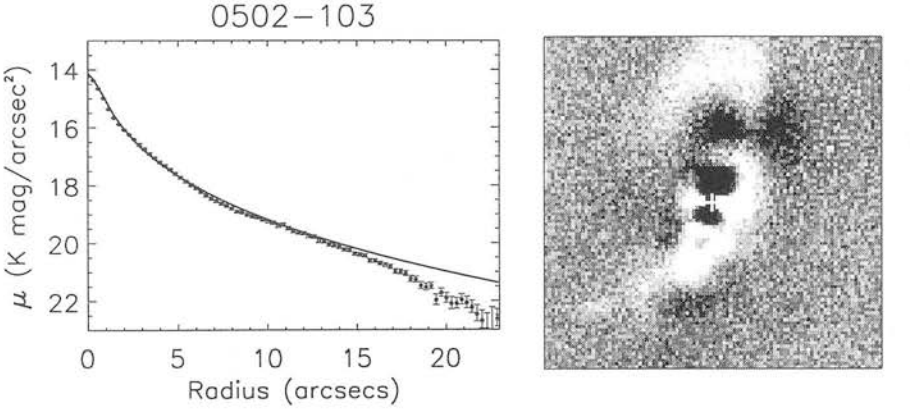

Figure 4.16: Profile of 0502−103 in K band

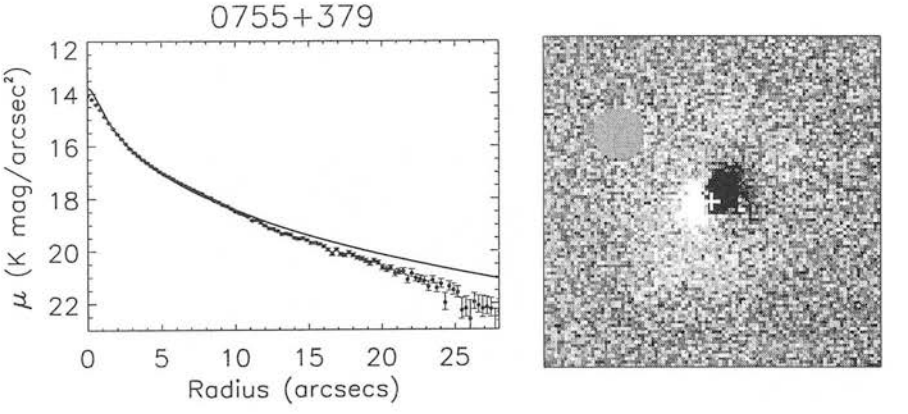

Figure 4.17: Profile of 0755+379 in K band

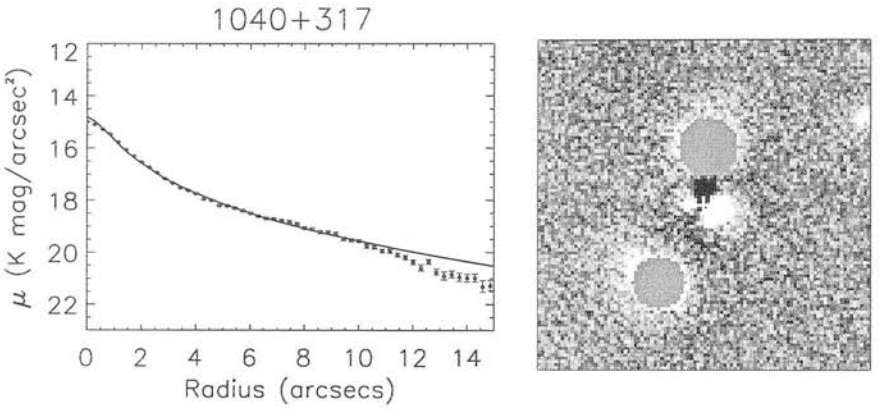

Figure 4.18: Profile of 1040+317 in K band

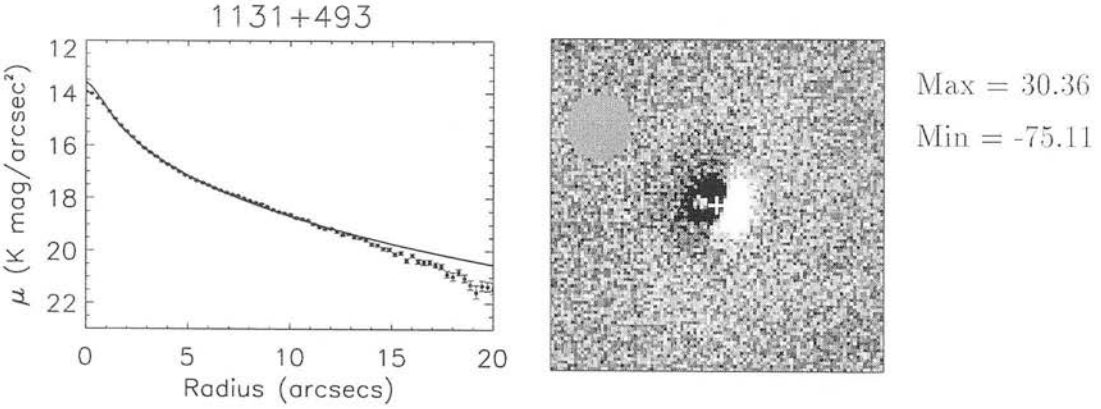

Figure 4.19: Profile of 1131+493 in K band

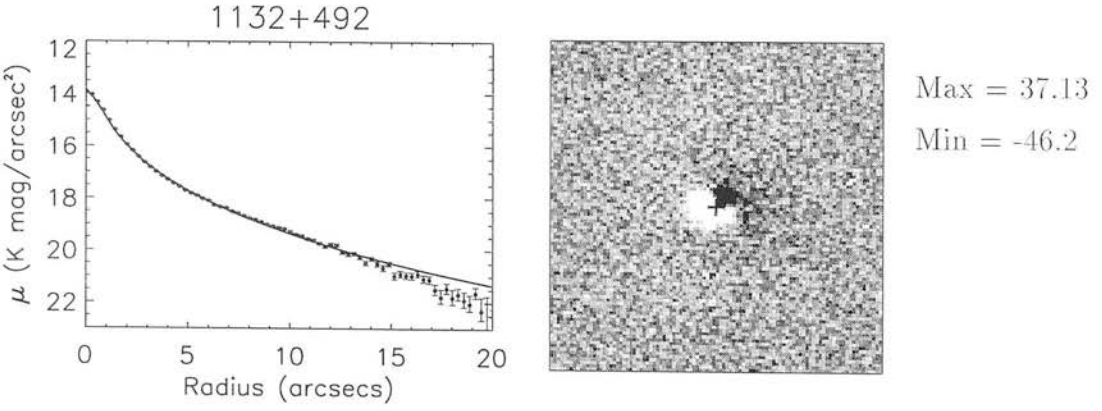

Figure 4.20: Profile of 1132+492 in K band

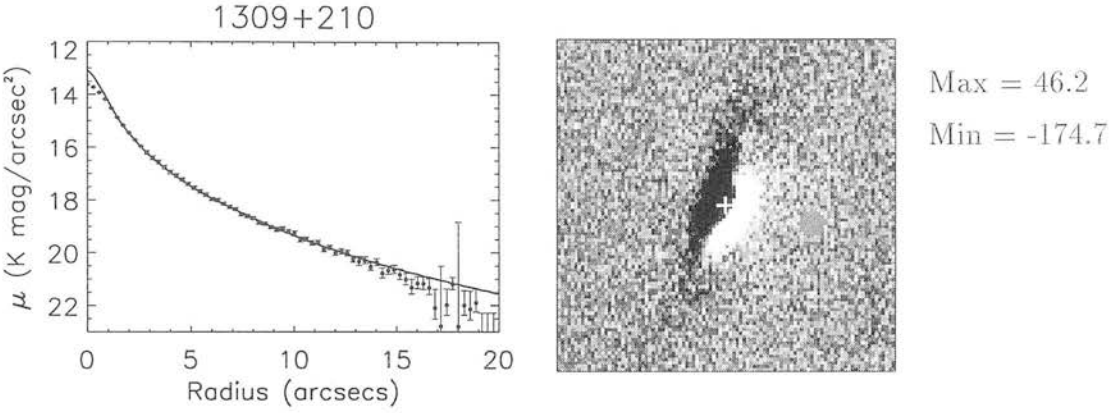

Figure 4.21: Profile of 1309+210 in K band

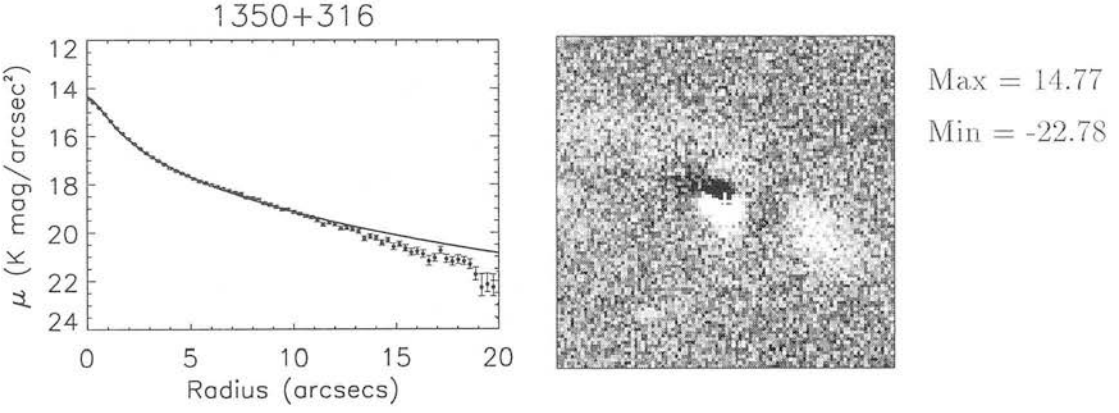

Figure 4.22: Profile of 1350+316 in K band

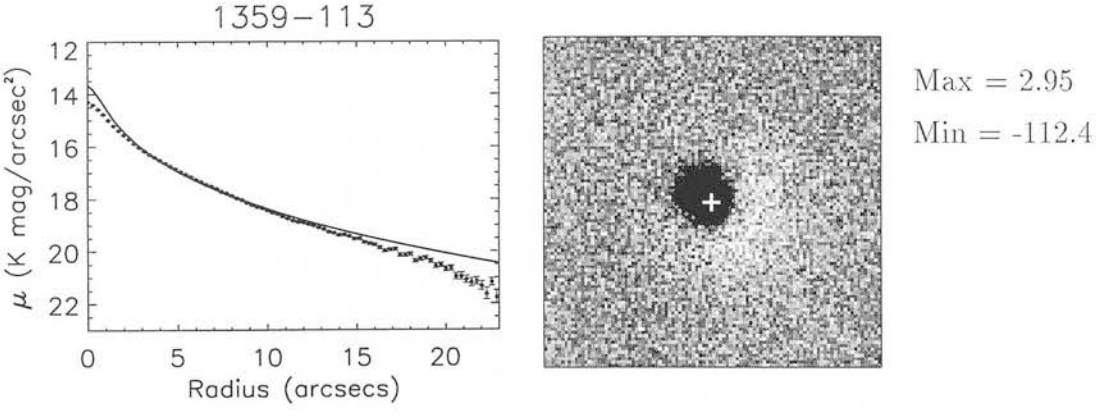

Figure 4.23: Profile of 1359−113 in K band

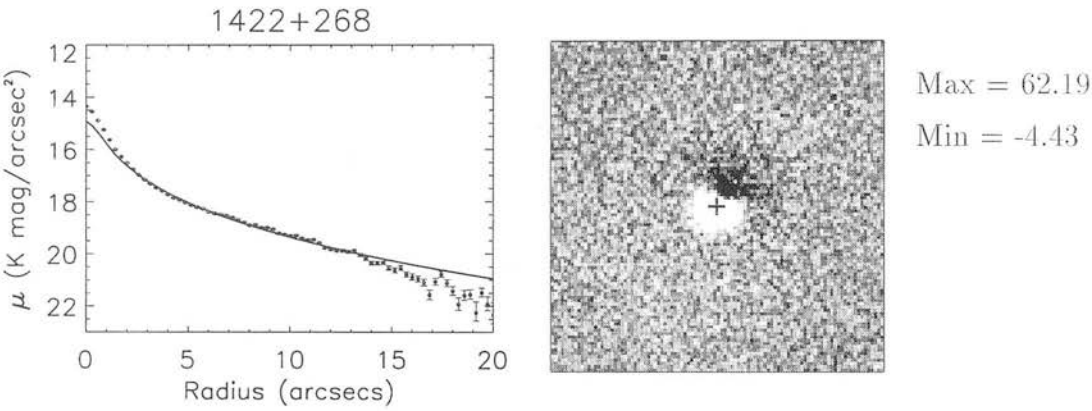

Figure 4.24: Profile of 1422+268 in K band

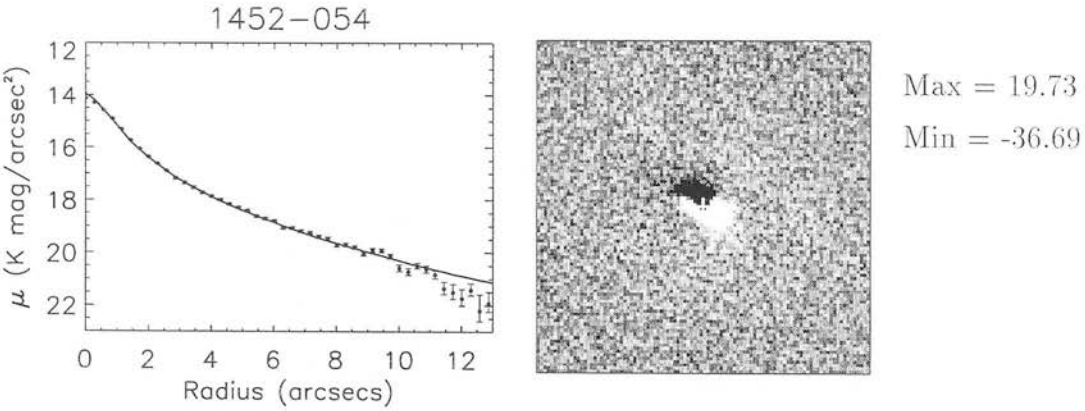

Figure 4.25: Profile of 1452−054 in K band

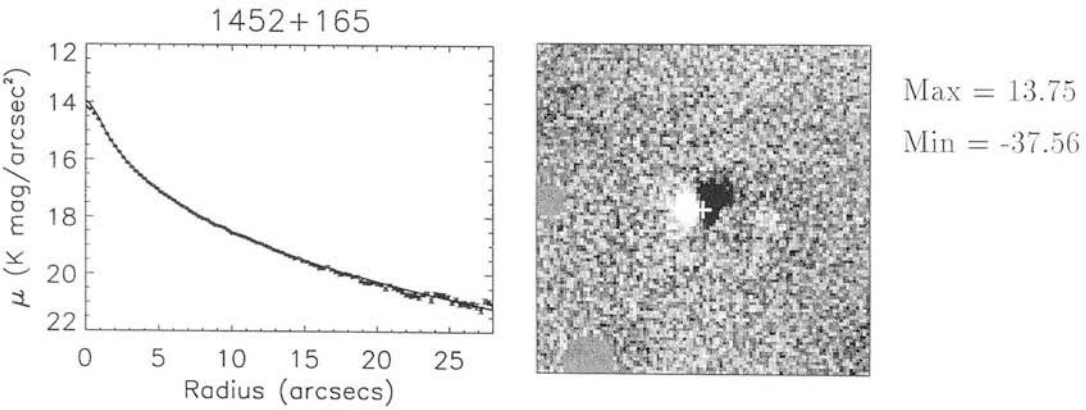

Figure 4.26: Profile of 1452+165 in K band

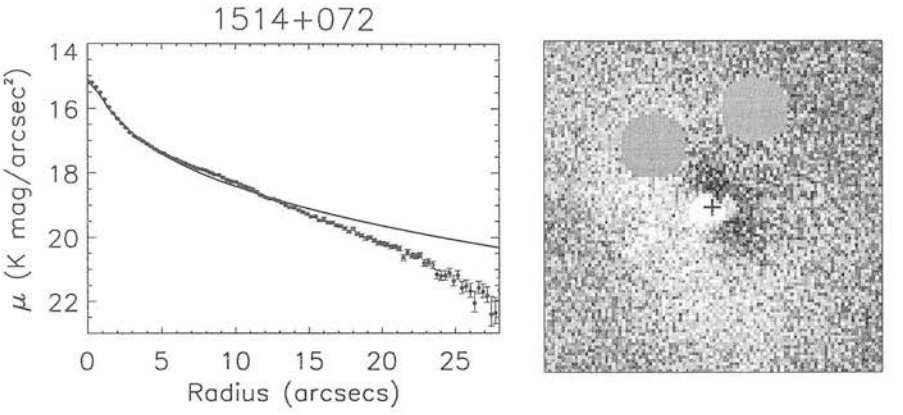

Figure 4.27: Profile of 1514+072 in K band

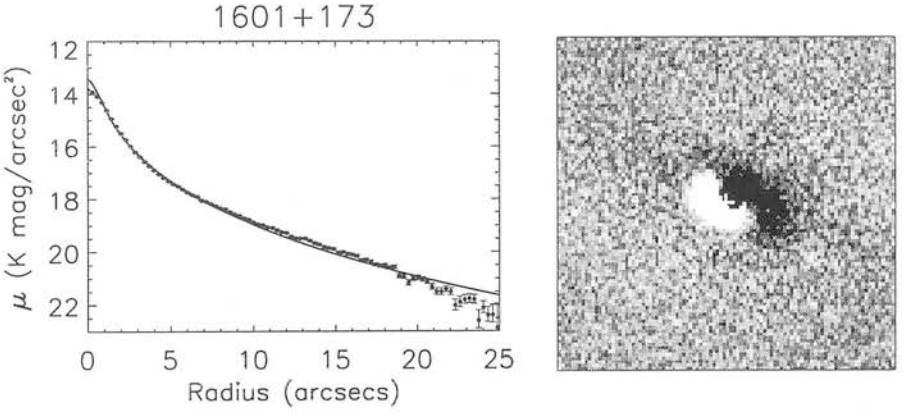

Figure 4.28: Profile of 1601+173 in K band

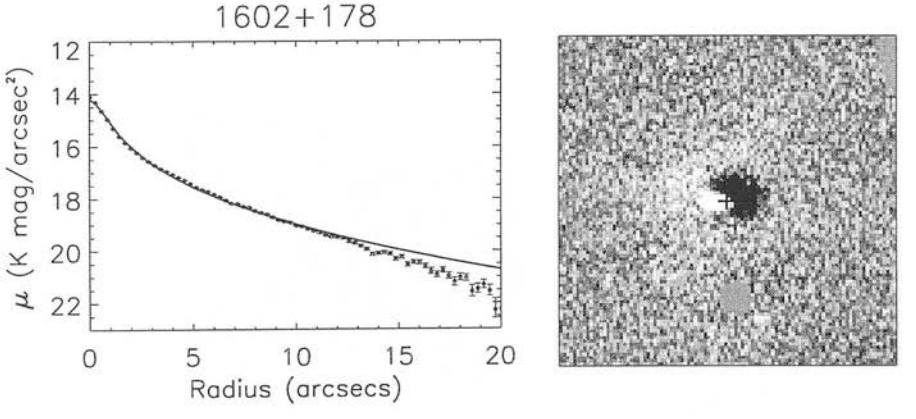

Figure 4.29: Profile of 1602+178 in K band

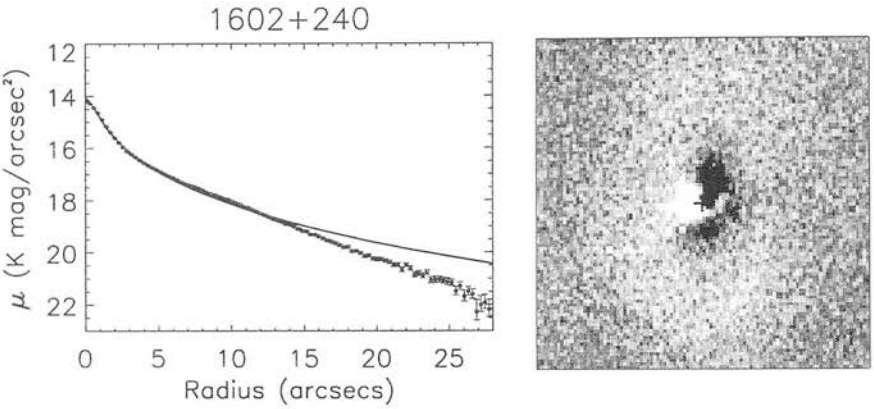

Figure 4.30: Profile of 1602+240 in K band

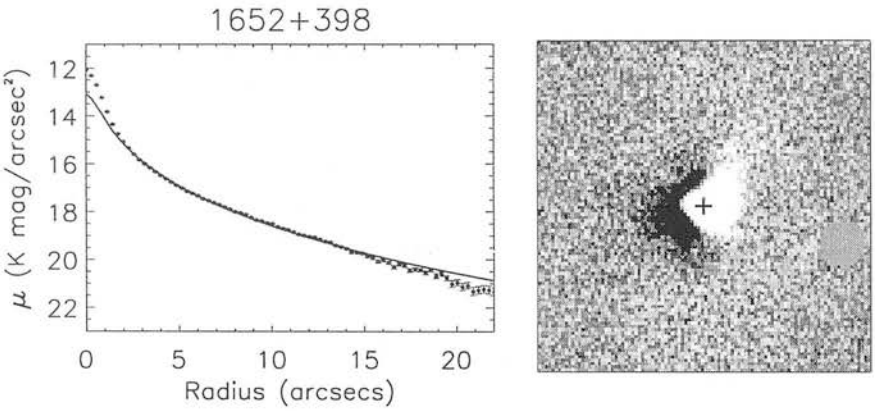

Figure 4.31: Profile of 1652+398 in K band

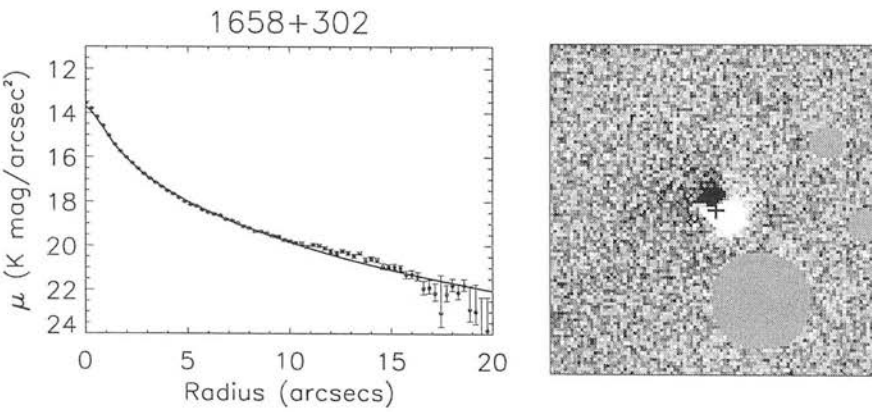

Figure 4.32: Profile of 1658+302 in K band

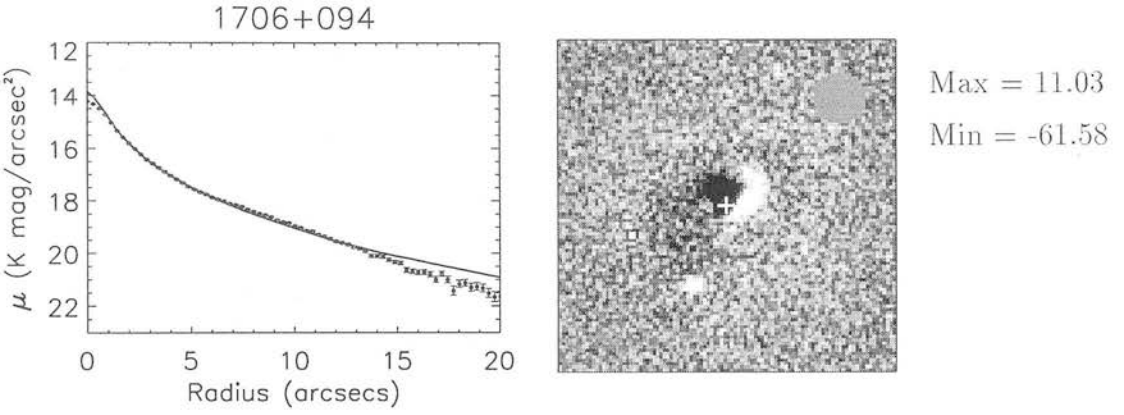

Figure 4.33: Profile of 1706+094 in K band

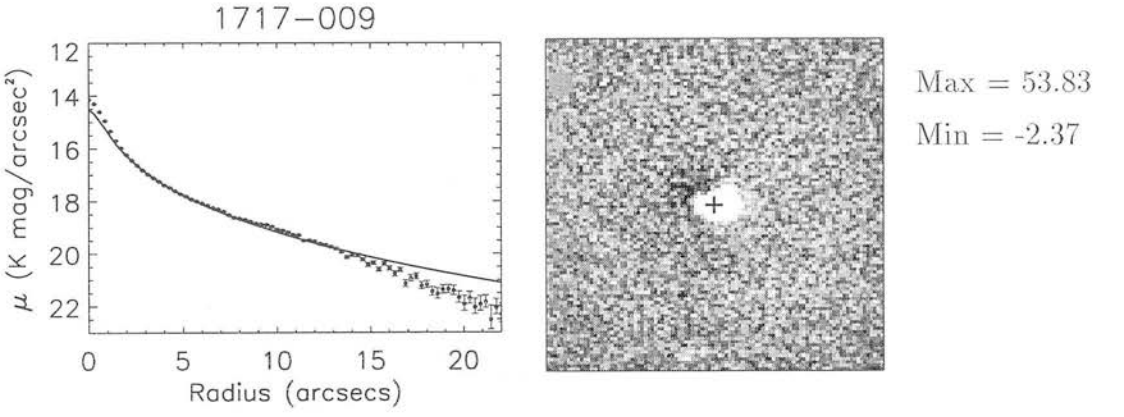

Figure 4.34: Profile of 1717−009 in K band

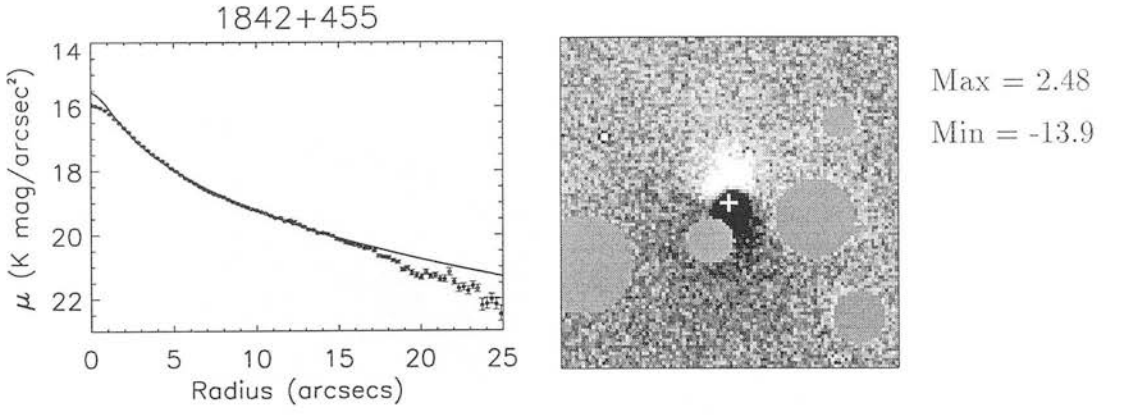

Figure 4.35: Profile of 1842+455 in K band

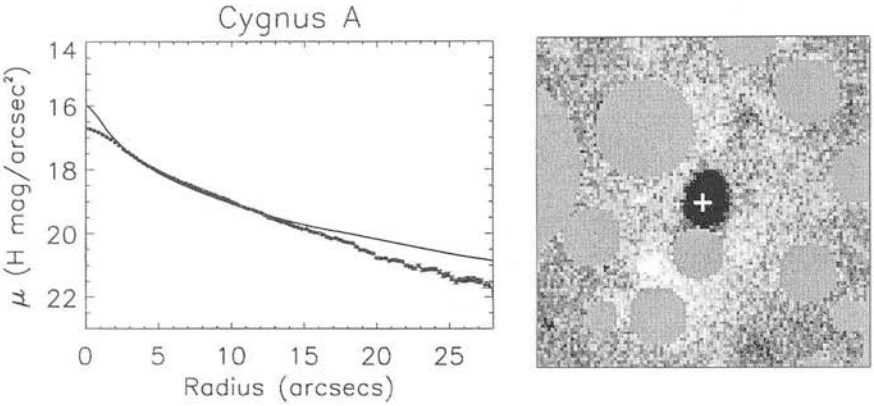

Figure 4.36: Profile of Cygnus A in H band

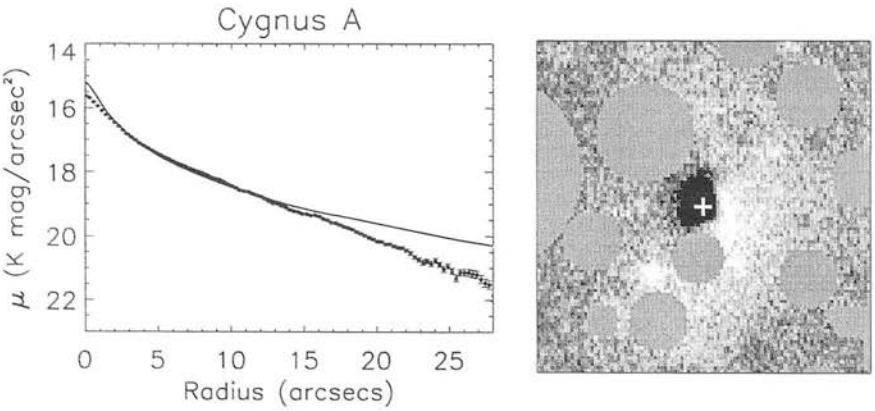

Figure 4.37: Profile of Cygnus A in K band

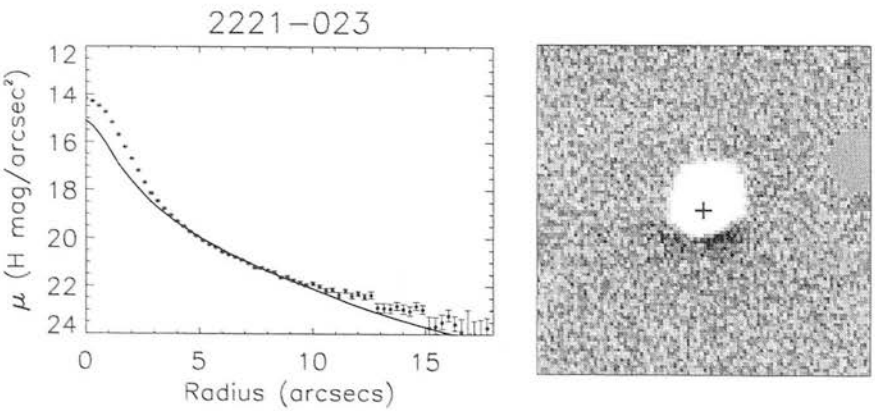

Figure 4.38: Profile of 2221−023 in H band

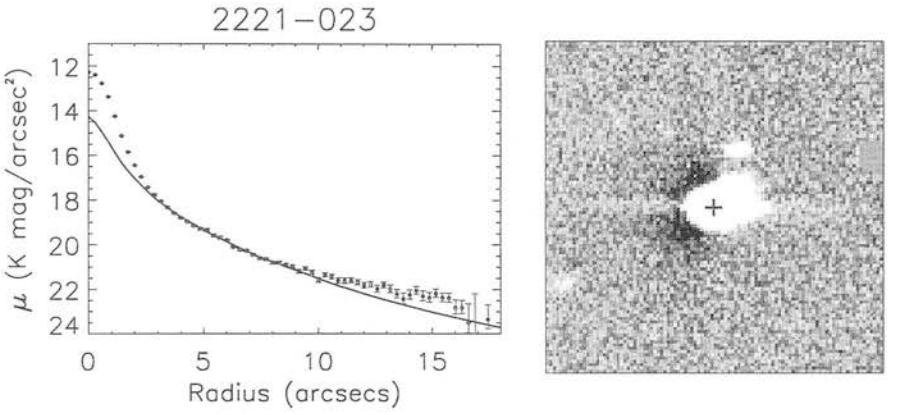

Figure 4.39: Profile of 2221−023 in K band

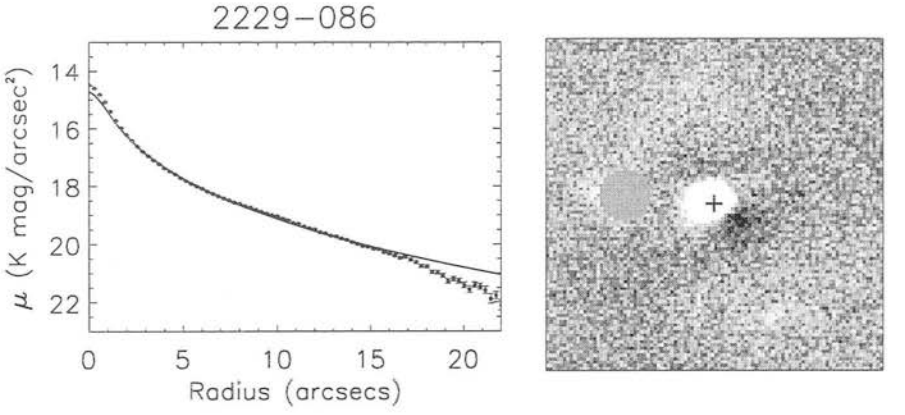

Figure 4.40: Profile of 2229−086 in K band

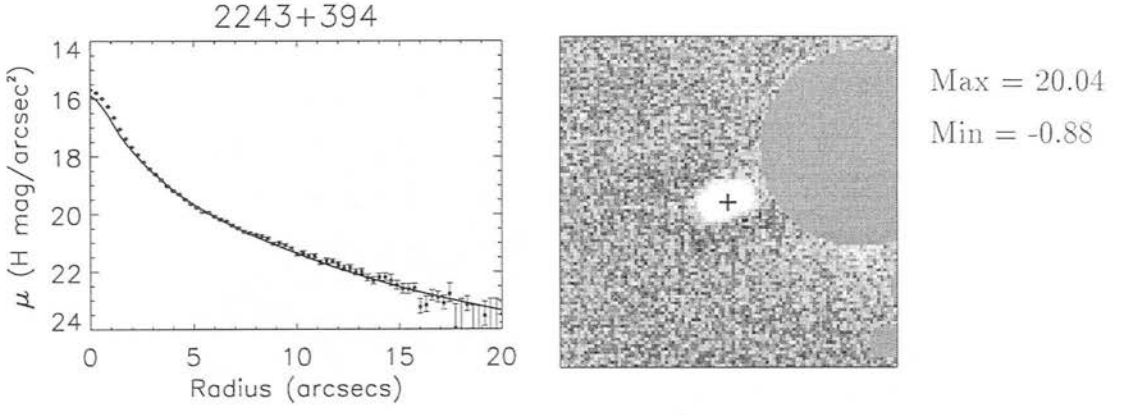

Figure 4.41: Profile of 2243+394 in H band

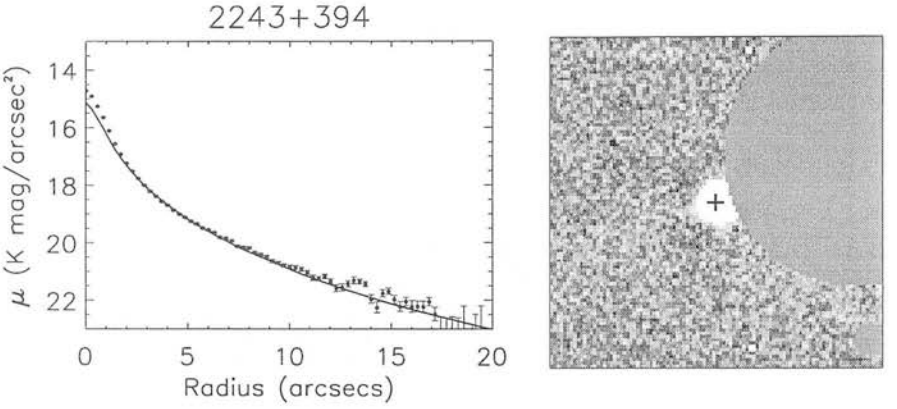

Figure 4.42: Profile of 2243+394 in K band

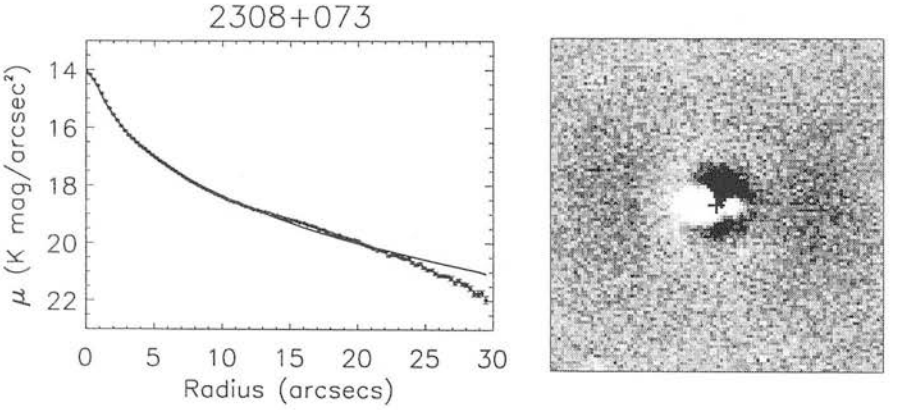

Figure 4.43: Profile of 2308+073 in K band

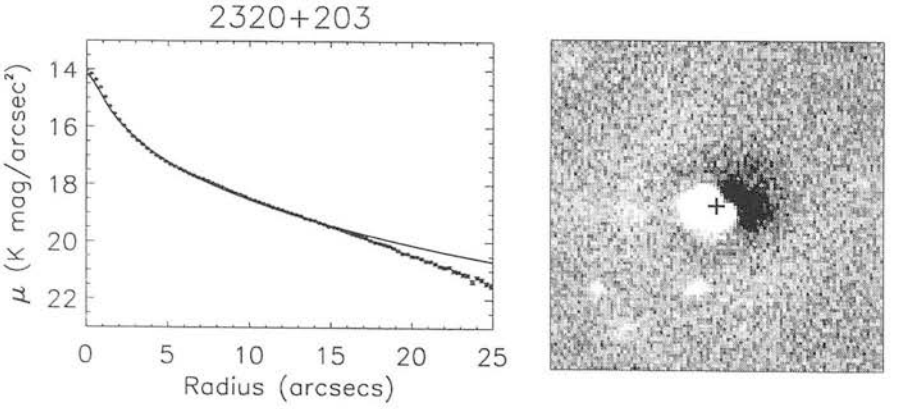

Figure 4.44: Profile of 2320+203 in K band

4.3 Galaxy parameters

Having calculated parameters for the sample of radio galaxies it is interesting to see how they compare to the parameters of 'normal' elliptical galaxies. Figure 4.45 shows the $\mu_e - r_e$ projection of the fundamental plane. The FR I radio sources are marked as stars whilst the FR II sources are marked as squares. There is an insufficient number of FR II sources to be able to draw any conclusion as to whether there is a difference in the parameter space preferred by the two types of radio sources. A least absolute deviation fit to the points yields a best fit line with slope $\mu_e = 2.89\log_{10} r_e + 16.43$, which is similar to the relation obtained by Taylor *et al.* (1996) in the K band of $\mu_{1/2} = 2.95_{\pm 0.55}\log_{10} r_{1/2} + 16.24_{\pm 0.75}$ where $\mu_e = \mu_{1/2}$ and $r_e = r_{1/2}$ for a de Vaucouleurs model. The values of μ_e have been corrected to $z = 0$ from the raw values in table 4.5 by a K–correction of $K(z) = -3z$, similar to the value found by Glazebrook *et al.* (1994). From a study of ellipticals in the Virgo cluster Capaccioli, Caon & D'Onofrio (1992) found an upper boundary to the scale–lengths of 'ordinary' galaxies, beyond which only brightest cluster, cD galaxies and luminous ellipticals with boxy isophotes are found. They conclude that objects belonging to the 'bright' family have probably undergone merging. As most of the objects lie beyond this boundary, and AGN activity is thought to be caused by mergers, it is indeed evidence supporting the idea of larger scale–lengths for galaxies which have undergone mergers.

It is also interesting to use the two known parameters to predict the third parameter in the fundamental plane: the velocity dispersion, σ_v. The values obtained can then be compared with any values estimated in section 3.7. The parameterisation of the fundamental plane was that calculated in the K band by Mobasher *et al.* (1999) of $\log_{10} r_e = 1.38_{\pm 0.26}\log_{10}\sigma + 0.30_{\pm 0.02}\mu_e + c$. The normalisation constant c is not given, so it has been calculated from the two galaxies with the most well–defined velocity dispersions from the literature, 0325+023 ($\sigma = 189 \pm 5$, $c = -8.17$) and 0356+102 ($\sigma = 163 \pm 6$, $c = -8.15$) and has been taken to be $c = -8.16$. The velocity dispersion estimates are given in table 4.6. It can be seen that, on the whole, the values compare very well with the measured values, implying that the radio galaxies do follow the fundamental plane relation for elliptical galaxies and are indeed 'normal' elliptical galaxies.

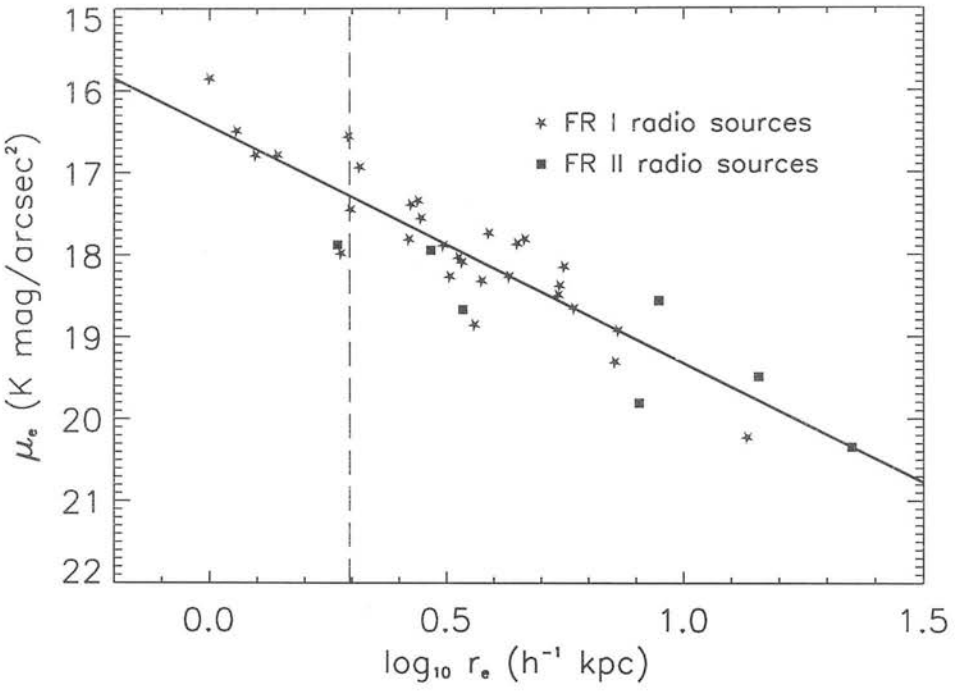

Figure 4.45: A Kormendy $\mu_e - r_e$ relation for the model fitting results. The FR I radio sources are marked with a star and the FR II sources are marked with a square. The slope of the best fitting line has $\mu_e = 2.89 \log_{10} r_e + 16.43$. The vertical dashed line is from Capaccioli *et al.* 1992, marking the interval between 'ordinary' and 'bright' ellipticals, corrected for the cosmology adopted in this thesis.

4.4 Initial extinction estimates

4.4.1 Conversion of magnitudes to fluxes

The magnitudes have been converted to fluxes in this and further analyses by taking the definition of a magnitude as given by

$$m = -2.5 \log_{10} \frac{\int f_\nu d\nu \; F(\nu)}{\int f_\nu^{\rm vega} d\nu \; F(\nu)}. \qquad (4.10)$$

where $f_\nu^{\rm vega}$ is a spectrum of the reference star Vega (α-Lyrae). $F(\nu)$ is the effective filter response, a parameter which describes the amount of light from the object that is actually recorded by the detector. It is dependent on:

- the filter transmission function;
- wavelength dependent response of the detector and the telescope optics (quan-

Object	σ_{FP} kms^{-1}	σ_{spec} kms^{-1}	Object	σ_{FP} kms^{-1}	σ_{spec} kms^{-1}
0055−016	265	199±18	1422+268	216	
0106+130	224	227±20	1452+165	333	
0207+095	289		1452−054	216	
0208−067	236		1514+072	218	197±36,253±12
0217+017	284		1601+173	289	
0300+162	160	198, 242±26	1602+178	204	
0325+023	184	189±5	1602+240	260	243±24,278±40
0356+102	166	163±6	1652+398	335	
0419+140	233	170	1658+302	233	
0431−134	221	207	1706+094	262	
0502−103	241	304	1717−009	174	
0755+379	315	291	1842+455	328	365±23
1040+317	166		Cygnus A	295	
1131+493	276	283±25	2221−023	234	
1132+492	216		2229−086	367	266
1309+210	293		2243+394	222	119
1350+316	252	185±20	2308+073	324	278, 237±33
1359−113	304		2320+203	266	

Table 4.6: Velocity dispersion estimates from the fundamental plane equation. The third column gives values estimated from spectra. The values with errors are taken from the online Hypercat catalogue (www-obs.univ-lyon1.fr/hypercat/intro.html) and references within, whilst those without errors were estimated in Section 3.7. The agreement between the two methods of estimating the velocity dispersion is surprisingly good.

tum efficiency);

- the wavelength–dependent transmission of the atmosphere.

Digitised filter transmission profiles for all the wavebands have been obtained. The WHT optical filter profiles have then been multiplied by an estimate of the quantum efficiency of the detector used taken from the WHT web page[4]. Kitt Peak produce filter profiles with the response function of the detector already folded in, whilst the infrared filter profiles have been multiplied by an estimate of the atmospheric transmission, which is the most important consideration at these wavelengths. Plots of the filter profiles are shown in figures 4.46 and 4.47. The magnitude of a 1 Jy source, the value needed to convert from magnitudes to fluxes, is given in table 4.7 for each filter. The flux (in Janskys) is then calculated

[4]http://www.ing.iac.es/~eng/detectors/ccd_tek5.htm

by

$$S(\mathrm{Jy}) = 10^{-0.4(m-m_{(1\mathrm{Jy})})}. \tag{4.11}$$

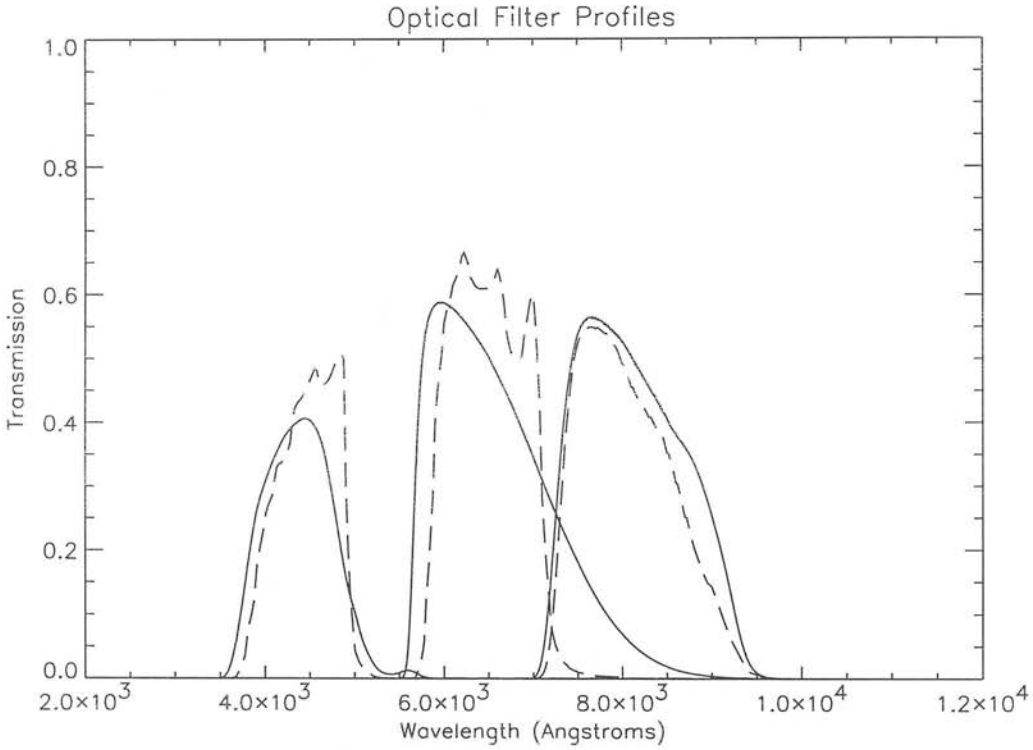

Figure 4.46: Effective filter response of all the optical filters used in this study. The dotted line shows the Kitt Peak Mould B, R and I filters with the CCD response function folded in. The solid line shows the WHT Harris B, R and I filters multiplied by an estimate of the quantum efficiency.

4.4.2 Results

Assuming the unified schemes for radio–loud AGN are correct, any detected nuclear sources should have the colours of a standard quasar reddened by a certain amount of dust along the line–of–sight. Therefore it is necessary to quantify the reddening to estimate the extinction. Firstly the nuclear $K - L'$ sources have been corrected for Galactic extinction along the line of sight using the Schlegel, Finkbeiner & Davis (1998) E($B - V$) estimates of each source from table 3.3. This has then been converted to an estimate of the infrared Galactic reddening $E(K - L')$ using the newest estimate of the interstellar extinction law from Fitzpatrick (1999). Generally the corrections for extinction within the Milky Way

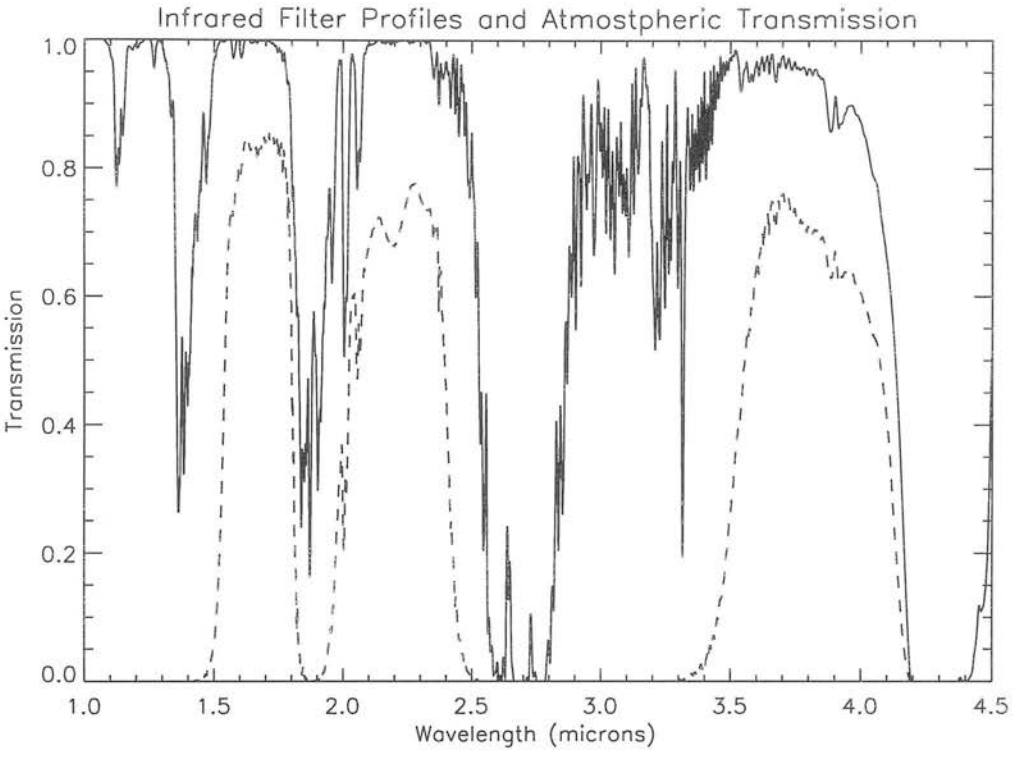

Figure 4.47: The effective filter response of the UKIRT filters and the atmospheric transmission on Mauna Kea. The dotted line shows the filter profile multiplied by the atmospheric transmission for the H, K and L' filters, whilst the solid line displays the transmission profile of the atmosphere. It can be seen that the filters are centered on the obvious windows in the infrared sky.

Filter	$\lambda_{\rm eff}$ [μm]	m(1Jy)
B Mould	0.44	8.952
B Harris		8.913
R Mould	0.65	8.665
R Harris		8.671
I Mould	0.83	8.427
I Harris		8.424
H	1.63	7.501
K	2.19	7.022
L'	3.90	5.932

Table 4.7: The magnitude of a 1 Jy source in each filter, taking account of the effects of atmospheric transmission for the infrared filters and the quantum efficiency of the detector for the optical filters.

were negligible, the maximum was 0.14 mag. The choice of adopted extinction curve is fairly unimportant as most recent estimates converge in the infrared

portion of the spectrum and only for the UV portion do they differ significantly.

It was then interesting to investigate whether an unreddened quasar could account for the observed unreddened nuclear colours. Parameterising the intrinsic spectral energy distribution of the quasar in the infrared as a powerlaw with exponent α ($f_\nu \propto \nu^\alpha$), the value of α necessary to explain the observed colour was calculated. Neugebauer *et al.* (1987) find a median value of $\alpha = -1.4$ for the optically selected Palomar–Green sample of quasars in the near infrared ($1 - 2.2\,\mu$m), with a range from -0.12 to -2.07. Edelson, Malkan & Rieke (1987) find a slightly flatter value of -1.09 for quasars in the range $2.2 - 25\,\mu$m. Therefore any source requiring a value of $\alpha < -2$ almost definitely contains some amount of extinction along the line–of–sight. The next step is to assume some intrinsic spectral shape for the quasar. As explained in chapter 1 DWMG use an extrapolation of the radio data to estimate the shape of spectral energy distribution in the infrared in two ways, estimating values of $\alpha = -0.18$ and $\alpha = -1$. Owing to the lack of radio data and not necessarily believing that an extrapolation of the radio data provides a good fit to the spectral shape in the infrared, we chose to use a value of $\alpha = -1$. Many authors tend to use the Palomar–Green value of -1.4, but as this is a median value taken from fits in the $1 - 2.2\,\mu$m range and the spectral energy distribution appears to flatten off slightly longwards of $2.2\,\mu$m, the chosen value of $\alpha = -1$ appears more appropriate in the K to L' region of the spectrum.

The intrinsic colour of an $\alpha = -1$ source is calculated by integrating the spectral energy distribution under the filter profiles in a similar manner to equation 4.10. At the redshift range of all the objects in the sample the colour is $(K - L') = 1.68$. Therefore the net reddening by the dust along the line of sight is given by

$$\mathrm{E}(K - L') = (K - L')_{obs} - \mathrm{E}(K - L')_{MW} - 1.68. \qquad (4.12)$$

The amount of visual extinction at the source is then calculated by shifting the K and L' filters to their emitted wavelengths and using the interstellar extinction curve of Fitzpatrick (1999) again to calculate the inferred extinction in A_V. It is indeed possible that the shape of the interstellar extinction curve in these distant galaxies is intrinsically different from the one measured in our own galaxy, as for example, conditions near an active nucleus may cause differently sized dust grains to form. However the extinction curve from our own galaxy is used as nothing else is available.

The K band magnitudes are then dereddened by this estimated amount of red-

dening to give the unobscured K band magnitude. This is then converted to a power by using Mattig's formula (Mattig 1958) to calculate the luminosity distance of the source

$$d_L = \frac{2c}{H_0\Omega^2}\left\{\Omega z + (\Omega - 2)[-1 + (\Omega z + 1)^{1/2}]\right\} \tag{4.13}$$

assuming $\Omega = 1$ and $H_0 = 100h$

$$d_L = \frac{2c}{100h}\left\{z - [(z+1)^{1/2} - 1]\right\}. \tag{4.14}$$

The power of the source is dependent on the choice of value for H_0, but the value quoted in the table can be increased to give the results in a favourite cosmology by adding $-2\log h$.

The initial extinction estimates are given in table 4.8. Method (a) uses the K band nuclei estimated from the surface brightness modelling whilst method (b) uses the K nucleus as estimated from the scale and subtract method. It can be seen that method (b) does not provide consistent answers. The implied power of the sources is within the same range as the Palomar–Green quasars at $2.2\,\mu$m (Neugebauer *et al.* 1987).

Object	Method	$K - L'_{MW\,corr}$ [mag]	±	$-\alpha$	E$(K - L')$ [mag]	A_V [mag]	±	$\log_{10}(\nu L_\nu)$ $[L_\odot]$	±
0055−016	a	> 4.55		> 5.83	> 2.87	> 51.0		< 10.06	
0106+130	a	3.07	0.22	3.34	1.39	24.3	3.8	10.14	0.18
	b	3.14	0.22	3.46	1.46	25.5	3.8	9.98	0.18
0206+355	b	3.03	0.16	3.27	1.35	24.2	2.8	9.72	0.13
0207+095	a	3.14	0.22	3.46	1.46	24.6	3.7	10.03	0.18
0217+017	a	2.94	0.25	3.11	1.26	22.5	4.5	9.55	0.21
0300+162	a	1.22	0.30	0.22	− 0.46			8.71	0.04
	b	1.43	0.25	0.57	− 0.25			8.62	0.04
0325+023	a	2.84	0.25	2.95	1.16	20.9	4.5	9.17	0.21
0356+102	a	2.86	0.16	2.98	1.16	21.0	2.9	9.37	0.13
	b	3.53	0.16	4.11	1.85	33.4	2.9	9.68	0.13
0419+140	a	1.84	0.29	1.27	0.16	2.8	5.0	8.95	0.26
0431−134	a	> 4.58		> 5.88	> 2.90	> 52.0		< 10.13	
0502−103	a	> 3.20		> 3.56	> 1.52	> 27.2		< 9.77	
0755+379	a	> 4.93		> 6.47	> 3.25	> 58.0		< 10.38	
1040+317	a	2.54	0.15	2.44	0.86	15.5	2.7	8.83	0.12
1131+493	a	> 2.91		> 3.07	> 1.23	> 22.1		< 9.29	
1132+492	a	2.38	0.10	2.17	0.70	12.6	1.8	8.97	0.08
1309+210	a	> 2.83		> 2.93	> 1.23	> 20.8		< 9.46	
1350+316	a	3.83	0.09	4.62	2.15	38.2	1.6	9.94	0.76
1422+268	a	1.16	0.11	0.12	− 0.52			8.81	0.01
1452+072	a	> 2.87		> 3.00	> 1.15	> 21.1		< 9.42	
1514+072	a	2.01	0.24	1.55	0.33	5.9	4.3	8.39	0.20
1652+398	a	1.59	0.08	0.84	− 0.09			9.76	0.01
1842+455	a	> 4.72		> 6.12	> 1.19	> 51.1		< 10.84	
Cygnus A	a	> 5.04		> 6.66	> 3.36	> 60.3		< 10.41	
	b	3.22	0.17	3.59	1.61	28.2	3.0	10.07	0.14

continued on next page

Object	Method	$K - L'_{MWcorr}$ [mag]	$\pm$	$-\alpha$	$E(K-L')$ [mag]	A_V [mag]	$\pm$	$\log_{10}(\nu L_\nu)$ $[L_\odot]$	$\pm$
2221−023	a	< 2.46		< 2.31	< 0.78	< 13.7		> 10.92	
2229−086	a	1.79	0.30	1.18	0.11	1.9	5.0	9.38	0.25
2243+394	a	2.10	0.25	1.70	0.42	7.1	4.3	9.61	0.21
	b	2.96	0.25	3.15	1.28	21.8	4.3	9.98	0.21
2308+073	a	2.79	0.16	2.87	1.11	19.7	2.8	9.66	0.13
2320+203	a	2.23	0.16	1.92	0.55	9.8	2.8	9.26	0.13

Table 4.8: Initial extinction estimates. Column 1 gives the name of the object, columns 3 and 4 give the Galactic extinction corrected $K - L'$ colour of the nuclear source. For method (a) the K band value is taken from table 4.5 and the L' value taken from column 4 of table 5.20. Method (b) uses the K band estimate from the 'scale and subtract' method in table 4.1. Column 5 gives the necessary value of the spectral index which would be needed to explain the observed colour. Column 6 gives the necessary reddening towards a quasar or starburst with an intrinsic spectral energy distribution with $\alpha = -1$. For those objects where a significant amount of reddening is necessary to explain the nuclear colour an estimate of the visual extinction is made in column 7. The final columns give the intrinsic power of the nuclear source in solar luminosities.

Chapter 5

Line strength measurements and nuclear stellar population predictions

5.1 Introduction to stellar population modelling

This chapter addresses the question of how the stellar populations in an elliptical galaxy affect the nuclear infrared colours. In the previous chapter it was assumed that the L' flux was entirely non–thermal in origin. This assumption is at best not proven and therefore requires investigation. Figure 5.1 shows the $K - L'$ colour versus redshift of a central 3″ aperture of all the galaxies analysed previously. Also drawn is the locus of three old stellar populations with varying metallicities. It can be seen that a few objects lie above the oldest, most metal–rich population and therefore their nuclear colours are not "normal". Lilly, Longair & Miller (1985) drew a similar plot and found those galaxies with strong optical emission lines to have infrared excesses. It seems to be a similar case here; of the spectra obtained, those with emission lines do lie above the maximum colours predicted from stellar populations.

The best way of accurately predicting the nuclear population without the effects of dust interference is to consider small regions of the spectrum such as absorption features. These features are much less sensitive to dust than consideration of the whole continuum or broad–band colours, which are essentially the integrated flux from large regions of the spectrum. The Lick/IDS index system allows an estimate of the best fit stellar population model from optical spectra, the model is then used

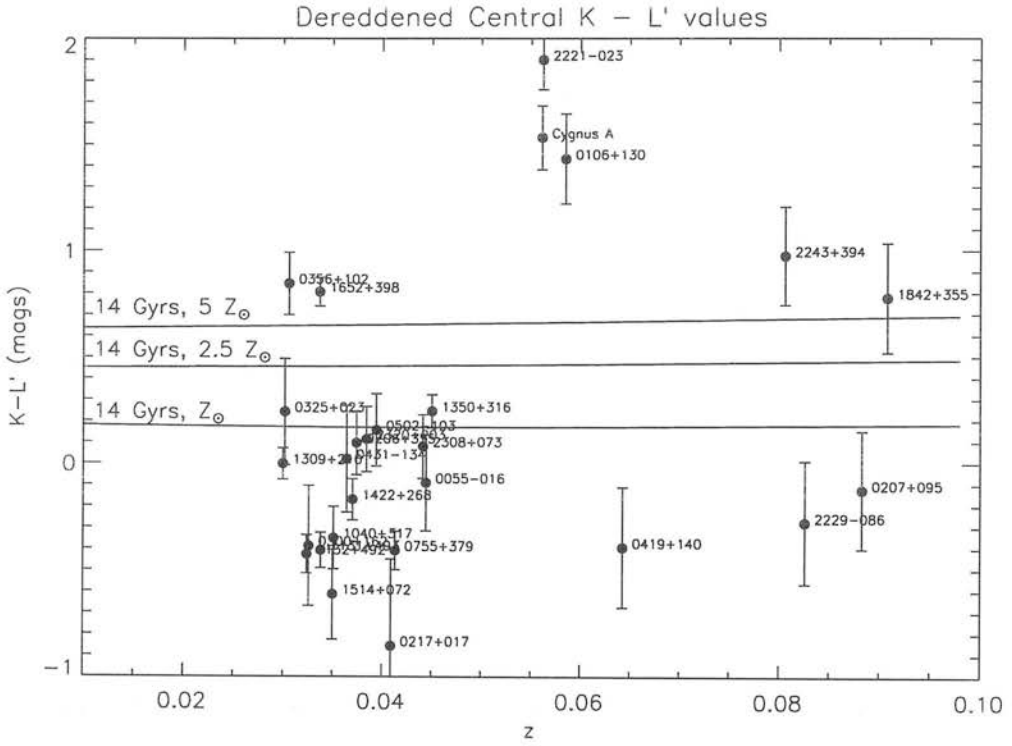

Figure 5.1: $K - L'$ colours of central 3″ apertures against object redshift. The colours have been dereddened using the extinction estimates from table 3.4, so that the expected $K - L'$ reddening due to the Milky Way has been removed.

to predict the contribution to the stellar population at infrared wavelengths. The system is introduced in section 5.2 and the measurement of these indices from the spectra obtained in chapter 3 are carried out in section 5.3. The entire spectra are also fitted to different stellar population models in section 5.5 for comparison with the results from the index analysis and infrared colours predicted from these too. Finally for those galaxies in the sample for which spectra have not been obtained, an estimate of the infrared nuclear stellar population is made from the available optical and infrared images, the acquisition of which was described in chapter 2.

5.1.1 Spectral synthesis modelling

Although much mention has already been made of comparing observed spectra with synthetic models, nothing has been said on the actual origin and authenticity of these models. Essentially the idea of a simple stellar population (SSP) is that stars of the same metallicity are born at the same time with an initial mass

function (IMF) and then evolve over time according to stellar evolution. The integrated spectrum of the population can be computed at any time by simply summing up the individual spectra of the stars at that instant. There are two main shapes of IMF used, Salpeter (Salpeter 1955) and Miller–Scalo (Scalo 1986). They both follow a power–law shape for main sequence stars and only at the low mass end do they differ, where the Miller–Scalo IMF turns over and the number of very low mass stars starts to decrease. Observations which attempt to measure the IMF have only been successful in the Milky Way and a few very nearby neighbours, due to the necessity to resolve individual stars and then trace their evolution back in time. The observations currently point towards the Salpeter model being a slightly better fit. The universality of the IMF has been shown by sensible agreement between models and observations in other galaxies. It is conceivable that differences may be found in the future possibly arising from the low mass turnover point occurring at different masses. Although much work has been carried out to construct stellar populations from different IMFs the differences are in fact very slight for elliptical galaxies. Most of the galaxy light is dominated by giants at the main sequence turnoff point for ages of about 10 Gyr with masses of about 1 $M_{\odot}$, where the IMFs are similar. For this reason the stellar population models used in this chapter are all for Salpeter IMFs. In fact the differences between models from different authors (Charlot, Worthey & Bressan 1996) are far greater than any introduced by using different IMFs. Disagreement over stellar interior models, modelling of the post main–sequence ages and stellar atmospheres produce SSPs which predict absolute ages varying by around 20%.

As mentioned above an SSP is constructed by integrating the spectra from a number of either observed or theoretical stars. In fact it is the contribution to the flux in the various passbands of all the mass–bins along an isochrone which is summed, starting from a lower mass limit and ending at the last point on the isochrone. Post main–sequence phases of stellar evolution are then computed separately *e.g.* Charlot & Bruzual (1991), Bruzual & Charlot (1993). Although elliptical galaxies can often be well fitted by a passively evolving stellar population such as an SSP, the power of stellar population modelling becomes clear when different SSPs are combined together to construct composite stellar populations (CSPs). These can be constructed by either assuming an exponentially decreasing star–formation rate or assuming that the star–formation occurs in bursts. The

chemical enrichment history of the galaxy can also be accounted for by assuming some prescription for the feedback of material into stars, introducing more metal-rich stars into the population over time. Dust effects can also be modelled by taking expressions for the expected reddening, either assuming the dust is evenly distributed within the stars, or the more simple assumption of an intervening layer of dust.

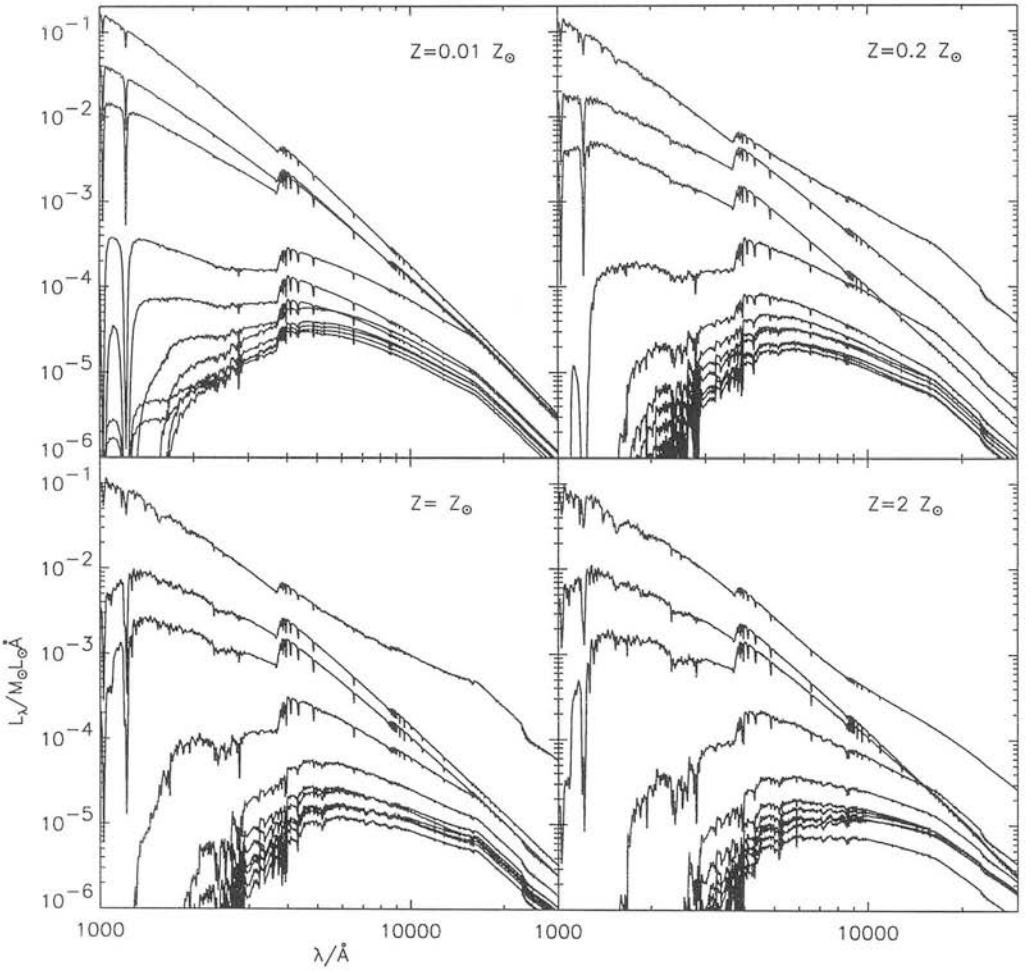

Figure 5.2: Spectral energy distributions of the single age, single metallicity models from Jimenez *et al.* 1999. Four metallicities are displayed and for each metallicity eleven ages, from top to bottom: 0.01, 0.07, 0.3, 1, 3, 5, 7, 9, 11, 13 and 15 Gyr. In all cases, after the first Gyr or so, the hot blue stars have evolved leaving an older redder population.

The models used in this chapter are those by Raul Jimenez (Jimenez *et al.* 1999) and Guy Worthey (Worthey 1994) which both have varying age and metallicity. Other authors have produced only solar metallicity, $Z_{\odot}$, models so far. Worthey provides both index measurements and SEDs whilst Jimenez provides just SEDs. In both cases the SEDs cover the wavelength range between 90.9Å and 1.6×10^6Å, however only the optical and near–infrared regions are shown in figure 5.2.

The treatment of the post main–sequence phase of stellar evolution is much improved in the models of Jimenez. Worthey truncates at the helium flash, which means that once stars have evolved beyond the helium burning phase their contribution to the overall SED is neglected. This is not ideal when attempting to accurately predict the infrared colours of a population from its optical spectrum as the horizontal branch giant stars contribute significantly towards the infrared flux. Jimenez calculates his models up to the tip of the red giant branch (RGB) for all but the most massive stars which are truncated at the carbon ignition point, providing a much more realistic output spectrum. His models are also calculated at much higher mass resolution which successfully samples the rapid stages of stellar evolution and results in bluer models than other authors. See figure 5.3 for a clear indication of the discrepancies between three different SSPs at infrared wavelengths. Although there do appear to be significant differences between the models at wavelengths $> 1\ \mu$m, in fact the overall shape of the models is very similar owing the spectrum being dominated by blackbody emission. The main differences between the plots of the models in this region are multiplicative, as the scaling is normalised at 6000Å. Careful comparisons between models and observations in the ultraviolet portion of the spectrum, where the main differences lie, are in progress (Nolan, Dunlop & Jimenez 2000). This has yet to be carried out in the infrared, but since Jimenez's bluer models do appear to provide better fits to the age of an object such as the Sun, this is evidence that his overall treatment is indeed more realistic.

As mentioned in chapter 1 there is a well–known degeneracy between age and metallicity so that the integrated spectrum of a population with a certain age and metallicity has a similar shape to that of a population with a lower metallicity and higher age (Worthey 1994). The match between the spectra is fortunately not identical, so the degeneracy can be lifted by concentrating on smaller features such as the strength of certain absorption lines which may be more susceptible to age effects than metallicity effects. A scheme for doing just this has been developed by

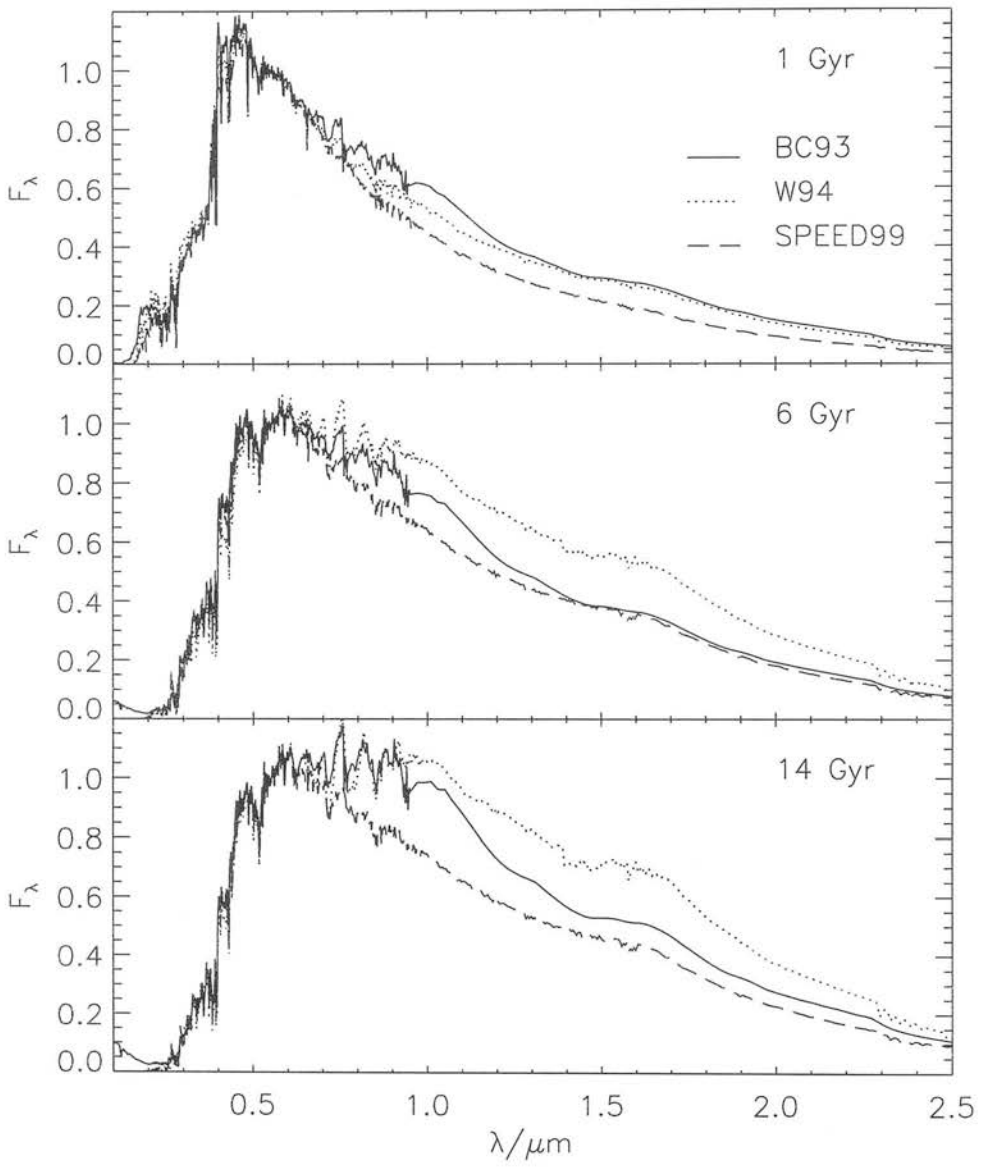

Figure 5.3: Comparison of the spectral energy distribution of three different model SSPs in the infrared (taken from Jimenez *et al.* 1999, figure 10). The filled lines are models by Bruzual and Charlot 1993, the dotted lines are those by Worthey 1994, and the dashed line are the Jimenez *et al.* 1999 models, which are consistently bluer than the others owing to their more complete treatment of the post main-sequence stages of stellar evolution.

a group working at the Lick Observatory in California, the quantities measured are called line strength indices. The history and implementation of the Lick

scheme is described below.

5.2 Introduction to the Lick/IDS system

Between 1972 and 1984 an extensive spectral library of stars, globular clusters and galaxies was obtained on the 3m Shane Telescope at the Lick Observatory using the Image Dissector Scanner (IDS). The spectra cover the 4000 – 6400 Å range and have a variable resolution of 8 – 11.5 Å over that range. As the same instrument was used for all the spectra, although the spectra have fairly low and variable resolution, it is the most stable library of spectra obtained at present. Since completion, the library has been used as a tool to study the stellar populations of both elliptical galaxies and globular clusters. To enable this, 21 indices have been defined which, whilst similar to the measurement of the equivalent width of an absorption feature, also define regions outside the feature which set the level of a pseudo–continuum. The neighbouring continuum regions are chosen so that they are insensitive to velocity dispersion broadening but still close enough to the feature to be a good representation of the continuum at that point. They are also chosen so that they have consistently less absorption than the actual feature. The index is then measured by integrating the flux under this new pseudo–continuum, thereby ensuring that the spectral shape or the strength of any neighbouring metal features does not affect the index measurement.

The development of the Lick system has been published in a series of papers: Burstein *et al.* 1984; Faber, Burstein & Gaskell 1985; Burstein, Faber & Gonzalez 1986; Gorgas *et al.* 1993; Worthey *et al.* 1994; Trager *et al.* 1998. The fourth and fifth papers in the series introduce the concept of fitting functions which allow the comparison of synthetic spectra with observed spectra. The spectral library does not cover the entire parameter space of stellar luminosity, temperature, gravity and composition, so model atmospheres, or a combination of observed spectra and model atmospheres, are often used to construct stellar population models. The absorption–line strengths of synthetic spectra do not accurately represent those in observed stars with the same parameters. The fitting functions are empirically derived polynomials which express a measured stellar index as a function of surface temperature, surface gravity and [Fe/H]. Indices for a SSP are then calculated by integrating the contribution to the index from each star included in the population. The problem with using these fitting functions

to predict observed indices is that the polynomials are derived from stars with Galactic abundance ratios. There is significant evidence that elliptical galaxies have enhanced α-elements relative to iron *e.g.* Worthey, Faber & Gonzalez (1992).

5.2.1 Index definitions

There are two definitions of indices employed: those for narrow features usually due to atomic species which are referred to as atomic indices (I_a); and those for wider features due to molecular–band features which are referred to as molecular indices (I_m) (Gonzalez 1993).

$$I_a \equiv \int_{\lambda_{c1}}^{\lambda_{c2}} \left(1 - \frac{S(\lambda)}{C(\lambda)}\right) d\lambda \tag{5.1}$$

$$I_m \equiv -2.5 \log_{10} \frac{\int_{\lambda_{c1}}^{\lambda_{c2}} \frac{S(\lambda)}{C(\lambda)} d\lambda}{\lambda_{c1} - \lambda_{c2}} \tag{5.2}$$

where λ_{c1} and λ_{c2} are the limits of the central bandpass in Å, $S(\lambda)$ is the object spectrum and $C(\lambda)$ is the linearly interpolated pseudo–continuum. $C(\lambda)$ is defined such that

$$C(\lambda) \equiv S_b \frac{\lambda_r - \lambda}{\lambda_r - \lambda_b} + S_r \frac{\lambda - \lambda_b}{\lambda_r - \lambda_b} \tag{5.3}$$

where

$$\begin{aligned} S_b &\equiv \frac{\int_{\lambda_{b1}}^{\lambda_{b2}} S(\lambda) d\lambda}{\lambda_{b2} - \lambda_{b1}}, \qquad \lambda_b \equiv (\lambda_{b1} + \lambda_{b2})/2 \\ S_r &\equiv \frac{\int_{\lambda_{r1}}^{\lambda_{r2}} S(\lambda) d\lambda}{\lambda_{r2} - \lambda_{r1}}, \qquad \lambda_r \equiv (\lambda_{r1} + \lambda_{r2})/2 \end{aligned}$$

and λ_{b1}, λ_{b2}, λ_{r1} and λ_{r1} are the limits in the blue and red continuum regions respectively. The exact values for the bandpasses are given in table 5.1. Another feature also studied is the magnitude of the 4000Å break (Bruzual 1983; Gorgas *et al.* 1999). This is defined for historical reasons as:

$$D_{4000} \equiv \frac{\int_{4050}^{4250} S(\nu) d\lambda}{\int_{3750}^{3950} S(\nu) d\lambda} \equiv \frac{\int_{4050}^{4250} \lambda^2 S(\lambda) d\lambda}{\int_{3750}^{3950} \lambda^2 S(\lambda) d\lambda}. \tag{5.4}$$

There are also three more non–standard indices which are combinations of the previously defined ones, which were first introduced by Gonzalez (1993) in an

attempt to find a mean metallicity indicator:

$$< \mathrm{Fe} > = \frac{\mathrm{Fe5270} + \mathrm{Fe5335}}{2} \tag{5.5}$$

$$\mathrm{Fe_3} = \frac{\mathrm{Fe5270} + \mathrm{Fe5335} + \mathrm{Fe4383}}{3} \tag{5.6}$$

$$[\mathrm{MgFe}] = \sqrt{\mathrm{Mg}b < \mathrm{Fe} >} \tag{5.7}$$

Index Name	Central Bandpass	Continuum Bandpasses	Type	Origin
OII λ 3727	3695.000 – 3740.000	3665.000 – 3695.000	A	Gonzalez
		3750.000 – 3760.000		
D4000		3750.000 – 3950.000	B	Bruzual
		4050.000 – 4250.000		
$H\delta_A$	4083.500 – 4122.250	4041.600 – 4079.750	A	Worthey
		4128.500 – 4161.000		
$H\delta_F$	4091.000 – 4112.250	4057.250 – 4088.500	A	Worthey
		4114.750 – 4137.250		
CN1	4142.125 – 4177.125	4080.125 – 4117.625	M	Lick
		4244.125 – 4284.125		
CN_2	4142.125 – 4177.125	4083.875 – 4096.375	M	Lick
		4244.125 – 4284.125		
Ca 4227	4222.250 – 4234.750	4211.000 – 4219.750	A	Lick
		4241.000 – 4251.000		
$H\gamma_A$	4319.750 – 4363.500	4283.500 – 4319.750	A	Worthey
		4367.250 – 4419.750		
$H\gamma_F$	4331.250 – 4352.250	4283.500 – 4319.750	A	Worthey
		4354.750 – 4384.750		
Fe 4383	4369.125 – 4420.375	4359.125 – 4370.375	A	Lick
		4442.875 – 4455.375		
Ca 4455	4452.125 – 4474.625	4445.875 – 4454.625	A	Lick
		4477.125 – 4492.125		
Fe 4531	4514.250 – 4559.250	4504.250 – 4514.250	A	Lick
		4560.500 – 4579.250		
Fe 4668	4634.000 – 4720.250	4611.500 – 4630.250	A	Lick
		4742.750 – 4756.500		
$H\beta$	4847.875 – 4876.625	4827.875 – 4847.875	A	Lick
		4876.625 – 4891.625		
$H\beta_p$	4851.320 – 4871.320	4815.000 – 4845.000	A	Gonzalez
		4880.000 – 4930.000		
OIII λ 4959	4948.920 – 4978.920	4885.000 – 4935.000	A	Gonzalez
		5030.000 – 5070.000		
OIII λ 5007	4996.850 – 5016.850	4885.000 – 4935.000	A	Gonzalez
		5030.000 – 5070.000		
Fe 5015	4977.750 – 5054.000	4946.500 – 4977.750	A	Lick
		5054.000 – 5065.250		
Mg1	5069.125 – 5134.125	4895.125 – 4957.625	M	Lick
		5301.125 – 5366.125		
Mg2	5154.125 – 5196.625	4895.125 – 4957.625	M	Lick
		5301.125 – 5366.125		
Mgb	5160.125 – 5192.625	5142.625 – 5161.375	A	Lick
		5191.375 – 5206.375		
Fe 5270	5245.650 – 5285.650	5233.150 – 5248.150	A	Lick
		5285.650 – 5318.150		
Fe 5335	5312.125 – 5352.125	5304.625 – 5315.875	A	Lick
		5353.375 – 5363.375		
Fe 5406	5387.500 – 5415.000	5376.250 – 5387.500	A	Lick
		5415.000 – 5425.000		
Fe 5709	5696.625 – 5720.375	5672.875 – 5696.625	A	Lick
		5722.875 – 5736.625		
Fe 5782	5776.625 – 5796.625	5765.375 – 5775.375	A	Lick
		5797.875 – 5811.625		
Na5895	5876.875 – 5909.375	5860.625 – 5875.625	A	Lick
		5922.125 – 5948.125		
TiO_1	5936.625 – 5994.125	5816.625 – 5849.125	M	Lick
		6038.625 – 6103.625		

Table 5.1: Bandpass definitions for all the indices used, in order of increasing wavelength. Type A indicates an atomic index measured in Å, M a molecular index measured in magnitudes and B the 4000Å break. The origin of each index definition is given in the final column: the Lick indices are from Trager (1997), the Gonzalez emission features are from Gonzalez (1993), the Worthey Balmer features are from Worthey & Ottaviani (1997). The 4000Å break feature is as defined by Bruzual (1983).

5.2.2 Error estimation

There are many sources of error in the estimation of index values, both from photon noise, readout noise and systematic effects. The systematic effects are from a variety of sources such as incorrect skyline subtraction, wavelength calibration and radial velocity estimation which have all been investigated and quantified in chapter 3. The Lick/IDS library spectra have been flux calibrated using a tungsten lamp rather than a standard star which causes those indices with a broad bandpass, to be offset from those measured from CCD frames. Gonzalez (1993) calculates that around 0.017 mag needs to be added to the value of the Mg_2 index to account for this.

Gonzalez (1993) and Cardiel *et al.* (1998) have derived analytical expressions which can be used to calculate the random error in the index from knowledge of the photon and readout noise in each spectral bin. Both authors emphasize strongly the importance of creating error frames from the raw data and reducing the error and galaxy frames in parallel. This was attempted in the reduction of the spectra presented here, but owing to the "black box" nature of some of the reduction procedures in the IRAF software environment, it proved extremely tricky and unreliable. Eventually it was decided that the simplest solution was to use the RMS variation within a 5 pixel moving window as an estimate of the error in each pixel. These errors should be uncorrelated as all the pixels are independent. The equations used to calculate the errors are:

$$\sigma\left[I_a\right] = \frac{S_c}{C_c}\sqrt{\left(\frac{\sigma_{S_c}}{S_c}\right)^2 + \frac{\sigma_{S_b}^2}{C_c^2}\left(\frac{\lambda_r - \lambda_c}{\lambda_r - \lambda_b}\right)^2 + \frac{\sigma_{S_r}^2}{C_c^2}\left(\frac{\lambda_b - \lambda_c}{\lambda_r - \lambda_b}\right)^2} \tag{5.8}$$

$$\sigma\left[I_m\right] = \frac{2.5 \times 10^{0.4 I_m}}{2.3026(\lambda_{c_2} - \lambda_{c_1})}\sigma\left[I_a\right]. \tag{5.9}$$

where

$$\begin{aligned}
\lambda_c &\equiv (\lambda_{c_2} + \lambda_{c_1})/2 \\
C_c &\equiv C(\lambda_c) \\
S_c &\equiv \int_{\lambda_{c_1}}^{\lambda_{c_2}} S(\lambda) d\lambda \\
\left(\frac{\sigma_{S_c}}{S_c}\right)^2 &\equiv 1/\int_{\lambda_{c_1}}^{\lambda_{c_2}} \frac{S^2(\lambda)}{\sigma^2 \lambda} d\lambda \\
\sigma_{S_b}^2 &\equiv S_b^2/\int_{\lambda_{b_1}}^{\lambda_{b_2}} \frac{S^2(\lambda)}{\sigma^2 \lambda} d\lambda
\end{aligned}$$

$$\sigma^2_{S_r} \equiv S_r^2 / \int_{\lambda_{r_1}}^{\lambda_{r_2}} \frac{S^2(\lambda)}{\sigma^2 \lambda} d\lambda.$$

5.3 Measuring indices

A program was written to measure observed indices using the prescription outlined above. The pixels were considered as discrete points, sampling the integrated flux from $(\lambda_i - \Delta\lambda/2)$ to $(\lambda_i + \Delta\lambda/2)$, where $\Delta\lambda/2$ is the dispersion of the spectrum and λ_i the wavelength of pixel i. The contribution of a pixel which was contained only partly within a bandpass was considered to be proportional to the percentage of the pixel within it. The accuracy of the index measuring code was tested on sample spectra provided by Guy Worthey on his webpage[1] for exactly this purpose. The calculated index values were always found to agree with the published values to better than 2% and in most cases to better than 0.5%. Only the blue arm spectra were used in the index analysis as the large size of the CCD and the choice of dichroic and grating meant that the whole of the Lick spectral range fitted onto this chip.

5.3.1 Transformation to the Lick/IDS system

In order to compare like with like it is important to transform the data to the Lick/IDS system. A good summary of how to do this is provided by Worthey & Ottaviani (1997). Ideally, repeat observations of stars in the Lick library using the same instrument, setup and reduction as the galaxy spectra, are necessary to quantify the offset of each index from the Lick system and get a better handle on the systematic errors. Unfortunately this is not possible here as the necessity of these observations was not realised until after the observing run. However, Kuntschner (1998) did carry out this analysis and found zero or small offsets for all the indices except for Fe 4383 ($+0.60 \pm 0.13$) and the known case of Mg_2 ($+0.023 \pm 0.003$) mentioned previously. To account for this Gonzalez's estimate of 0.017 mag has been added to the final Mg_2 index results presented in section 5.3.3. Gonzalez (1993) also applied empirically calculated corrections for emission features (OIII) which appear within the central passbands of other features, such as Hβ and Fe 5015 whereby $\Delta H\beta \equiv 0.7$ [OIII] λ5007 and Δ Fe 5015 $\equiv 1.0$ [OIII] λ5007. This

[1] http://199.120.161.183:80/~worthey/html/system.html

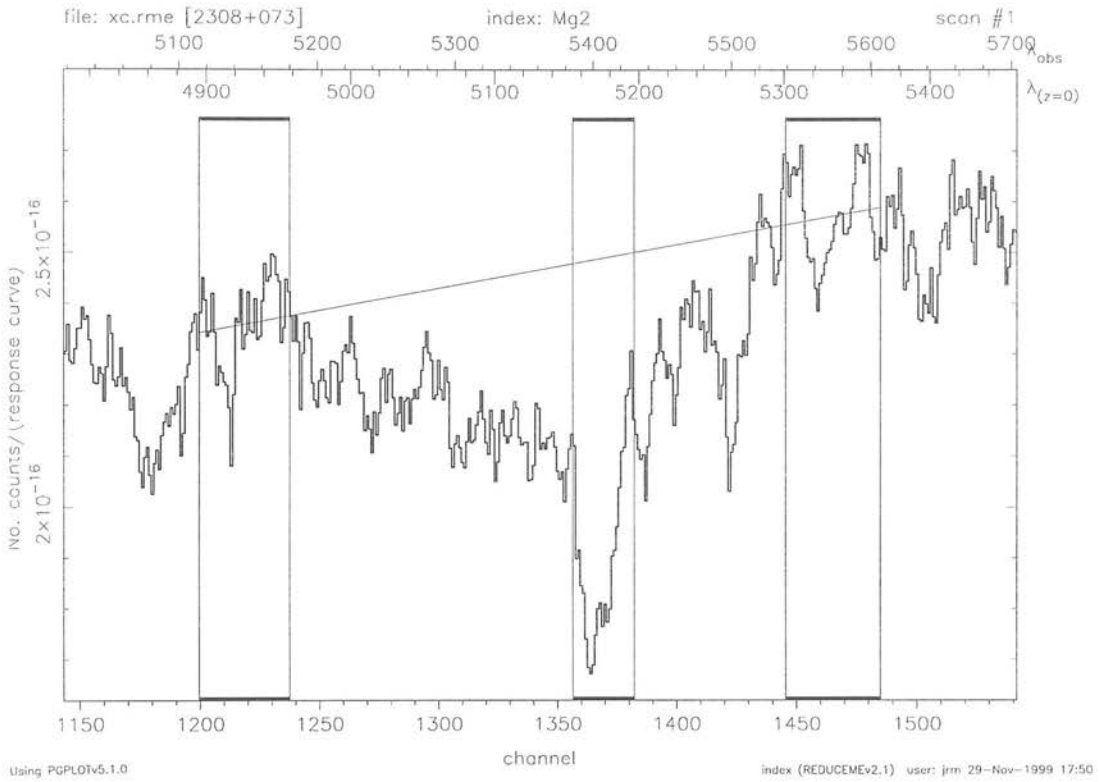

Figure 5.4: The Mg_2 index with the passbands overplotted as an example of an index measuring region.

correction has already been applied in the plots presented in section 5.4 but not to the index values given in section 5.3.3. In fact the necessity of this correction has been questioned by Carrasco *et al.* (1996), where they advise use of combinations of indices which are uncontaminated by emission, if at all possible.

It is also important to degrade the observed spectra to the resolution of the IDS detector. As mentioned in section 5.2 this is low and variable with wavelength, see table 5.2. Before the observed spectra and associated error spectra were smoothed to the Lick resolution, they were shifted to their rest–frame wavelength using the values calculated in section 3.6. The spectra were then put onto a log–wavelength scale and separated into five sections (<4200, 4200–4650, 4650–5150, 5150–5700, >5700) which represent as closely as possible the different resolution regions of the detector. Each of the regions were then smoothed independently to the resolution of the Lick detector using different width Gaussian filters.

The index values and random errors were then calculated from the smoothed spectra. The wavelength axis was then shifted by $\pm$ the error in the radial velocity estimation and the indices recalculated. The radial velocity error was

λ (Å)	FWHM (Å)
4000	11.5
4400	9.2
4900	8.4
5400	8.4
6000	9.8

Table 5.2: Wavelength dependent resolution of the Lick/IDS detector.

taken to be the average difference between these values and the original index value. All sources of error were then summed in quadrature.

5.3.2 Velocity dispersion correction

As mentioned in section 3.7 velocity broadening causes absorption features in galaxies to be broader than those from individual stars. Depending on the amount of broadening and width of the bandpasses this could cause the actual feature to creep into the neighbouring continuum bands, lowering the continuum level, or just causing the feature to appear weaker over the central band. As the Lick indices are originally calculated from stars with no broadening, it is necessary to correct all the index values for the effect of broadening. In the manner of Davies, Sadler & Peletier (1993) empirical correction factors, $C(\sigma)$, were calculated using the observations of late–type K and M stars taken at the same time as the galaxy spectra, which have spectra similar to that of elliptical galaxies. The late–type stars are assumed to have zero intrinsic velocity dispersion. The stellar spectra were first all smoothed to the Lick resolution, in the same manner as the galaxy spectra and then broadened again using a series of Gaussian filters in steps of 20 kms^{-1}. Indices were then calculated for all the smoothed and broadened spectra. The correction factor is

$$C(\sigma)_a = \frac{\mathrm{index}(O)}{\mathrm{index}(\sigma)} \tag{5.10}$$

for the atomic indices and

$$C(\sigma)_m = \mathrm{index}(O) - \mathrm{index}(\sigma) \tag{5.11}$$

for the molecular indices. The most deviant data point was removed and the final adopted correction factor curve was then calculated from the mean of the remaining correction factors. The actual correction for each index was calculated by interpolating the correction factor curve at the correct velocity dispersion

for the galaxy. The corrections were multiplicative for the atomic indices and additive for the molecular indices.

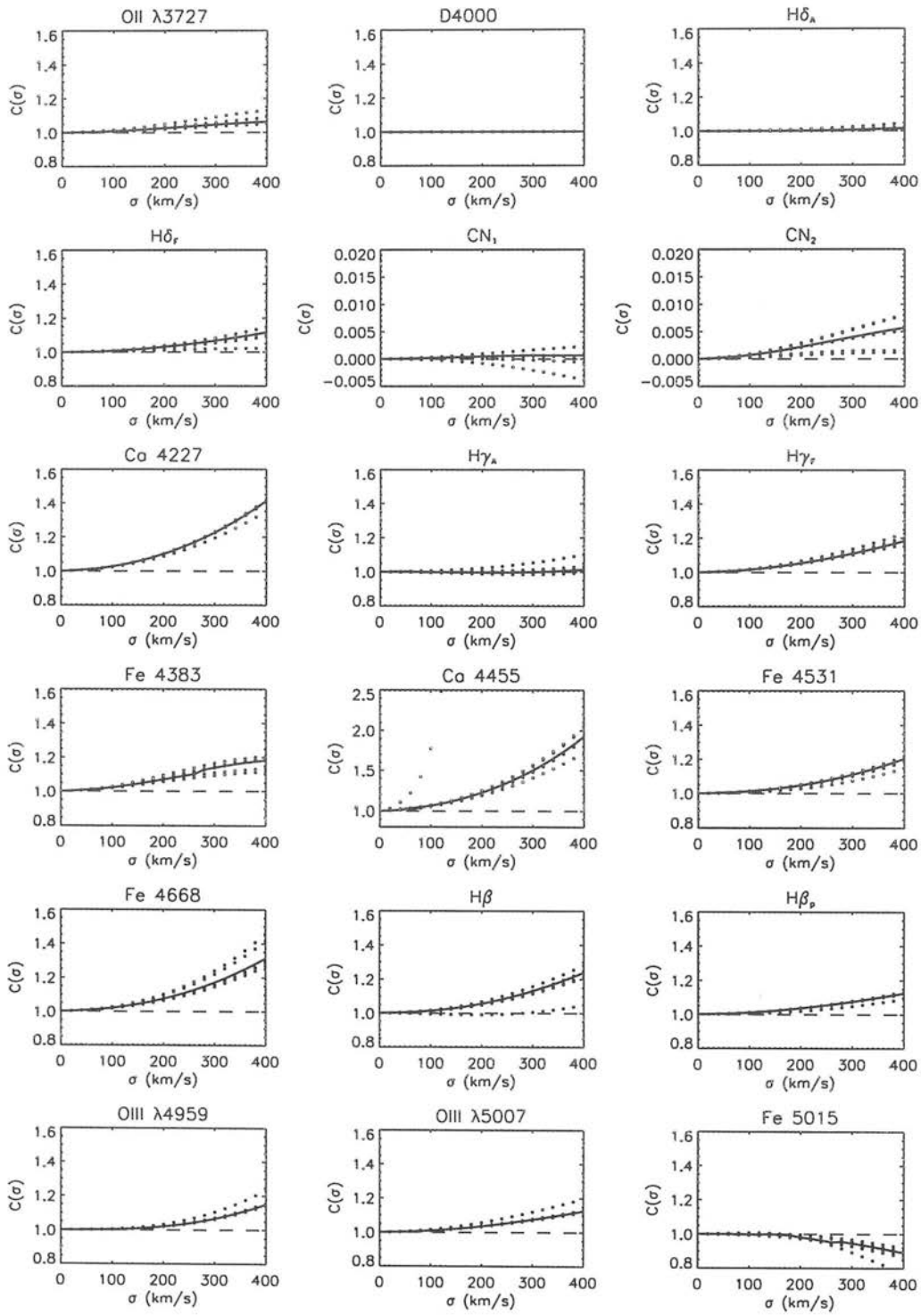

Figure 5.5: Velocity dispersion correction factors. The solid line represents the mean of all but the most deviant data point in each σ–bin.

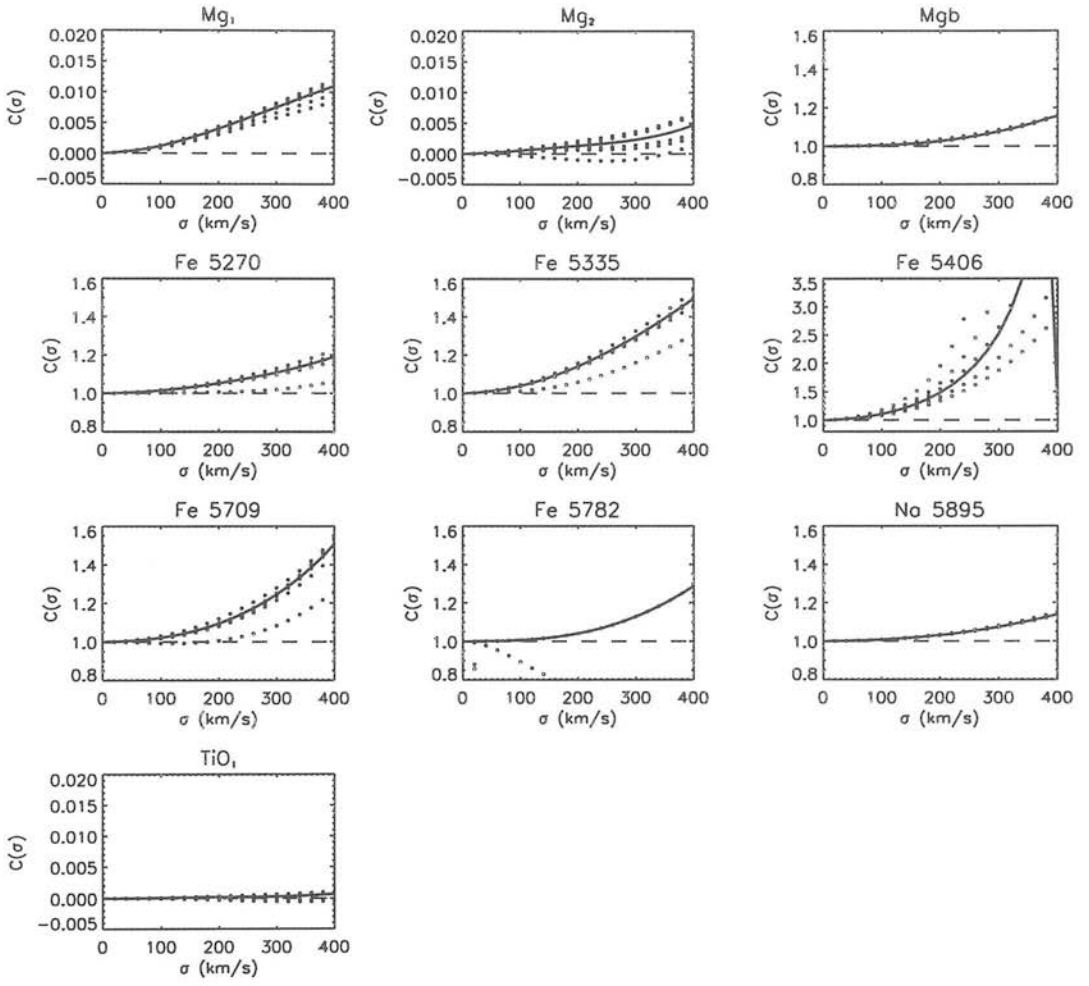

Figure 5.6: Velocity dispersion correction factors (*cont.*)

5.3.3 Final nuclear index measurements

Tables 5.3–5.5 give the full set of index values for central 0.6″ spectral extractions, which have been wavelength calibrated, flux calibrated and extinction corrected as discussed in chapter 3.

Index Name	0300+162	±	0325+023	±	0356+102	±	0419+140	±	0431−134	±	0502−103	±
OII λ 3727	−3.74	1.73	−50.33	22.90	−37.58	2.71	4.77	3.80	−0.23	1.02	−37.00	2.38
D4000	2.33	0.00	2.83	0.11	2.01	0.00	2.18	0.00	2.18	0.00	1.73	0.00
$H\delta_A$	0.52	0.52	−4.15	3.83	−3.55	0.27	−1.34	0.75	−1.01	0.32	3.62	0.35
$H\delta_F$	1.23	0.42	−4.73	2.68	−1.67	0.28	0.30	0.49	1.20	0.29	3.24	0.34
CN_1	0.016	0.012	0.012	0.906	0.113	0.007	0.180	0.026	0.080	0.010	−0.055	0.008
CN_2	0.068	0.017	−0.002	0.128	0.115	0.008	0.229	0.032	0.120	0.012	−0.041	0.010
Ca 4227	0.55	0.41	4.18	1.09	0.81	0.20	1.88	0.36	0.81	0.22	0.95	0.18
$H\gamma_A$	−8.23	0.58	−2.13	2.94	−11.29	0.87	−7.44	0.78	−6.58	0.39	0.47	0.30
$H\gamma_F$	−3.14	0.37	0.41	1.82	−4.27	0.59	−2.03	0.54	−2.09	0.22	1.28	0.16
Fe 4383	6.48	0.63	4.88	4.10	7.69	1.30	3.35	0.76	4.99	0.42	2.15	0.49
Ca 4455	1.65	0.34	1.48	1.22	0.44	0.31	1.21	0.53	1.31	0.24	0.29	0.17
Fe 4531	3.03	0.41	0.43	2.18	3.10	0.28	3.40	0.57	2.84	0.28	1.56	0.36
Fe 4668	4.93	0.59	5.33	3.45	4.44	0.35	6.23	0.81	7.39	0.31	2.82	0.40
$H\beta$	1.14	0.29	3.65	1.40	−3.59	0.35	1.02	0.39	1.09	0.14	−0.23	0.41
$H\beta_p$	1.47	0.18	2.23	1.02	−3.16	0.92	1.30	0.23	1.40	0.11	0.11	0.46
OIII λ 4959	−1.03	0.28	−0.60	1.26	−20.21	0.69	−1.61	0.30	−1.25	0.15	−0.26	0.20
OIII λ 5007	0.29	0.21	−6.50	1.27	−55.79	15.31	−0.76	0.21	0.01	0.10	−4.28	0.73
Fe 5015	4.38	0.64	−7.74	4.10	−22.57	0.92	1.35	0.54	3.27	0.33	−0.46	0.38
Mg1	0.143	0.006	0.215	0.030	0.238	0.004	0.118	0.007	0.160	0.004	0.076	0.005
Mg2	0.283	0.011	0.341	0.040	0.343	0.009	0.285	0.011	0.307	0.008	0.140	0.007
Mgb	3.78	0.43	2.25	1.62	4.58	0.44	4.26	0.42	4.80	0.34	3.17	0.39
Fe 5270	2.47	0.33	3.91	1.39	2.68	0.22	4.48	0.78	2.46	0.19	1.56	0.23
Fe 5335	2.04	0.43	2.64	1.63	2.74	0.33	1.57	0.53	2.35	0.26	1.72	0.28
Fe 5406	−1.39	0.49	−3.08	1.81	1.76	0.18	2.41	0.33	2.15	0.19	0.88	0.16
Fe 5709	−1.23	0.46	−0.06	2.17	0.81	0.15	0.93	0.26	0.13	0.15	0.82	0.19
Fe 5782	0.36	0.17	2.44	1.57	0.45	0.13	0.25	0.25	0.80	0.14	0.64	0.18
Na5895	4.21	0.37	1.57	2.37	3.87	0.34	0.58	0.82	4.49	0.32	3.92	0.48
TiO_1	−0.003	0.005	0.040	0.071	0.087	0.003	−0.123	0.065	0.130	0.005	0.246	0.009

Table 5.3: Final index values for the entire RG spectroscopy sample.

Index Name	0755+379	±	0833−016	±	1004+146	±	2221−023	±	2229−086	±	2243−394	±
OII λ 3727	−9.61	0.95	−5.58	1.28	−6.70	1.18	−8.38	0.43	−1.38	1.07	−58.00	3.18
D4000	1.91	0.00	2.34	0.00	2.35	0.00	1.07	0.00	2.32	0.00	2.01	0.00
Hδ_A	−0.81	0.22	0.16	0.33	−1.10	0.28	−4.33	0.24	−3.60	0.29	−2.84	0.34
Hδ_F	0.39	0.17	−0.10	0.25	−1.32	0.22	−2.53	0.25	−0.42	0.20	−0.57	0.23
CN_1	0.103	0.006	0.014	0.008	0.059	0.007	0.113	0.005	0.113	0.010	0.097	0.008
CN_2	0.128	0.007	0.064	0.012	0.096	0.012	0.112	0.006	0.119	0.011	0.104	0.011
Ca 4227	0.84	0.13	1.34	0.20	1.07	0.21	−0.11	0.13	0.64	0.21	0.61	0.22
Hγ_A	−6.07	0.31	−9.22	0.41	−7.99	0.46	−17.45	0.65	−3.51	0.33	−9.73	0.67
Hγ_F	−2.89	0.17	−3.33	0.19	−2.72	0.24	−4.61	0.61	−1.95	0.20	−4.76	0.56
Fe 4383	4.31	0.36	7.26	0.41	6.12	0.51	12.17	0.98	2.06	0.48	4.38	0.79
Ca 4455	0.63	0.19	1.77	0.30	0.76	0.26	−0.14	0.15	0.47	0.28	−0.36	0.29
Fe 4531	3.04	0.23	3.45	0.31	2.99	0.27	0.30	0.28	3.35	0.32	2.69	0.34
Fe 4668	6.92	0.22	6.37	0.38	7.07	0.45	−8.34	0.47	8.33	0.45	6.68	0.41
Hβ	0.20	0.14	1.25	0.16	1.60	0.14	−6.81	0.62	1.80	0.21	−3.33	0.34
Hβ_p	0.39	0.12	1.60	0.012	1.67	0.10	−7.50	0.77	1.66	0.15	−2.89	0.63
OIII λ 4959	−3.02	0.13	−1.56	0.16	−0.93	0.17	−29.40	1.46	−1.60	0.16	−11.45	0.54
OIII λ 5007	−4.63	0.35	0.41	0.10	0.68	0.12	−96.30	17.08	−0.08	0.17	−30.90	4.19
Fe 5015	−2.61	0.31	3.04	0.29	3.33	0.32	−44.46	2.82	3.25	0.49	−18.29	1.00
Mg1	0.170	0.003	0.156	0.004	0.177	0.004	0.381	0.004	0.150	0.005	0.228	0.004
Mg2	0.287	0.006	0.300	0.007	0.345	0.009	0.288	0.007	0.326	0.010	0.311	0.013
Mgb	4.21	0.26	4.39	0.28	4.61	0.35	1.02	0.27	4.42	0.37	4.80	0.50
Fe 5270	2.32	0.16	2.38	0.17	2.77	0.26	−0.92	0.18	3.01	0.30	2.42	0.28
Fe 5335	1.95	0.25	2.41	0.24	1.72	0.24	0.58	0.24	2.38	0.32	2.39	0.32
Fe 5406	1.78	0.14	−0.07	0.25	2.49	0.18	0.32	0.17	1.51	0.25	1.01	0.20
Fe 5709	0.92	0.15	−0.51	0.18	0.62	0.11	0.24	0.17	0.22	0.16	0.76	0.25
Fe 5782	0.42	0.09	0.51	0.15	0.29	0.16	0.10	0.09	0.39	0.28	−0.55	0.42
Na5895	3.83	0.26	4.12	0.29	4.78	0.37	3.42	0.25	7.07	4.15	12.04	2.30
TiO_1	0.237	0.004	−0.037	0.005	−0.004	0.005	−0.71	0.009				

Table 5.4: Final index values continued.

Index Name	2308+073	±
OII λ 3727	−0.48	0.84
D4000	2.34	0.00
$H\delta_A$	−2.25	0.22
$H\delta_F$	−0.28	0.21
CN_1	0.090	0.006
CN_2	0.121	0.011
Ca 4227	1.12	0.21
$H\gamma_A$	−6.35	0.35
$H\gamma_F$	−2.04	0.19
Fe 4383	4.61	0.32
Ca 4455	1.23	0.22
Fe 4531	3.49	0.23
Fe 4668	8.13	0.24
$H\beta$	1.40	0.13
$H\beta_p$	1.66	0.11
OIII λ 4959	−0.96	0.10
OIII λ 5007	0.48	0.07
Fe 5015	3.83	0.29
Mg1	0.155	0.003
Mg2	0.308	0.007
Mgb	4.16	0.26
Fe 5270	2.69	0.15
Fe 5335	2.19	0.17
Fe 5406	2.23	0.16
Fe 5709	0.90	0.11
Fe 5782	0.57	0.12
Na5895	4.19	0.29
TiO_1	0.156	0.005

Table 5.5: Final index values continued.

5.4 Age and metallicity estimates from indices

To break the age/metallicity degeneracy combinations of indices need to be found which are nearly orthogonal to each other in age and metallicity space. Gonzalez (1993) found $H\beta$ to be a good age indicator and [MgFe] a good metallicity indicator. They are plotted together in figure 5.7 with the index values from the Worthey (1994) models overplotted in a grid. The correction for emission has been included in the $H\beta$ values. The metallicity in these grids is given in units of [Fe/H] where $\log\left(\frac{Z}{0.02}\right) = x\,[Fe/H]$, or $Z = 10^x \times 0.02$. For the rest of this chapter absolute metallicities will always be used, so a conversion between the two systems is given in table 5.6.

As the nuclear radio galaxy spectra do contain significant narrow-line emission, the emission contamination is quite high. It would be better to find combinations of indices which are less affected by emission. Kuntschner & Davies (1998) have

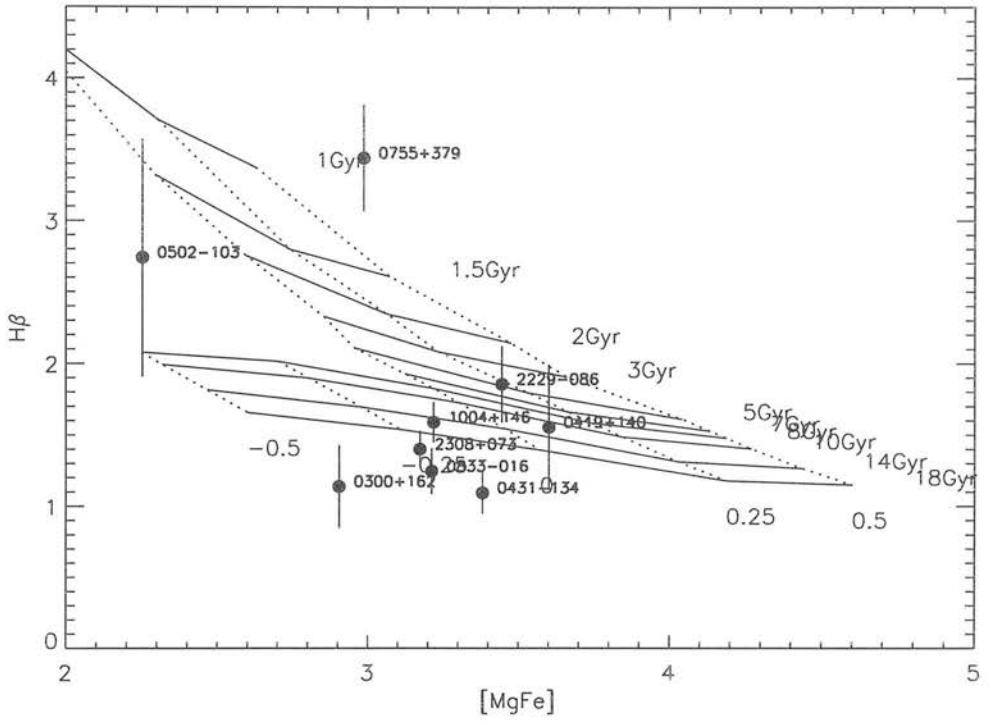

Figure 5.7: Hβ versus MgFe for the entire spectroscopy sample. Overplotted are single age, single metallicity models from Worthey, (1994). The metallicity is given in units of [Fe/H]. The Hβ values have been corrected for emission as detailed in section 5.3.1.

x [Fe/H]	Z
−0.50	0.006
−0.25	0.011
0.00	0.02 ($Z_\odot$)
0.25	0.036
0.50	0.063

Table 5.6: Conversion between metallicity units.

investigated another combination of indices: Fe 4668 and Hγ_A. Fe 4668 is also often referred to as $C_2$4668 as it has been found that the index is more sensitive to the carbon abundance than the iron abundance (Trager *et al.* 1998). These are plotted in figure 5.8 with the model predictions overplotted. Many of the points still lie outwith the grid, which is an indication that emission is still contaminating the index. Kuntschner & Davies (1998) state that although the absolute age calibration may not be correct, the relative ages implied by the plot still hold. 0502−103 is a galaxy which can be seen to be in the process of merging from the

K band image and is also a member of the Arp's catalogue of peculiar galaxies, most of which have turned out to be merging galaxies. The merger has caused a burst of new star formation which lowers the luminosity weighted age of the galaxy by outshining the older stellar population.

The final age and metallicity estimates are found by interpolating the grid in figure 5.8 at the position of the galaxy index value.

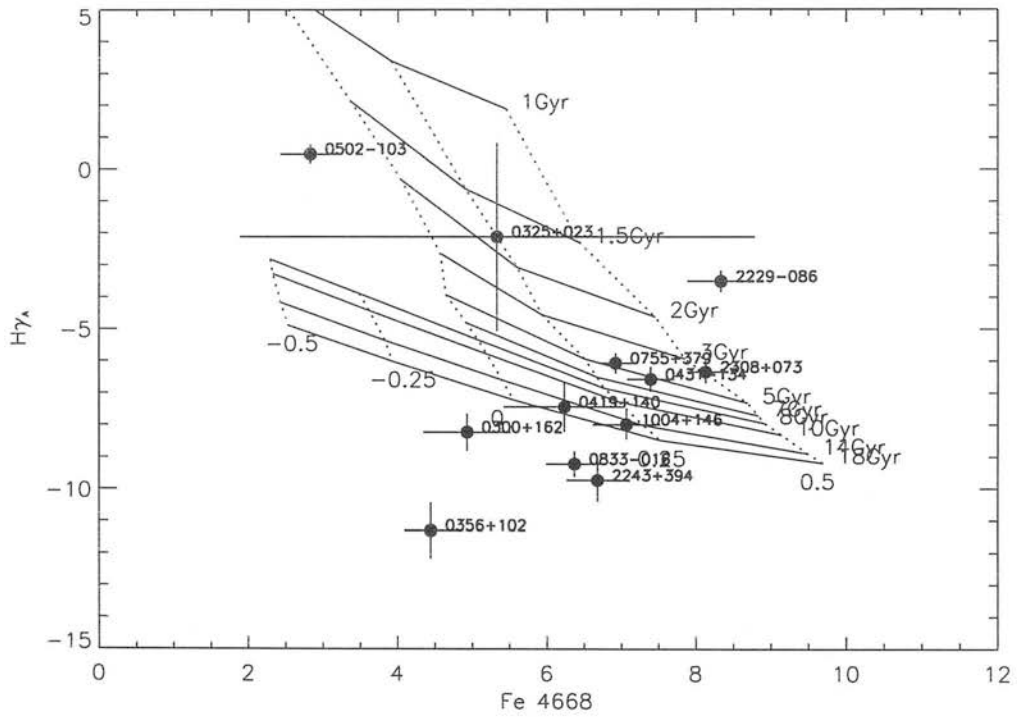

Figure 5.8: $H\gamma_A$ versus Fe 4668 for the entire spectroscopy sample. Overplotted are single age, single metallicity models from Worthey, (1994). The metallicity is given in units of [Fe/H].

5.5 Continuum age and metallicity estimates

The whole optical continuum has been fitted with both the Worthey (1994) models and Jimenez *et al.* (1999) SSP models for a selection of radial extractions of each object. Although it has previously been mentioned that the strength of stellar population modelling is the ability to construct composite stellar populations from adding various SSPs together; in practice single–age SSPs provided a good

fit. Fitting CSPs constructed mainly from a single old stellar population with a small percentage (0.01 – 5%) of newer (1 Gyr) stars was carried out, but the extra parameter space did not change the following conclusions and only increased the degeneracy between the parameters. Similar comments apply to evolutionary stellar population modelling, with stellar populations constructed from exponentially decreasing star–formation rates and gradually increasing metallicities.

The spectra have been extracted radially in 0.6″ apertures either side of the nucleus. Apart from the case of 0502−103 where significant rotation was observed (see section 3.6.2), the radial extractions equidistant from the nucleus on each side have been summed to create an average spectrum of the object at that radius. The blue and red arm spectra have also been combined, to enable fitting of as much of the continuum as possible, in a similar manner to that described in section 3.8. The spectra were then resampled at the resolution of the models by taking the mean value of the pixels within each new larger wavelength bin. The error on the new rebinned points was taken to be standard error on the mean in each of the bins. As in the index analysis it is important to compare like with like, so technically it is also necessary to broaden the models to account for the velocity dispersion of the galaxy. This has not been done here as it was found that the spectral resolution of the models is coarse enough (between 10 and 20 Å) to be insensitive to the velocity dispersion.

The Jimenez *et al.* (1999) models are produced at 1 Gyr intervals in the range 0–14 Gyr, and at metallicities of Z=0.0002, 0.004, 0.02, 0.05 and 0.1. Z=0.02 is solar metallicity, so therefore the range is from $0.01Z_{\odot}$to $5Z_{\odot}$. The Worthey (1994) models are produced for the parameter space shown in Figures 5.7 and 5.8. The models have been interpolated at 0.5 Gyr intervals and approximately equal intervals in log Z to construct intermediate age and metallicity models. Owing to the restricted size of the parameter space it was computationally feasible to estimate the best fit by calculating the value of χ^2 at each point in the grid and taking the minimum. Figure 5.9 shows the whole χ^2 map for a fit. The contours have been normalised so that the minimum occurs at a value of $\chi^2 = 1$. The degeneracy between age and metallicity can clearly be seen as a valley running diagonally across the centre. Rather than taking the position of the minimum value of χ^2 as indicative of the absolute age and composition in the observed valley, it is probably more informative in this analysis to say that the best guess lies somewhere within the central "banana" shaped contour. However, the stellar

population used to estimate the infrared colour of the nucleus was that given by the minimum value of χ^2.

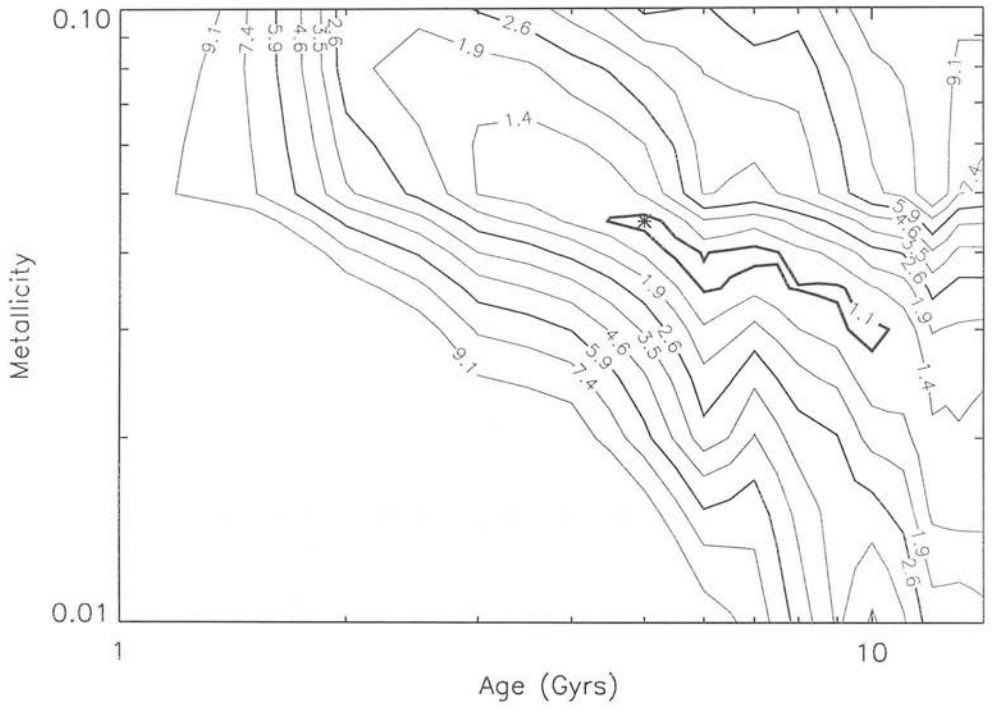

Figure 5.9: A χ^2 map of age and metallicity for the 1st radial extraction of 2308+073. The χ^2 contours are in units of the minimum value, the age/metallicity degeneracy can clearly be seen.

Tables 5.7–5.18 give the age and metallicity estimates from consecutive 0.6″ apertures for both sets of model SSPs. The second and third columns give the age and metallicity of the best fit SSP for each extraction, whilst the final column gives the best fit age model when the metallicity is forced to be the same as solar. This is more informative as it allows a gradient in age to be seen across the galaxy with the central regions appearing older. In fact it is more common to find a gradient in metallicity across an elliptical galaxy as measured by radial gradients in metal–sensitive indices across a galaxy (*e.g.* Carollo, Danziger & Buson 1993, Fisher, Franx & Illingworth 1996 and Kobayashi & Arimoto 1999). A galaxy can then be considered as coeval with the central regions being more metal–rich. 2221−023 is not presented below as its broad–line emission spectrum completely swamps the spectrum of any old stellar population and makes the model fitting

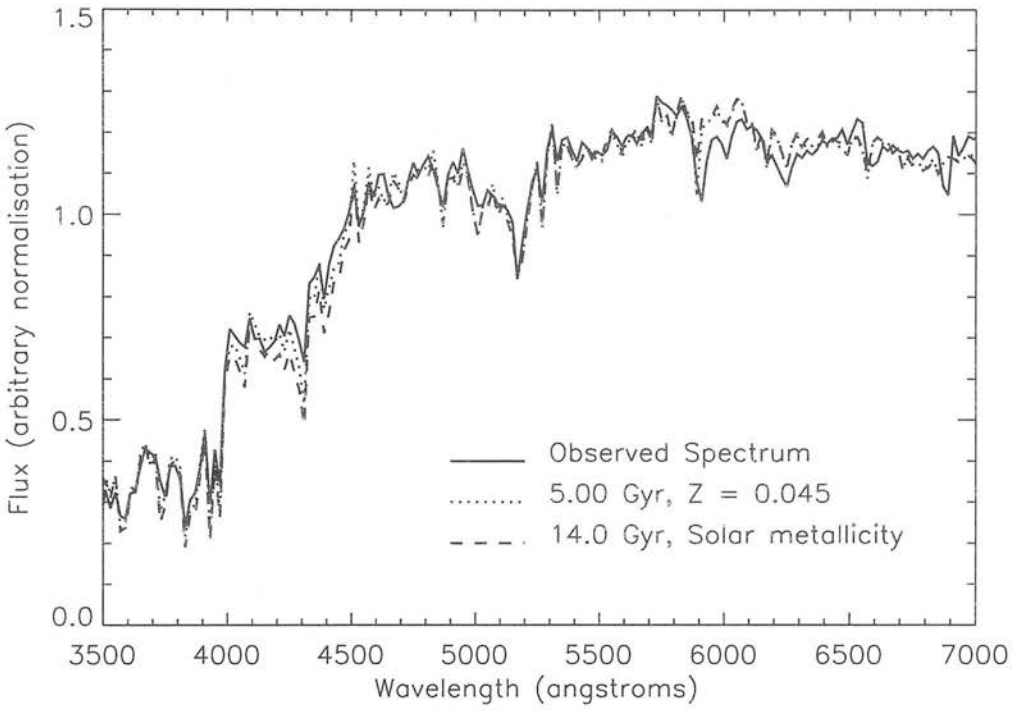

Figure 5.10: Rebinned observed spectrum and best fitting SSPs for the 1st radial extraction of 2308+073. The SSPs shown are the best fit when age and metallicity are free parameters and the best fit age when the metallicity is kept at the solar value.

procedure unreliable.

Aperture Number	Jimenez Models Z	Age [Gyr]	$Age_{Z_\odot}$ [Gyr]	Worthey Models Z	Age [Gyr]	$Age_{Z_\odot}$ [Gyr]
Nucleus	0.02	12.0	12.0	0.04	3.5	9.0
1	0.02	12.0	12.0	0.045	3.0	8.0
2	0.035	9.0	12.0	0.035	3.5	7.0
3	0.015	12.5	10.5	0.0112	9.0	5.0
4	0.015	11.0	9.5	0.03	2.0	2.5
5	0.015	11.0	9.5	0.03	2.0	2.5
6	0.03	7.0	9.5	0.02	2.5	2.5

Table 5.7: 0300+162 age and metallicity estimates

Aperture Number	Jimenez Models Z	Age [Gyr]	Age$_{Z_\odot}$ [Gyr]	Worthey Models Z	Age [Gyr]	Age$_{Z_\odot}$ [Gyr]
Nucleus	0.1	1.5	7.0	0.03	1.0	1.5
1	0.04	12.5	13.0	0.0112	15.5	8.0
2	0.004	13.0	7.0	0.02	2.0	2.0
3	0.02	7.5	7.5	0.0632	1.0	2.0
4	0.02	4.0	4.0	0.03	1.0	1.5

Table 5.8: 0325+023 age and metallicity estimates

Aperture Number	Jimenez Models Z	Age [Gyr]	Age$_{Z_\odot}$ [Gyr]	Worthey Models Z	Age [Gyr]	Age$_{Z_\odot}$ [Gyr]
Nucleus	0.045	5.5	14.0	0.0112	17.0	8.5
1	0.04	7.0	14.0	0.0112	17.0	6.5
2	0.035	5.0	9.5	0.03	2.0	2.5
3	0.04	4.0	9.0	0.025	2.0	2.0
4	0.035	4.0	6.5	0.02	2.0	2.0
5	0.03	4.0	7.0	0.05	1.5	2.0
6	0.015	9.0	6.0	0.02	2.0	2.0
7	0.02	5.0	5.0	0.04	1.5	2.0

Table 5.9: 0356+102 age and metallicity estimates

Aperture Number	Jimenez Models Z	Age [Gyr]	Age$_{Z_\odot}$ [Gyr]	Worthey Models Z	Age [Gyr]	Age$_{Z_\odot}$ [Gyr]
Nucleus	0.02	7.0	7.0	0.04	1.5	2.0
1	0.04	4.5	10.0	0.02	2.5	2.5
2	0.04	4.0	6.0	0.02	2.0	2.0
3	0.04	2.0	5.0	0.03	1.5	1.5
4	0.01	11.5	6.0	0.02	2.0	2.0

Table 5.10: 0419+140 age and metallicity estimates

Aperture Number	Jimenez Models			Worthey Models		
	Z	Age [Gyr]	Age$z_\odot$ [Gyr]	Z	Age [Gyr]	Age$z_\odot$ [Gyr]
Nucleus	0.03	10.0	14.0	0.0112	14.0	7.5
1	0.015	13.0	11.5	0.0112	10.0	5.5
2	0.035	7.0	10.5	0.02	5.0	5.0
3	0.045	3.5	10.0	0.03	2.5	4.0
4	0.02	7.5	7.5	0.06	1.5	2.0
5	0.02	7.5	7.5	0.0632	1.5	2.0
6	0.02	7.0	7.0	0.055	1.5	2.0

Table 5.11: 0431−134 age and metallicity estimates

Aperture Number	Jimenez Models			Worthey Models		
	Z	Age [Gyr]	Age$z_\odot$ [Gyr]	Z	Age [Gyr]	Age$z_\odot$ [Gyr]
Nucleus	0.004	7.5	4.5	0.035	1.5	2.0
l1	0.004	7.5	4.5	0.035	1.5	2.0
l2	0.004	7.5	3.0	0.03	1.5	2.0
l3	0.004	8.0	5.0	0.02	2.0	2.0
l4	0.004	9.0	6.0	0.02	2.5	2.5
l5	0.004	8.5	5.5	0.02	2.0	2.0
l6	0.004	7.5	4.5	0.035	1.5	2.0
l7	0.004	7.0	3.0	0.025	1.5	1.5
l8	0.004	7.5	5.0	0.035	1.5	2.0
l9	0.004	9.0	6.0	0.02	2.0	2.0
l10	0.007	6.5	3.0			
r1	0.004	7.0	3.0	0.035	1.5	2.0
r2	0.001	9.0	2.0	0.025	1.5	1.5
r3	0.001	9.0	2.0	0.02	1.5	1.5
r4	0.004	8.0	5.0	0.035	1.5	2.0
r5	0.04	5.0	10.0	0.02	2.5	2.5
r6	0.04	4.5	10.0	0.02	2.0	2.0
r7	0.004	8.5	5.5	0.03	1.5	1.5
r8	0.004	8.5	5.5	0.035	1.5	2.0
r9	0.004	7.0	3.0	0.03	1.5	1.5
r10	0.004	7.0	3.0	0.025	1.5	1.5

Table 5.12: 0502−103 age and metallicity estimates

Aperture Number	Jimenez Models			Worthey Models		
	Z	Age [Gyr]	$Age_{Z_\odot}$ [Gyr]	Z	Age [Gyr]	$Age_{Z_\odot}$ [Gyr]
Nucleus	0.01	12.0	10.0	0.0112	8.0	2.5
1	0.015	14.0	10.0	0.0112	10.5	5.5
2	0.03	9.5	11.5	0.015	8.5	6.0
3	0.04	7.0	14.0	0.0112	12.5	6.5
4	0.03	10.0	14.0	0.0112	12.5	6.5
5	0.035	6.5	11.5	0.0112	9.5	5.0
6	0.04	7.0	14.0	0.0112	11.5	6.0
7	0.035	7.0	11.0	0.0112	8.0	5.0
8	0.015	12.5	11.0	0.03	2.5	4.0
9	0.015	13.0	10.5	0.0112	9.0	5.0

Table 5.13: 0755+379 age and metallicity estimates

Aperture Number	Jimenez Models			Worthey Models		
	Z	Age [Gyr]	$Age_{Z_\odot}$ [Gyr]	Z	Age [Gyr]	$Age_{Z_\odot}$ [Gyr]
Nucleus	0.02	11.5	11.5	0.035	3.0	6.5
1	0.02	11.5	11.5	0.035	3.0	6.0
2	0.02	11.0	11.0	0.035	2.5	5.0
3	0.045	3.0	9.5	0.035	2.0	5.0
4	0.045	3.5	10.5	0.0112	8.0	5.0
5	0.045	3.0	9.0	0.0632	1.5	2.5
6	0.025	7.0	8.0	0.0632	1.5	2.0
7	0.025	7.0	8.5	0.055	1.5	2.0

Table 5.14: 0833−016 age and metallicity estimates

Aperture Number	Jimenez Models			Worthey Models		
	Z	Age [Gyr]	$Age_{Z_\odot}$ [Gyr]	Z	Age [Gyr]	$Age_{Z_\odot}$ [Gyr]
Nucleus	0.06	3.5	12.0	0.04	3.0	6.5
1	0.05	3.5	11.5	0.035	3.0	6.0
2	0.06	3.0	11.5	0.035	2.5	5.0
3	0.02	11.0	11.0	0.035	2.5	5.0
4	0.02	9.0	9.0	0.0632	1.5	2.0
5	0.02	9.0	9.0	0.0632	1.5	2.0
6	0.02	8.5	8.5	0.055	1.5	2.0
7	0.02	7.5	7.5	0.055	1.5	2.0
8	0.02	7.5	7.5	0.055	1.5	2.0
9	0.1	1.5	4.5	0.06	1.0	1.5

Table 5.15: 1004+146 age and metallicity estimates

Aperture Number	Jimenez Models Z	Age [Gyr]	$Age_{Z_\odot}$ [Gyr]	Worthey Models Z	Age [Gyr]	$Age_{Z_\odot}$ [Gyr]
Nucleus	0.05	3.0	11.0	0.035	2.5	5.0
1	0.06	2.5	9.5	0.0632	1.5	5.0
2	0.045	3.0	9.5	0.03	2.0	2.5
3	0.06	2.0	9.0	0.0632	1.5	2.5
4	0.045	3.0	9.5	0.03	2.0	4.5
5	0.045	2.5	7.0	0.05	1.5	2.0

Table 5.16: 2229−086 age and metallicity estimates

Aperture Number	Jimenez Models Z	Age [Gyr]	$Age_{Z_\odot}$ [Gyr]	Worthey Models Z	Age [Gyr]	$Age_{Z_\odot}$ [Gyr]
Nucleus	0.04	7.0	11.5	0.0112	14.0	7.0
1	0.03	10.0	14.0	0.0112	16.0	16.0
2	0.01	13.0	9.5	0.0112	8.0	8.0
3	0.004	13.0	7.0	0.02	2.0	2.0
4	0.007	10.0	5.0	0.035	1.5	1.5
5	0.004	10.0	4.0	0.03	1.5	1.5

Table 5.17: 2243+394 age and metallicity estimates

Aperture Number	Jimenez Models Z	Age [Gyr]	$Age_{Z_\odot}$ [Gyr]	Worthey Models Z	Age [Gyr]	$Age_{Z_\odot}$ [Gyr]
Nucleus	0.045	5.5	13.5	0.0112	16.5	8.0
1	0.045	5.0	14.0	0.0112	12.5	6.5
2	0.035	7.0	10.5	0.0112	9.0	5.0
3	0.04	5.0	10.0	0.0112	8.5	4.5
4	0.035	5.5	10.0	0.0112	8.0	4.0
5	0.015	12.5	10.0	0.0112	10.0	5.5
6	0.015	12.0	11.5	0.0112	9.0	5.0
7	0.03	10.0	12.0	0.0112	12.5	6.5
8	0.015	12.5	12.0	0.0112	9.5	5.0
9	0.03	10.0	11.5	0.0112	11.5	6.0
10	0.015	12.5	11.0	0.0112	9.0	5.0

Table 5.18: 2308−073 age and metallicity estimates

5.6 Predicting infrared colours

Having estimated the best fitting nuclear stellar population it is now important to see the infrared colours predicted by these models. Broad-band magnitudes are calculated by integrating the spectral energy distributions of the models in the filter of choice, using the definition of a magnitude given in equation 4.10. The wavelength of the models are shifted bluewards by a factor of $(1 + z)$ to the observed wavelength to ensure that the filter samples correctly the emitted region of the spectrum for each galaxy. Calibrated K and L' magnitudes are not available for each model as the spectra were not photometrically fluxed, but this does not affect the $K - L'$ colour of the model. This is identical to the procedure used to calculate the $K - L'$ colour of the models in figure 5.1.

Table 5.19 gives the $K-L'$ colour of the model predicted from index measurements and continuum fitting for each nuclear spectrum.

		Worthey Models		Jimenez Models
Object	z	Index Fitting	Continuum Fitting	
0300+162	0.0326	0.184	0.187	0.228
0325+023	0.0302	0.164	0.153	0.403
0356+102	0.0306	0.179	0.181	0.481
0419+140	0.0643	0.215	0.080	0.245
0431−134	0.0364	0.200	0.174	0.376
0502−103	0.0394	0.157	0.161	0.221
0755+379	0.0413	0.190	0.161	0.221
0833−016	0.0300	0.203	0.181	0.233
1004+146	0.0294	0.233	0.186	0.485
2229−086	0.0826	0.196	0.177	0.447
2243+394	0.0806	0.205	0.181	0.480
2308+073	0.0441	0.196	0.178	0.485

Table 5.19: Estimated $K - L'$ colour of the nuclear stellar populations from 3 methods: index fitting of Worthey's models and continuum fitting of Worthey's and Jimenez's models.

The next step is to investigate the stellar contribution to the measured L' flux, by using an estimate of the stellar K band flux and the $K - L'$ values estimated above. The stellar K band flux can be estimated in two ways: either from the K band model fits ($\hat{K}_*$) or from photometry of the observed image ($K_{\rm obs}$). From figure 5.1 at the beginning of the chapter it can be seen that Cygnus A shows an

infrared excess above the model limits, though it did not show evidence for an unresolved nuclear excess at K from the model fits in chapter 4. This is probably accounted for by a central dust lane, which attenuates the K band flux more than the L' flux, thereby making the colour index appear redder. Use of the model fits could therefore reconstruct correctly the galaxy profiles in the absence of central dust lanes, assuming an $r^{1/4}$ surface brightness profile represents the true galaxy profile. Alternatively use of the observed K band nuclear magnitude places a model independent upper limit on the stellar K band nuclear flux which can then be used to infer an upper limit on the stellar L' value, with any excess being securely attributed to a reddened quasar continuum. Stellar L' values have therefore been deduced in both ways. The value of the $K - L'$ colour is taken to be that deduced from the continuum fits with the Jimenez *et al.* (1999) models as they predict the reddest colours and as explained in section 5.1.1 provide the most accurate prediction of the infrared stellar populations. For those galaxies where spectra are not available, a $K - L'$ colour of 0.5 is assumed, which is around the reddest value predicted here.

Table 5.20 shows the predicted stellar L' magnitudes and, for comparison, the observed magnitude, to deduce whether a secure infrared excess can be detected. The surprising result from this table is the accuracy with which it has been possible to detect the galaxy at L' in cases where there is obviously no excess. The observed L' colours have been predicted in most cases within the errors. Those galaxies for which a secure excess can be inferred are marked with a "yes" in the final column. The magnitude of the $L'_{\rm nuc}$ component has been calculated by subtracting the estimated flux of the stellar component in column 4 from the observed flux value and then converting the flux to magnitudes. It is interesting to note that excesses have been found in all FR II sources for which L' observations are available, whilst excesses have only been found in only two out of the remaining twenty FR I sources.

5.7 Revised extinction estimates

Table 5.21 gives the revised extinction estimates for those galaxies with an infrared excess detected at L', presented in a similar manner to table 4.8. The object 2221−023 has been excluded from the table as the nuclear K and L' magnitudes are both upper limits as the source was bright enough to saturate at both

Object	$K-L'_\star$	$\hat{K}_\star$	$\hat{L}'_\star$	$K_{\rm obs}$	$L'^{\rm max}_\star$	$L'_{\rm obs}$	Excess?	$L'_{\rm nuc}$
0055−016	0.50	13.04	12.54	13.41	12.91	12.91	no	
0106+130	0.50	13.49	12.99	13.24	12.74	11.73	yes	12.14
0206+355	0.50			12.33	11.83	11.75	no	
0207+095	0.50	13.54	13.04	13.50	13.00	12.96	no	
0217+017	0.50	12.97	12.27	12.70	12.20	12.28	no	
0300+162	0.23	13.27	13.04	12.96	12.73	13.05	no	
0325+023	0.40	13.43	13.03	13.24	12.84	12.45	yes	13.41
0356+102	0.48	13.12	12.64	12.95	12.47	11.95	yes	12.77
0419+140	0.25	13.59	13.34	13.40	13.15	13.43	no	
0431−134	0.38	12.84	12.46	12.97	12.59	12.33	yes	12.67
0502−103	0.20	12.85	12.65	12.92	12.72	11.92	yes	12.69
0755+379	0.22	12.41	12.19	12.55	12.33	12.37	no	
1040+317	0.50	13.48	12.98	13.44	12.94	13.33	no	
1131+493	0.50	12.31	11.81	12.38	11.88	12.49	no	
1132+492	0.50	12.68	12.18	13.59	13.09	12.65	no	
1309+210	0.50	11.98	11.48	12.14	11.64	11.72	no	
1350+316	0.50	13.02	12.52	13.00	12.50	12.48	no	
1422+268	0.50	13.57	13.07	13.16	12.66	13.15	no	
1452+072	0.50	12.88	12.38	12.58	12.08	12.76	no	
1514+072	0.50	12.51	12.01	13.46	12.96	13.84	no	
1652+398	0.50	11.86	11.36	11.15	10.65	10.15	yes	10.58
1842+455	0.50	13.89	13.39	14.02	13.52	12.72	yes	13.57
Cygnus A	0.50	13.67	13.17	13.84	13.34	12.07	yes	12.56
2221−023	0.50	13.31	12.81	<11.36	<10.86	9.02	yes	<9.05
2229−086	0.45	13.23	12.78	13.02	12.57	12.99	no	
2243+394	0.48	13.96	13.48	13.59	13.11	12.69	yes	13.41
2308+073	0.49	12.59	12.10	12.50	12.01	12.02	no	
2320+203	0.50	12.79	12.29	12.59	12.09	12.11	no	

Table 5.20: Comparison of estimated and observed L' magnitudes. The first column gives the name of the object, the second the predicted $K-L'$ colour used to turn the stellar 3″ K magnitudes in columns three and five into estimates of the stellar 3″ L' magnitudes in columns four and six. The stellar K band flux has been estimated in two ways: from the K band model fits ($\hat{K}_\star$); and from photometry of the observed image ($K_{\rm obs}$). Column seven gives the observed L' magnitude from table 2.7 for ease of comparison. The errors on the K magnitudes are < 0.01 and those for the L' magnitudes are just the photometry errors with values between 0.07 and 0.28, shown in table 2.7. Column 8 shows whether a secure excess can be claimed and the final column gives the magnitude of this excess if detected.

wavelengths. It has been assumed that the nuclear excess can again be attributed to a reddened quasar with an intrinsic $(K-L')$ colour of 1.68. The possibility of

a starburst nucleus is questioned in the next section.

Object	$K - L'_{MWcorr}$ [mag]	$\pm$	$-\alpha$	E$(K-L')$ [mag]	A_V [mag]	$\pm$	$\log_{10}(\nu L_\nu)$ $[L_\odot]$	$\pm$
0106+130	2.66	0.22	2.65	0.98	17.1	3.8	9.80	0.19
0325+023	1.88	0.25	1.33	0.20	3.6	4.2	8.38	0.20
0356+102	2.04	0.16	1.60	0.36	6.5	2.9	8.71	0.34
0431−134	> 2.30		> 2.04	> 0.59	> 10.6		> 8.21	
0502−103	> 2.72		> 2.75	> 1.02	> 18.2		> 9.25	
1652+398	1.16	0.08	0.12	−0.52			9.74	0.01
1842+455	> 3.88		> 4.70	> 2.19	> 36.8		> 10.13	
Cygnus A	> 4.62		> 5.95	> 2.87	> 50.3		> 10.39	
2243+394	1.40	0.25	0.50	−0.30			9.26	0.04

Table 5.21: Final extinction estimates for those objects with a secure infrared excess detected. The columns are the same as table 4.8. Column 1 gives the name of the object, column 2 gives the Galactic extinction corrected $K - L'$ colour of the nuclear source with the K band value taken from table 4.5 and the L' value taken from column 4 of table 5.20. Column 4 gives the necessary value of the spectral index which would be needed to explain the observed colour. Column 5 gives the necessary reddening towards a quasar or starburst with an intrinsic spectral energy distribution with $\alpha = -1$. For those objects where a significant amount of reddening is necessary to explain the nuclear colour an estimate of the extinction is made in column 6. The final columns give the intrinsic power of the nuclear source in solar luminosities.

5.7.1 Nuclear starburst connection

Nuclear starbursts are intricately connected with AGN activity (Heckman 1999), therefore it is still plausible that the nuclear excesses are just heavily reddened young stellar populations. Or more plausibly a circumnuclear starburst surrounding an even more buried AGN nucleus, such as are found in ULIRGs. To investigate this possibility, the $K - L'$ colours of various metallicity bursts of star–formation at different ages are plotted in figure 5.11, for a population at a redshift of 0.03. It can be seen that the intrinsic colour of a stellar population at any age ($K - L' < 0.73$) is much bluer than that of a quasar ($K - L' = 1.68$).

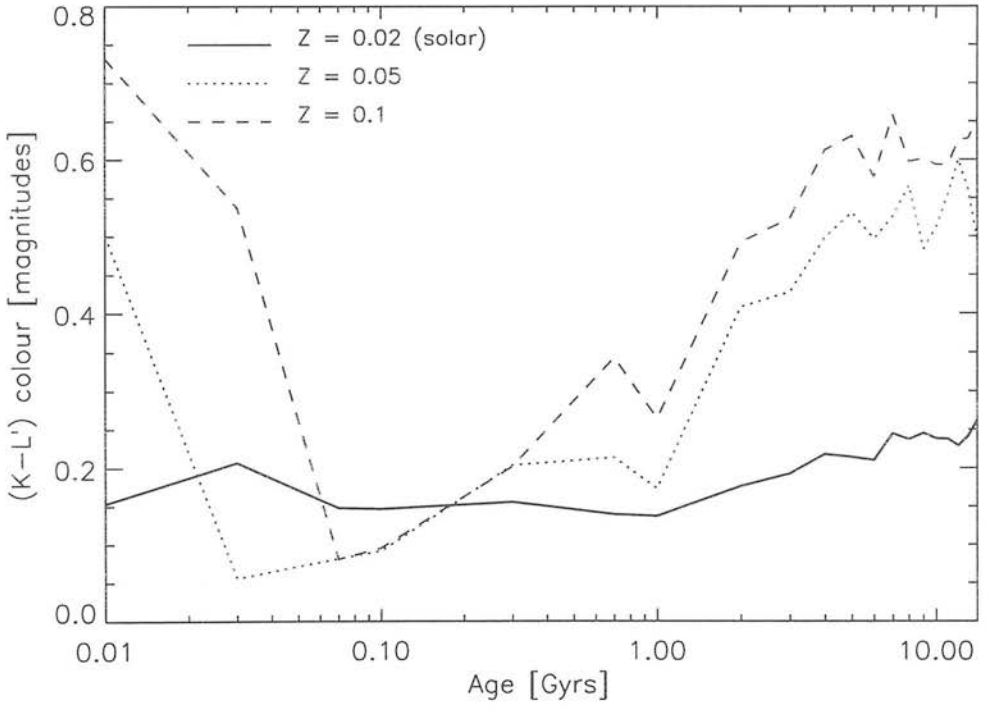

Figure 5.11: The $(K - L')$ colour of bursts of star–formation at different ages at $z = 0.03$, calculated from the stellar population models of Jimenez *et al.* (1999). The solid line is for a $Z_{\odot}$ metallicity burst, the dotted line is for 2.5 $Z_{\odot}$ burst and the dashed line is for a 5 $Z_{\odot}$ burst.

Table 5.22 gives the expected extinction towards an extremely metal–rich nuclear starburst ($Z = 5\ Z_{\odot}$) with an intrinsic $K - L'$ colour of 0.73. The nuclei of elliptical galaxies are found to be more metal–rich than the outer regions and are therefore expected to have super–solar metallicities. The most metal–rich starbursts will

have the reddest colours and will suffer the least extinction for a given nuclear $K - L'$ colour. This will therefore imply a minimum possible luminosity for a starburst nucleus. It can be seen from table 5.22 that the implied luminosity in all cases is greater than 1×10^9 $L_\odot$. Whilst this not completely implausible for a nearby starburst ($L_{10\,\mu m} = 1 \times 10^9$ $L_\odot$ in M82, Joseph 1987), it is unlikely that all these sources contain only metal-rich, highly luminous starburst nuclei without the existence of some AGN activity. A more realistic intrinsic $K - L'$ colour of 0.2 for a solar metallicity starburst, would increase the implied luminosities of the starburst by around 10^{10} $L_\odot$. This is still within the limits of a plausible luminosity for a starburst nucleus, therefore other observations would be needed to distinguish beyond doubt between an AGN and a starburst. AGN emission would be highly polarized and variable as they arise from much smaller regions than starbursts.

Object	E($K - L'$) [mag]	± [mag]	A_V [mag]	± [mag]	$\log_{10}(\nu L_\nu)$ [$L_\odot$]	±
0106+130	1.93	0.22	33.7	3.8	10.59	0.18
0325+023	1.15	0.25	20.8	4.5	9.18	0.21
0356+102	1.31	0.16	23.7	2.9	9.49	0.13
0431−134	> 1.57		> 19.7		> 9.07	
0502−103	> 1.99		> 35.6		> 10.16	
1652+398	0.43	0.08	7.7	1.4	10.09	0.07
1842+455	> 3.15		> 52.9		> 10.93	
Cygnus A	> 3.89		> 68.1		> 11.23	
2243+394	0.67	0.25	11.4	4.3	9.81	0.21

Table 5.22: Extinction estimates for a possible starburst nucleus. The second column gives the reddening towards the nucleus assuming am intrinsic $K - L'$ colour of 0.73. The fourth column gives the extinction estimate and the sixth column gives the intrinsic power of the nuclear source in solar luminosities.

Chapter 6

Conclusions of the census

As a result of the work presented so far, non–thermal infrared excesses have been detected in ten out of the twenty–eight radio galaxies for which both K and L' data were obtained. Of these twenty–eight objects, eighteen objects had known radio morphologies obtained from literature: seven were classified as FRII radio sources, one as a core dominated radio source and the rest as FRI sources. The remaining unclassified sources were taken to be FRI sources in chapter 2 from both their 1.4GHz radio luminosity and I band magnitude. All seven of the FRII sources and the core–dominated BL Lac were found to contain infrared excesses. The BL Lac is the most likely candidate in unified schemes for a FRI source observed along the radio jet axis. Only two of the FRI sources were found to contain an infrared excess, with the observed L' magnitude of the rest of the objects being consistent with that expected from the stellar population.

It is now important to test how the estimated extinction values fit into the current unified schemes picture. For example, if tori were fairly similar from galaxy to galaxy, it is expected that less extinction will be observed if the line of sight to the radio galaxy was closer to the radio axis. Section 6.1 examines various correlations between the observed properties of the radio galaxies and compares these with these with unified schemes. Section 6.3 summarises the work presented in this thesis and discusses possible further tests to clarify the picture obtained of the nuclear regions of AGN.

6.1 Tests of the unified models for FRII radio sources

6.1.1 Properties of the obscured nuclear component

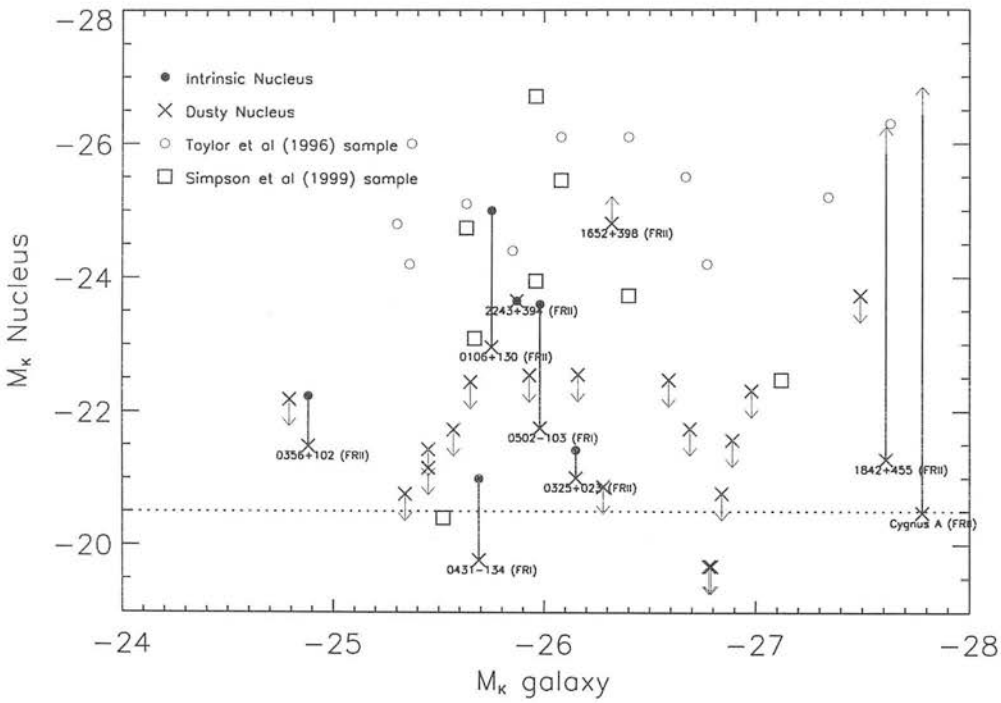

Figure 6.1: Galaxy integrated absolute K magnitude versus nuclear absolute magnitude. The nuclear and galaxy magnitudes have been K–corrected assuming $\alpha = -1$ and $\alpha = 0$ spectral energy distributions respectively. The crosses show the magnitude of the reddened nuclei of the objects in this sample whilst the filled circles and lower limits show the magnitude of the intrinsic nuclei, where present. For comparison, the magnitudes of the reddened nuclei of samples of radio galaxies from Taylor *et al.* (1996) and Simpson, Ward and Wall (1999) are also shown. These other samples are selected from brighter radio surveys than the sample here and so are expected to contain intrinsically brighter nuclei. The horizontal dotted line shows the K band boundary for quasars. The morphology of the radio galaxies is also indicated.

It is first important to see if the buried nuclei could indeed be unified with radio–loud quasars. Surveys have shown that whilst the nuclei of radio–quiet quasars and Seyfert galaxies span the whole range of optical luminosities up to $M_V = -29$,

no radio–loud quasars are found with $M_V > -23$ (Peacock, Miller & Longair 1986). The optical–to–infrared colour of a quasar is around $B - K = 2.5$, so this translates to an infrared limit for potential buried radio–loud quasar sources of $M_K = -20.5$. Figure 6.1 plots the reddened and unreddened colours of the nuclei against their absolute host galaxy magnitude. The absolute magnitudes have been K–corrected assuming the nucleus and galaxy have spectral energy distributions in the infrared with $\alpha = -1$ and $\alpha = 0$ respectively. It can be seen that all the filled black circles and lower limits do indeed lie above the dotted line marking the quasar boundary, which is evidence in favour of them being possible candidates for obscured radio–loud quasars. Also plotted on the same figure are upper limits, marking the absolute magnitude of the K band nuclei which do not appear to have infrared excesses. Marked on this same figure are samples of radio galaxies from Taylor *et al.* (1996) and Simpson, Ward & Wall (1999) which have also had infrared nuclei detected from two–dimensional surface brightness modelling. These latter points represent the observed magnitude of the reddened nucleus, so the intrinsic magnitude may be much brighter. The Taylor *et al.* (1996) radio galaxy sample has been selected so that it contains only FRII sources and is indistinguishable from their high luminosity radio–loud quasar sample in both radio power, radio spectral index and redshift. It is therefore not surprising that the detected nuclei lie in a region above the objects in this sample as the nuclei are expected to be intrinsically much brighter. The Simpson, Ward & Wall (1999) sample has been taken from the 3CRR catalogue, selecting all the NELGs below a redshift of 0.43. As this catalogue consists of some of the most radio–luminous objects in the sky it is also expected that most of these objects will contain more luminous nuclei than those seen in this sample.

In unified schemes the core and total radio power of the quasar are thought to be connected to the optical luminosity and hence the black hole mass (Franceschini, Vercellone & Fabian 1998). A plot of the core radio power at 5 GHz against the absolute nuclear magnitude for the FRII sources is given in figure 6.2 and a similar plot, but this time with total radio power is given in figure 6.3. The dotted lines on these plots represent the least absolute deviation fit to the filled circle points. It can be seen that whilst a strong correlation is possibly not apparent between the nucleus and the core radio power there is substantial evidence for a trend between the strength of the nucleus and the total radio power. This is similar to the result found by Franceschini, Vercellone & Fabian (1998) who

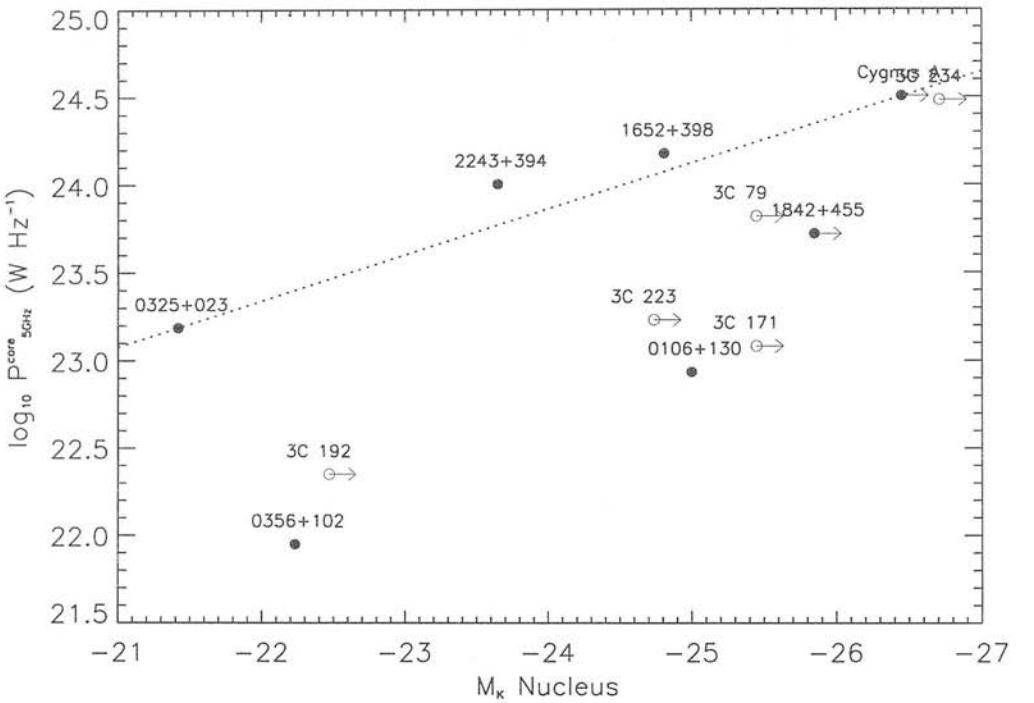

Figure 6.2: Core radio power versus absolute nuclear magnitude for the FRII radio galaxies. The filled circles are extinction estimates from this sample whilst the open circles are from Simpson, Ward & Wall (1999). Note that 1652+198 is unusually luminous, it is a BL Lac so the core flux is thought to be beamed and amplified along the line of sight. The core radio data are taken from Giovannini *et al.* (1988), Giovannini, Feretti & Comoretto (1990) and Morganti, Killeen & Tadhunter (1993). The dotted line corresponds to $y = -0.26x + 17.57$.

found a much stronger connection between total radio power and black hole mass than between core radio power and black hole mass. The fact that the total radio power does seem to be connected at all to the strength of the nucleus is further evidence for the observed nucleus actually being an obscured quasar rather than a starburst nucleus. Any deviations in the relationship could then be attributed to differences in accretion rate onto the black hole.

The core radio flux may not be expected to correlate with the strength of the nuclear source as core fluxes often suffer from beaming effects, whereby the strength of the core is enhanced along lines–of–sight close to the radio jet. Assuming this to be true, information can be gained on the viewing angle from the relative strength of the core to the total radio flux. For the BL Lac, 1652+398, which is a flat spectrum radio source, the core flux is definitely expected to be beamed

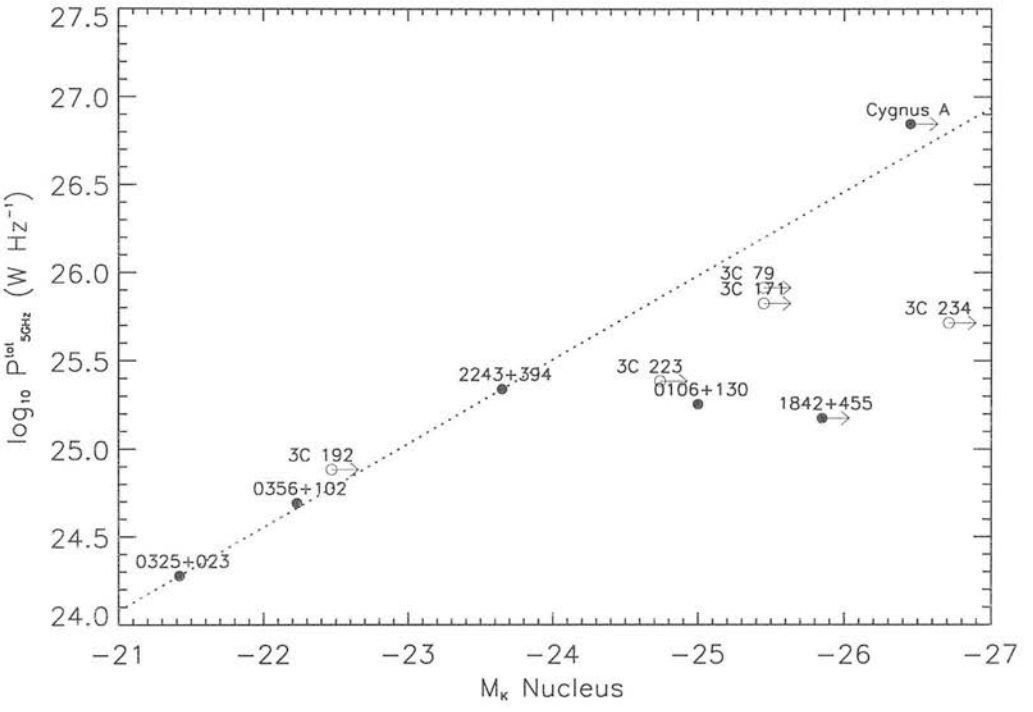

Figure 6.3: Total radio power versus absolute nuclear magnitude for the FRII radio galaxies. The filled circles are extinction estimates from this sample whilst the open circles are from Simpson, Ward & Wall (1999). The total flux at 5 GHz is taken from Pauliny-Toth & Kellermann (1968). The dotted line corresponds to $y = -0.48x + 14.07$.

along the line–of–sight, it is now necessary to obtain information on the viewing angle of the other radio galaxies.

6.1.2 Viewing angle dependence

As mentioned in chapter 1, the core dominance parameter, or core–to–lobe ratio, R, is a widely used orientation indicator. High R sources are thought to have the core component beamed along the line of sight, indicating a viewing angle closer to the radio jet than low R sources. The viewing angle dependence of the extinction is investigated in figure 6.4 for the FRII objects where core and total radio fluxes at 5 GHz were available. The total flux at 5 GHz is taken from Pauliny-Toth & Kellermann (1968). The open circles in the plot are extinction estimates from Simpson, Ward & Wall (1999). For their sample alone they claim that the hypothesis that A_V is uncorrelated with R can be rejected

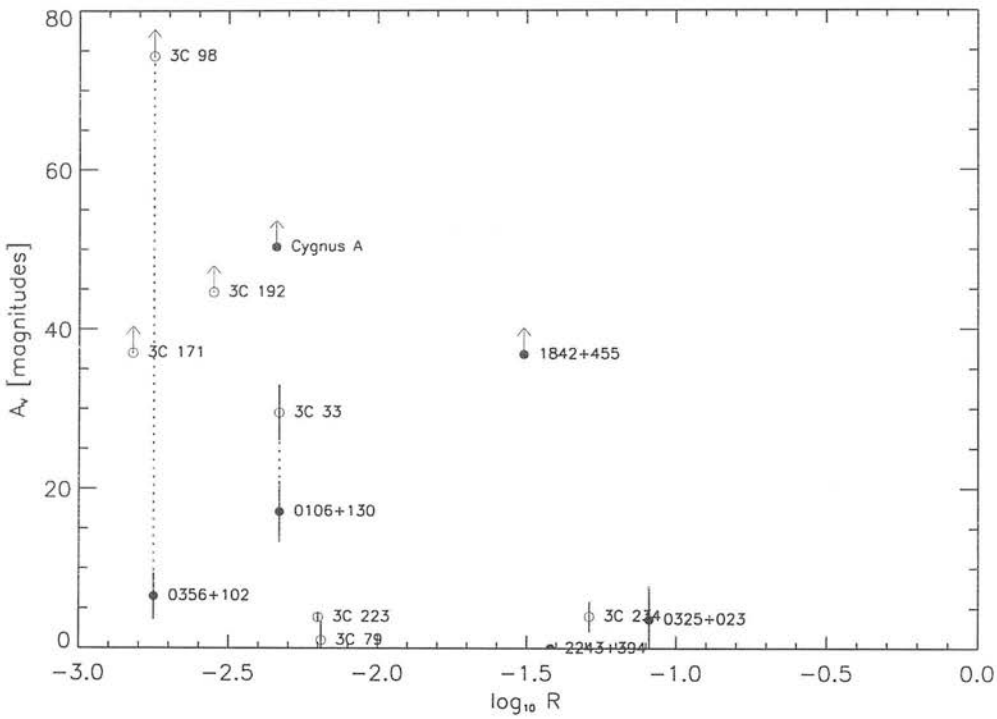

Figure 6.4: Radio core–to–lobe ratio, R versus estimated extinction for the FRII radio galaxies. The total flux at 5 GHz is taken from Pauliny-Toth & Kellermann (1968). The filled circles are extinction estimates from this sample whilst the open circles are from Simpson, Ward & Wall (1999). Dotted lines connect the differing extinction estimates for the two objects common to both samples. An anti–correlation with R is expected from unified schemes.

at the 95% confidence level using a generalized Kendall's rank correlation statistic. This statistic is used as it allows a complete treatment of upper and lower limits. However, the implied correlation appears to rely heavily on one point in their plot, that of 3C 98 (0356+102), for which they predict > 74.3 magnitudes of extinction. As discussed in chapter 4 this object does appear to contain a significant K band nucleus, but not quite centered on the galaxy centre, thereby causing this discrepancy in estimated extinction values. Shifting 3C 98 to a much lower extinction, results in the diagram becoming a scatter plot. The points in figure 6.4 do appear to lie within an envelope, such that there are no points with R > -1, although this may be a selection effect as 2221−023, the only BLRG has been excluded as it is saturated in all the images. The Simpson, Ward & Wall sample has been chosen to avoid objects with broad lines, which may be the ones with R values lying in this region. It must also be remembered that R does not

vary linearly with viewing angle. Simpson, Ward & Wall (1999) have estimated the a priori distribution of viewing angles with R. This is shown graphically in figure 6.5.

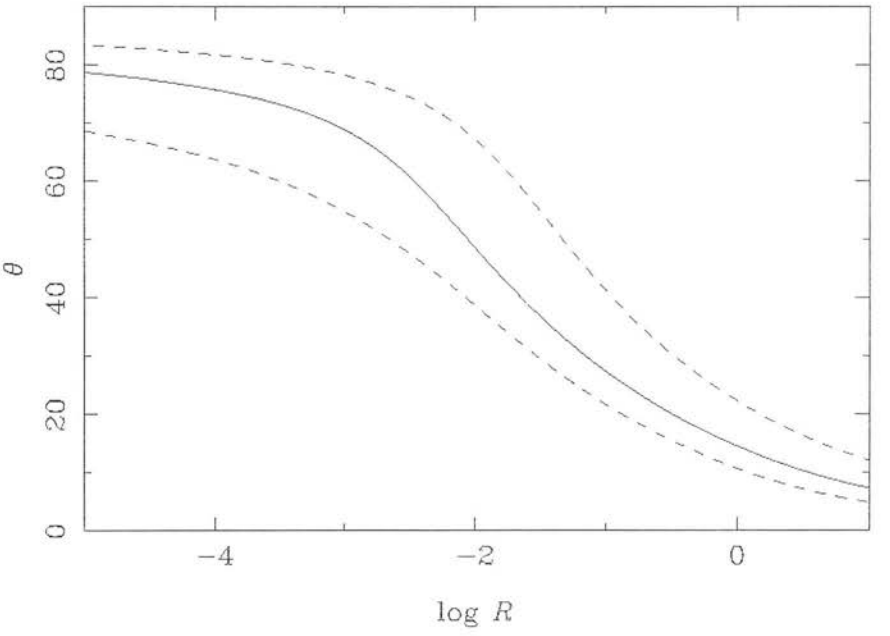

Figure 6.5: The probability density function (pdf) of viewing angle, θ, as a function of core–to–lobe ratio, R, taken from Simpson, Ward & Wall (1999). The solid line shows the maximum of the pdf with the dotted lines indicating the 1σ limits. θ is measured from the radio jet so that $\theta = 0°$ is a view down the jet and $\theta = 90°$ is a view transverse to the jet.

Simpson, Ward & Wall have estimated the stellar component of the L' data by comparing the $K - L'$ colours with the $K - L'$ colour of β Peg, a late–type star, rather than by modelling the whole stellar population. However, they do find the nuclear $K - L'$ colours of both 3C 171 and 3C 192 to be consistent with late–type stellar populations, so these points should arguably also be removed from the plot. The lack of an anti–correlation can then be seen clearly in the combination of datasets shown in figure 6.4.

The lack of any clear correlation is a challenge to the most basic interpretations of unified schemes whereby the objects are intrinsically the same, but viewed at different angles to the line of sight, with extinction that varies smoothly with viewing angle. This null result is important as it means that more complicated scenarios need to be visualised to explain the dusty environments around AGN. A possible interpretation is that the obscuring material, whilst still being torus–

shaped, may be lumpy within the torus, thereby leading to chance lines of sight where the extinction is lower than along other lines of sight. Another possibility is that whilst the extinction does depend smoothly on the viewing angle, the intrinsic dust content of the galaxy affects the thickness of the torus that is capable of forming. The thickness of the torus may then also depend on factors such as accretion rate and nuclear luminosity.

6.1.3 Galaxy size dependence

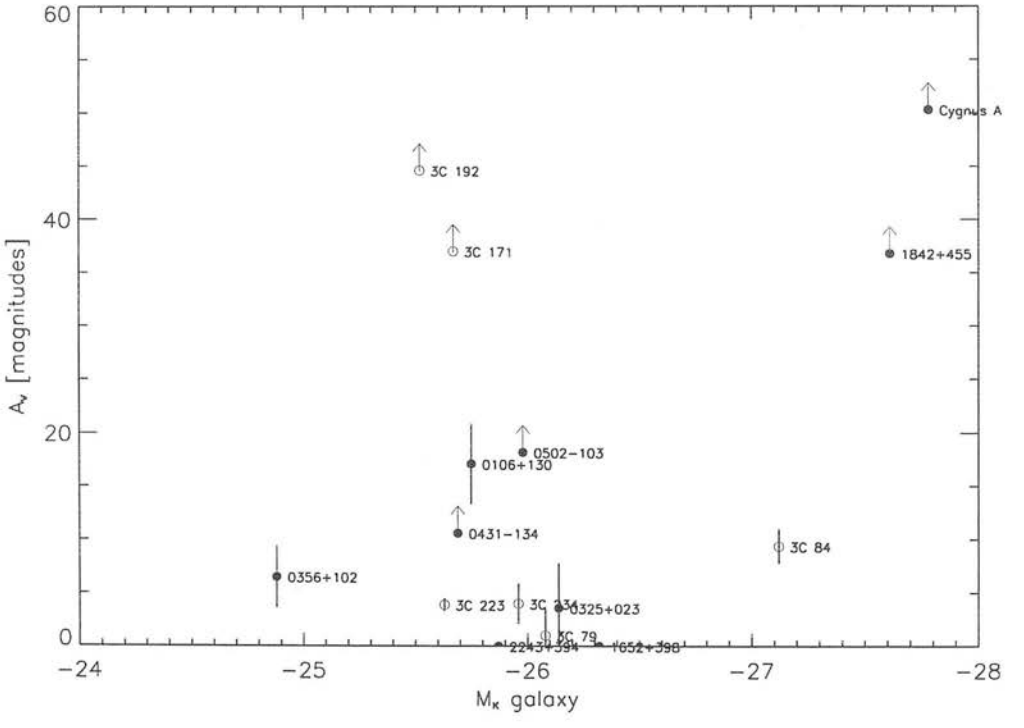

Figure 6.6: Galaxy integrated absolute K magnitude versus estimated extinction for the FRII radio galaxies. The filled circles are extinction estimates from this sample whilst the open circles are from Simpson, Ward & Wall (1999). FRI and FRII sources are plotted, the FRI sources are 0431−134, 0502−103, 3C 84 and 1652+398. Considering the K band magnitude to be representative of the size of the size, there is a definate trend for the larger galaxies to be more dusty.

Figure 6.1 gave a hint that the size of the galaxy may affect the thickness of the torus as the larger galaxies to the left of the plot were being reddened more than the smaller ones. To investigate this, the integrated galaxy luminosity was

plotted against estimated extinction for both this sample and that of Simpson, Ward & Wall; this plot is presented in figure 6.6. Interestingly, if 3C 192 and 3C 171 are ignored, which is viable given their consistency with stellar populations, there is an obvious trend amongst the remaining objects for the bigger galaxies to show higher extinction and therefore to be more dusty. Although the number of objects in this plot is too small to assess the statistical significance of the trend, if this were indeed found to be true it would have very interesting consequences for combined theories of AGN and galaxy formation. Baum and O'Dea (private communication) have recently found evidence for radio galaxies being more dusty than 'normal' passive ellipticals. Since all ellipticals are thought to form by mergers, this implies that the radio galaxies have merged more recently than 'normal' ellipticals, and therefore that the AGN activity is then either triggered or enhanced by the merger. Hughes, Dunlop & Rawlings (1997) have also recently shown that radio galaxies are detected at sub–millimetre wavelengths, which implies that they have undergone huge, dusty, recent bursts of star–formation.

6.2 Unified schemes for FRI sources

Looking at the sample of FRI galaxies separately, buried nuclei are only detected in three out of twenty–one objects. This could be for two reasons, either because the intrinsic luminosity of the nucleus is too faint to be detected, or the extinction is too great, or a combination of both reasons. The evidence for unifying FRIs with the beamed BL Lacs is quite convincing from relative number density and linear size arguments (Padovani & Urry 1990). However, there is a lack of unbeamed and unobscured objects. This could mean that the opening angle of the torus for FRIs is much smaller than it is in FRIIs. Barthel (1989) estimated the opening angle to be around 45° in a sample of $z = 0.5 - 1.0$ FRIIs. The number of non–detections of obscured nuclei in FRIs adds weight to this argument, a rough calculation would put the opening angle at $\sim 8°$ ($\sin\theta \simeq 3/21$), which would explain the lack of low luminosity counterparts to broad–line radio galaxies or reddened quasars. This would then add weight to the argument that the opening angle of the torus and therefore the morphology of the radio emission depends upon the luminosity of the central source, *i.e.* the receding torus model (see figure 1.6). This could also qualitatively explain the large numbers of low luminosity AGN (NLXGs) seen in X–ray surveys, but not seen in optical

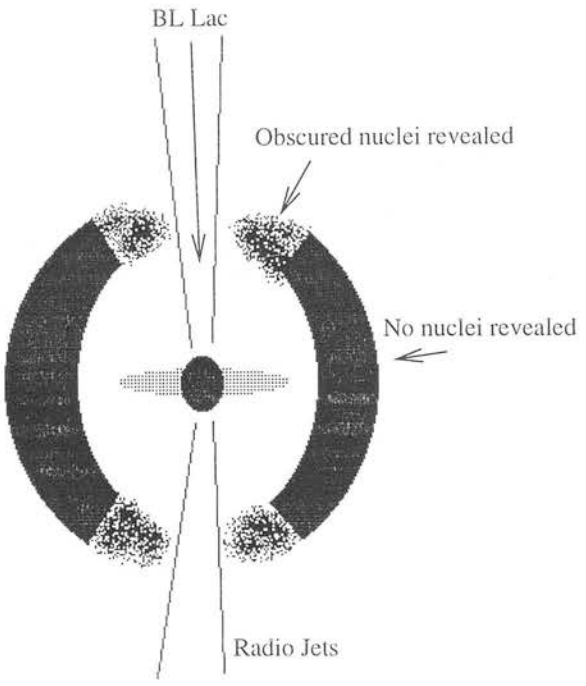

Figure 6.7: Possible unification scheme for FRI radio galaxies and BL Lacs. Either the edges of the torus are less thick than in the centre allowing for the buried nuclei to be detected in the regions of lower extinction, or the radiation is beamed along these directions enhancing the luminosity above the detection limits and allowing the nucleus to be detected.

surveys. In these objects the 'torus' may be completely closed up around the AGN and be more spherical in shape. Figure 6.7 shows a cartoon of a possible unification scheme for FRI radio galaxies, where the torus 'thins out' around the poles allowing the nucleus to be seen with modest reddening.

Another serious possibility is that in FRIs both the optical and radio flux may be beamed, causing non–isotropic emission of optical/infrared radiation. This means that even without the postulated obscuring torus very little optical light would be seen along lines of sight perpendicular to the radio jets. A test of this scenario would be to see if the infrared excess in FRIs is highly polarized and variable, implying the presence of blazar–type emission. If the excess were not found to be variable, then it is more likely that it is probably due to a circumnuclear starburst.

6.3 Summary and discussion

This thesis has presented infrared images and optical spectra for a sample of low–redshift radio galaxies, with the aim of carrying out a unique census of the extinction towards the nuclei of these objects. Two–dimensional surface brightness profiles were fitted to K band images to deconvolve the stellar and nuclear light. The results of the model fits provided evidence that these galaxies were indeed 'normal' elliptical galaxies as they followed the same Kormendy relation as the general population of elliptical galaxies. The range of observed scale–lengths provided evidence for most of the radio galaxies being amongst the biggest and brightest types galaxies known. The successful comparison of the predicted velocity dispersions from the fundamental plane relation with those measured from the spectra or found in the literature, adds further weight to the argument that the radio galaxies are indeed 'normal' elliptical galaxies. Combining the measured excess nuclear component at K with the observed L' data has allowed an initial estimate of the extinction towards the nucleus to be made.

Optical spectra of the nuclear regions of all the objects were then analysed to compare both absorption line indices and the overall continuum with stellar population models. The best fit age and metallicity model was taken to be that from the overall continuum analysis of Jimenez's models. This model was then examined in the infrared where broad–band $K - L'$ colours were calculated by integrating the spectral energy distribution under the UKIRT filter profiles. This enabled a prediction of the infrared colour of the stellar component of the nucleus to be made. Two estimates of the stellar component of the L' flux were then made by combining the $K - L'$ colour taken from the model fits with two estimates of the K band stellar nuclear flux. The first estimate was taken from the surface brightness fits and the second from the observed K magnitude, treated as a maximum value, which would give a model independent upper limit on the stellar L' value. Any significant excess of the observed nuclear L' flux over the stellar value was taken to be an observation of the non–thermal AGN component shining through. This revised estimate of the nuclear non–thermal L' component combined with the excess K band flux from the surface brightness model fits allowed a more accurate estimate of the observed $K - L'$ colour of the quasar to be made. Assuming the intrinsic shape of the quasar's spectral energy distribution to follow power–law shape with exponent $\alpha = -1$, the reddening towards this

quasar could then be estimated. The extinction A_V, towards the object at optical wavelengths was then calculated. The possibility of the excess being due to a dusty nuclear starburst was also considered but dismissed as the required high luminosity and high metallicity of a starburst to fit the observations is extremely unlikely, especially without some form of AGN activity.

Most of the objects were found to have nuclear colours which were consistent with old stellar populations. Considering the number of predictions and estimates made in this analysis, the consistency of the results with stellar populations was very pleasing. This meant that the the argument for the ten out of the twenty–eight galaxies which were shown to contain infrared excesses to contain AGN nuclei was strengthened.

Finally the objects for which a nuclear excess was detected have been examined in detail, under the assumption that the excess can be attributed to a buried quasar. The inferred nuclear K band absolute magnitudes would put the objects into the quasar category of $M_V < -23$ as was shown in figure 6.1.

All the FRII radio galaxies in the sample were found to contain infrared excesses. For these the inferred nuclear K magnitudes were then correlated with both core radio power and total radio power. A tentative correlation was found between intrinsic nuclear luminosity and total radio emission which adds weight to the argument that the infrared excesses can be attributed to buried quasars, as the radio emission is thought to be correlated with the strength of the nuclear source. The viewing angle of the FRII sources was then calculated from the core–to–lobe ratio, which assumes that the core radio emission is boosted when viewed close to the line of sight. Unexpectedly, the inferred extinction of the FRII objects does not seem to correlate with core–to–lobe ratio. This could be either because the core dominance parameter is not actually a good orientation indicator, or because the extinction actually does not change smoothly with viewing angle. The estimated extinction was then compared with absolute total K magnitude taken from the model galaxy fits, integrated to infinity as shown in figure 6.6. There is a hint from this plot that the extinction does seem to increase with increasing galaxy size.

Examining the FRI radio galaxies separately, only three out of a total of twenty–one objects were found to contain infrared excesses, which could be because the nucleus is fainter or the extinction greater in FRIs than FRIIs, or a combination

of both reasons. If this were the case then the relative numbers of obscured and unobscured FRIs and FRIIs could then be explained by a receding torus model whereby the torus has a smaller opening angle in lower luminousity objects.

It would be very interesting if the correlation between extinction and galaxy size was found to be true. However, we must still consider the possibility that the infrared excesses are not caused by buried quasars at all and the correlation is just intrinsic to the galaxy interstellar medium. Cygnus A was found by Tadhunter *et al.* (1999) to have a K band excess which was highly polarised (Packham *et al.* 1998). This implied that the observed excess is probably a near–nuclear reflection nebula rather than the actual obscured nucleus itself. The X–ray data also implied an obscuring column of nearer 170 magnitudes of extinction which is much higher than the inferred infrared extinction. This difference may be resolved by using a higher dust/gas ratios in the nucleus than used previously to calculate the X–ray extinction. To settle this debate finally, would require hard X–ray and infrared imaging polarimetry observations of the entire sample, which are not currently available. Accurate core radio positions would enable a proper estimate of the infared excess at the exact position of the radio core, which should be the expected position of the black hole. This would then resolve controversies such as the differing estimates of the extinction towards the nucleus of 3C 98. Variability and polarimetry studies would help to finally distinguish between buried quasars and/or buried nuclear starbursts as the infrared sources.

Bibliography

Almaini O., Shanks T., Boyle B. J., Griffiths R. E., Roche N., Stewart G. C., Georgantopoulos I., 1996. *Mon. Not. R. astr. Soc.*, **282**, 295.

Almaini O., Shanks T., Griffiths R. E., Boyle B. J., Roche N., Georgantopoulos I., Stewart G. C., 1997. *Mon. Not. R. astr. Soc.*, **291**, 372.

Antonucci R. R. J., Miller J. S., 1985. *Ap. J.*, **297**, 621.

Antonucci R., 1993. *Ann. Rev. Astron. Astrophys.*, **31**, 473.

Aretxaga I., Cid Fernandes R., Terlevich R. J., 1997. *Mon. Not. R. astr. Soc.*, **286**, 271.

Axon D. J., Bailey J., Hough J. H., 1982. *Nature*, **299**, 234.

Baker J. C., 1997. *Mon. Not. R. astr. Soc.*, **286**, 23.

Barthel P. D., Arnaud K. A., 1996. *Mon. Not. R. astr. Soc.*, **283**, L45.

Barthel P. D., 1989. *Ap. J.*, **336**, 606.

Begelman M. C., Rees M. J., 1978. *Mon. Not. R. astr. Soc.*, **185**, 847.

Bender R., Burstein D., Faber S. M., 1997. In: *Galaxy Scaling Relations: Origins, Evolution and Applications*, 95, eds da Costa L. N., Renzini A.

Bender R., Saglia R. P., Gerhard O., 1994. *Mon. Not. R. astr. Soc.*, **269**, 785.

Blandford R. D., McKee C. F., Rees M. J., 1977. *Nature*, **267**, 211.

Bolton J., Wright A., Savage A., 1979. *Aust. J. Phys. Astrophys. Suppl.*, **46**.

Bowen D. V., Pettini M., Boyle B. J., 1998. *Mon. Not. R. astr. Soc.*, **297**, 239.

Boyle B., McMahon R., Wilkes B., Elvis M., 1995. *Mon. Not. R. astr. Soc.*, **276**, 315.

Bridle A. H., Perley R. A., 1984. *Ann. Rev. Astron. Astrophys.*, **22**, 319.

Bruzual A. G., Charlot S., 1993. *Ap. J.*, **405**, 538.

Bruzual A. G., 1983. *Ap. J.*, **273**, 105.

Burstein D., Heiles C., 1978. *Ap. J.*, **225**, 40.

Burstein D., Faber S. M., Gaskell C. M., Krumm N., 1984. *Ap. J.*, **287**, 586.

Burstein D., Faber S. M., Gonzalez J. J., 1986. *Astron. J.*, **91(5)**, 1130.

Cannon R. D., Penston M. V., Brett R. A., 1971. *Mon. Not. R. astr. Soc.*, **152**, 79.

Capaccioli M., Caon N., D'Onofrio M., 1992. *Mon. Not. R. astr. Soc.*, **259**, 323.

Cardelli J. A., Clayton G. C., Mathis J. S., 1988. *Ap. J.*, **329**, L33.

Cardelli J. A., Clayton G. C., Mathis J. S., 1989. *Ap. J.*, **345**, 245.

Cardiel N., Gorgas J., Cenarro J., Gonzalez J. J., 1998. *Astron. Astrophys. Suppl.*, **127**, 597.

Carollo C. M., Danziger I. j., Buson L., 1993. *Mon. Not. R. astr. Soc.*, **265**, 553.

Carrasco L., Buzzoni A., Salsa M., Recillas-Cruz E., 1996. In: *Fresh Views of Elliptical Galaxies*, p. 235, eds Buzzoni A., Renzini A., Serrano A.

Chapman A., Beard S., Mountain C., Pettie D., Pickup D., Wade R., 1990. In: *Instrumentation in Astronomy VII*, p. 34, ed. Crawford D., SPIE - Int. Soc. Opt. Eng., Bellingham, WA.

Charlot S., Bruzual A. G., 1991. *Ap. J.*, **367**, 126.

Charlot S., Worthey G., Bressan A., 1996. *Ap. J.*, **457**, 625.

Cohen A., Porcas R., Browne I., Daintree E., Walsh D., 1977. *Mem. R astr. Soc.*, **84**, 1.

Cohen M. H., Ogle P. M., Tran H. D., Goodrich R. W., Miller J. S. 1999. astro-ph/9909215.

Colina L., Sparks W. B., Macchetto F., 1991. *Ap. J.*, **370**, 102.

Comastri A., Setti G., Zamorani G., Hasinger G., 1995. *Astron. Astrophys.*, **296**, 1.

Dalle Ore C., Faber S. M., Gonzalez J. J., Stoughton R., Burstein D., 1991. *Ap. J.*, **366**, 38.

Davies R. L., Sadler E. M., Peletier R. F., 1993. *Mon. Not. R. astr. Soc.*, **262**, 650.

de Vaucouleurs G., 1948. *Ann. Astrophys*, **11**, 247.

Di Nella H., Garcia A. M., Garnier R., Paturel G., 1995. *Astron. Astrophys. Suppl.*, **113**, 151.

Djorgovski S., Davis M., 1987. *Ap. J.*, **313**, 59.

Djorgovski S., Weir N., Matthews K., Graham J. R., 1991. *Ap. J.*, **372**, L67.

Dressler A., Lynden-Bell D., Burstein D., Davies R. L., Faber S. M., Terlevich R., Wegner G., 1987. *Ap. J.*, **313**, 42.

Dunlop J. S., Peacock J. A., 1993. *Mon. Not. R. astr. Soc.*, **263**, 936.

Eckart A., Genzel R., 1997. *Mon. Not. R. astr. Soc.*, **284**, 576.

Economou F., Lawrence A., Ward M. J., Blanco P. R., 1995. *Mon. Not. R. astr. Soc.*, **272**, L5.

Edelson R. A., Malkan M. A., Rieke G. H., 1987. *Ap. J.*, **321**, 233.

Faber S. M., Jackson R. E., 1976. *Ap. J.*, **204**, 668.

Faber S. M., Burstein D., Gaskell C. M., 1985. *Ap. J. Suppl.*, **57**, 711.

Fabian A. C., Nandra K., Reynolds C. S., Brandt W. N., Otani C., Tanaka Y., Inoue H., Iwasawa K., 1995. *Mon. Not. R. astr. Soc.*, **277**, L11.

Fabian A. C., Barcons X., Almaini O., Iwasawa K., 1998. *Mon. Not. R. astr. Soc.*, **297**, L11.

Fanaroff B. L., Riley J. M., 1974. *Mon. Not. R. astr. Soc.*, **167**, 31.

Fanti R., Fanti C., Schilizzi R. T., Rendong N., Parma P., van Breugel W. J. M., Venturi T., 1990. *Astron. Astrophys.*, **231**, 333.

Fath E. A., 1908. *Lick Obs. Bull.*, **5**, 71.

Fisher D., Franx M., Illingworth G., 1996. *Ap. J.*, **459**, 110.

Fitzpatrick E. L., 1999. *Publ. Astron. Soc. Pacific*, **111**, 63.

Fowler W. A., Hoyle F., 1963. *Royal Greenwich Observatory Bulletin*, **67**, 301.

Franceschini A., Vercellone S., Fabian A. C., 1998. *Mon. Not. R. astr. Soc.*, **297**, 817.

Freeman K. C., 1970. *Ap. J.*, **160**, 811.

Ghez A. M., Klein B. L., Morris M., Becklin E. E., 1998. *Ap. J.*, **509**, 678.

Giovannini G., Feretti L., Gregorini L., Parma P., 1988. *Astron. Astrophys.*, **199**, 73.

Giovannini G., Feretti L., Comoretto G., 1990. *Ap. J.*, **358**, 159.

Glazebrook K., Peacock J. A., Collins C., Miller L., 1994. *Mon. Not. R. astr. Soc.*, **266**, 65.

Gonzalez J. J., 1993. *PhD thesis*, University of Califonia, Santa Cruz.

Gorgas J., Faber S. M., Burstein D., Gonzalez J. J., Courteau S., Prosser C., 1993. *Ap. J. Suppl.*, **86**, 153.

Gorgas J., Cardiel N., Pedraz S., Gonzalez J. J., 1999. *Astron. Astrophys. Suppl.*, **139**, 29.

Greenstein J. L., Schmidt M., 1964. *Ap. J.*, **140(1)**, 1.

Grueff G., Vigotti M., 1972. *Astron. Astrophys. Suppl.*, **6**, 1.

Grueff G., Vigotti M., 1979. *Astron. Astrophys. Suppl.*, **35**, 371.

Gunn J. E., Oke J., 1975. *Ap. J.*, **195**, 255.

Harms R. J., Ford H. C., Tsvetanov Z. I., Hartig G. F., Dressel L. L., Kriss G. A., Bohlin R., Davidsen A. F., Margon B., Kochhar A. K., 1994. *Ap. J. Lett.*, **435**, L35.

Hazard C., Mackey M. B., Shimmins A. J., 1963. *Nature*, **197**, 1037.

Heckman T. M., 1978. *Publ. Astron. Soc. Pacific*, **90**, 241.

Heckman T. M. 1999. astro-ph/9912029.

Heisler C. A., Lumsden S. L., Bailey J. A., 1997. *Nature*, **385**, 700.

Hes R., Barthel P. D., Fosbury R. A. E., 1993. *Nature*, **362**, 326.

Hill G. J., Goodrich R. W., DePoy D. L., 1996. *Ap. J.*, **462**, 163.

Hughes D. H., Dunlop J. S., Rawlings S., 1997. *Mon. Not. R. astr. Soc.*, **289**, 766.

Illingworth G., Freeman K. C., 1974. *Ap. J. Lett.*, **188**, L83.

Inglis M. D., Brindle C., Hough J. H., Young S., Axon D. J., Bailey J. A., Ward M. J., 1993. *Mon. Not. R. astr. Soc.*, **263**, 895.

Iwasawa K., Fabian A. C., Reynolds C. S., Nandra K., Otani C., Inoue H., Hayashida K., Brandt W. N., Dotani T., Kunieda H., Matsuoka M., Tanaka Y., 1996. *Mon. Not. R. astr. Soc.*, **282**, 1038.

Jackson N., Browne I. W. A., 1990. *Nature*, **343**, 43.

Jackson C. A., Wall J. V., 1999. *Mon. Not. R. astr. Soc.*, **304**, 160.

Jackson N., Tadhunter C., Sparks W. B., 1998. *Mon. Not. R. astr. Soc.*, **301**, 131.

Jimenez R., Dunlop J. S., Padoan P., Peacock J. A., MacDonald J., Jørgensen U. G. 1999. submitted to MNRAS.

Joseph R. D., 1987. In: *Starbursts and Galaxy Evolution*, p. 293, eds Thuan T., Montmerle T., Tran Thanh Van J.

Kauffmann G., Haehnelt M. 1999. astro-ph/9906493.

Khachikian E. Y., Weedman D. W., 1974. *Ap. J.*, **192**, 581.

Kinney A. L., Antonucci R. R. J., Ward M. J., Wilson A. S., Whittle M., 1991. *Ap. J.*, **377**, 100.

Kobayashi C., Arimoto N. 1999. astro-ph/9907091.

Koide S., Shibata K., Kudoh T., 1999. *Ap. J.*, **522**, 727.

Kolatt T. S., Bullock J. S., Somerville R. S., Sigad Y., Jonsson P., Kravtsov A. V., Klypin A. A., Primack J. R., Faber S. M., Dekel A., 1999. *Ap. J. Lett.*, **523**, L109.

Kormendy J., Richstone D., 1995. *Ann. Rev. Astron. Astrophys.*, **33**, 581.

Kormendy J., 1977. *Ap. J.*, **217**, 406.

Koyama K., Awaki H., Iwasawa K., Ward M. J., 1992. *Ap. J. Lett.*, **399**, 129.

Krisciunas K., Sinton W., Tholen D., A.Tokunaga, Golisch W., Griep D., Kaminski C., Impey C., Christian C., 1987. *Publ. Astron. Soc. Pacific*, **99**, 887.

Kühr H., Pauliny-Toth I., Witzel A., Schmidt J., 1981. *Astron. J.*, **86**, 854.

Kühr H., Johnston K., Odenwald S., Adlhoch J., 1987. *Astron. Astrophys. Suppl.*, **71**, 493.

Kulkarni V., Calzetti D., Bergeron L., Rieke M., Axon D., Skinnner C., Colina L., Sparks W., Daou D., Gilmore D., Holfeltz S., Mackenty J., Noll K., Ritchie C., Schneider G., Schultz A., Storrs A., Suchkov A., Thompson R., 1998. *Ap. J. Lett.*, **492**, 121.

Kuntschner H., Davies R. L., 1998. *Mon. Not. R. astr. Soc.*, **295**, L29.

Kuntschner H., 1998. *PhD thesis*, University of Durham.

Landau R., Golisch B., Jones T. J., Jones T. W., Pedelty J., Rudnick L., Sitko M. L., Kenney J., Roellig T., Salonen E., Urpo S., Schmidt G., Neugebauer G., Matthews K., Elias J. H., Impey C., Clegg P., Harris S., 1986. *Ap. J.*, **308**, 78.

Landini M., Natta A., Oliva E., Salinari P., Moorwood A., 1984. *Astron. Astrophys.*, **134**, 284.

Lara L., Cotton W. D., Feretti L., Giovannini G., Venturi T., Marcaide J. M., 1997. *Ap. J.*, **474**, 179.

Lawrence A., 1991. *Mon. Not. R. astr. Soc.*, **252**, 586.

Leggett S. *IRCAM Manual.* Joint Astronomy Centre, Hilo, Hawaii, 1998. http://www.jach.hawaii.edu/UKIRT.new/instruments/ircam/ircam3.html.

Lilly S. J., Longair M. S., Miller L., 1985. *Mon. Not. R. astr. Soc.*, **214**, 109.

Lynden-Bell D., 1969. *Nature*, **223**, 690.

Magorrian J., Tremaine S., Richstone D., Bender R., Bower G., Dressler A., Faber S. M., Gebhardt K., Green R., Grillmair C., Kormendy J., Lauer T., 1998. *Astron. J.*, **115**, 2285.

Martel A. R., Baum S. A., Sparks W. B., Wyckoff E., Biretta J. A., Golombek D., Macchetto F. D., De Koff S., McCarthy P. J., Miley G. K., 1999. *Ap. J. Suppl.*, **122**, 81.

Mathis J. S., Cardelli J. A., 1992. *Ap. J.*, **398**, 610.

Matthews T. A., Sandage A. R., 1963. *Ap. J.*, **138**, 30.

Mattig W., 1958. *Astron. Nachr.*, **284**, 109.

McCarthy P. J., Van Breugel W., Spinrad H., Djorgovski S., 1987. *Ap. J. Lett.*, **321**, L29.

McCarthy P. J., 1993. *Ann. Rev. Astron. Astrophys.*, **31**, 639.

McHardy I. M., Jones L. R., Merrifield M. R., Mason K. O., Newsam A. M., Abraham R. G., Dalton G. B., Carrera F., Smith P. J., Rowan-Robinson M., Abraham R. G., 1998. *Mon. Not. R. astr. Soc.*, **295**, 641.

McLeod K. K., Rieke G. H., 1995. *Ap. J.*, **441**, 96.

McLure R. J., Dunlop J. S., Kukula M. J. 1999. in preparation.

McLure R. J., Kukula M. J., Dunlop J. S., Baum S. A., O'Dea C. P., Hughes D. H., 1999. *Mon. Not. R. astr. Soc.*, **308**, 377.

Meier D. L., 1999. *Ap. J.*, **522**, 753.

Miller J. S., Goodrich R. W., Mathews W. G., 1991. *Ap. J.*, **378**, 47.

Miyoshi M., Moran J., Herrnstein J., Greenhill L., Nakai N., Diamond P., Inoue M., 1995. *Nature*, **373**, 127.

Mobasher B., Guzman R., Aragon-Salamanca A., Zepf S., 1999. *Mon. Not. R. astr. Soc.*, **304**, 225.

Mobasher B., Sharples R. M., Ellis R. S., 1993. *Mon. Not. R. astr. Soc.*, **263**, 560.

Morganti R., Killeen N. E. B., Tadhunter C. N., 1993. *Mon. Not. R. astr. Soc.*, **263**, 1023.

Mulchaey J. S., Koratkar A., Ward M. J., Wilson A. S., Whittle M., Antonucci R. R. J., Kinney A. L., Hurt T., 1994. *Ap. J.*, **436**, 586.

Nandra K., George I. M., Mushotzky R. F., Turner T. J., Yaqoob T., 1997. *Ap. J.*, **477**, 602.

Nandra K., George I. M., Mushotzky R. F., Turner T. J., Yaqoob T., 1997. *Ap. J. Lett.*, **488**, 91.

Neugebauer G., Green R. F., Matthews K., Schmidt M., Soifer B. T., Bennett J., 1987. *Ap. J. Suppl.*, **63**, 615.

Nicholson D., 1990. *PhD thesis*, University of Edinburgh.

Nolan L. A., Dunlop J. S., Jimenez R. 2000. in preparation.

Ogle P. M., Cohen M. H., Miller J. S., Tran H. D., Fosbury R. A. E., Goodrich R. W., 1997. *Ap. J. Lett.*, **482**, 37.

Orr M. J. L., Browne I. W. A., 1982. *Mon. Not. R. astr. Soc.*, **200**, 1067.

Osterbrock D. E., Parker R. A. R., 1965. *Ap. J.*, **141**, 892.

Osterbrock D. E., 1989. *"Astrophysics of gaseous nebulae and active galactic nuclei"*, Mill Valley, CA, University Science Books.

Owen F. N., Laing R. A., 1989. *Mon. Not. R. astr. Soc.*, **238**, 357.

Owen F. N., White R. A., 1991. *Mon. Not. R. astr. Soc.*, **249**, 164.

Packham C., Young S., Hough J. H., Axon D. J., Bailey J. A., 1997. *Mon. Not. R. astr. Soc.*, **288**, 375.

Packham C., Young S., Hough J. H., Tadhunter C. N., Axon D. J., 1998. *Mon. Not. R. astr. Soc.*, **297**, 936.

Padovani P., Urry C. M., 1990. *Ap. J.*, **356**, 75.

Pauliny-Toth I. I. K., Kellermann K. I., 1968. *Astron. J.*, **73**, 953.

Peacock J. A., Nicholson D., 1991. *Mon. Not. R. astr. Soc.*, **253**, 307.

Peacock J. A., Wall J. V., 1981. *Mon. Not. R. astr. Soc.*, **194**, 331.

Peacock J. A., Miller L., Longair M. S., 1986. *Mon. Not. R. astr. Soc.*, **218**, 265.

Penston M. V., Cannon R. D., 1969. *Commmunications of the Konkoly Observatory, Hungary*, **65**, 485.

Peterson B. M., 1993. *Publ. Astron. Soc. Pacific*, **105**, 27.

Pogge R. W., 1988. *Ap. J.*, **328**, 519.

Press W. H., Teukolsky S. A., Vetterling W. T., Flannery B. P., 1996. *Numerical Recipes in Fortran 77: The art of Scientific Programming*, Cambridge University Press.

Prestage R. M., Peacock J. A., 1988. *Mon. Not. R. astr. Soc.*, **230**, 131.

Rieke G. H., Lebofsky M. J., 1985. *Ap. J.*, **288**, 618.

Rowan-Robinson M., 1977. *Ap. J.*, **213**, 635.

Salpeter E. E., 1955. *Ap. J.*, **121**, 161.

Sandage A., 1965. *Ap. J.*, **141**, 1560.

Sanders D. B., Phinney E. S., Neugebauer G., Soifer B. T., Matthews K., 1989. *Ap. J.*, **347**, 29.

Sargent W. L. W., Schechter P. L., Boksenberg A., Shortridge K., 1977. *Ap. J.*, **212**, 326.

Scalo J. M., 1986. *Fundamentals of Cosmic Physics*, **11**, 1.

Scheuer P. A. G., Readhead A. C. S., 1979. *Nature*, **277**, 182.

Schlegel D. J., Finkbeiner D. P., Davis M., 1998. *Ap. J.*, **500**, 525.

Setti G., Woltjer L., 1989. *Astron. Astrophys.*, **224**, L21.

Seyfert C. K., 1943. *Ap. J.*, **97**, 28.

Simkin S. M., 1974. *Astron. Astrophys.*, **34**, 129.

Simpson C., Ward M., Kotilainen J., 1994. *Mon. Not. R. astr. Soc.*, **271**, 250.

Simpson C., Ward M., Wall J. V. 1999. in preparation.

Simpson C., 1994a. *PhD thesis*, The University of Oxford.

Simpson C., 1994b. *Mon. Not. R. astr. Soc.*, **271**, 247.

Simpson C., 1998. *Mon. Not. R. astr. Soc.*, **297**, L39.

Singal A. K., 1993. *Mon. Not. R. astr. Soc.*, **262**, L27.

Smith E. P., Heckman T. M., Illingworth G. D., 1990. *Ap. J.*, **356**, 399.

Statler T. S., 1995. *Astron. J.*, **109(3)**, 1371.

Stockton A., Ridgway S. E., Lilly S. J., 1994. *Astron. J.*, **108**, 414.

Tadhunter C., Tsvetanov Z., 1989. *Nature*, **341**, 422.

Tadhunter C. N., c. Packham, Axon D. J., Jackson N. J., Hough J. H., Robinson A., Young S., Sparks W., 1999. *Ap. J. Lett.*, **512**, 91.

Tadhunter C. N., Metz S., Robinson A., 1994. *Mon. Not. R. astr. Soc.*, **268**, 989.

Tanaka Y., Nandra K., Fabian A., Inoue H., Otani C., Dotani T., Hayashida K., Iwasawa K., Kii T., Kunieda H., Makino F., Matsuoka M., 1995. *Nature*, **375**, 659.

Taylor G. L., Dunlop J. S., Hughes D. H., Robson E. I., 1996. *Mon. Not. R. astr. Soc.*, **283**, 930.

Terlevich R., Tenorio-Tagel G., Franco J., Melnick J., 1992. *Mon. Not. R. astr. Soc.*, **255**, 713.

Terlevich R. J., Tenorio-Tagle G., Rozyczka M., Franco J., Melnick J., 1995. *Mon. Not. R. astr. Soc.*, **272**, 198.

Thornton, R. J. J., Stockton A., Ridgway S. E., 1999. *Astron. J.*, **118**, 1461.

Tonry J., Davis M., 1979. *Astron. J.*, **84(10)**, 1511.

Tonry J., Davis M., 1981. *Ap. J.*, **246**, 666.

Toomre A., Toomre J., 1972. *Ap. J.*, **178**, 623.

Toomre A., 1977. *Ann. Rev. Astron. Astrophys.*, **15**, 437.

Trager S. C., Worthey G., Faber S. M., Burstein D., Gonzalez J. J., 1998. *Ap. J. Suppl.*, **116**, 1.

Trager S. C., 1997. *PhD thesis*, University of California, Santa Cruz.

Turner T. J., George I. M., Nandra K., Mushotzky R. F., 1998. *Ap. J.*, **493**, 91.

Ueno S., Koyama K., Nishida M., Yamauchi S., Ward M. J., 1994. *Ap. J. Lett.*, **431**, 1.

Ulrich M.-H., Maraschi L., Urry C. M., 1997. *Ann. Rev. Astron. Astrophys.*, **35**, 445.

Urry C. M., Padovani P., 1995. *Publ. Astron. Soc. Pacific*, **107**, 803.

Van Der Marel R. P., 1999. *Astron. J.*, **117**, 744.

Ward M. J., Blanco P. R., Wilson A. S., Nishida M., 1991. *Ap. J.*, **382**, 115.

Weedman D. W., 1976. *Quar. J. R. astr. Soc.*, **17**, 227.

White S. D. M., Huchra J., Latham D., Davis M., 1983. *Mon. Not. R. astr. Soc.*, **203**, 701.

Wilson A. S., Tsvetanov Z. I., 1994. *Astron. J.*, **107**, 1227.

Woltjer L., 1959. *Ap. J.*, **130**, 38.

Worthey G., Ottaviani D. L., 1997. *Ap. J. Suppl.*, **111**, 377.

Worthey G., Faber S. M., Gonzalez J. J., Burstein D., 1994. *Ap. J. Suppl.*, **94**, 687.

Worthey G., Faber S. M., Gonzalez J. J., 1992. *Ap. J.*, **398**, 69.

Worthey G., 1994. *Ap. J. Suppl.*, **95**, 107.